DETECTION OF EXHAUST PARTICULATE INDUCED BLOOD CLOTTING ANOMALIES USING RHEOMETRIC TECHNIQUES

Rebecca Hudson

BEng, MSc

Submitted to Swansea University in fulfilment of the requirements for the degree of Doctor of Philosophy

Swansea University

2020

Abstract

Characterisation of viscoelastic materials through exploitation of the frequency independent gel point (GP) can be used to study blood clotting anomalies. Information regarding the sol-gel transition can be obtained for gelling systems by employing small amplitude oscillatory shear (SAOS) measurements over a range of oscillatory shear frequencies. Analysis of the fractal dimension, d_f, at the GP has previously been used as a biomarker for pathologies related to thromboembolic disease. This thesis investigates the potential adverse clotting characteristics induced by the presence of exhaust particulates using rheometric techniques.

SAOS experiments conducted using a combined motor transducer (CMT) rheometer are susceptible to inertial artefacts at high frequencies, leading to potentially significant error in the reported GP. Herein, the development and evaluation of an enhanced rheometer inertia correction procedure (ERIC) is shown to allow valid GP data to be obtained post-acquisition at previously inaccessible frequencies. The potential impact of soot particulates on coagulation is likely to be small due to the weakly elastic gelling systems being studied, thus necessitating the use of the ERIC procedure to remove the presence of any inertial artefacts causing miscalculation of the GP.

Fibrin gels were studied as model blood clots to assess the effects of the inclusion of soot particulates on the GP. The impact of the inclusion of increasing concentrations of soot solution on the GP proved inconclusive after the application of ERIC. However, in whole blood clots, the post-ERIC GP d_f data indicated an increase in the density of the clot formed with increasing soot concentration, suggesting an elevated health risk as a possible result of interruption of the clotting cascade due to soot particulates.

Declarations and Statements

This work has not previously been accepted in substance for any degree and is not being concurrently submitted in candidature for any degree.

Signed [redacted]

Dated ….2nd December 2020...

(Candidate)

This thesis is the result of my own investigations, except where otherwise stated. Other sources are acknowledged by footnotes giving explicit references. A bibliography is appended.

Signed [redacted]

Dated ….2nd December 2020...

(Candidate)

I hereby give consent for my thesis, if accepted, to be available for photocopying and for inter-library loan, and for the title and summary to be made available to outside organisations.

Signed [redacted]

Dated ….2nd December 2020…

(Candidate)

Certificate of Originality

This thesis is submitted to Swansea University under the supervision of Dr D J Curtis of the College of Engineering in Swansea University in candidature for the degree of Doctor of Philosophy. The material in this thesis is the original work of the author except where acknowledgment to other authors is expressed.

Signed …[redacted]

Dated ….2nd December 2020….

Rebecca Hudson

(Candidate)

Signed ..[redacted]

Dated ….2nd December 2020...

Dr D J Curtis

(Supervisor)

Table of Contents

Acknowledgements

Firstly, I would like to thank Dr D. J. Curtis for his continued guidance, support and supervision over the course of my PhD. I also extend my thanks to Prof. P. R. Williams and Prof. K. M. Hawkins for their advice and expertise. Special thanks go to Dr A. J. Holder for his assistance through my experimental work.

My sincere thanks also go to Swansea University, the British Society of Rheology (BSR) and the National Research Network (NRN) Wales for their financial support.

I would like to thank all the generous blood donors who made the work herein possible. I appreciate the time that each volunteer found (often on multiple occasions) to help me continue my research. I am indebted to the phlebotomists for their skills and for giving up their time to take blood donations.

I would like to acknowledge Dr E. Durand (Cardiff University) for providing the soot solution used throughout the work presented in this thesis.

A heartfelt thank you goes to my family and friends who have gone through every step of this journey with me. Special thanks must go to my parents, for always being on the end of the phone, painstakingly reading every word and providing an immeasurable amount of encouragement. Finally, I would like to express my gratitude and appreciation to my partner Chris, who's belief and support has never wavered, I am so grateful.

List of Figures

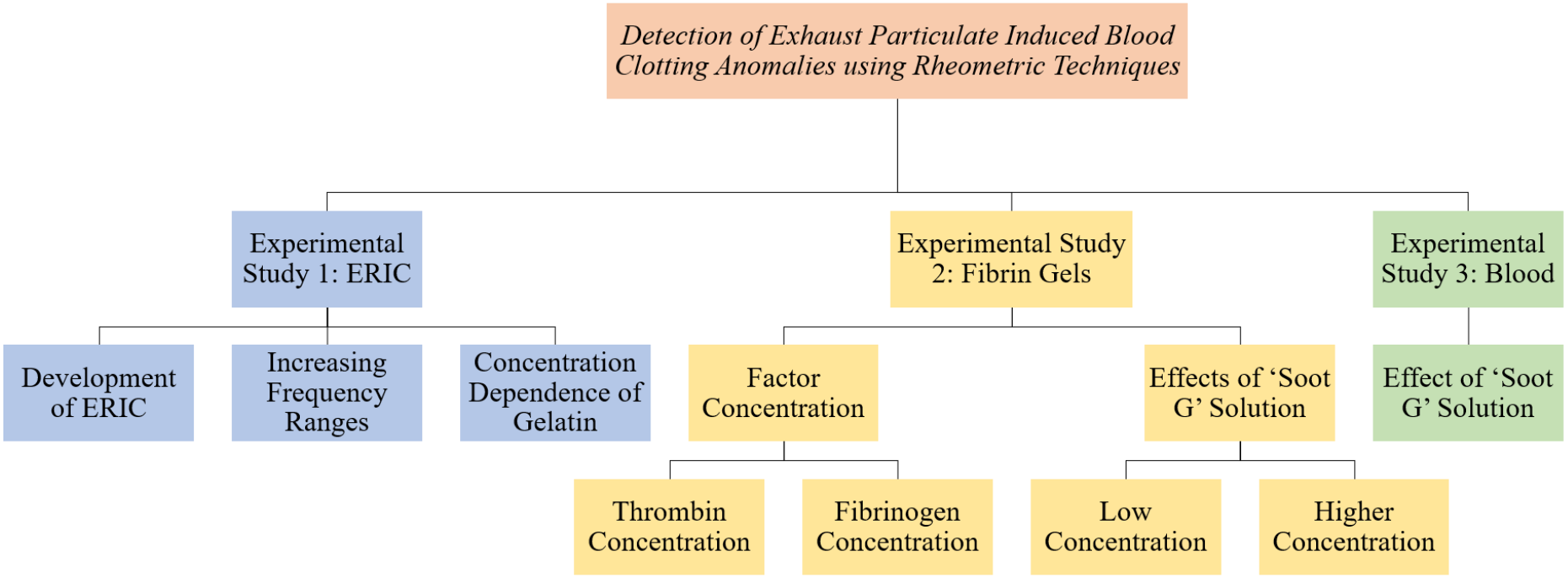

Visual overview of experimental work conducted as part of this thesis.

Chapter 1 Rheology and Rheometry

1.1 Overview

The flow and deformation behaviour of materials has long been studied, but only in recent decades has the field of rheology developed into the diverse discipline it is today. 'Rheology' can be defined as the 'study of the deformation and flow of matter' (1–3). Works by both Hooke and Newton in the 17th Century present the boundaries of present day rheology (4). Hooke referred to 'springs' in his 'Theory of Elasticity' (1678), whilst Newton's 1687 'Principia' detailed 'lack of slipperiness' (2).

Not all materials can be described as Newtonian fluids or as Hookean solids as these characteristics are displayed at the limits of the material (where the phase angle between the input and output waveforms is $\delta = 90°$ and $\delta = 0°$, respectively). Between these limits, materials exhibit viscoelastic properties studied by rheologists (3).

Many studies have been conducted on the gelation of polymer solutions (5–7) and the work presented herein focuses on gelatin, fibrin-thrombin gel systems and blood clots. The sensitivity of the rheological properties of biopolymer gels to their underlying microstructure lends itself to the detection of clotting anomalies as a result of the presence of particulate matter, specifically soot.

1.2 Hookean solids

For a Hookean solid, an instantaneous finite deformation response is observed upon the application of a shear stress, σ, to an unstrained system. The deformation remains constant whilst the stress, σ, is applied (2). Elastic materials obey Hooke's Law which states that the shear stress is proportional to the applied strain. This can be represented mathematically as:

$$\sigma = G\gamma \qquad \text{Equation 1.1}$$

The constant of proportionality, G, is referred to as the 'elastic modulus' whilst γ denotes strain. Upon removal of the stress, the material returns to its original state.

1.3 Newtonian Liquids

Newtonian fluids exhibit a linear relationship between shear stress, σ, and shear strain rate, $\dot{\gamma}$. The viscosity of a Newtonian fluid is dependent on the temperature and

pressure. Examples of Newtonian fluids are water and glycerine (2,8). If a stress, σ, is applied to the system, there is an instantaneous strain rate response, $\dot{\gamma}$. If zero stress is applied, there is a resulting zero shear strain rate. The deformation rate is independent of time until the applied stress is removed.

The viscosity of the fluid is defined by the derivative of the stress-strain relationship and for a Newtonian fluid (which displays a shear rate independent viscosity) can be defined mathematically as:

$$\sigma = \mu\dot{\gamma} \qquad \text{Equation 1.2}$$

Flow occurs when adjacent layers in the fluid move relative to each other, causing the fluid to deform (1). Individual planes within the fluid are represented by 'A' in Figure 1-1.

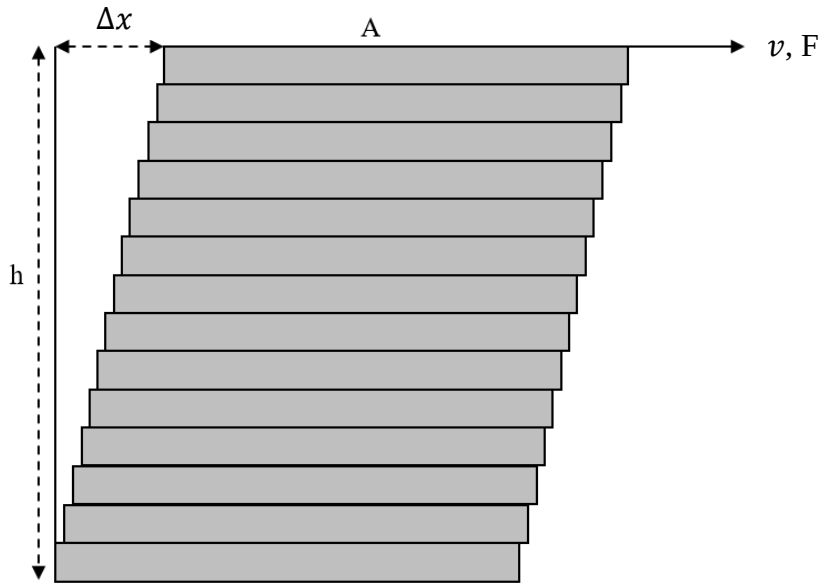

Figure 1-1 *A diagram of the hypothetical layers that allow deformation of the fluid when a stress is applied. The area , A, and the force, F, applied to the fluid are used to determine the stress component whilst the displacement, x, and velocity, v along with the height, h, can be used to determine the strain and strain rate respectively as shown in Equations 1.3 and 1.4.*

The deformation gradient between the hypothetical layers in the fluid, the shear strain, γ, can be determined by Equation 1.3. The upper-most layer in the fluid will have the highest displacement, which is defined as Δx (Figure 1-2), whilst the lowest layer remains stationary.

$$\gamma = \frac{\Delta x}{h} \qquad \text{Equation 1.3}$$

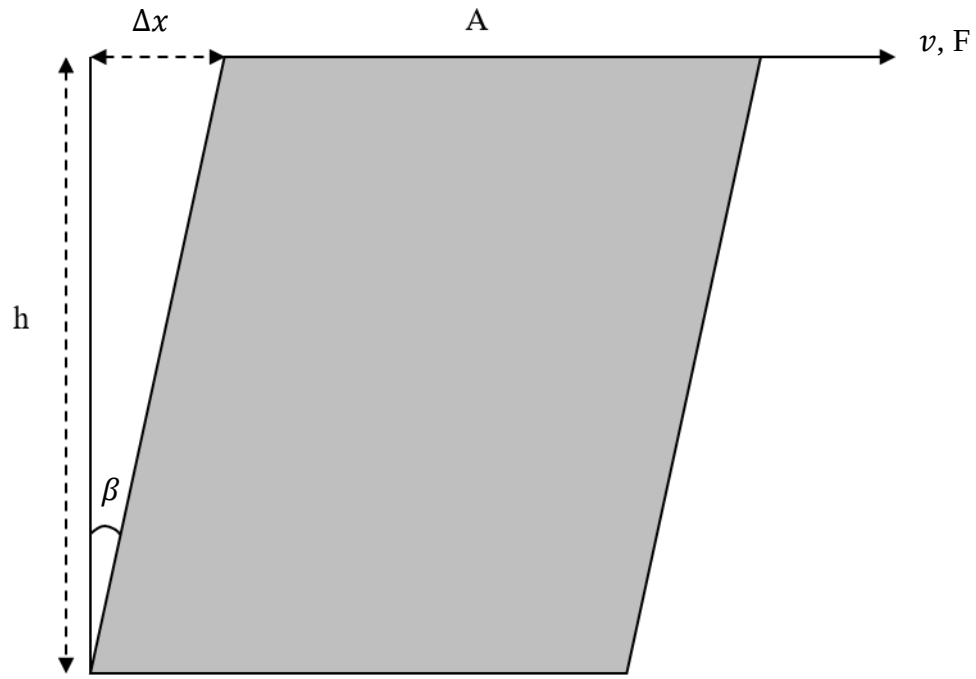

Figure 1-2 *A simple shear flow diagram. The parameters presented can be used to determine the shear strain and shear strain rate.*

The shear strain increases as stress is applied provided the constituent components of the fluids can move relative to each other (8). The velocity gradient at right angles to the direction of flow is called the shear strain rate (2) and is defined as $\dot{\gamma}$ in Equation 1.4. It is the rate of change of strain within the fluid over time. If the force applied to the fluid is doubled, the velocity gradient also doubles (2).

$$\dot{\gamma} = \frac{v}{h} \qquad \text{Equation 1.4}$$

Shear stress can be defined as the force per unit area (1) and is represented by σ as shown:

$$\sigma = \frac{F}{A} \qquad \text{Equation 1.5}$$

The viscosity of a material can be defined as its resistance to deformation (9). For Newtonian fluids undergoing simple shear flow, the viscosity can be defined by rearranging Equation 1.2 to give;

$$\mu = \frac{\sigma}{\dot{\gamma}} \qquad \text{Equation 1.6}$$

1.4 Non-Newtonian Liquids

Non-Newtonian fluids display a non-linear relationship between shear stress, σ, and shear strain rate, $\dot{\gamma}$. The viscosity of a non-Newtonian fluid is dependent on the shear strain rate applied. Examples of non-Newtonian fluid behaviour include shear thinning and shear thickening (Figure 1-3). Shear thinning behaviour is the most commonly seen category of non-Newtonian fluid and is observed when the viscosity of the fluid decreases as the shear strain rate increases (8). An example of an everyday shear thinning fluid is tomato ketchup (10). Blood also demonstrates shear thinning properties (11). Shear thickening behaviour involves viscosity increases due to an increase in the applied shear strain rate. Corn starch solutions are examples of shear thickening systems (12). Materials may also exhibit a yield stress which must be overcome before viscous flow occurs. Sludges provide an example of such materials (13).

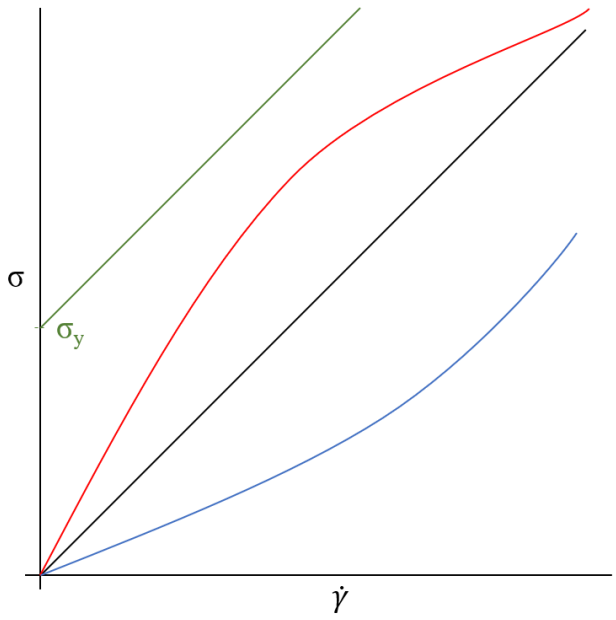

Figure 1-3 *Flow curves for Newtonian (black), shear-thinning (red), shear thickening (blue) and Bingham plastic (green) behaviour in fluids. The yield stress of the Bingham plastic is represented by* σ_y.

1.5 Linearity

A linear system is described by the Boltzmann superposition principle (Equation 1.7) such that 'each stress applied to a material produces a strain independent of that produced by other stresses' (14,15). If the stress applied to the material is increased by a given factor, the resulting strain response will also increase by the same factor (2).

$$\sigma = \int_{-\infty}^{t} G(t-t')\dot{\gamma}(t')dt' \qquad \text{Equation 1.7}$$

1.5.1 Linear Viscoelastic Region

The linear viscoelastic region (LVR) is the region in which the dynamic processes within the system can be determined without compromising the microstructure of the sample (16). Within the LVR, it can be assumed that the storage modulus, G', and the loss modulus, G'', are independent of strain amplitude and that an oscillatory wave response is sinusoidal (17). The superposition principle suggests small strains, indicating that the linear viscoelastic limit is a few per cent (14). Hawkins et al. determined using harmonic analysis that for fibrin gels, the strain limit should not exceed 2% (18).

In materials undergoing a sol-gel transition, it is possible to analyse the linearity of the data obtained by monitoring the harmonic ratios within the system. During the application of an oscillatory shear stress, the third harmonic contribution can be used to analyse the degree of the non-linear response of the sample (18,19). The third harmonic is typically monitored as it generally gives the most intense response with respect to the fundamental frequency (17). The waveform can be assumed to be sinusoidal without the presence of harmonics. If the shape of the reported waveform is no longer sinusoidal, it suggests that the data is no longer linear.

Probing a material outside of the LVR requires additional parameters to fully describe the materials response, for example, the harmonic response (20) or more complex descriptions of non-linear viscoelastic behaviour as reviewed by Hyun et al (17). Large Amplitude Oscillatory Shear (LAOS) experiments can be conducted to assess the non-linear viscoelastic response of complex fluids. The response waveform in the non-linear regime deviates from a sinusoidal waveform as G' and G'' are a function of the strain amplitude (17) and are undefined outside of the LVR.

1.6 Viscoelasticity

Viscoelastic materials have both viscous and elastic characteristics. The linear-viscoelastic response of a sample can give an indication as to the microstructure of the materials (2). The elastic component can be represented using a 'spring' and viscous behaviour can be described using a 'dashpot' (Figure 1-4).

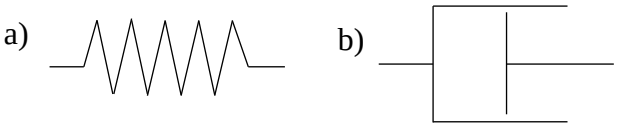

Figure 1-4 *Representation of a) a 'spring' used to describe an elastic element and b) a 'dashpot' used to characterize the viscous element in a rheological system.*

1.6.1 Viscoelastic Solid

If a shear stress, σ, is applied to the surface of a material, a Hookean solid is immediately deformed and remains deformed until the stress is removed (2). The model used to describe a viscoelastic solid (VES) undergoing strain is the Kelvin-Voigt model (Section 1.7.2). Equation 1.1 can be rewritten as Equation 1.8 to show the relationship between the stress and the strain is linear with G as the constant of proportionality (15). The lag between the input and output waves can be determined as the phase angle, δ. Due to the linear relationship, the lag between the sinusoidal input strain wave and output stress wave is said to be 'in-phase' and $\delta = 0°$ (Figure 1-5 and Equation 1.9). A material displaying a phase angle of 0° is said to be purely elastic.

$$G = \frac{\sigma}{\gamma} \qquad \text{Equation 1.8}$$

$$\delta = \tan^{-1}\frac{G''}{G'} = 0 \qquad \text{Equation 1.9}$$

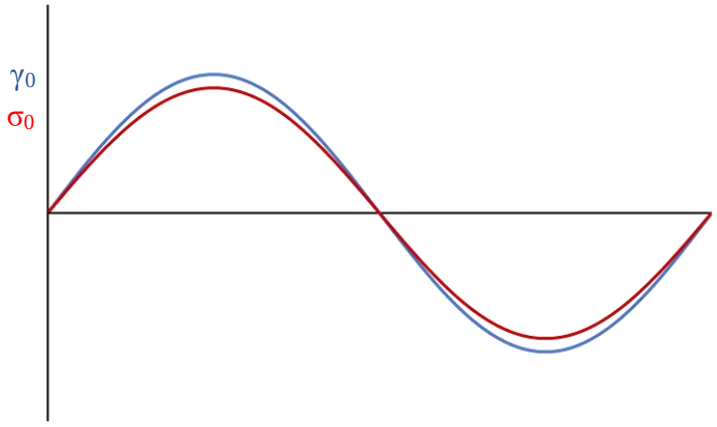

Figure 1-5 *Input stress waveform (red) and output strain waveform (blue) for a viscoelastic solid.*

1.6.2 Viscoelastic Liquid

For liquids displaying viscoelastic characteristics, the term 'viscoelastic liquid' (VEL) is used. Such materials can be described by the Maxwell model (Section 1.7.1). For Newtonian liquids, as described in Section 1.3, the stress is linearly related to the shear strain rate. In this case, stress and strain are 90° 'out of phase' as indicated by the lag between the input and output waves (Figure 1-6). Values of δ approaching 90° (when $\delta \leq 90°$) represent highly viscoelastic behaviour of a material undergoing oscillatory shear (15).

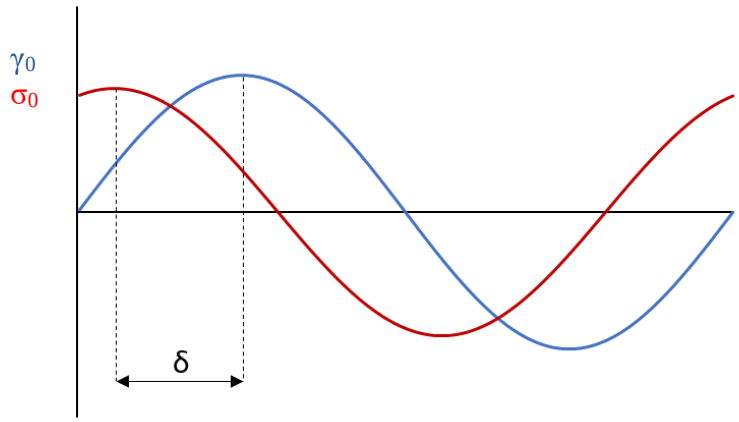

Figure 1-6 *Input (blue) and output (red) waveforms for a viscoelastic liquid.*

1.7 Mechanical Models

Simple mechanical models can be useful tools when thinking about viscoelastic behaviour. As discussed in Section 1.6, these models are built on the concept of 'springs' and 'dashpots' to represent elastic and viscous behaviour of a material respectively.

1.7.1 Maxwell Model

A Maxwell model is comprised of spring and dashpot components in series configuration, as seen in Figure 1-7. It is commonly used to describe behaviour of viscoelastic liquids over a typical frequency range of 10^{-2} to 10^{2} Hz (1). In a step strain experiment, the spring element will instantaneously respond, whereas the movement of the piston through the dashpot causes a reduction in the stress on the spring over time (15).

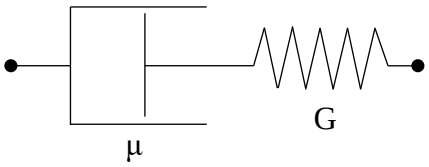

Figure 1-7 *A schematic diagram of a simple Maxwell model used to describe viscoelastic behaviour. Viscosity is represented by μ and G refers to the elastic modulus.*

If a step strain is applied to a single Maxwell element, the rate of extension can be established as Equation 1.10 (14). This can be rewritten for $t > 0$ by integrating with respect to time to give Equation 1.11, which describes the stress decay over time when a step strain is applied (15).

$$\frac{d\dot{\gamma}}{dt} = \frac{1}{G}\frac{d\sigma}{dt} + \frac{1}{\mu}\sigma \qquad \text{Equation 1.10}$$

$$\sigma = G\gamma_0 e^{-\frac{Gt}{\mu}} \qquad \text{Equation 1.11}$$

From Equation 1.11, the relaxation time, τ, of the system is can be defined in Equation 1.12 (14).

$$\tau = \frac{\mu}{G} \qquad \text{Equation 1.12}$$

The stress relaxation time of a material is the time taken for the stress to relax to $1/e$ of its original value (2).

During the oscillation of a single Maxwell element, the G' and G'' parameters can be determined as Equation 1.13 and Equation 1.14, where ω represents the angular frequency.

$$G' = \frac{G(\omega\tau)^2}{1 + (\omega\tau)^2} \qquad \text{Equation 1.13}$$

$$G'' = \frac{G\tau\omega}{1 + (\omega\tau)^2} \qquad \text{Equation 1.14}$$

The behaviour described by these two equations can be seen in Figure 1-8. The behaviour of the storage and loss modulus for a single Maxwell model describes the initial sections of the viscoelastic spectrum.

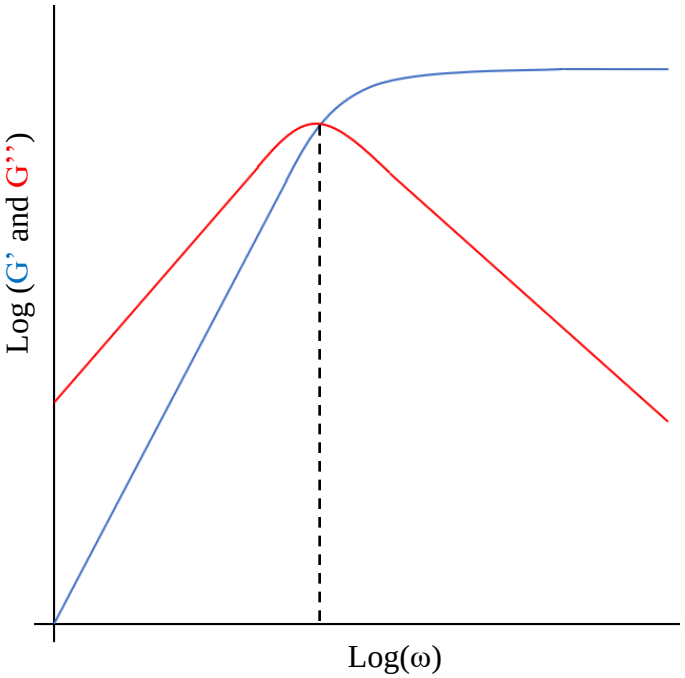

Figure 1-8 *shows the behaviour of G' (blue) and G'' (red) in a Maxwell system under oscillatory conditions. The cross over frequency (dashed line) can be used to determine the relaxation time of the material.*

The relaxation time of a single Maxwell element can also be determined graphically where $G' = G''$ (Figure 1-8). The angular frequency, ω, at the cross over point is related to the relaxation time as shown in Equation 1.15.

$$\omega = \frac{1}{\tau} \qquad \text{Equation 1.15}$$

1.7.2 Kelvin-Voigt Model

A Kelvin-Voigt model represents typical viscoelastic solid behaviour. In a Kelvin-Voigt model, the 'spring' and 'dashpot' components are arranged in a parallel configuration with the fixing remaining square at all times (Figure 1-9). In this arrangement, the strain in the spring is always equal to the strain in the dashpot (2).

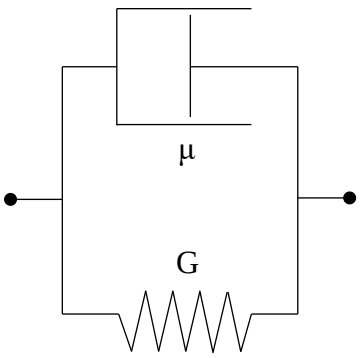

Figure 1-9 *A schematic diagram representing a Kelvin-Voigt Model used to describe viscoelastic behaviour. The elastic modulus is represented by G and μ refers to the viscosity of the sample.*

The forces being applied to the spring and the dashpot can be represented in Equation 1.16 where $G\gamma$ signifies the force on the spring and $\mu\frac{d\gamma}{dt}$ the force on the dashpot (14).

$$\sigma = G\gamma + \mu\frac{d\gamma}{dt} \qquad \text{Equation 1.16}$$

The strain in the system can be described by (14):

$$\gamma = \frac{\sigma_0}{G}\left(1 - e^{-\left(\frac{G}{\mu}\right)t}\right) \qquad \text{Equation 1.17}$$

The retardation time, τ_r, is defined as:

$$\tau_r = \frac{\mu}{G} \qquad \text{Equation 1.18}$$

The total stress, σ_T, for a Kelvin model is given as the sum of the individual stress in each element (2), such that;

$$\sigma_T = \sigma_E + \sigma_V \qquad \text{Equation 1.19}$$

The strain growth within a system fitting a Kelvin model is limited by the retardation time (2). Figure 1-10 shows the development of the stress over time (solid) for a Kelvin model as well as the instantaneous response of a Hookean spring (dashed).

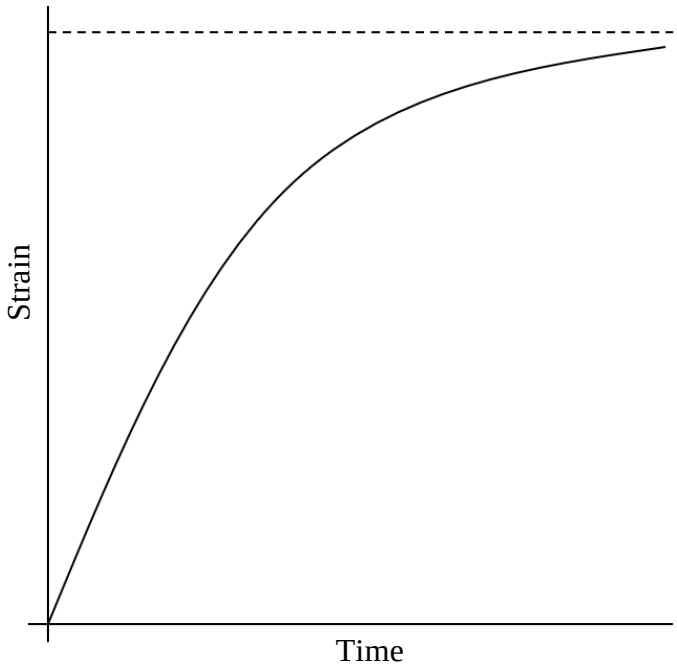

Figure 1-10 *The retarded stress growth experienced by a system described by a Kelvin model. The instantaneous strain response experienced by a Hookean spring is also presented (dashed).*

1.7.3 Burgers Model

Burgers Model is a combination of both a standard Maxwell model and Kelvin Voigt model in a series configuration (Figure 1-11).

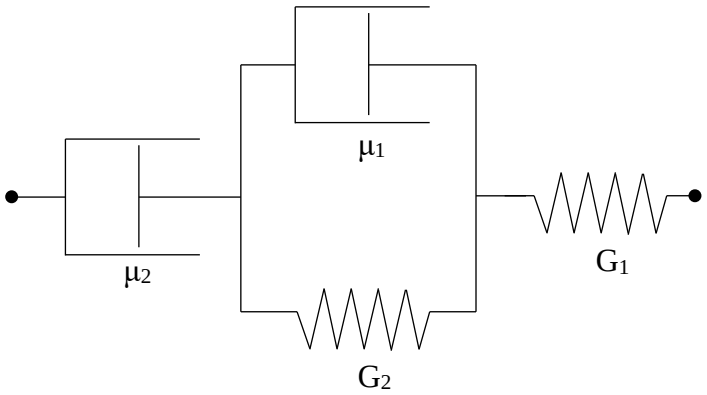

Figure 1-11 *A schematic diagram of a Burgers Model used to represent the viscoelastic behaviour of a material. The viscosity of the sample is represented by μ and the elastic modulus is shown by G.*

By combining the mathematical equations outlined for the Maxwell and Kelvin-Voigt model, Burgers model can be described as in Equation 1.20 (8).

$$\gamma = \sigma\left(\frac{1}{G_1} + \frac{1}{G_2}\left(1 - e^{-\frac{G}{\mu_1}t}\right) + \frac{t}{\mu_2}\right) \qquad \text{Equation 1.20}$$

In a creep experiment, once a stress is applied, the Maxwellian element within the Burgers model exhibits an elastic response whilst the Kelvin-Voigt element displays a delayed response as the spring is inhibited by the dashpot (1,8).

1.8 Stress Relaxation Experiments

Stress relaxation experiments require the sudden application of a constant strain before monitoring the resultant decay in stress with time (1), as seen in Figure 1-12. Whilst ideal Hookean solids do not undergo stress relaxation, viscoelastic solids may display only partial stress relaxation (9). For viscoelastic liquids that are capable of steady-state shearing deformation, the stress will steadily decay if the flow is suddenly stopped and the stress may reduce completely to zero (21). For small deformation within the linear range, the stress relaxation modulus can be defined as

$$G(t) = \frac{\sigma(t)}{\gamma} \qquad \text{Equation 1.21}$$

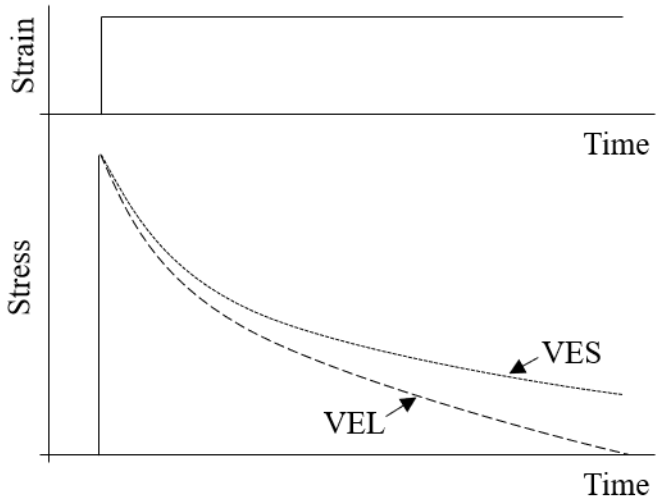

Figure 1-12 *Example of a step transient experiment with the resultant stress decay observed due to stress relaxation. A viscoelastic solid (VES) will relax to a plateau whereas a viscoelastic liquid (VEL) may decay to zero.*

1.9 Small Amplitude Oscillatory Shear Experiments

Small amplitude oscillatory shear (SAOS) is a popular method for assessing the linear viscoelastic behaviour of a material. It involves the application of sinusoidally varying perturbations (either stress or strain), whereas steady shear experiments are sheared in one direction.

The microstructure of materials, such as gels, can be broken down by large amplitude oscillations. A benefit of using SAOS is that the microstructure of the sample material is not compromised (22). Stress controlled SAOS using a combined motor transducer (CMT) rheometer involves a sinusoidal stress waveform being applied to the sample with the upper geometry before the deformation response waveform is analysed at the same plate (9). In contrast, when conducting SAOS experiments using a separate motor transducer (SMT) rheometer, the strain input is applied at one plate, whilst the deformation output is measured at a second geometry (16). It is necessary to conduct SAOS experiments within the linear viscoelastic range (16), whereby the strain limit is not exceeded (23), to ensure that the microstructure of the gelling material is not compromised.

1.10 Artefacts

Rheological data suffers from inertial artefacts that are most apparent at high frequencies (24–27) and sample mutation at low frequencies (28,29). In order to

correct for inertial influences within CMT rheometer data, the Enhanced Rheometer Inertia Correction procedure was developed as discussed in Chapter 3.

1.10.1 Inertial Artefacts

Inertia artefacts can cause erroneous data collection using CMT systems due to the design of the rheometer. The instrument is required to move (i) the sample under investigation and (ii) the rheometer motor, geometry and spindle which all contribute to the total torque. It is not the same case for SMT rheometers, as the torque sensing element does not move, resulting in no instrument inertia artefacts as the torque is determined independently of the motor (30).

Low viscosity fluids, such as weak gelling systems, are particularly susceptible to inertial artefacts (25,26,31). Above the resonant frequency, the G' values errors reported for viscoelastic gels can increase quadratically (24). In the context of gelling materials, inertial artefacts are most dominant when gel networks with weak structures are subjected to high frequencies (24–27). To avoid the exaggerated response caused by instrument inertia, the material torque, M_m, must exceed the torque required to operate the instrument, M_i, (Equation 1.22) (31). The loss modulus, G'', is unaffected by the presence of instrument inertia.

$$M_m > M_i \qquad \text{Equation 1.22}$$

The δ_{raw} is a measure of the phase shift between the displacement and the torque signals measured by the instrument (32) where $\delta_{raw} < 180°$ (31). It is often used as an indication of the extent to which the inertial artefacts pollute the raw data. Instrument manufacturers recommend caution where the raw phase angle exceeds 150° (9,31,32). Since the phase angle for a viscoelastic material is in the range of $0° < \delta < 90°$, any reported $\delta_{raw} > 90°$ must contain an inertial artefact element (31).

To correct for the effects of inertia caused by the rheometer itself prior to each experiment, a standard inertia calibration (SIC) procedure is required. The procedure involves calibrating the system without the presence of a sample so that the geometry inertia and instrument inertia can be determined. The software used to control the TA Instruments CMT rheometers, TRIOS, uses the calibrated values to routinely apply an inertia correction to the reported storage modulus (G'_{raw}), such that

$$G' = G'_{raw} - I_c \omega^2 k_g \qquad \text{Equation 1.23}$$

where I_c denotes a calibrated Inertia Constant and k_g a geometry factor (32). It is only possible to determine the inertia constant to a finite precision, resulting in some uncertainty regarding the accuracy of G' extracted from the raw waveforms where a substantial proportion of the G'_{raw} term is dominated by a large $I_c\omega^2 k_g$ term.

1.11 Loss and storage moduli

1.11.1 Storage Modulus

The storage modulus, G', can be described as the magnitude of the stress in-phase with the strain (33) and is a measure of the solid like response (recoverable energy) due to deformation of the material (1) (Equation 1.24). When $\delta = 0°$, G' is equal to the complex modulus, G^*.

$$G' = \frac{\sigma_0}{\gamma_0}\cos(\omega t) \qquad \text{Equation 1.24}$$

1.11.2 Loss Modulus

The loss modulus, G'', quantifies the component of stress which is 90° out of phase with the applied stress waveform (33) and is defined as the measure of the energy dissipated by the material in a single oscillation (Equation 1.25).

$$G'' = \frac{\sigma_0}{\gamma_0}\sin(\omega t) \qquad \text{Equation 1.25}$$

1.11.3 Complex Modulus

The complex modulus, G^*, is defined as the overall resistance of a material to deformation (34) and can be calculated as the ratio of peak stress, σ_0, and peak strain, γ_0.

$$G^* = \frac{\sigma_0}{\gamma_0} \qquad \text{Equation 1.26}$$

Alternatively, it may be calculated from real and imaginary parts of the response (G' and G'' respectively) as:

$$G^* = G' + iG'' \qquad \text{Equation 1.27}$$

1.11.4 Loss tangent

The loss tangent shown in Equation 1.28 can be used as a measure of the ratio of energy lost to energy stored in a cyclic deformation (21). From the storage and loss moduli, the loss tangent of a material can be defined as an alternative method for determining δ as seen in Equation 1.16. Previous studies (35,36) have used $tan\delta = 1$ to estimate the GP at the point at which $G' = G''$. This is not feasible as the cross over between the

$G'(t)$ and $G''(t)$ moduli cannot be applied to all polymer networks. For a gelling materials, G' and G'' scale as identical power laws with respect to frequency, $G' \sim G'' \sim \omega^{\alpha}$, where $0 < \alpha < 1$ (37).

$$\tan(\delta) = \frac{G''}{G'} \qquad \text{Equation 1.28}$$

1.11.5 Viscoelastic spectrum

The viscoelastic master curve shown in Figure 1-13 is representative of viscoelastic fluid behaviour over a wide frequency range, usually in the range of 0.1 to 100 rad s^{-1} (16). The regions within the plot are defined as the 'viscous/terminal' region, 'transition to flow' region, 'rubbery/plateau' region, 'leathery/transition' region and the 'glassy region' as the frequency range increases (1). Although material specific, many frequency sweep experiments are conducted in the highlighted region. Though for most materials it is not possible to observe all of the regions in Figure 14, it is possible to extend the range of the viscoelastic data available using time-temperature superposition (TTS). TTS combines the materials viscoelastic properties (for almost exclusively amorphous polymer melts) obtained at varying temperatures and allows measurements over a wide range of frequencies by means of a scale change to build a master curve (38).

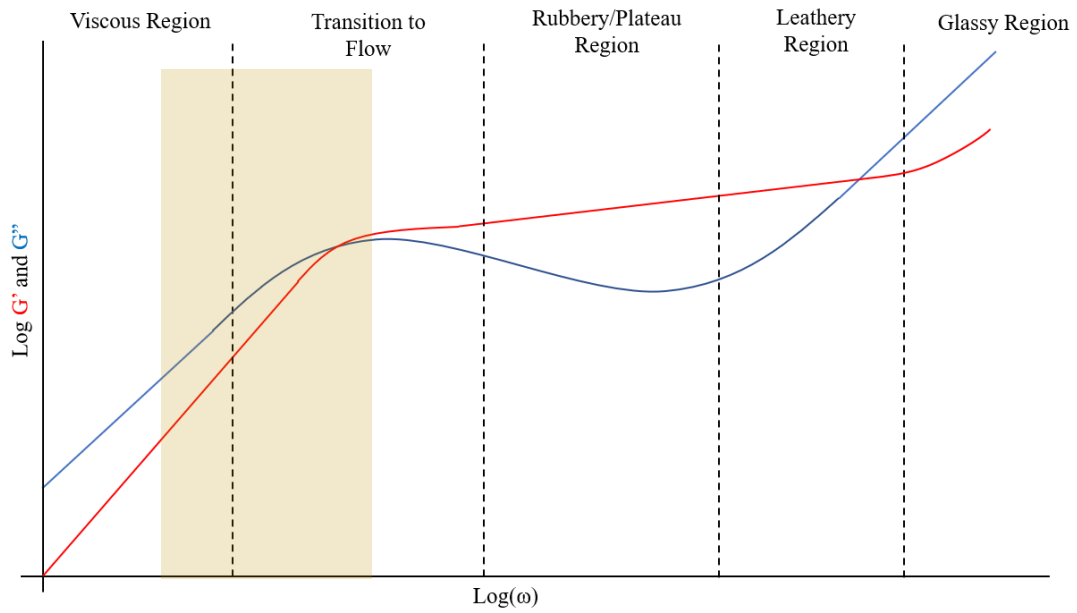

Figure 1-13 *The viscoelastic spectrum for non-Newtonian liquids representing both the storage, G′, (in red) and loss, G", (in blue) moduli through the defined regions.*

The ‘viscous region’ is experienced by all materials as fluids exhibit viscous flow and solids display creep behaviour (1). Both G' and G'' initially increase with frequency and G' is dominant. Due to the inverse relationship between frequency and time, at low frequencies (and therefore long times), liquid-like behaviour is observed (16,39). The viscous region of the spectrum can be described by a simple Maxwell model (15).

Once in the ‘transition to flow region’, G'' and G' cross over. The cross over in G' and G'' is sometimes analysed to determine the longest relaxation time (1).

In the ‘rubbery/plateau region’, the elastic behaviour of the material is dominant as there is a constant increase in the G' component whilst G'' falls to a minimum before increasing again. The ‘plateau’ refers to the flat nature of the G' modulus within the frequency range. In this region, materials exhibit a more elastic, rubbery response.

The penultimate region in the viscoelastic spectrum is termed the ‘leathery region’. In this regime, a second, higher, crossover between the G' and G'' components can be observed. The material in question would be ‘leathery’ to touch as it displays more solid-like behaviour than in previous lower frequency regions. As a result of the high frequency relaxation and dissipation mechanisms of the material, the G'' component increases faster than the G' value (1).

Finally, the moduli pass into the ‘glassy region’ where G'' continues to increase further as frequency increases. The solid-like behaviour observed in the ‘leathery’ and ‘glassy’ higher frequency (and short time) regions (16,39) can be described using a Kelvin-Voigt Model (15). At high frequencies within the glassy region, polymers begin to exhibit a more crystalline structure (2) and as a result ‘glassy behaviour’ is observed.

1.12 Rheometers

For the TA Instruments AR-2000ex, AR-G2 CMT and ARES-G2 SMT rheometers used throughout the work presented herein, there are a large variety of geometry set ups available. The geometry selected is based upon the test material properties.

1.12.1 Combined Motor Transducer Rheometers

For combined motor transducer (CMT) rheometers, the instrument is required to both accelerate the moving components of the rheometer whilst also deforming the sample under investigation. For the work presented herein, studies were conducted using both AR-2000ex and AR-G2 CMT rheometers (both TA Instruments). CMT rheometers,

also referred to as stress controlled rheometers, are susceptible to inertial artefacts in weak gel or low viscosity systems due to the design of the instrument (25), as discussed in Chapter 3.

The key components are housed within the aluminium structure of the rheometer head. A schematic diagram of the discussed components can be seen in Figure 1-14. The drag cup drive motor [4] present in the TA Instruments AR-2000ex and AR-G2 rheometers is non-contact which ensure that the torque to inertia ratio is low (39). The motors are capable of providing a torque range covering 0.1 μN.m to 200 mN.m (40) which allows analysis of a wide range of materials from low viscosity samples to solids (39–41). By avoiding the use of permanent magnets, errors associated with residual torques are eradicated (40).

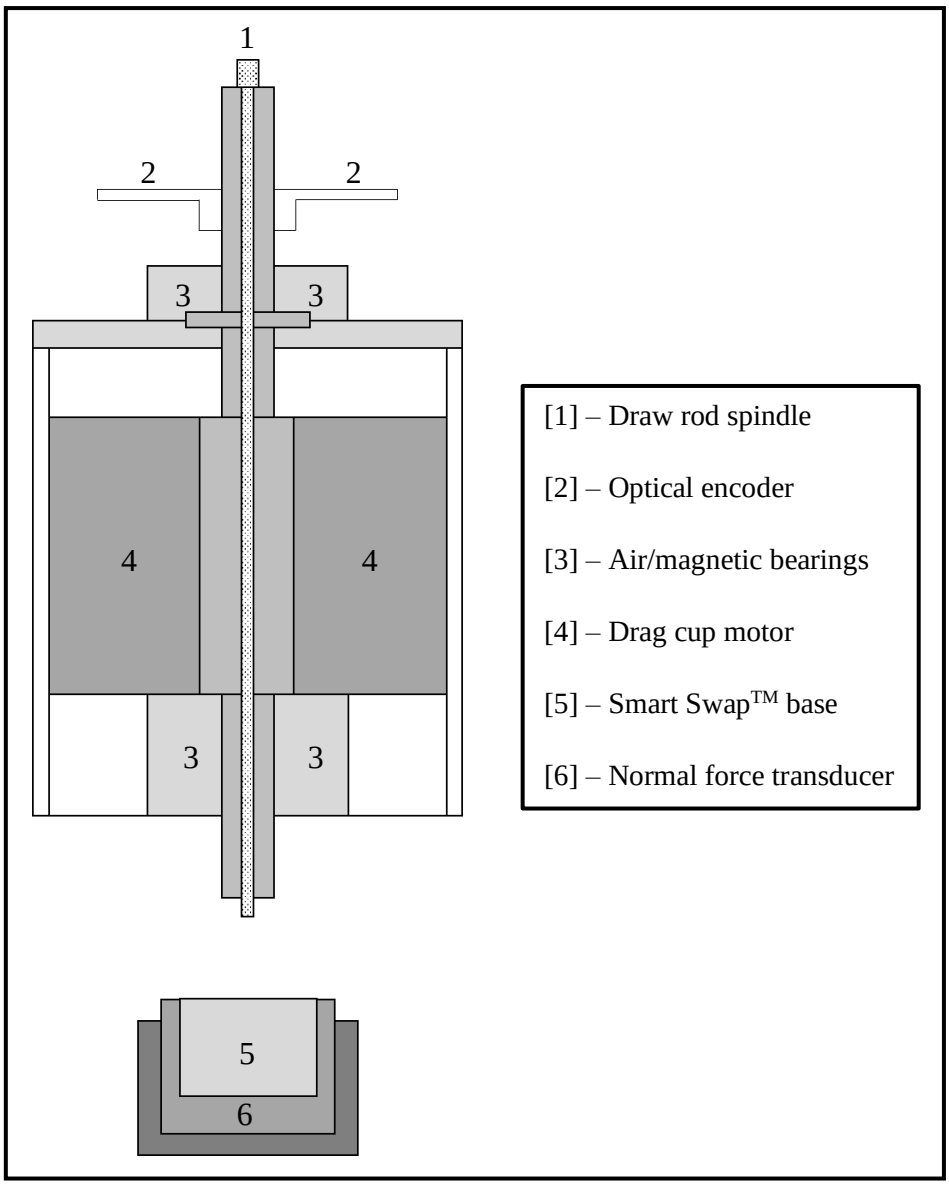

Figure 1-14 *A schematic diagram of a combined motor transducer (CMT) rheometer. The individual components are described by the attached key.*

The frictionless, porous carbon air bearings [3] in the AR 2000ex rheometer result in low levels of residual torque which is corrected during the Rotational Mapping calibration procedure (40). To prevent error due to axial force, the AR2000ex air bearing is ultra-stiff (41). By comparison, the AR-G2 rheometer contains a magnetic bearing [3] (42). Electromagnetic actuators are positioned above and below an iron thrust plate and the current is varied to maintain the position of the bearing (42).

For CMT rheometers, the angular deflection is recorded by the optical encoder [2] which analyses small displacements (strain output) with high resolution ensuring that measurements can be obtained at low and high shear rates (40,41).

The geometry required for each experimental procedure is attached to the CMT rheometers via the draw rod [1]. The head of the instrument is controlled using a linear ball slide (39–41). It is possible to automatically set the required gap using the rheometer software. A vital part of the standard calibration procedure requires 'zero gapping' of the instrument. To achieve this, the normal force is monitored by the normal force transducer [6] with 'zero gap' being identified upon a sudden increase in the normal force (39). The desired temperature control accessory, for example, a Peltier plate, may be attached to the rheometer via a patented Smart Swap™ system in the base of the rheometer (40).

1.12.2 Separate Motor Transducer Rheometers

Several studies reported in this thesis required the use of a separate motor transducer (SMT) ARES-G2 rheometer (TA Instruments). The design and data acquisition methods differ from those outlined for CMT rheometers in Section 1.12.1. The transducer is separate from the moving components of the rheometer, as seen in Figure 1-15. During data acquisition, the torque sensing element remains static (43) such that SMT rheometers are not subject to instrument inertia artefacts.

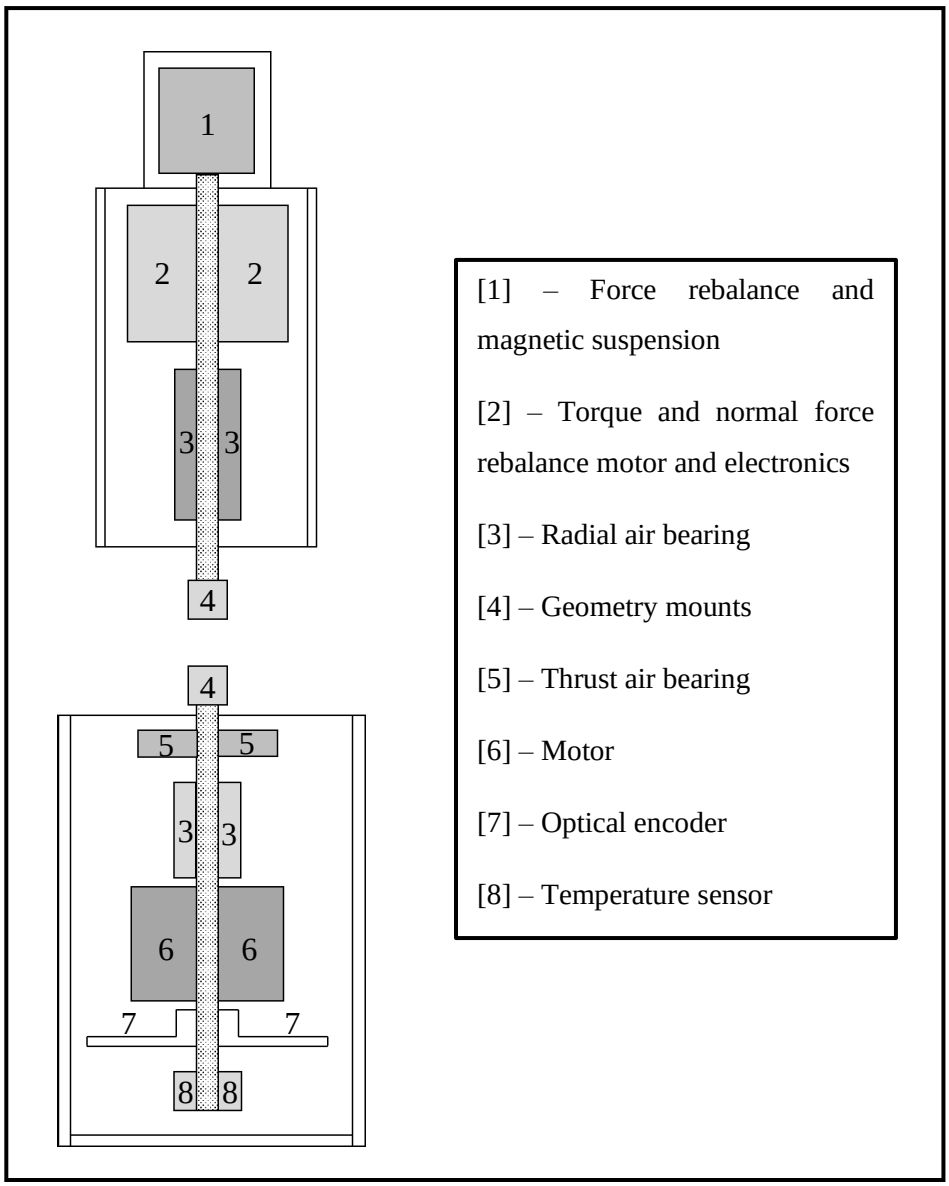

Figure 1-15 *A schematic diagram of a separate motor transducer (SMT) rheometer. The motor and the torque sensing element are separate therefore eliminating inertial artefacts from the system.*

1.12.3 Peltier Plate

Peltier plates are a typical temperature control system (Figure 1-16) employed with cone and plate, parallel plate and concentric cylinder geometries. The system uses the Peltier thermoelectric effect [3] to rapidly and accurately control heating and cooling of the plate surface (44). The direction of the current applied between the semiconductors results in either heating or cooling of the Peltier plate (14). Peltier plate systems suitable for use with AR-2000ex and AR-G2 rheometers can operate in the range of -20 °C up to 200 °C accurate to ± 0.1 °C (39,41). A platinum sensor [2] is required in the centre of the set up to ensure ease of measurement and control. The

chrome surface [1] of the Peltier plate is ideal for use with biological samples as the surface is resilient and easy to clean. A separate water bath is required to ensure that the Peltier system does not overheat over long periods of continuous use.

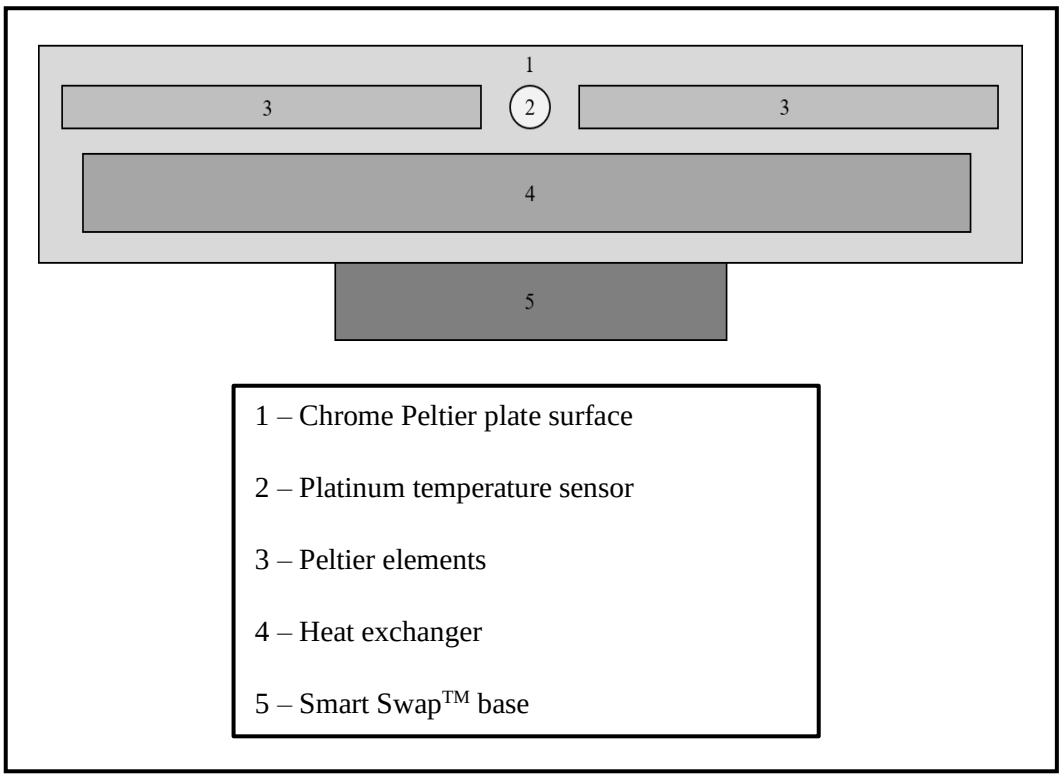

Figure 1-16 *A schematic Peltier plate set-up commonly used with combined motor transducer (CMT) rheometers. The individual components of the system are described in the adjoining key.*

1.12.4 Loading Criteria

1.12.4.1 'Gap Loading' Criterion

Sample inertia can be considered negligible by ensuring that the 'gap loading' criterion is met (45). The velocity gradient across the geometry is treated as uniform throughout the sample material if the density of the sample is small compared with $\frac{G\prime}{d^2 f^2}$ where d is the shearing gap and f is the oscillating frequency, thus satisfying the 'gap loading' criterion. (15,21,45). Shearing gaps should be $d < 2mm$ (15). To satisfy the criteria, the studies presented herein used gaps that were carefully considered to ensure that an appropriate shearing gap was used for the materials being tested.

1.12.4.2 'Surface Loading' Criterion

The 'surface loading' limit requires the volume of solution in contact with the driven surface to be sufficiently large in order to prevent interference from shear waves reflected from other boundaries (45). For viscoelastic materials, the shearing gap is

required to be sufficiently large so that the amplitude of the waveform becomes negligible before the opposite surface is reached (21). If the 'surface loading' limit is not met, the inertial effects present within the sample are dominant (45).

1.12.5 Geometries

In combination with the rheometers and Peltier plate accessory systems outlined in Section 1.12, a well-defined sample geometry must be used for rheological tests to ensure shear rate and strain parameters are correctly identified. Geometries vary in size and material, dependent on the samples being tested. Typically, upper geometries are available in stainless steel, titanium, aluminium and acrylic (40) in 20 mm, 40 mm, 50 mm and 60 mm diameters (9,39,41).

The stress wave may be applied in the form of torque which is then converted back to stress by the instrument. This conversion can be seen in Equation 1.29, where M represents the torque input, r the position vector from the origin and F the force. The torque input is a measure of the force causing rotation within the sample material.

$$M = r \times F \qquad \text{Equation 1.29}$$

The shear stress in the system can be defined using Equation 1.30, where σ represents the shear stress, k_σ is the conversion factor, r is the radius of the geometry and M the torque element. The conversion factor is dependent on the type of geometry used (i.e. parallel plate and cone-and-plate). The torque conversion factor for parallel plate systems is geometry dependent due to the r^3 term (9).

$$\sigma = \frac{2}{\pi r^3} M = k_\sigma M \qquad \text{Equation 1.30}$$

1.12.5.1 Cone and plate

A range of cone and plate geometries are available for use with the AR2000ex and AR-G2 rheometers. Typically cone geometries have small angles between 0.5° and 4° (41). Due to the truncation gap between the Peltier plate and the cone geometry (highlighted in red in Figure 1-17), the samples being tested should be single phase and homogenous (44). The truncation gap should be greater than or equal to ten times the size of the particles present (9) to avoid them becoming trapped between the shearing surfaces (1). As the viscosity of the test material decreases, the diameter of the geometry employed generally increases. The velocity profile of a cone and plate geometry can be seen in Figure 1-18. The velocity gradient across the sample remains

constant as a function of distance from the axis of rotation, resulting in a uniform strain rate (1,9).

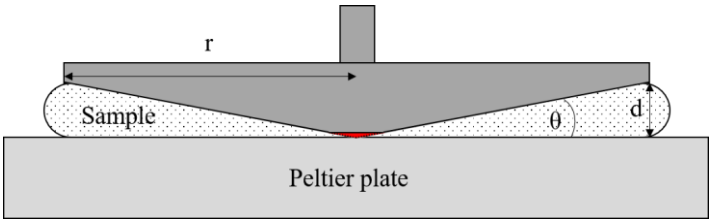

Figure 1-17 *A schematic diagram of a cone and plate rheometer geometry set up with radius, r, gap, d and angle, θ. The truncation gap is highlighted in red.*

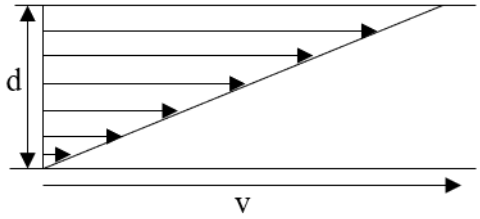

Figure 1-18 *Velocity profile across a cone and plate geometry with an upper moving plate and a lower stationary plate* (15).

1.12.5.2 Parallel plate

A parallel plate system consists of two horizontal parallel geometries of radius, r, and gap, d, as seen in Figure 1-19. Parallel plate geometries are typically used in conjunction with Peltier plates to allow temperature control of the test samples. In contrast to the cone and plate system described above, parallel plates can be used to analyse materials containing larger particles but the chosen geometry gap should be at least ten times larger than the size of the largest particles present to ensure that the microstructure of the sample is not compromised (9). For low viscosity samples, a large diameter plate can be used, but as the viscosity increases, the size of the plate should be decreased in order to work with appropriate experimental conditions. The sample is loaded between the plates before a stress is applied (8) and, unlike the cone and plate geometry system, the applied strain rate is not uniform across the diameter of the parallel plate geometry (44). The gap chosen should satisfy the Schrag 'gap loading' criterion (Section 1.12.4.1) to ensure the velocity gradient across the gap is uniform, which renders any sample inertia effects negligible (45). Benefits of parallel plate geometries are that a small volume of sample is required compared with concentric cylinder geometries and they can be used over a wide range of viscosities (9).

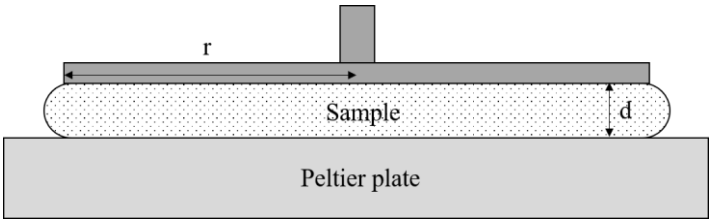

Figure 1-19 *Schematic diagram of a parallel plate geometry system with radius, r, and gap, d.*

1.12.5.3 Double gap concentric cylinders

Double gap concentric cylinders employ a 'bob' and 'cup' design with the sample placed in the void between the shearing surfaces, as seen in Figure 1-20. The area of the shearing surface is much greater than that of the parallel plate or cone and plate systems and therefore the volume of test material is greater (46). This type of geometry is often used for very low viscosity samples that would not be retained in a parallel plate or cone and plate set up (16). With narrow gap concentric cylinder set ups, the shear rate across the sample is nearly uniform (1,46).

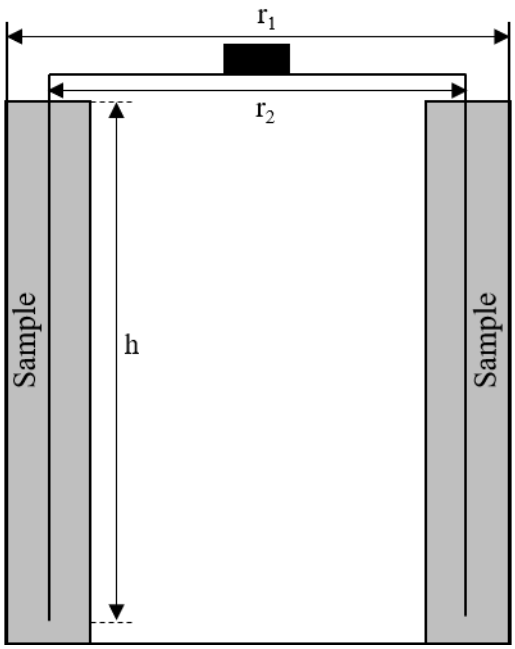

Figure 1-20 *Double Gap Concentric Cylinder setup. The radius of the cup is shown as r_1, the radius of the geometry as r_2 and the height of the sample as h.*

1.13 Gelation and the Gel Point

Applications of GP analysis for physical and chemical gels are widespread as discussed in many example studies (6,47–50). A material undergoing gelation passes through a sol-gel transition (51,52), with the specific gel point (GP) information

available for analysis of the evolving material microstructure (53,54). Gelation occurs when the number of intermolecular interactions within the polymer has exceeded the critical extent of reaction (55).

A critical gel can be defined as a real sample that is arbitrarily close to the GP but is neither a viscoelastic liquid or viscoelastic solid by nature (56). For a critical gel, the viscoelastic response at the GP can be defined as the Winter-Chambon gel equation (36,57,58), such that:

$$\boldsymbol{\tau_s}(t) = S\int_{-\infty}^{t}(t-t')^{-\alpha}\dot{\boldsymbol{\gamma}}(t')dt' \qquad \text{Equation 1.31}$$

Where τ_s is the stress tensor, S and α are material properties and $\dot{\gamma}$ is the deformation rate (58). The GP cannot be defined as the crossover of the $G'(t)$ and $G''(t)$ moduli as it is not applicable to all polymer networks. At the GP of a gelling material, the storage and loss moduli scale as identical power laws with respect to frequency, such that $G'\sim G''\sim\omega^{\alpha}$ with the conditions that $0<\alpha<1$ (37). In such a circumstance, SAOS can be used to identify the GP from the loss tangent (53) (Equation 1.28) which is frequency independent and can be related to the stress relaxation component, α, at the GP using Equation 1.32 (59).

$$\alpha = \frac{2\delta}{\pi} \qquad \text{Equation 1.32}$$

As seen in Equation 1.32, the stress relaxation component follows a power law (56,60), the measurement of which is limited by sample mutation (28) and inertial artefacts. The gel strength is represented by S and $0 < \alpha < 1$ remains true.

$$G(t) = St^{-\alpha} \qquad \text{Equation 1.33}$$

The transition between viscoelastic liquid and viscoelastic solid occurs at a critical time, t_c, or extent of cross-linking, p_c (56). As seen in Figure 1-21, the conversion of the sol to gel increases as the relaxation modulus decreases, resulting in longer relaxation times. At the GP, the relaxation time diverges to infinity (56).

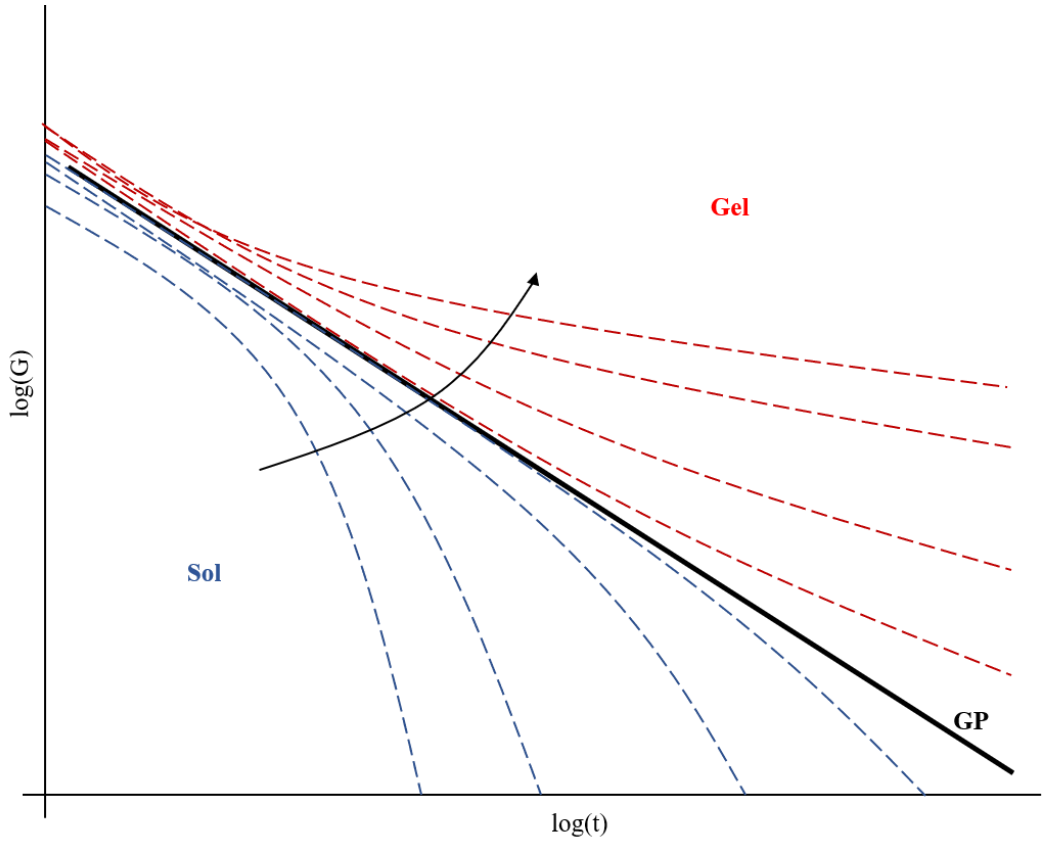

Figure 1-21 *The relaxation spectrum of a linear viscoelastic sample undergoing oscillatory shear. The GP is defined as the critical extent of cross linking, p_c, whilst the pre-gel and post-gel regimes shown in blue and red, respectively.*

It is advantageous to obtain GP data using SAOS as it is appropriate for transient materials. An example of a GP obtained using a standard SAOS procedure can be seen in Figure 1-22. It is possible to access the stress relaxation exponent using this technique using the phase angle reported at the GP, δ_{GP}.

$$\alpha = \frac{\delta_{GP}}{90} \qquad \text{Equation 1.34}$$

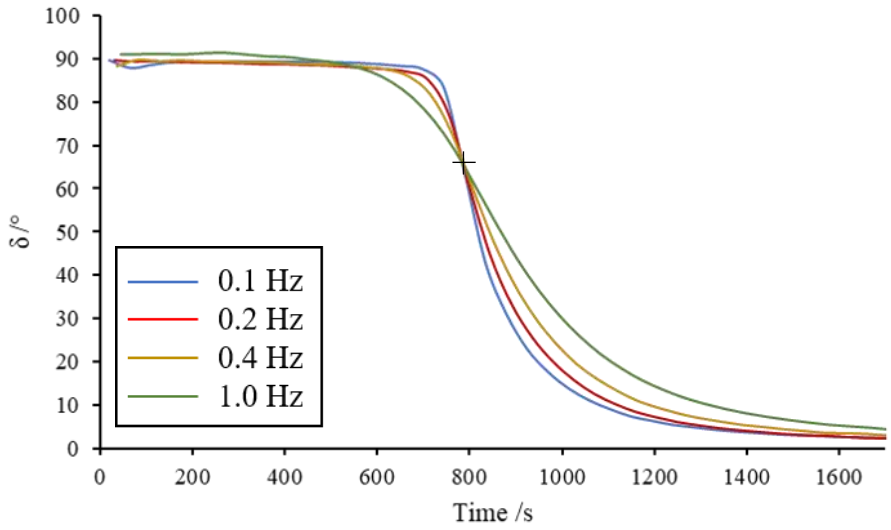

Figure 1-22 *An example 2.5 wt% gelatin GP obtained using a SAOS procedure employing four frequencies to determine the frequency independent GP. The reported phase angle can be used to determine the stress relaxation exponent.*

1.13.1.1 Percolation Theory

Flory and Stockmayer developed a classical theory for gelation in the early 1940's that allows prediction of the point of gelation based on polymerisation of monomers and the model is not limited to stoichiometrically balanced conditions (55,61). This theory has been further developed to describe gelation of a polymer using percolation theory.

Percolation theory can be explained by considering a lattice in which the squares are independently either 'occupied' or 'empty' regardless of the nature of neighbouring squares (62). Clusters of 'occupied' squares are formed based on the probability, p_o, of occupation (63). Each square can be assumed to represent a small monomer and a number of joined occupied squares can be assumed to be a cluster (Figure 1-23 (63)). The percolation threshold, p_c, is defined as the probability at which there is initial formation of an infinite cluster within an infinite lattice (64).

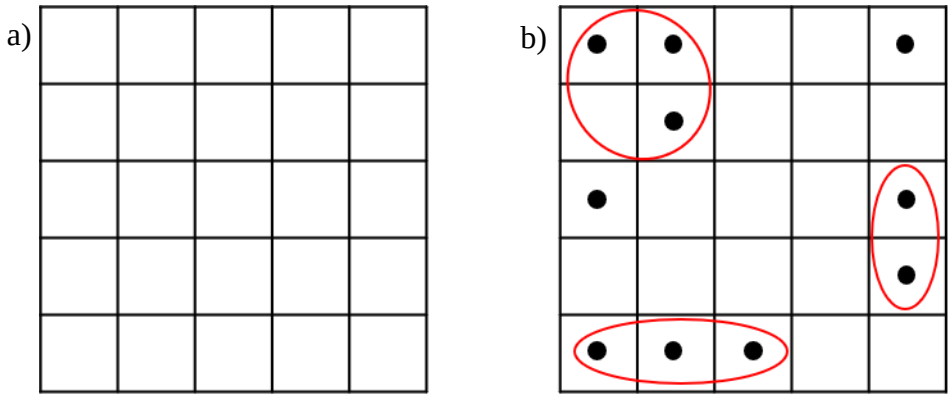

Figure 1-23 a) *shows an empty lattice where all of the squares are unoccupied and no clusters have formed and* ***b)*** *represents the formation of clusters (a presence of more than one dot in adjoining squares). Single dots surrounded by empty squares are not considered to be clusters. Clusters are circled in red.*

The site percolation model described above defines a static model and does not incorporate cluster movement. Models that describe cluster-cluster aggregation are dynamic and allow for the movement of clusters, as discussed in the following sections.

1.13.1.2 Diffusion-limited cluster aggregation

Diffusion-limited cluster aggregation (DLCA) is based on the idea that each initial interaction between clusters results in the formation of a permanent bond (22) and all particles are simultaneously activated (53). Many studies have been conducted in the area of diffusion-limited aggregation and the technique has been applied to several materials, including colloids and biopolymers (65–69). The clusters of aggregates grow in size immediately after a collision occurs with an individual, randomly moving particle (70). When two clusters combine, they become a single mass that can associate with further clusters. Because of this immediate association between clusters, the sticking probability, p_s, is assumed to be equal to one ($p_s = 1$) in a DLCA regime (71). The immediate agglomeration of the clusters leads to an open network structure as the bonds formed are irreversible. The fractal dimension, d_f, can give an indication of the structure of the network with a typical d_f value reported for a network formed by DLCA in the range of $1.7 \leq d_f \leq 1.9$ (22,71).

1.13.1.3 Reaction-limited cluster aggregation

If the monomers in a system do not react on the first interaction, it is possible for them to bond in alternative locations rather than the extremities of the growing cluster causing a denser network to form (22). This model is referred to as *reaction-limited*

cluster aggregation (RLCA). An RLCA regime is slower to form a network than DLCA due to a slower rate in cluster growth (66). By comparison to DLCA, the clusters in RLCA systems must further interact with large numbers of collisions before a permanent association if formed (72). As the mass of the cluster formed increases, the number of potential bonding sites also increases which results in larger clusters growing faster than smaller ones (66). The sticking probability, p_s, of the respective clusters is assumed to be much smaller than one ($p_s \ll 1$) in an RLCA regime (71). The fractal dimension, d_f, for RLCA is ≈ 2.0 – 2.1 (22,66,71–73).

1.13.1.4 Activation-limited aggregation

Curtis et al. proposed an alternative aggregation model that incorporates an activation profile for the rod-like monomers in incipient blood clots to determine the effect on the fractal dimensions reported at the GP (53). This model is referred to as *activation-limited aggregation* (ALA). The work was conducted to model incipient blood clot formation in an attempt to explain the fact that fractal dimension of incipient blood clots decreases with increasing gel time, conversely to that expected from a transition from DLCA to RLCA mechanisms. It has been shown that slower theoretical RLCA models report higher d_f values for the incipient gel (66), whereas previous rheological studies conducted reported lower d_f values for whole blood (74) and fibrin gels (18,75). The number of active clusters in the fibrin-thrombin gels increases with the progression of the thrombin concentration, which is characterised by the inclusion of the activation profile in the model (53).

1.14 Rheometry for Gel Point Detection

The work presented in this thesis requires the use of standard SAOS experiments as described in Section 1.9. Alternative rheometric techniques for the detection of the GP include Fourier Transform Mechanical Spectroscopy (FTMS) and Optimal Fourier Rheometry (OFR).

FTMS combines several constituent harmonic frequencies into a composite waveform, with resulting data being studied individually using Fourier analysis (7). The technique is advantageous for studying rapidly gelling systems as it dissociates the frequency and time dependence of the fluid characteristics to obtain data at multiple frequencies concurrently as the microstructure evolves with time (76). As the technique is based upon the Boltzmann Superposition Principle, higher stresses are observed as the stress

for each frequency is combined, resulting in the linear viscoelastic limit for weak gelling systems being exceeded (18).

A later study conducted by Curtis et al. showed the development of the OFR technique, which can also be used for the characterisation of rapidly gelling systems by employing a frequency modulated (chirp) waveform (77). OFR results in an increased number of data points in comparison with FTMS, so whilst there is strong agreement between the two techniques, the OFR GP is determined to a greater degree of precision (77). The technique lends itself to biopolymers, such as collagen, undergoing gelation at physiologically relevant conditions.

1.14.1 Sample Mutation Artefacts

To assess the potential artefacts within a gelling system associated with evolving rheological properties, the sample mutation criterion can be employed. Winter's sample mutation number, N_{mu}, can be calculated using Equation 1.35 (28,78), where Δt refers to the acquisition time of the data point in question (28).

$$N_{mu} = \frac{\Delta t}{G'} \frac{dG'}{dt} \qquad \text{Equation 1.35}$$

Sample mutation data should be assessed and discarded if found to exceed $N_{mu} > 0.15$ (28). The dimensionless mutation number is calculated using the lowest frequency G' response.

Chapter 2 Materials

2.1 Gelatin

Gelatin is a natural biopolymer manufactured by the denaturation of collagen (47) from animal tissues by hydrolysis (79) and has common uses in the food and pharmaceutical industries (80,81). The viscoelastic and thermoreversible properties of gelatin are the result of the formation of an extensively cross-linked network (82–85). At low temperatures, the polymer chains form a triple helix structure (83,86,87) which produces a 3D gel network in line with gelation described by percolation theory (88). The thermoreversible nature of gelatin, due to the presence of weak hydrogen and van der Waals forces (86,89), has been comprehensively studied (47,48,57,84). The evolving viscoelastic properties of gelatin undergoing a sol-gel transition can be effected by temperature and concentration (90). Gelatin displays near Newtonian properties at temperatures exceeding the maximum gelation temperature of 33.6°C (84). The formation of a gel network at temperatures below the maximum gelation temperature makes gelatin an ideal gelling system for the validation of novel rheometric procedures (18,38,91).

2.2 Blood

Human blood is responsible for the transport and circulation of nutrients required for cell metabolic activities and gases, such as oxygen and carbon dioxide, around the body (92). Whole blood consists of red blood cells (RBCs), white blood cells (WBCs), platelets and other cellular elements suspended in plasma (11). It displays the behaviour of a non-Newtonian shear thinning fluid at the low shear rates associated with venous flow ($< 50\ s^{-1}$) (93,94). The presence of RBCs (erythrocytes) within whole blood are responsible for the shear thinning properties observed rheologically (93).

RBCs are biconcave in shape with a diameter of ~ 8 μm (95) and a thickness of ~ 2 μm (96). The fraction of the total volume of blood sample occupied by RBCs is referred to as the haematocrit. The haematocrit and the viscosity of the plasma are responsible for the overall viscosity of blood (93). Human blood has a unique haematocrit dependent critical stress, the yield stress, below which it will not flow. This is due to the stacking of the RBCs present in the blood, causing a three dimensional rouleaux formation (97). At low shear rates, measurement of the yield stress is influenced by the separation of blood into plasma and cell aggregates (98).

Therefore, rheological models cannot be used to accurately describe the impact of haematocrit on the yield stress (99).

2.2.1 The coagulation cascade

Haemostasis requires (i) initially stopping the bleeding at the injury site and (ii) fibrin network formation (100) which stabilises the clot. The coagulation cascade is triggered upon vascular injury which exposes blood to the extravascular tissue (101). It involves a series of pro- and anticoagulant enzyme activation events that result in the activation and subsequent polymerisation of soluble fibrinogen monomers to insoluble fibrin and formation of an incipient fibrin clot network (53,102). Clots are formed from soluble fibrinogen (also referred to as Factor I) and thrombin that is generated from prothrombin (Factor II) produced in the liver, to form insoluble fibrin strands that aid haemostasis and prevent blood loss (103,104).

The clotting process initially follows either the *extrinsic* or *intrinsic* pathways with the latter stages following a *common* pathway that results in a blood clot (Figure 2-1). The *extrinsic* pathway, or tissue factor (TF) pathway (102), is activated by the presence of TF, which is discharged from endothelial cells due to vascular damage. The TF activates enzymes present in the blood resulting in coagulation (104). The *intrinsic* pathway, or contact pathway, is triggered without TF coming into contact with the blood or plasma (102). It follows a similar route to the *extrinsic* pathway but is initiated by the activation of Factor VII (105) rather than contact between TF and the enzymes within blood. The *intrinsic* pathway is not considered to be a parallel pathway in comparison to the *extrinsic* pathway. However, both converge to follow a *common* pathway, resulting in a platelet plug and eventual clot formation (104).

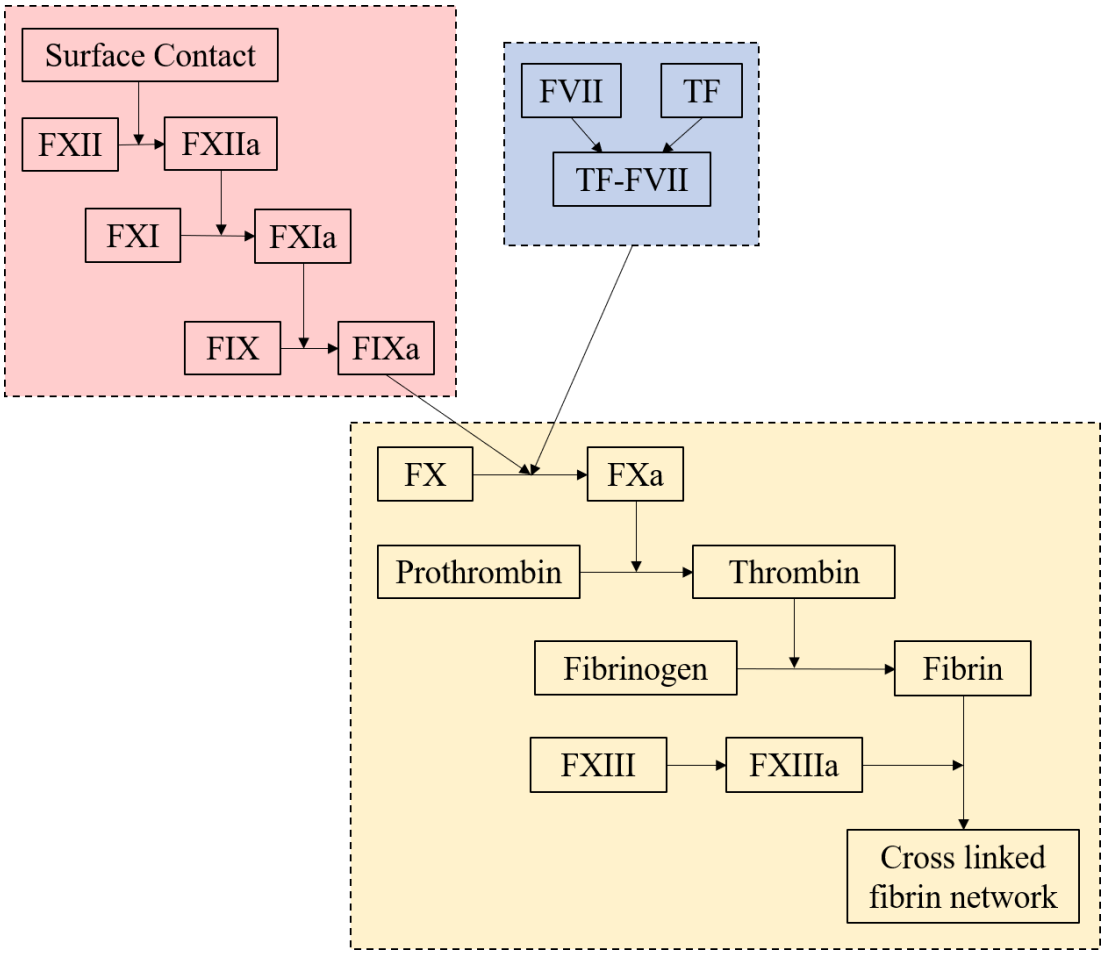

Figure 2-1 *The clotting cascade. The clotting process follows either the extrinsic (shown in blue) or intrinsic pathway (shown in red) depending on the initiating stages. Both the intrinsic and extrinsic pathways follow the common pathway (shown in yellow) to form a fibrin network that results in haemostasis.*

2.2.1.1 Tissue Factor

Tissue Factor (TF) is a protein found in the subendothelial cells that initiates the *extrinsic* clotting cascade by acting as a transmembrane receptor for clotting Factors VII and VIIa, forming the complex TF-VIIa (106,107). The TF-VIIa complex formed due to vascular injury leads to the activation of further factors that convert prothrombin to thrombin, resulting in the formation of an insoluble fibrin network clot (108).

2.2.1.2 Fibrinogen

Fibrinogen (Factor I) molecules are large complex hexameric glycoproteins, with a mass of 340 kDa and length of 46 nm (103,109,110). Each protein is comprised of two sets of three different polypeptide chains (Aα, Bβ and γ) connected by 29 disulphide cross-links (111–113), as shown in Figure 2-2. It is the third most common protein found in human plasma (110).

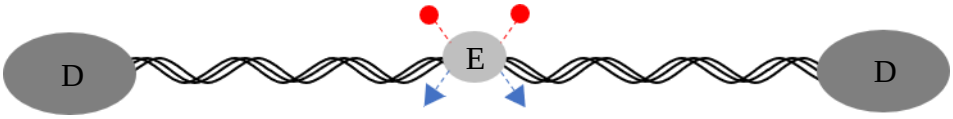

Figure 2-2 *A simplified tri-nodular fibrinogen protein molecule with a central E nodule and two distal D domains. The fibrinopeptides A (FPA – blue triangles) and B (FPB – red circles are cleaved away from the fibrinogen molecule by the thrombin present, allowing the fibrinogen to bind with an A or B binding site on an alternative fibrinogen D nodule.*

The fibrinogen concentration in plasma for healthy patients is 2 mg $ml^{-1} \leq$ [fibrinogen] $\leq$ 5 mg ml^{-1} (110–112). Fibrinogen concentrations can be increased under pathological conditions such as infection (114), injury (115) and can be as high as 7 mg ml^{-1} due to acute inflammation (112). It has been reported that fibrinogen levels within the blood are increased during the final trimester of pregnancy (116,117). On the contrary, acute trauma can depress the fibrinogen concentration level present in the blood to a critical level of $\leq$ 1 mg ml^{-1}, affecting haemostasis and increasing the risk of haemorrhage (118,119).

2.2.1.3 Thrombin

Thrombin is responsible for the conversion of fibrinogen to a fibrin network by proteolysis (120). The prothrombin (Factor II) zymogen present is activated to give thrombin (Factor IIa) (121). Small amounts of thrombin initiate the coagulation cascade by activating platelets, converting the fibrinogen present to fibrin and moderating the production of Factor XIIIa that is responsible for the cross-linking between the fibrin polymers to strengthen the clot (101,107,122). As the final enzyme in the cascade, thrombin is generated in two phases of varying magnitude, with the initial small spike in thrombin preparing the coagulation cascade for a greater thrombin burst (123). The peak volume of thrombin produced is post-fibrin clot formation (101,111). It is possible for thrombin to convert 10^5 times its own weight in fibrinogen to fibrin which suggests that it is catalytic in the clotting process (124). Increased thrombin concentrations lead to decreased clotting time as thrombin behaves as a modulator during fibrin gel formation (120). The immediate lysis of the clot is prevented due to the presence of thrombin activated inhibitors (125).

2.3 Fibrin Gels

2.3.1 Fibrinogen polymerisation

Once a clot is fully formed, the final volume of fibrin present comprises 0.25% of the total volume of the clot with liquid pervading the other, much larger, fraction between the polymer strands (126).

Initially in fibrinogen polymerisation (Figure 2-3), fibrinopeptide A (FPA) are preferentially cleaved from the E domain before the fibrinopeptide B (FPB) allowing the D domain of alternative fibrinogen molecules to form protofibrils which support lateral associations that contribute to the clot network (127,128). Cleaving FPA and FPB from the fibrinogen monomer exposes 'A' and 'B' sites that allow the corresponding 'a' and 'b'' pockets on the β and γ nodules to bind, resulting in polymerisation (110,111). In order for polymerisation to be successful, consecutive fibrin 'a' pockets must not be defective as it has been suggested that A:a interactions are essential for fibrin polymerisation (128).

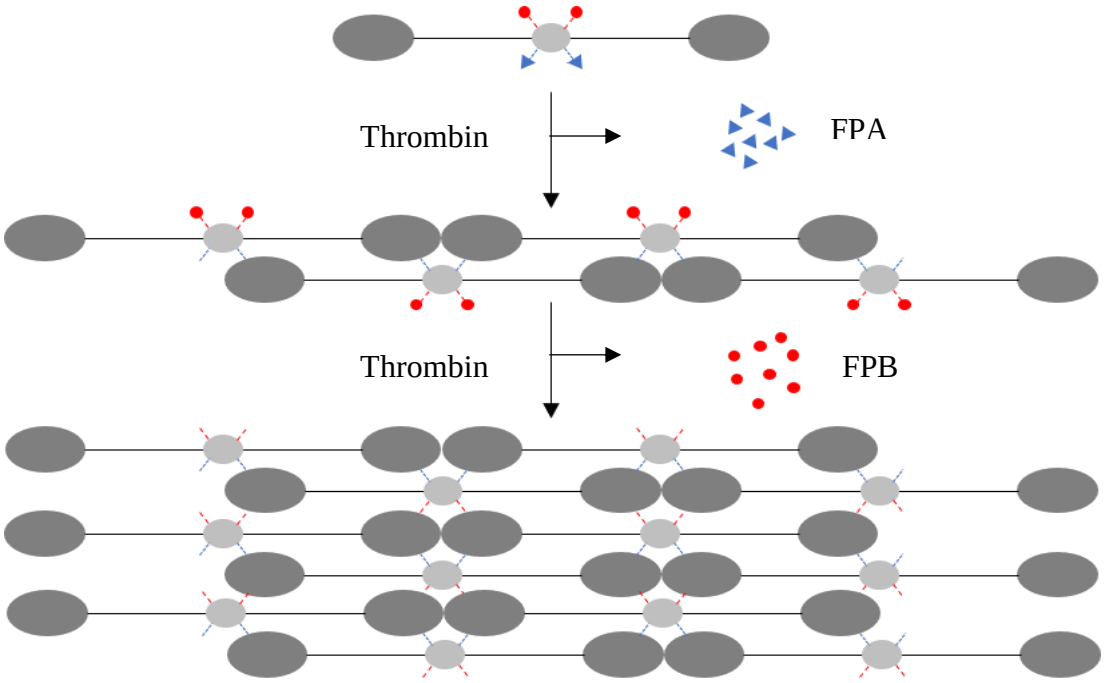

Figure 2-3 *The conversion of fibrinogen to a fibrin network due to the presence of thrombin. Initially, the FPA (blue triangles) are cleaved from the E domain of each fibrinogen protein. The FPB (red circles) are also split from the fibrinogen protein to form the fibrin network by lateral aggregation of the protofibrils. Reproduced from A. S. Wolberg, "Thrombin generation and fibrin clot structure,"* Blood Rev., *vol. 21, no. 3, pp. 131–142, 2007 © 2007 with permission from Elsevier Ltd.*

The cross linking between the protofibrils to form the gel network are due to transglutaminase (Factor VIII) activation resulting in a more stable clot (129). A high density of crosslinks between the fibrin protofibrils has a dramatic effect on the viscoelastic properties and mechanical strength of the final clot as the stiffness is increased, meaning that irreversible deformation is almost disregarded (126).

At low thrombin concentrations, fibrin networks are formed from thicker fibres with few branch points due to the lateral aggregation between the protofibrils (130). The clotting time for fibrin gels with the inclusion of a low thrombin concentration is much slower than of those with high thrombin concentrations (75). At higher thrombin concentrations, the fibres are thinner with much denser branching as the conditions inhibit the lateral aggregation of the protofibrils, resulting in a much denser final network microstructure (126). Examples of fibrin networks formed for both high and low thrombin concentrations can be seen in Figure 2-4.

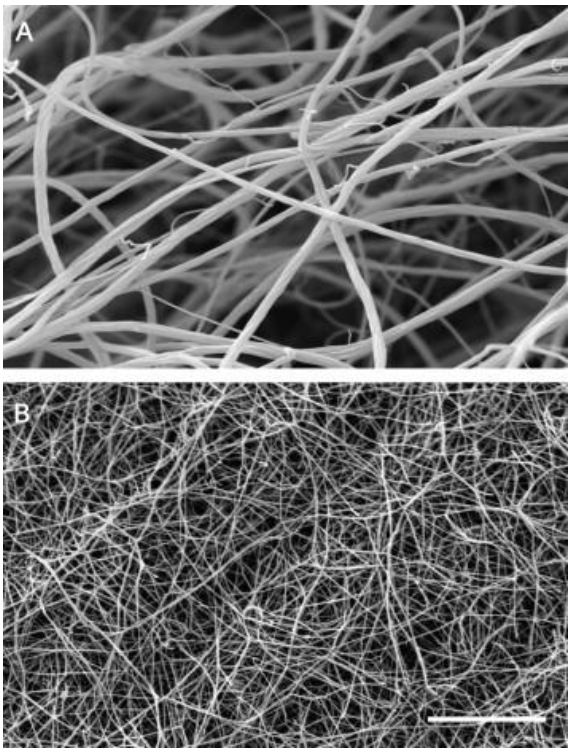

Figure 2-4 *SEM images obtain of fibrin clots from recalcified plasma at a) a low thrombin concentration and b) a high concentration. At low thrombin concentrations, the fibres formed are thick with few branch points whereas at high thrombin concentrations, the fibres produced are much thinner with many branch points. The scale bar shows 5 μm and is applicable to both images. Reprinted from J. W. Weisel, "The mechanical properties of fibrin for basic scientists and clinicians,"* Biophys. Chem.*, vol. 112, no. 2-3 SPEC. ISS., pp. 267–276, 2004. © 2004 with permission from Elsevier Ltd.*

2.3.1.1 Fibrinolysis

The fibrin clots formed during haemostasis are broken down by enzymes during fibrinolysis. The fibrin network is broken down by the presence of plasmin produced by the proteolysis of plasminogen (131). The plasminogen is activated by tissue-plasminogen activator (tPA) (121) which is slowly discharged into the blood by the damaged endothelium (125). The structure of the clot formed during coagulation affects the susceptibility of the clot to fibrinolysis (111). Clot networks formed with low thrombin concentrations produce thicker fibres that are less resistant to fibrinolysis than thrombi formed of thinner fibres due to the 3D structure of the clot having a rate limiting effect on the activity of plasmin (111). Drugs such as streptokinase form a complex with plasminogen and can be administered in order to treat myocardial infarction by promoting blood clot lysis (132).

2.3.2 Thrombosis

In healthy patients, both blood coagulation and clot fibrinolysis are closely related and highly regulated to ensure that haemostasis is achieved (121). Previous studies have shown that an increased concentration of fibrinogen within the blood can increase the risk of cardiovascular disease (114,133) such as venous thromboembolism (VTE), myocardial infarction and stroke (134). It has been estimated that 1:100 patients will suffer VTE in the latter stages of life (135). Research shows that insoluble fibrin is a key element of both venous and arterial occlusions (136). Venous blood clots are more fibrin rich than arterial clots which have a tendency to be more platelet-rich (137)

Proteins and factors present within the blood are responsible for the formation of blood clots through coagulation. For patients suffering from cardiovascular disease, it is possible for the blood clots to form in blood vessels, resulting in VTE. Deep vein thrombosis (DVT) and pulmonary embolisms (PE) are examples of a blood clot forming intravenously (138). Clots that are densely structured with small pores increase the risk of thrombosis resulting in altered functionality, such as resistance to fibrinolysis and modified viscoelastic properties (139). Lysis due to the presence of plasmin is less efficient on thrombi formed of thinner fibres due to hypercoagulability common in patients experiencing DVT, PE, myocardial infarction and stroke (127).

The risk of VTE is increased with ‘genetic risk factors’ (for instance, age and natural deficiencies in anticoagulant such as antithrombin) and ‘acquired risk factors’ (for

example, major surgery, obesity and oral contraceptives) (135). A prevalent 'acquired risk' is exposure to cigarette smoke, which increases the risk of thrombosis due to raised fibrinogen concentration and lower levels of TF pathway inhibitor (140).

2.3.3 Fractal Analysis

2.3.3.1 Characterisation of clot structure using fractal dimension

A study conducted by Ariëns highlighted the difference in clot characteristics, with patients suffering from thrombosis forming denser, more compact clots in comparison to those considered healthy (141). More recent studies have employed a quantitative analysis of clot structure using fractal dimension, d_f, as a novel biomarker to assess the clinical implications of various health issues on coagulation (54,142–144). A 'healthy' range of d_f was determined from healthy patients that defines a 'healthy index' which may be used as a reference in studies of the pathologies/agonists on thrombosis using rheological techniques. The 'healthy index' value was established to be 1.74 ± 0.07 ($n = 52$) (74,145,146).

The effects of anticoagulants, such as heparin, have been rheologically studied to determine the impact on the clot structure formed (74). As the heparin concentration is increased, the reported d_f values decrease (from d_f = 1.71 at 0.175 U ml^{-1} of heparin to d_f = 1.57 at 0.8 U ml^{-1}) (146). Patients with VTE are usually treated with anticoagulants resulting in reduced healthy d_f of 1.69 ± 0.046, whilst the group of patients with VTE showed an increased d_f value of 1.73 ± 0.055, which despite anticoagulants is very similar to that of the healthy index (147). Using the sensitive rheological techniques, it was possible to distinguish between single- and recurrent-VTE patients as an increased d_f for recurrent-VTE patients of 1.74 ± 0.049 was observed in comparison with the single-VTE patients of 1.71 ± 0.060 (147). Therefore, single-VTE patients who exhibit elevated d_f values could be at risk of recurrent VTE (147).

Comparison to the healthy index value has shown a significant increase in the d_f reported for patients suffering from prothrombotic illnesses. Stanford et al observed an increase in d_f for those treated for ischaemic stroke as 1.760 ± .053 (148). Obstructive coronary artery disease (CAD) also resulted in a significantly increased d_f value of d_f =1.748 ± 0.057 when clots were analysed rheologically (149).

The effect of primary percutaneous coronary intervention (pPCI) treatment of myocardial infarction (MI) on clotting parameters was studied by Lawrence et al (150). A decrease in d_f was reported from 1.751 ± 0.052 pre-treatment to 1.634 ± 0.058 immediately post-treatment. After 24 hours, the d_f returned to a similar value to pre-treatment (d_f = 1.742 ± 0.041) and close to the healthy index value of d_f = 1.74 ± 0.07.

The sensitivity of the rheological techniques used results in accurate d_f data being obtained for a range of prothrombotic illnesses. The research reported herein applied the GP analysis to studying the effect of soot particulate on the blood clots microstructure in both model blood clots and those formed from samples of whole blood obtained from healthy volunteers.

These studies (54,143,148,149) used GP analysis to determine d_f which is linked to the stress relaxation characteristic of the incipient gel network through Muthukumar's Relation.

2.3.3.2 Muthukumar Relationship

Branching network microstructures can be examined using fractal analysis (5,151). The fractal dimension, d_f, of a branched polymer sample can be determined to give an insight into the internal microstructure of a gelling material at a given point in time. For screened polymer solutions, Muthukumar presented Equation 2.1 to show the relationship between stress relaxation exponent, α, and d_f, where $d_e = 3$ for networks forming a 3D embedding space and $\alpha = \frac{\delta}{90}$.

$$\alpha = \frac{d_e(d_e + 2 - 2d_f)}{2(d_e + 2 - d_f)} \qquad \text{Equation 2.1}$$

To determine the fractal dimension from an observed phase angle, Equation 2.1 can be rearranged to isolate the d_f term to give:

$$d_f = \frac{10\alpha - 15}{2\alpha - 6} \qquad \text{Equation 2.2}$$

For both screened and unscreened polymers, resulting d_f values from experimental data can range from $1 \leq d_f \leq 3$ (22,152). Due to the relationship shown in Equation 1.40, the d_f value obtained is sensitive to the reported phase angle. More compact networks are associated with higher d_f values, whereas low values of d_f are

representative of more ‘open’ networks (53). For ‘open’ network structures, the stress relaxation is more efficient due to the inverse power law behaviour of the stress relaxation exponent, α, at the GP.

2.3.4 Alternative techniques for the analysis of clot formation

Alongside rheological procedures, alternative techniques can be used to assess the gel network formation. These include thromboelastography (TEG) and prothrombin time to assess blood coagulation, as well as microscopy techniques such as Scanning Electron Microscopy (SEM) and Laser Scanning Confocal Microscopy (LSCM) for image analysis of the fibrin network within clot structure.

2.3.4.1 Thromboelastography

Previously, thromboelastography (TEG) has been used as a method of measuring the viscoelasticity of blood (153). Developed in 1948, TEG assesses the efficiency of blood coagulation in a convenient manner without the need for repetition (154). A small volume of blood is placed into a heated (37 °C) oscillating cuvette and a torsion wire is suspended in the sample. As the clot begins to form, the mechanical properties are recorded by amplification of the motion of the torsion wire (155). Only a small volume of blood is required from the patient, but there are variations in how the data is obtained that limits the technique (156). Whilst it is possible to assess hypercoagulability and predict postoperative pathologies such as MI from the resulting thromboelastgraph (157), it is not possible to obtain information on the incipient clot network (158). TEG can be considered a ‘pseudo-rheometric’ technique in that it assesses the clot’s basic mechanical properties, but these are potentially non-linear and not reported in a scientifically meaningful manner.

2.3.4.2 Prothrombin Time

Prothrombin time is a measure of how long it takes for blood to clot via the *extrinsic*, tissue factor pathway (159). It can be used to identify factor deficiencies by measuring the time for plasma to clot after the addition of thromboplastin (160,161). The technique is quick to obtain results but the various preparation methods used to prepare thromboplastin reagents can result in a deviation in results, even in the same plasma (160).

2.3.4.3 Scanning Electron Microscopy

Scanning electron microscopy (SEM) images obtained of fibrin networks within a blood clot can be characterised both qualitatively and quantitively due to the quality of the images obtained. Some studies refer to the network formed as ‘dense/open’ (74,141,162) or as having ‘thicker/thinner fibres’ (163). However, the structure of the clot can be characterised quantitatively by the ‘number of branched points’, the ‘diameter of the fibres’ formed and the ‘size of the pores’ (128). The SEM preparation procedure for biological samples can be lengthy and invasive which can result in the disturbance of the microstructure of the clot formed. It is only possible to observe mature clot structures using SEM as the sample networks must be fully formed before being fixed and dehydrated prior to imaging.

2.3.4.4 Laser Scanning Confocal Microscopy

Due to the sensitivity of laser scanning confocal microscopy (LSCM), it is possible to observe mature structures as well as dynamic processes within biological material (164,165). LSCM can be used to obtain 3D images of fibrin gel networks using an ion laser. This is achieved by capturing a series of sequential images of the network that can be processed to give 3D representation of the sample (166). The sample must contain a fluorophore labelled fibrinogen component to provide contrast within the image (167). To prevent bleaching of the added label molecules, care should be taken during preparation and imaging to avoid excess exposure to light before using a low laser power to acquire images (166).

2.3.4.5 Platelet Function

Platelet function can be assessed by aspirating blood at high shear rates through a membrane coated with biochemical stimuli and measuring the time required for complete occlusion (168,169). The technique is quick and easy to operate and gives accurate results (169) but a major limitation is the inability of the technique to give predictive or specific information on a particular blood coagulation disorder (170).

2.3.4.6 Evaluation of Coagulation Factor Biomarkers

The addition of thrombin to citrated plasma samples produces a visible clot that can be assessed using light absorption, with the time taken for the visible clot to form being inversely proportional to the fibrinogen concentration (171,172). The technique is

quick to perform and has been employed in several studies (173,174). However, a new standard curve must be created for each new batch of thrombin reagent (171).

2.4 Soot Particulate Matter

The health risks associated with the inhalation of particulate matter (PM) have been extensively studied (161,175,184,176–183). It has been suggested that both long- and short-term exposure to air pollution PM can have a detrimental effect on health, such as myocardial ischemia and infarction, stroke and thromboembolism (179,182,185,186). It has been estimated that globally 800,000 people die prematurely from cardiopulmonary diseases related to air pollution per annum (185,187). Particles translocating into the blood can reach vulnerable areas and even a relatively low number of particles in the blood stream can result in potential health issues (188). Further research is required in order to improve understanding of the potential adverse impacts of PM in air pollution on human health.

2.4.1 Origins and Classification of Particulate Matter

PM present in the air consists primarily of dust, smoke and soot particulates from combustion processes (176,179,189–191), where soot is a by-product of the incomplete combustion of diesel fuel (192,193). Exhaust matter contains a large proportion of carbon in the form of graphite with diameters in the range of 10 nm to 30 nm (194,195) with some soot PM reaching up to 1 mm in size (196,197). Typically, the core of combustion particles contains elemental carbon with additional hydrocarbons, metals and sulphates forming a coating (186,196,198). The PM produced during the combustion process has been shown to have acute and chronic adverse health effects (199–204).

Carbon black is often used as a model compound for soot produced during the combustion process (205). However, carbon black has a much higher surface area than exhaust PM as exhaust soot consists of aggregated carbonaceous particles, combined by tars and resins (206). The aggregated particles, which are fractal in nature, are comprised of multiple near-spherical particles with much larger diameters of 60 nm to 100 nm (195,207,208).

Inhalable airborne PM is classified based on the aero-diameter of the particles present (192,209). PM with diameter in at least one dimension of < 0.1 μm can be described as ultrafine (177). The concentration of ultrafine particles in the air is estimated to be

in the range of 1-2 μg m^{-3} with sporadic increases up to 20-50 μg m^{-3} (210). Particles < 2.5 μm diameter are considered to be fine particulate matter ($PM_{2.5}$) and particles with aero-diameters in the range 2.5 μm < $d_{PM} \leq$ 10 μm are referred to as coarse particulate matter, PM_{10} (189). The World Health Organisation has declared that PM with a diameter < 10 μm is the most harmful element in air pollution (178). The European Union states that the daily mean air quality limit for PM_{10} as 50 μg m^{-3} (211,212) and $PM_{2.5}$ as 25 μg m^{-3} (190). Baccarelli et al. present data representative of the median airborne PM_{10} concentration in the Lombardia Region, Italy, as in the range 44.3 μg m^{-3} to 68.5 μg m^{-3} with the maximum value recorded in winter (161). The US limit for exposure to $PM_{2.5}$ over a period of 24 hours was reduced in 2006 from 65 μg m^3 to 35 μg m^3 (185,213).

Ultrafine particles can rapidly aggregate to form larger particles (176). Typically, particles with an aero-diameter < 2.5 μm are able to penetrate into the gas-exchange region of the respiratory tract (209) and can remain in circulation for several months (184,199). As a result, it is possible for the $PM_{2.5}$ to trigger an acute cardiac event in patients with underlying cardiopulmonary disease such as myocardial infarction (180,214). Individuals with occupations that expose them to high levels of PM are also susceptible to increased risks of cardiovascular disease, for example, workers in the steel industry (175).

2.4.2 Potential Health Risks Associated with Airborne Particulate Matter

The components of airborne pollution can enter the lungs through inhalation and cause inflammation and more severe health issues. During times of peak PM concentration in megacities, it is possible for an adult to inhale in excess of 20,000 μg of PM (assuming a total volume of 20 m^3 of air is inhaled) (168). Whilst some studies have shown that inhaling PM can increase the risk of thrombosis and altered blood coagulation, not all have agreed due to the biological nature of the findings (185,215). Coarse PM_{10} particles are removed from the respiratory system in the upper airway by the cilia (184,204), whereas fine $PM_{2.5}$ can penetrate further into the terminal bronchioles (178,184) and ultrafine $PM_{0.1}$ can translocate across the pulmonary epithelium into the bloodstream (179,184,185,191,199,201,210).

Recent studies have shown that even short-term exposure to $PM_{2.5}$ (in the range of two hours) can increase the patient's risk of cardiopulmonary disease (168,214). It has been

suggested that for each 10 μg m^3 daily increase in $PM_{2.5}$ exposure, the risk of death due to cardiovascular disease increases by 1% (176,185). Smaller particles can penetrate further into the lungs and remain suspended for extended timescales (176). The subsequent inflammation of the lungs causes oxidative stress and increased blood coagulability (216), resulting in thrombotic diseases such as myocardial infarction and ischemic stroke (182).

The translocation of the PM into the blood stream leads to the activation of platelets and initiation of the coagulation cascade (182,217). Coarse particles that are inhaled into the lungs cannot be transferred into the blood stream (185). However, ultrafine particles can be inhaled deep into the lungs before being translocated into the blood stream and organs within a matter of minutes (178,185,202). Particles with a diameter of ≤ 1 μm passed through the epithelial barriers from the lungs into the blood stream via the capillaries (218). Nemmar et al. suggest that the PM inhaled may be capable of rapid translocation into the bloodstream, resulting in an immediate impact on haemostasis (178,202).

The mechanisms initiated by PM that are able to translocate across the gas-blood barrier have conventionally been thought to include oxidative stress, thrombogenesis, inflammatory response and elevated blood plasma viscosity that could result in cardiopulmonary disease (173,183,185,215,219,220). Oxidative stress is the disruption in the production of free radicals and antioxidants in the body (221). The process typically occurs if there is an excess of damaging oxidants (for example, after exposure to ultrafine diesel exhaust PM (179)) which develops into a tissue injury or inflammatory response (184,216).

Previous research has suggested a link between the inhalation of PM and an increased risk of cardiovascular disease, feasibly due to hypercoagulability and thrombosis (175). Seaton et al. suggested that the inhaled particles were responsible for inflammation within the lungs that increase the coagulability of blood, leading to potential cardiopulmonary events in individuals (222,223). The increased levels of coagulation proteins, such as fibrinogen and Factor VIII which are related to hypercoagulability, have also been associated with exposure to PM (224). With the inflammation caused by the inhalation of ultrafine particles, mediators that are capable of increasing blood coagulability may be triggered (173,203,222).

Elevated fibrinogen levels present in more viscous plasma can act as a biomarker for cardiovascular events (225) and could account for the increased risk of cardiovascular disease (173,226). Previous studies have resulted in contradictory conclusions as to whether fibrinogen levels are increased due to air pollution exposure. Some have demonstrated an increase in plasma viscosity and blood fibrinogen levels after exposure to airborne PM (181,185,226,227). Peters et al. suggested that the increase in plasma viscosity, due to elevated fibrinogen, could be because of increased exposure to PM with resulting inflammation of the airways (226). Schwartz et al. presented a study that also showed positive association between PM_{10} exposure and increased fibrinogen levels for US patients (228). Su et al. (229) demonstrated similar results to Seaton et al. (222), with fibrinogen levels increasing 0.71 mmol l^{-1} in patients with coronary heart disease after exposure to high levels of air pollution (216,229). However, a later study by Seaton et al., of 112 patients in Belfast and Edinburgh, presented contrary results suggesting that there was a negative association with PM_{10} exposure and plasma fibrinogen levels (230). Rückerl et al. also concluded that there were inconsistent results with regards to plasma fibrinogen levels after exposure to $\leq PM_{2.5}$ (223).

The inhalation of ultrafine PM and resultant pulmonary inflammation response may assist the translocation of the particles through the gas-blood barrier due to alterations in permeability of the alveoli (188,230). The rapid influence on mechanisms after only short-term exposure leads to increased thrombotic tendencies and thrombogenicity (215). An abundance of literature is in support of the concept that PM can increase cardiovascular events, such as thrombosis, ischemia and myocardial infarction (179,215,224,230).

2.4.3 Animal and human studies

Studies have previously been conducted using both animal and human models to assess the correlation between PM and the stimulation of haemostasis and thrombosis (182).

2.4.3.1 Animal studies

A vast number of animal studies have been conducted to assess the impact of PM on cardiopulmonary events. Miller et al. employed gold nanoparticles modelled on the size ranges of PM with inert biological properties to assess the effect on tissues after controlled exposure in mice (199). Over a size range of 2 nm to 200 nm, it was possible

to detect gold particles within the blood, particularly those with a smaller diameter, suggesting rapid translocation via a passive transport mechanism (199).

Kim et al. employed ultrafine carbon black particles to measure the thrombotic activity and inflammatory responses in rats (231). At high exposure levels of 10 mg kg^{-1}, carbon NP accelerated platelet-dependent haemostasis (231). Radomski et al. compared the effects of urban PM standard reference material and engineered carbon NP. The study indicated that both forms of carbon PM accelerate the time and rate of development of thrombosis in rats, with the engineered NP being more effective at inducing thrombosis than reference urban PM (232).

Nemmar et al. have conducted numerous animal studies as to the effect of PM on the increased risk of cardiopulmonary events (168,201,203,233–237). Hamster studies were conducted using a range of 20 nm – 50 nm diesel exhaust and comparable model particles instilled into the blood. These investigations revealed adverse effects on haemostasis due to platelet activation after exposure to PM, with an increased risk of thromboembolic disease (168,235–237). On the other hand, rat studies were less conclusive as to whether PM resulted in increased risk of cardiovascular issues. Cardiovascular and haemostatic variations were observed along with a pulmonary inflammation response, without a clear conclusion as to the mechanism involved (201,203).

2.4.3.2 Human studies

Miller et al. conducted additional human studies alongside the corresponding animal study involving the use of gold nanoparticles of a similar size to airborne PM (199). Healthy volunteers were exposed through inhalation to gold nanoparticles, with median aerodynamic diameters of 18 nm and 52 nm, before particles of both sizes were detected in the blood due to translocation (199). The conclusion that inhalation of PM can result in vascular dysfunction, atherothrombosis and acute myocardial infarction is in agreement with similar studies conducted by Mills et al. (238) and Lucking et al. (239).

Bind et al. detected an association between PM on plasma fibrinogen levels in a cohort of 704 patients. Increased particle levels were shown to increase fibrinogen levels present in plasma for patients without chronic medical conditions (173). The conclusion that airborne PM can increase the levels of biomarkers related to

cardiovascular disease is in agreement with research conducted by Zeka et al. (174). The study conducted by Zeka involved 710 male patients exposed to PM to assess the effects on thrombotic biomarkers, which showed increased fibrinogen levels over time after exposure (174).

Several studies have been conducted to better understand the effects of exposure to urban PM on pregnancy and early development (240–242). Investigations into the possibilities of PM passing through the placental barrier have been limited to animal studies as well as *in vitro* cell cultures and *ex vivo* models in human studies (240). Exposure to PM associated with combustion processes has been linked with reduced weight at birth (243,244), pre-term birth (242) and intrauterine developmental issues (241). Lamichhane et al. presented evidence for a significant decrease in birth weight of 10 g and 22 g for exposure to PM_{10} and $PM_{2.5}$ respectively (245). Pedersen et al showed evidence in support of lower full term birth weights when exposed to a 5 μg m^{-3} increase in $PM_{2.5}$ during pregnancy (243). Ritz et al. suggest that exposure to PM during the first trimester and prior to delivery may be responsible for pre-term birth, based on a population study in Los Angeles (242).

Some of the most comprehensive research to date into the effects of PM on cardiovascular disease has been conducted by Baccarelli et al. In a 2008 study of 871 male and female patients who had suffered DVT between 1995 to 2005 and 1210 control patients from across the Lombardy regions of Italy, the effects of PM_{10} on DVT risk was evaluated (224). Over the range of PM_{10} exposure studied, the relationship to DVT was approximately linear, with each increase in PM_{10} of 10 μg m^{-3} resulting in a 70% increase in risk of suffering DVT (224). A consequent 2010 study by the same authors suggested that living in close proximity to major traffic routes was responsible for an increased risk of suffering DVT (246). Once again, the exposure (proximity to a major road) and an increased risk of DVT was approximately linear suggesting that high levels of airborne PM elevate the risk of thrombotic tendencies (246). The findings reported by Baccarelli et al. are supported by research undertaken by Dales et al., which showed $PM_{2.5}$ to be a risk factor for VTE and PE in Santiago, Chile (247).

2.4.4 Previous techniques used for analysis of potential health effects of particulate matter

As discussed in Section 2.3.4, it is possible to analyse the coagulation of blood samples using a variety of techniques. Previous studies have employed the analysis of prothrombin time, microscopy and the evaluation of coagulation factors to gain an understanding of the effects of PM on blood clotting.

Studies by Bonzini and Baccarelli utilized prothrombin time to assess the potential health effects of PM_{10} exposure in patients living in the Lombardy region of northern Italy. In these cases, prothrombin time was successful in detecting a positive association with plasma clotting with the inclusion of PM (175,224).

A variety of microscopy techniques have been used in several studies to determine the implication of exposure to PM on patient health. Miller et al. used gold nanoparticles to assess the extent of translocation across the gas-blood barrier with sensitive Raman microscopy (199). In an earlier study, it was possible for Nemmar et al. to assess thrombus formation *in vivo* using an online video camera after staining the tissue with Rose Bengal, to determine the size of the developing thrombus from light intensity (234). In 2015 Pajnič et al. observed the *in vitro* alteration in the membrane structure of blood cells when exposed to different nanomaterials, such as carbon black, through SEM analysis (248).

The levels of coagulation factors present in the blood can give an indication of the effects of the presence of PM, as discussed by Zeka et al. and later Bind et al. (173,174). Fibrinogen levels can be analysed using an MDA 180 Coagulometer (171) to assess whether any fluctuations occur after exposure to PM. A similar light scattering technique of immunonephelometry was used by Rückerl et al. to determine the deviation in fibrinogen level as a marker of coagulation (223).

2.4.5 Therapeutic uses for nanoscale particles

Whilst PM produced by combustion processes appears to have a pernicious effect on the body, particles of a similar scale are often used for therapeutic uses. A wide range of nanomaterials have been extensively studied for use in the diagnosis and treatment of disease (249–251). Nanotechnology offers a wealth of options with regard to diagnosis and treatment of cardiovascular and pulmonary disorders (232,252).

It is possible to engineer procoagulant nanoparticles and particles with attached coagulation-initiating factors to treat coagulations disorders (253,254). Nanotextured TiO_2 has been shown to have haemo-compatible characteristics that lend themselves to translation onto existing clinical stents with insignificant thrombi formation whilst promoting endothelialisation (255). In a separate study, the application of 10 μm TiO_2 nanotubes to whole blood has demonstrated an increase in the strength of the clot formed due to the accelerated development of fibrin, whilst also reducing the clotting time (256).

Chapter 3 Assessment of potential inertial artefacts affecting combined motor transducer rheometers

3.1 Introduction

To ascertain information regarding the potential impact of soot particulates on the weak gelling materials under investigation, it was necessary to render any possible inertial artefacts within the system negligible. Significant discrepancies between gel point (GP) data obtained using combined motor transducer (CMT) and separate motor transducer (SMT) rheometers prompted an investigation into the effect of inertial artefacts on GP measurements. By exploiting the unique properties of the GP, it was possible to develop an Enhanced Rheometer Inertia Correction (ERIC) procedure for post-data acquisition correction. Inertial artefacts can cause large deviations from the true gel point in samples with weak incipient gel networks when probed using a CMT rheometer (25). Gelatin, a well characterised biopolymer, was used as a model system to analyse any deviation in the expected gel point over a concentration range of $2.5\ wt\% \leq C \leq 30\ wt\%$. The studies performed aimed to assess inertial artefacts that have potential to affect SAOS procedures implemented on CMT rheometers.

3.2 Literature Review

For CMT rheometers, the input (torque) and output (displacement) signals are measured at the same shearing surface (Figure 3-1) whilst for SMT rheometers the output signal (torque) is measured at the opposite plate to the input (displacement). Hence, for SMT rheometers, the torque sensing element remains stationary (43), making **instrument** inertia negligible in the system. In contrast, the CMT rheometer is required to both oscillate the moving components of the instrument *and* deform the sample under investigation using the input torque.

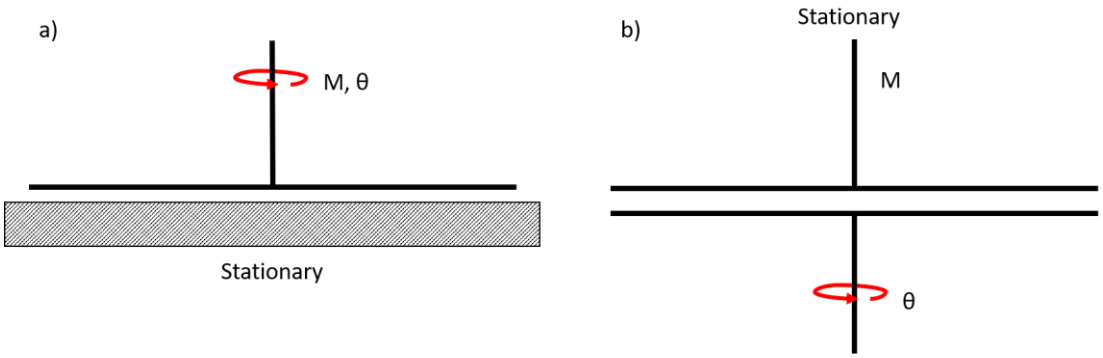

Figure 3-1 *The difference in (a) CMT and (b) SMT rheometer setups. The surface at which the torque, M, and displacement, θ, is measured are shown.*

Standard experimental procedures require the instrument to be calibrated prior to commencing sample testing (Section 3.4.2.1). The calibration involves the determination of the instrument inertia parameter, which is given to a finite level of precision. The TRIOS software used to control the CMT rheometer routinely applies an inertia correction for the storage modulus reported such that

$$G' = G'_{raw} - I_c \omega^2 k_g \qquad \text{Equation 3.1}$$

where G' refers to the actual storage modulus, I_c denotes the inertia constant, ω represents the angular frequency and k_g signifies a geometry factor (32). The accuracy of the raw waveforms used to extract the value of G' can cause uncertainty as the $I_c \omega^2 k_g$ may represent a significant proportion of the G'_{raw} component due to the inertia constant only being defined to a finitely precise value (31). A momentum balance can be used to show that the inertial contribution does not contain imaginary parts (24) and therefore the G'' value reported by the rheometer is not affected by the presence of instrument inertia (32). The raw phase angle is used to quantify the extent of inertial artefacts and leading manufacturers recommend caution for data sets that exceed some critical value. For the AR-2000ex CMT rheometer used throughout the study, the raw phase angle limit is stated by the manufacturer to be 150° (9).

The hypothesis of the work reported herein was that previously reported discrepancies between GP data, obtained using SMT and CMT rheometers for low concentration gelatin samples, were due to uncertainty in the inertia correction when using CMT rheometers. Furthermore, the characteristic rheological behaviour of the critical gel (60) could be exploited to develop an Enhanced Rheometer Inertia Correction (ERIC) procedure (257) and was able to correct for the discrepancy.

3.3 Enhanced Rheometer Inertia Correction Data Analysis

The ERIC procedure was designed for post-acquisition data validation and to allow GP acquisition at previously inaccessible frequencies. As stated in Section 3.4.2.1, a Standard Inertia Correction (SIC) procedure was carried out prior to commencing each experiment. However, with the aid of ERIC, it was possible to adjust data to reduce the effects of slight deviation in the calibrated inertial factors reported, resulting in the decrease in discrepancy of the reported gel point for CMT and SMT rheometers.

The true inertia constant, I_t, that characterises the geometry-instrument assembly can deviate by ΔI from the reported I_c determined during the SIC routine due to the definite precision and accuracy of the value recorded by the rheometer. As a result, Equation 3.1 can be rewritten as

$$G_t'(\omega) = G'(\omega) + (I_t - I_c)\omega^2 k_g \qquad \text{Equation 3.2}$$

$$= G'(\omega) + \Delta I \omega^2 k_g \qquad \text{Equation 3.3}$$

The accuracy of a GP can be indicated by the deviation of the roots where a root can be defined as the time and phase angle intersection of a pair of frequencies. GP with a large deviation in roots could be determined as less accurate than those with a small deviation. To monitor the change in the standard deviation of the roots of the GP, a MATLAB routine was developed to incrementally change ΔI.

The ERIC procedure was coded as a MATLAB routine (258) with a five-parameter logistic equation fitted to the $\delta(t)$ data for each frequency.

$$F = @(p, xdata)p(1) - p(2)./[1 + (xdata\ ./p(3)).\hat{}p(4)].\hat{} - p(5); \qquad \text{Equation 3.4}$$

A five-parameter logistic equation was used to ensure the curves generated were appropriately fitted to the data. The intersections of the fitted frequency curve pairs were established as a root. The mean phase angle and mean time of the roots were reported at the GP with the standard deviation giving an indication of the accuracy of the GP.

The ERIC code was further developed into a GUI for ease of use[1]. Once open, the software simply requires the input of the time, angular frequency, G' and G'' data from TRIOS, along with the correct parameter units (Figure 3-2). The 'Calibrated Inertia

[1] The GUI was developed by Dr D. J. Curtis, College of Engineering, Swansea University.

Constant', I_c, 'Geometry Stress Factor' and 'Geometry Strain Factor' must also be inputted in order to accurately convert the raw torque and displacement signals recorded by the rheometer into the respective stress and strain. The final step is to select the lower and upper correction boundaries, determine the correction increment and outline the 'fit' and 'search' regions.

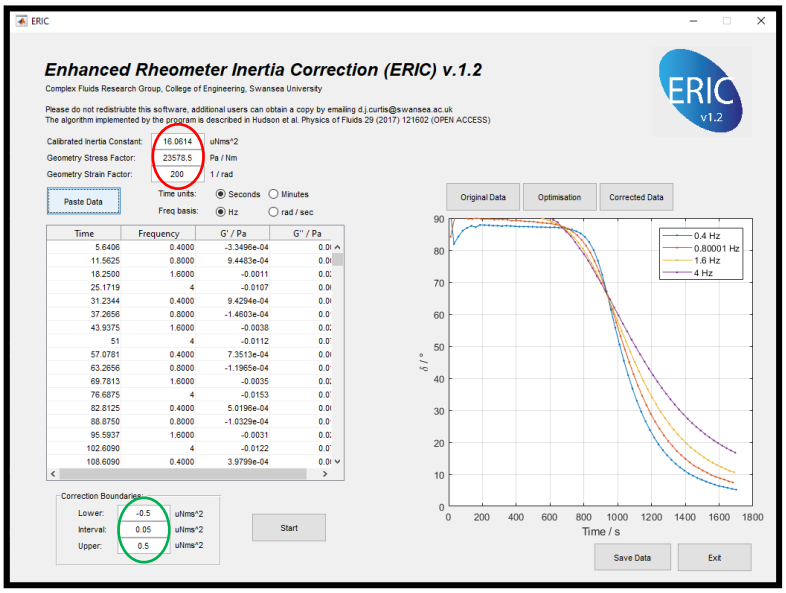

Figure 3-2 *An example dataset pasted into the ERIC GUI. The 'Calibrated Inertia Constant', 'Geometry Stress Factor' and 'Geometry Strain Factor' can be inputted for each specific dataset (circled in red). The lower and upper correction parameters (circled in green) can be altered to initially provide a coarse correction that can be refined to give a precise I_t value.*

The MATLAB procedure iterates between the determined correction boundaries using the given interval value to ascertain the corrected GP value. The optimisation for the data is also available once the correction procedure is complete. The 'Corrected Data' tab in the ERIC GUI shows the adjusted frequency curves and identifies the corrected GP (Figure 3-3). The 'Optimisation' tab (Figure 3-4) shows the minimum corrected phase angle and time data. The normalised deviation of the roots for the δ values is used to determine the ΔI for the dataset.

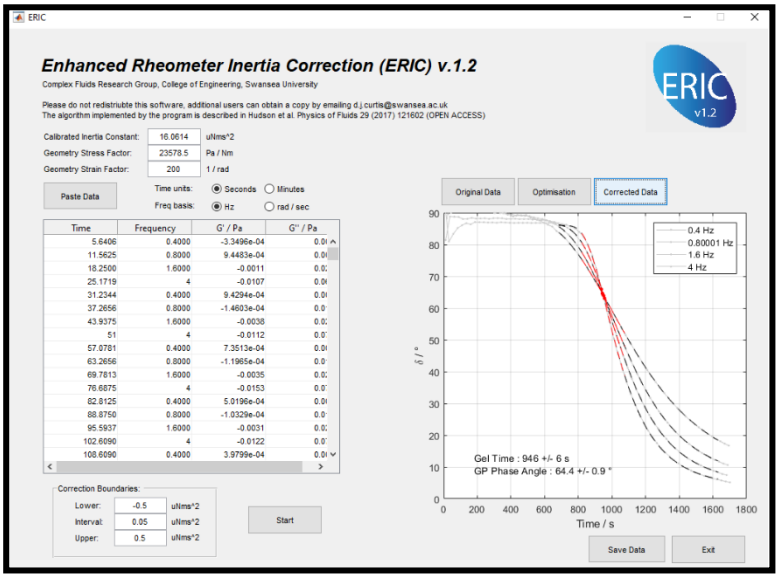

Figure 3-3 *shows a screenshot of the corrected dataset using a coarse search. The black dashed lines are the curves that have been fitted to the data using the five-parameter logistic equation. The 'search' region is shown by the red lines. The corrected GP is stated at the bottom of the plot for both the reported* δ *and* t_{gel}.

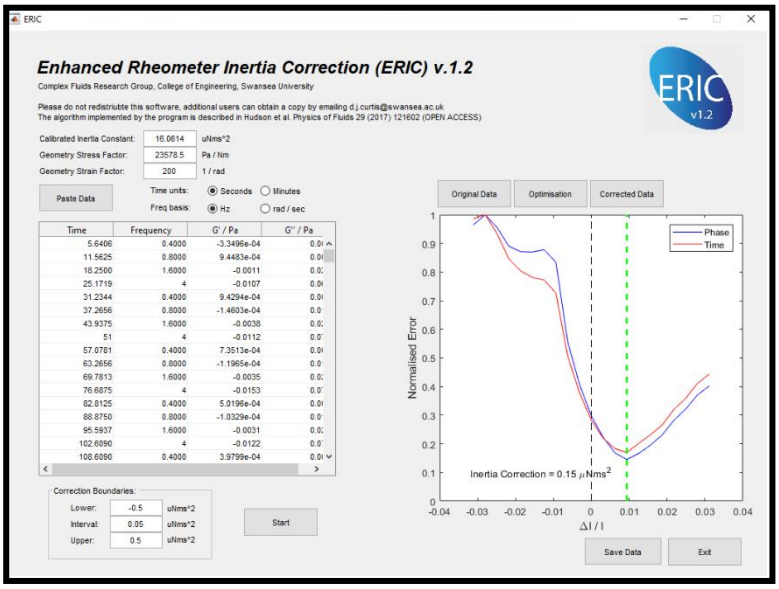

Figure 3-4 *gives an example of the 'Optimisation' tab for the post-ERIC data. The normalised deviation of the roots is shown for both the* δ *and time data with* ΔI *for the dataset being selected from the minimum deviation in roots of the* δ.

3.4 Enhanced Rheometer Inertia Correction Inertia Study Materials and Methods

3.4.1 Materials

Gelatin samples were prepared over the range of $2.5\ wt\% \leq [Gelatin] \leq 30\ wt\%$. Each gelatin sample was prepared using gelatin powder (Fisher G/0150/53) and type (I) deionised water. Quantities of gelatin powder and water were gently combined in a tube with agitation for approximately one minute. Once combined, the tubes were heated for 45 minutes in a preheated 60°C water bath. Throughout the heating process, to guarantee complete dissolution of the gelatin powder, the solutions were repeatedly inverted for one minute approximately every ten minutes to agitate without incorporating excess air. Each homogenous gelatin concentration sample was heated initially for a period of ≤ 45 minutes in a 60 °C water bath (18) to prevent degradation. Aliquots of each of the gelatin solutions were stored in a refrigerator (at 4°C) for no longer than seven days before being melted in a preheated 60°C water bath prior to use for a further 45 minutes.

3.4.2 Methods

3.4.2.1 Standard Inertia Calibration Procedure

A 60 mm acrylic parallel plate geometry and Peltier plate temperature control accessory were fitted to the stress controlled CMT rheometer (AR-2000ex, TA Instruments). A standard inertia calibration (SIC) procedure was carried out without a sample present to calibrate the value of I_c. This procedure involved (i) resetting the 'zero gap' of the instrument each time the upper geometry was refitted (to ensure that the gap used during testing of the sample was accurate) and (ii) determination of the 'geometry inertia' parameter. Finally, the air bearing was iteratively mapped using 'Precision Level 3' to correct for any residual torque (41). All calibrated parameters were saved within the TRIOS software for post data acquisition analysis.

3.4.2.2 Combined Motor Transducer Rheometer Inertial Artefact Study Procedure

To ensure that only the effect of the instrument inertia was then analysed, the experimental procedure used for the studies was carefully designed to remove the possibility of further issues affecting the GP. Prior to experiments being conducted, an aliquot of gelatin was heated for 45 minutes in a preheated 60°C water bath. During

this time the CMT rheometer was calibrated using the SIC procedure (see Section 3.4.2.1).

Once the gelatin sample had been sufficiently heated and all calibrations were complete, 124 µl was pipetted onto the surface of the Peltier plate set to 34 °C to prevent gelation prior to commencement of the test. A 60 mm acrylic parallel plate geometry was then lowered to a gap of 150 µm and the sample slowly sheared at 100 s^{-1} for 10s to ensure an even load across the parallel plate system. A gap of 150 µm was used to satisfy the Schrag gap loading criterion [2] (45). The loading of the sample was visually inspected before a small amount of low viscosity silicon oil (9.8 mPa.s Brookefield) was pipetted onto the free surface (i.e. circumference of the acrylic geometry). This precautionary measure prevented evaporation of the sample throughout the test. As soon as all loading steps were complete, the test was commenced.

The initial stage of the test procedure involved quenching from the loading temperature of 34 °C to the test temperature. All experiments using 2.5 wt% gelatin were conducted at a temperature of 19 °C at a torque amplitude of 10 µN.m. The stress relaxation exponent of the incipient gelatin gel has previously been reported to be independent on the concentration and gelation temperature (49). At 19 °C the t_{gel} was sufficiently long to minimise the sample mutation effects at the gel point (259) by maintaining a gelation time of approximately 900 s.

To study the effect of gradually increasing inertial contributions, gel point data was obtained using a variety of 'frequency decades'. Each decade contained four discrete frequencies including the highest and lowest frequencies in the decade. The frequency decade is denoted by the highest frequency in that decade, such that the 4 Hz decade included frequencies in the range 0.4 Hz to 4 Hz. The frequency decades studied were in the range 1 Hz (i.e. 0.1 Hz – 1 Hz) to 12 Hz (i.e. 1.2 Hz – 12 Hz). Each test ran for 3600 s which allowed the phase angle of the gel (at all frequencies) to reduce to $\delta <$ 20° so that sufficient data in the post gel point region was obtained for further analysis.

[2] A small gap ensured that the sample inertia could be neglected such that a constant velocity gradient existed in the shearing gap.

3.4.2.3 Separate Motor Transducer Rheometer Inertial Artefact Study Procedure

To allow comparison of CMT and SMT data, a series of experiments were conducted using an SMT rheometer (ARES-G2, TA Instruments). A Peltier plate temperature control system was used in conjunction with a 40 mm aluminium parallel plate geometry. A gap of 150 μm was used to satisfy the Schrag gap loading criterion[2] (45), with 108 μl of 2.5 wt% gelatin being pipetted onto the Peltier plate prior to lowering the upper geometry. The sample was loaded at 30 °C before being quenched to a test temperature 20 °C during a 100 s^{-1} pre-shear for a duration of 10 s. The pre-shear ensured that the sample was evenly distributed within the geometry gap. Data was collected using multiple consecutive frequency sweeps over a frequency range of 0.9-3.5 Hz. The strain amplitude was decreased by 25% from 100% where the torque exceeded 3 μNm to acquire valid measurements despite the transient nature of the gelation process. This procedure was developed to successfully report a resolvable torque signal at each stage of the gelation process whilst maintaining linear viscoelastic measurements. Harmonic analysis was conducted on torque signals to ensure linear viscoelastic conditions by confirming the absence of harmonic signals in the torque waveform.

3.4.2.4 CMT Rheometer Concentration Study Procedure

A separate gelatin concentration study was conducted over a range of $2.5\ wt\% \leq c \leq 30\ wt\%$ using a standard GP procedure with a fixed frequency decade of 0.3-3 Hz and the addition of the change of the test temperature parameter. Each concentration of gelatin required a unique test temperature (as outlined in Table 3-1) as gel time is strongly dependent on both the concentration and gelation temperature. By increasing the temperature as the gelatin concentrations increased, the gel time of each experiment was maintained at approximately 900 s.

Table 3-1 *The test temperatures required for each gelatin concentration.*

Concentration /wt%	**Temperature** /°C
2.5	19.0
5	22.5
10	26.0
15	27.5
20	29.5
25	31.5
30	32.5

The gelatin samples were quenched from 34 °C to the test temperature (i.e. for 10 wt% gelatin, the sample was quenched from 34 °C to 26 °C at a rate of 5 °C/min). For all concentrations, a frequency decade of 0.3 to 3 Hz was employed to reduce the possibility of inertial artefacts within the system. A torque input parameter of 10 μN.m was used for all experiments. Each experiment was set to run for 3600s in order to ascertain valid data both pre- and post-GP.

3.5 Results and Discussion

3.5.1 Gel Point Analysis and Correction

The TRIOS data for each GP was analysed using the GP Analysis software[3] to determine the apparent gel time (t_{gel}), phase angle (δ), raw phase angle (δ_{raw}), storage modulus (G') and loss modulus (G'') parameters (all at the GP). Further data analysis was completed using Microsoft Excel.

Figure 3-5 shows example CMT data for GPs at the extremities of the frequency range used for the study of inertial artefacts. Both examples were obtained using a gelatin concentration of 2.5 wt%. The data shown in Figure 3-5a outlines a well-defined GP obtained at a low frequency decade of 0.1-1Hz. The roots of the frequencies do not deviate significantly from the estimated GP as the inertial artefacts affecting the system are minimal. For comparison, the data displayed in Figure 3-5b illustrates phase angle data collected for the highest frequency decade (1.2-12Hz). It is clear that using this higher frequency decade generates a poorly defined, hard to identify GP and that there are several roots (i.e. crossovers between data at each pair of frequencies). The pre-GP data shows classic inertial issues as $\delta > 90°$.

[3] The previously unpublished bespoke GP Analysis Software was developed in house by Dr Dan Curtis and uses the 5-parameter logistic equation approach as described in Chapter 3..

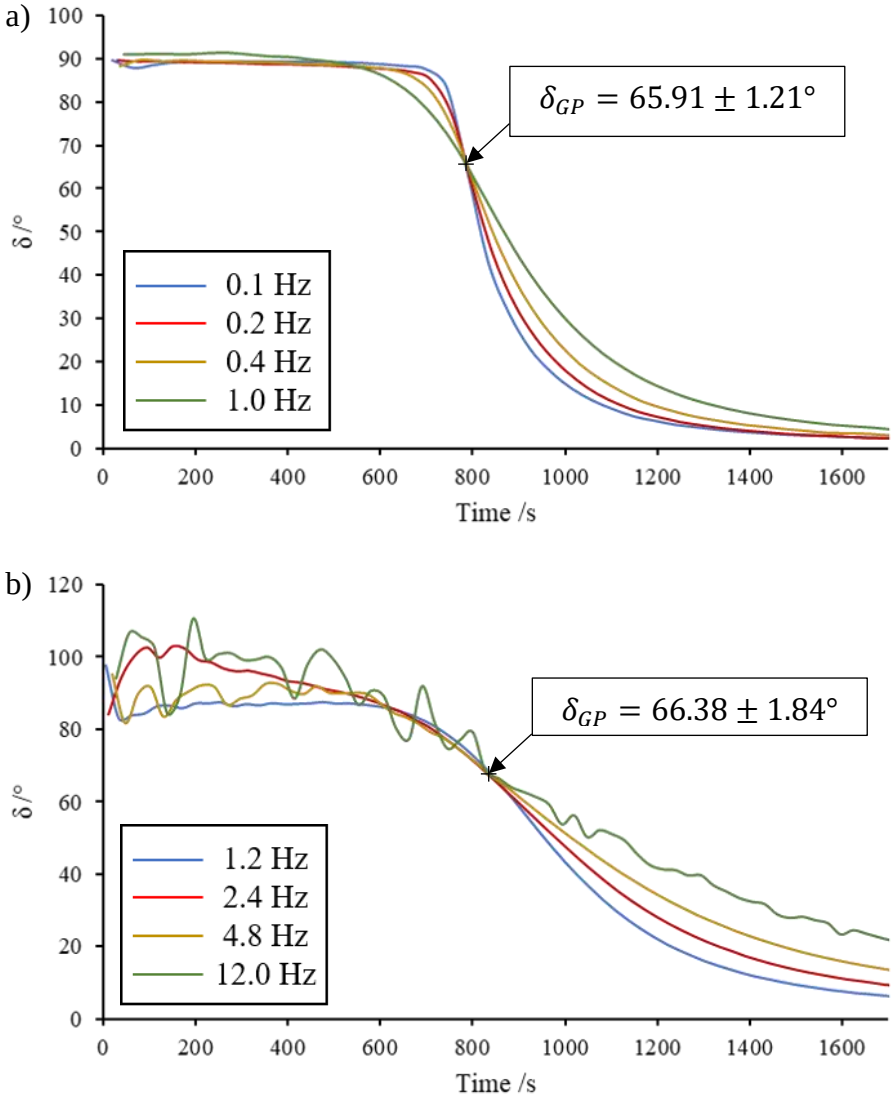

Figure 3-5 *Example GP data for 2.5 wt% gelatin at low and high frequency decades. The GP shown in a) was obtained over a frequency range of 0.1-1Hz whilst b) illustrates data acquired at a high frequency decade of 1.2-12Hz.*

As discussed in Section 3.3, the ERIC procedure was applied post-acquisition to all experimental data collected for both the frequency and concentration studies used to analyse the effect of inertia artefacts. Figure 3-6 illustrates the process undertaken during the ERIC procedure.

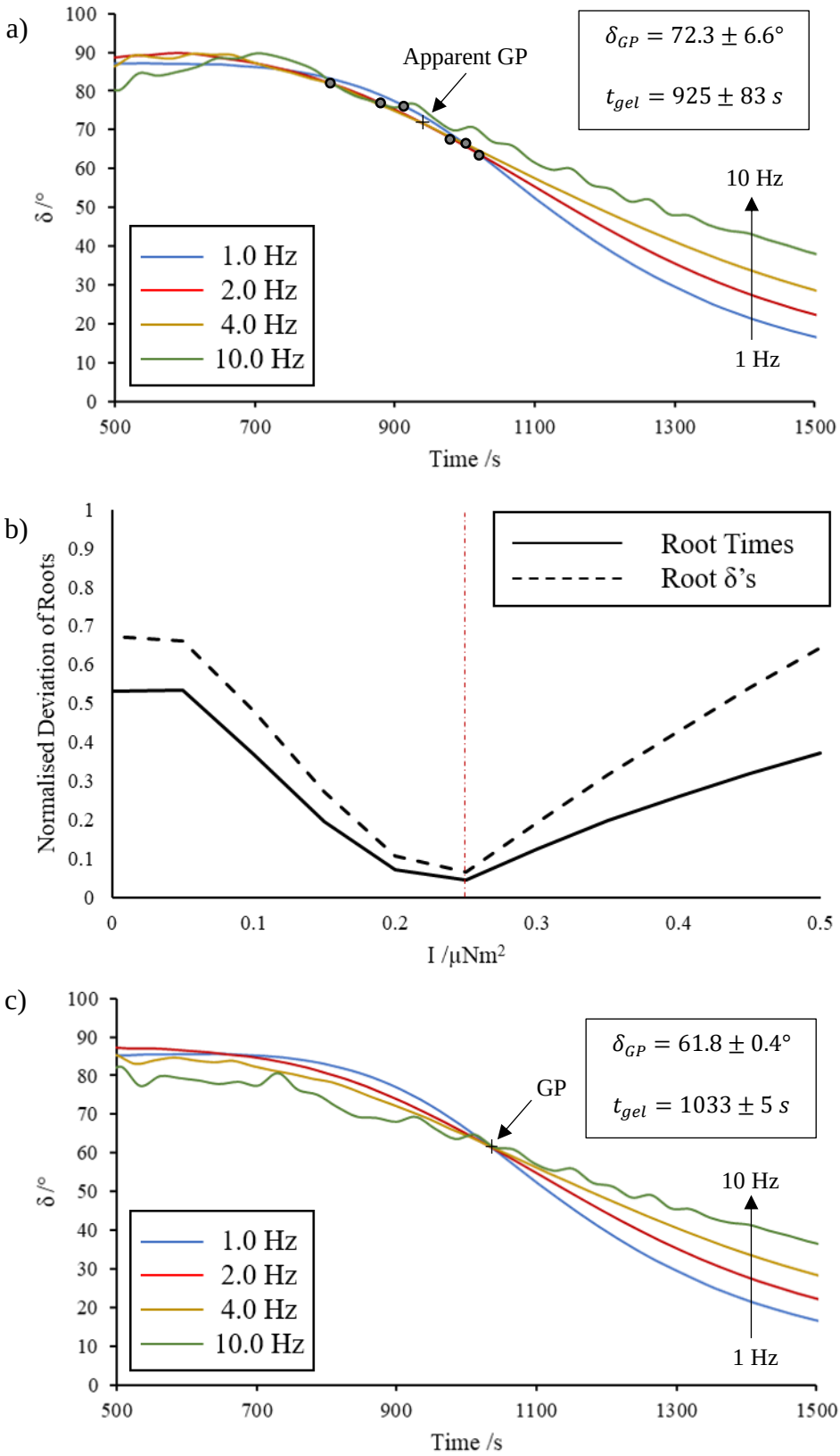

Figure 3-6 *outlines the ERIC procedure where a) illustrates an apparent gel point prior to correction obtained using a frequency decade of 1-10 Hz, b) shows the optimisation of the gel point data using the ERIC procedure and c) shows the ERIC corrected GP data for the data reported in a).*

Figure 3-6a shows an example of an apparent GP, defined as the mean root position, for data collected over a 1.0 – 10 Hz decade. The value of the uncorrected CMT rheometer GP was reported as 72.3 ± 6.6° using the GP Analysis software[3]. For an identical sample and procedure, the corresponding SMT rheometer GP was 62.7 ± 1.0°. The high standard deviation in the CMT rheometer GP reflects the large spread of the roots shown by the smaller grey circles Figure 3-6a. The uncertainty of the GP is a consequence of the finite precision of the standard inertia correction.

Figure 3-6b illustrates the optimisation of the inertia constant, I_t, using the ERIC procedure. The deviations of the roots, with respect to phase angle and time, were normalised and a value of ΔI was selected based on the minimum deviation, shown in the figure by the red dashed line. The 'search region' of the GUI was used to outline the area where $\delta(t)$ roots were considered to be relevant to the GP and was altered to exclude the extremities of the data that included incorrect cross-overs of the frequencies that may affect the GP reported.

Figure 3-6c shows the corrected GP data once the ERIC procedure had been implemented. The corrected phase angle reported, 61.8 ± 0.4°, is noticeably lower since the optimised true inertia value of 21.5422 μNm^2 was used to calculate the GP. The I_t value used represents a 0.46% change from the instrument calibrated value resulting in a GP in agreement with the SMT rheometer. The corrected data maintains phase angles of $\delta \leq 90°$ throughout, suggesting that there is negligible influence from inertial artefacts within the data.

Due to the frequency (ω^2) dependence of the inertia correction, it is not possible for the ERIC routine to falsely generate a gel point if the sample material does not exhibit this behaviour. For hypothetical, valid non-GP data in the vicinity of the gel point, it is feasible to define G'' and G' as separate frequency dependent power laws as in Equations 3.4 and 3.5 where $\varepsilon \neq \varphi$.

$$G'' = k_2\omega^{\varepsilon} \qquad \text{Equation 3.4}$$

$$G' = k_1\omega^{\varphi} \qquad \text{Equation 3.5}$$

Taking into consideration the above conditions, a corrected G' value, G'_C, would be expressed as

$$G'_c = k_1\omega^{\varphi} + k_i\omega^2 \qquad k_i = \Delta I k_g \qquad \text{Equation 3.6}$$

The above equations can be combined to give

$$G'_c = k_1\omega^{\varphi} + \Delta I k_g\omega^2 \qquad \text{Equation 3.7}$$

As previously discussed in Section 1.11.4, at the sol-gel transition,

$$tan\delta = \frac{G''}{G'} = constant \qquad \text{Equation 1.28}$$

Substituting Equation 3.4 and Equation 3.7 gives a modified equation that would express the sol-gel transition under the conditions specified above,

$$\frac{G''(\omega)}{G'_C(\omega)} = \frac{k_2\omega^{\varepsilon}}{k_1\omega^{\varphi} + \Delta I k_g\omega^2} \qquad \text{Equation 3.8}$$

A pseudo-GP would similarly require the $tan\delta$ parameter to be frequency independent, resulting in

$$\frac{k_2\omega^{\varepsilon}}{k_1\omega^{\varphi} + \Delta I k_g\omega^2} = c = constant \qquad \text{Equation 3.9}$$

Equation 3.9 can be rearranged to isolate the frequency independent coefficient:

$$\Delta I k_g = \frac{k_2}{c}\omega^{(\varepsilon-2)} + k_1\omega^{(\varphi-2)} \qquad \text{Equation 3.10}$$

For the frequency independent conditions to be met, the exponent values ε and φ would have to be equal to 2 to give a $\omega^0 = 1$, which is not viable at the GP (since a GP could only exist if $0 < \varepsilon = \varphi < 1$). It is also not feasible to have negligible k coefficients as the data would not be a valid GP if the G' and G'' components were zero.

3.5.2 Study of Increasing Frequency Intervals on Gelatin Gelation

For each frequency decade, repeat experiments were conducted using the procedure outlined in Section 3.4.2.2 and the average GP calculated. Error in the reported GP was recorded as the larger of either the standard deviation between repeats or the deviation of the roots reported (such that maximum uncertainty was reported). The data was plotted as frequency decade against phase angle before the gel points were corrected using the ERIC procedure (Figure 3-7). The highest frequency values are presented on the x-axis with the lowest frequency being a decade lower (e.g. the corresponding lowest frequency for 10 Hz was 1Hz). It is clearly shown that as the frequency decade increases, the value of the GP reported increased out of the range

predicted by an SMT rheometer (dashed line shows the mean SMT GP with the dotted lines referring to the standard deviation). As the value of the phase angle increases, the roots defined for the GP deviate further from the true value. Once corrected using ERIC, the data for all frequency decades falls back within the expected SMT limits, giving accurate and precise gel points. Whilst validating the previously accessible SAOS frequency ranges, ERIC also enables analysis of rapidly evolving strain sensitive gelling systems by use of higher frequency decades. Previous techniques, such as Fourier Transform Mechanical Spectroscopy reported by Hawkins (7) were shown to be inappropriate for such gelling systems. Where $N_{mu} > 0.15$, the data was discarded due to high sample mutation (259). Due to the range of high frequency decades employed during the study, some raw phase angle data fell outside of the 150° limit set by the manufacturer (9). However, this was not discarded prior to analysis using ERIC.

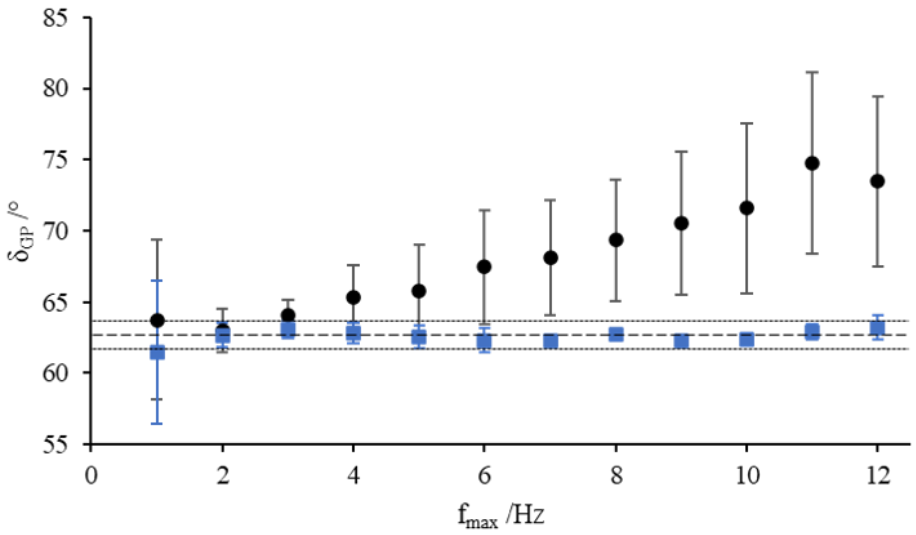

Figure 3-7 *Phase angles reported at the GP (black circles) over a range of increasing frequency decades along with the ERIC corrected δ_{GP} for the same dataset (blue squares).*

A comparison of phase angle as a function of raw phase angle is presented in Figure 3-8. The validity of the data was limited by the stated raw phase angle threshold of 150°, outlined by the manufacturer for the AR-2000ex rheometer used (9). As the raw phase angle approaches 180°, an increasing proportion of the applied force can be attributed to instrument inertia artefacts. As stated in Section 3.4.2.1, the SIC procedure involves calibration of the instrument inertia. The deviation in repeat calibration of the instrument inertia was calculated to be 0.15%, suggesting a systematic error in the instrument (Table 3-2). As a result, direct comparison with

rheometric data from other rheometers is not possible. The precision and accuracy of the corrected GP is a result of a 0.46% deviation from the calibrated inertia constant, I_c. The effect the deviation in the determined I_c has on the GP can limit the validity of the raw phase angle data as seen in Figure 3-7. The dashed and dotted horizontal lines represent the mean and standard division respectively of SMT data. Once the ERIC procedure was applied, data that would previously have been discarded due to limitations of the rheometer, fell back within the inertia free SMT rheometer boundaries.

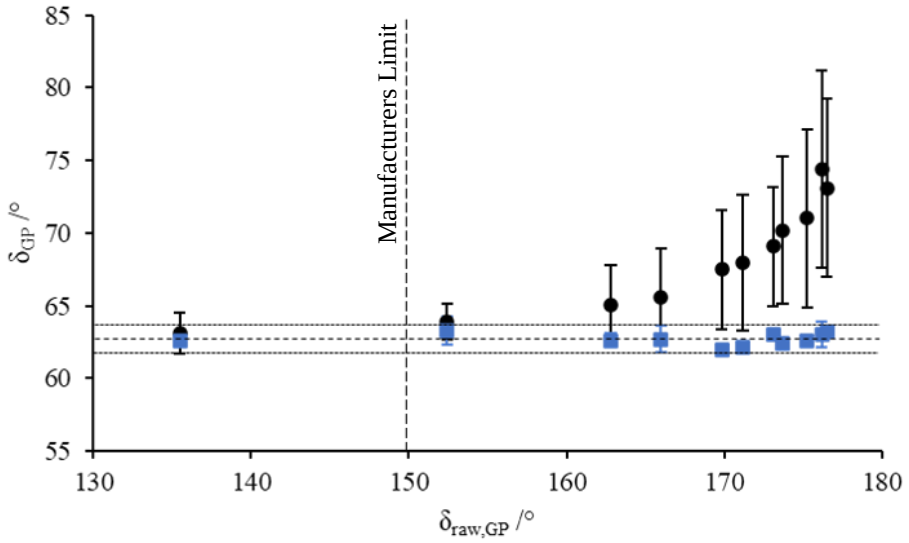

Figure 3-8 *The apparent and corrected GP data for the frequency study, shown with phase angle as a function of raw phase angle. The black circles represent the raw data and the blue squares the corrected data.*

Table 3-2 *The calibrated inertia constants reported for a CMT rheometer. The data was collected by repeatedly calibrating the instrument prior loading a sample.*

AR-G2(II) CMT Rheometer	
Geometry Inertia /µNms^2	**Instrument Inertia** /µNms^2
10.0922	18.9100
10.2577	18.9945
10.2139	18.9759
10.2628	18.9604
10.2605	18.9491
10.2190	18.9322

As discussed above, uncorrected GP data obtained using different CMT rheometers cannot be compared due to the discrepancy in calibrated inertia constants (where $\delta_{raw} > 150°$). To further explore the effect of inertial artefacts in driving variation between data obtained using different CMT rheometers, data for three AR-G2 rheometers was collected. Two CMT rheometers, AR-G2(I) and AR-G2(II) (serial numbers 10D4334 and 10D4328 respectively), were purchased at the same time, April 2010, and have identical usage and service histories. However, the third CMT rheometer analysed, AR-G2(III) (serial number 7A3292), purchased in February 2007, prior to both AR-G2(I) and AR-G2(II), has been moved between laboratories several times.

The data presented in Figure 3-9 compares GP data collected using both SIC and ERIC procedures. The GPs were determined using a frequency decade of 1-10 Hz on all CMT rheometers with a gelatin concentration of 2.5 wt%. The instruments concerned had undergone manufacturer calibration and servicing within the 12 months prior to the studies being conducted. The horizontal dashed and dotted lines represent the mean gel point phase angle and standard deviation respectively for an SMT rheometer.

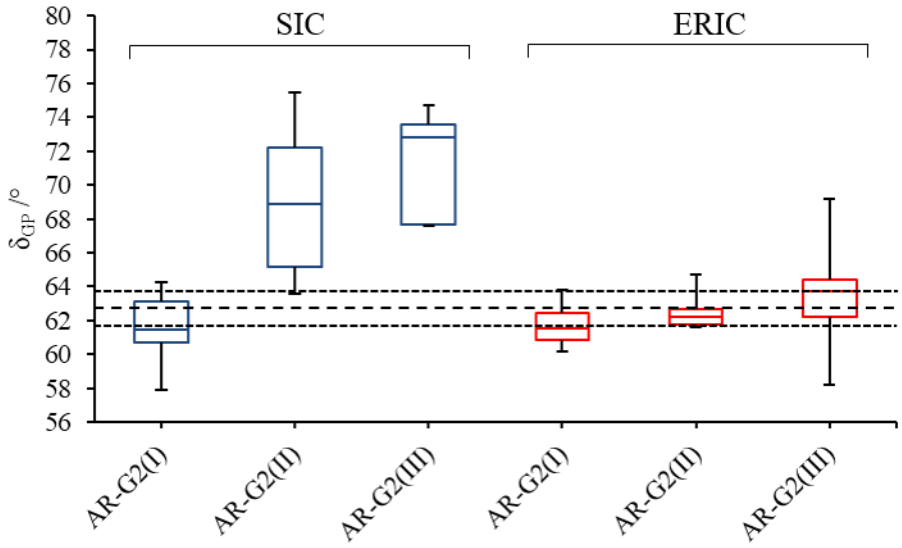

Figure 3-9 *The comparison reported GP data from three AR-G2 rheometers using both the SIC and the developed ERIC procedure. The horizontal dashed and dotted lines represent the mean and standard deviation of the data obtained using an SMT rheometer.*

The apparent GPs reported for each of the CMT rheometers were 61.5 ± 2.0° for AR-G2(I), 69.0 ± 4.4° for AR-G2(II) and 71.3 ± 3.0 for AR-G2(III). The raw GP data was then corrected using the ERIC procedure and the phase angle distributions between

SIC and ERIC analysed using a Student t-test ($n = 8$). There was no statistically significant difference reported between the uncorrected and ERIC corrected GP data for AR-G2(I) ($p = 0.39$) as the corrected GP was determined to be 61.8 ± 1.2°. This indicates that the SIC procedure is sufficiently accurate calibration for the AR-G2(I) rheometer. However, both the AR-G2(II) and AR-G2(III) CMT rheometers showed a significant difference in the reported GPs once corrected using ERIC. The corrected GPs were found to be 62.5 ± 1.0° and 63.5 ± 3.4° for AR-G2(II) and AR-G2(III) respectively once the ERIC procedure had been applied. A statistically significant difference between SIC and ERIC procedures was found for AR-G2(II) and AR-G2(III) ($p = 0.003$ and $p = 0.025$, respectively). These p values suggest that the SIC procedure was insufficient for the calibration of the inertia constants of the rheometers and the results require further analysis using the ERIC procedure.

It is clear from Figure 3-9 that when using the SIC procedure, the apparent uncorrected GPs returned for the AR-G2(I) and AR-G2(II) rheometers showed significant variation using a T-Test with two-tails and equal variances ($p = 0.0004$). Prior to correction, the AR-G2(II) and AR-G2(III) rheometers appear to show some agreement in the reported GP. However, after the application of the ERIC procedure, the CMT data for all three AR-G2 rheometers shows agreements with the SMT GP data of 62.7 ± 1.0° for an identical 2.5 wt% gelatin system.

As discussed, AR-G2(III) was purchased prior to AR-G2(I) and AR-G2(II) which could be a possible explanation for the reported GPs prior to the application of the ERIC procedure. AR-G2(III) was moved between several laboratories and due to the sensitivity of the instrument and the instrument limits approached in the study, it is possible that the GP accuracy was compromised. Despite being almost identical, AR-G2(I) and AR-G2(II) report different pre-ERIC GPs due to instrument-specific accuracy of the SIC procedure. Both AR-G2(I) and AR-G2(II) were manufactured in April 2010 with similar serials numbers of 10D4334 and 10D4328 respectively. Interestingly, TA Instruments do not employ quality control for phase angle measurement, which could explain the discrepancy in the phase angles reported by the different instruments. Consequently, it may be possible for ERIC to form the basis of a new quality control procedure.

3.5.3 Concentration Dependence of Gelatin Gelation

As described in Section 3.4.2.4, a study of the effect of concentration on stress relaxation exponent at the GP in gelatin gels was conducted. A range of concentrations, $2.5\ wt\% \leq [Gelatin] \leq 30\ wt\%$, and a set frequency decade of 0.3-3Hz were employed. The experimental procedure was kept identical to that of the frequency study with the results obtained initially analysed with the SIC procedure. Data was then processed, post-acquisition, using the ERIC procedure. A previously unreported dependence of the stress relaxation exponent on gelatin concentration was observed for low concentration gelatin gels, with a limiting δ_{GP} of 63° ($\alpha = 0.7$).

Figure 3-10 shows mean phase angles recorded over a range of gelatin concentrations using the SIC procedure (black circles) and clearly illustrates a gelatin concentration dependence. As the concentration of the gelatin increases, the phase angle reported decreases. The error bars plotted represent the standard deviation in the data.

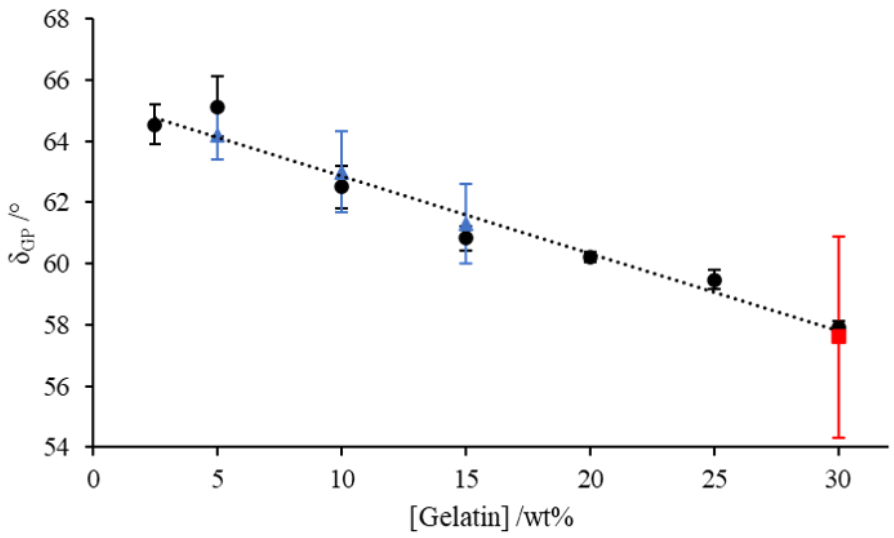

Figure 3-10 *A previously undocumented gelatin gelation concentration dependence was reported. Figure 10a) plots the uncorrected data recorded in the study (black circles) alongside data collected by (Hawkins et al., 2008) using SAOS and FTMS (blue triangles) over a range of 0.2 – 3.2 Hz and data published by (Curtis et al., 2015) using OFR and FTMS over a range of 0.1 – 10 Hz (red squares).*

Previous literature published by Hawkins *et al.* (7) and Curtis *et al.* (77) was used for comparison of the data. Both studies used a variety of discrete gelatin concentrations and rheometric methods to obtain GP data that agrees with the present study. Neither study reported gelatin concentrations as low as 2.5 wt%. However, the ERIC procedure allows accurate and precise GP data to be recorded at the extended lower boundary of

the concentration range. Curtis *et al.* used an SMT rheometer with a multi-frequency Optimal Fourier Rheometry (OFR) technique to obtain GP data for 30 wt% gelatin up to 10Hz (red square). The agreement between the present study and that of Curtis *et al.* (77) is due to the significantly higher viscosity of the 30 wt% gelatin used on the CMT rheometer. Higher gelatin concentrations result in the higher torque that reduces the raw phase angle to within the acceptable manufacturer limits for the CMT data presented. Fourier Transform Mechanical Spectroscopy (FTMS) was employed by Hawkins *et al.* using a CMT rheometer (7). There is excellent agreement between the data collected and that published in the study and it is likely that by using a SIC procedure on a CMT rheometer, the data experienced the previously discussed instrument inertia artefacts.

Figure 3-11 presents the uncorrected (black circles) and corrected data (blue squares) for the gelatin concentration study. The ERIC procedure uses the data provided by the TRIOS file to determine the true gel point. Once ERIC was applied, the data from both the CMT rheometer and the SMT rheometer came into agreement with the gel point for CMT being re-evaluated at 63.1 ± 0.6° post data-acquisition and the SMT gel point being given as 62.7 ± 1.0°. The agreement between the CMT and SMT provides validity of the ERIC procedure as the SMT rheometer is not influenced by instrument inertia.

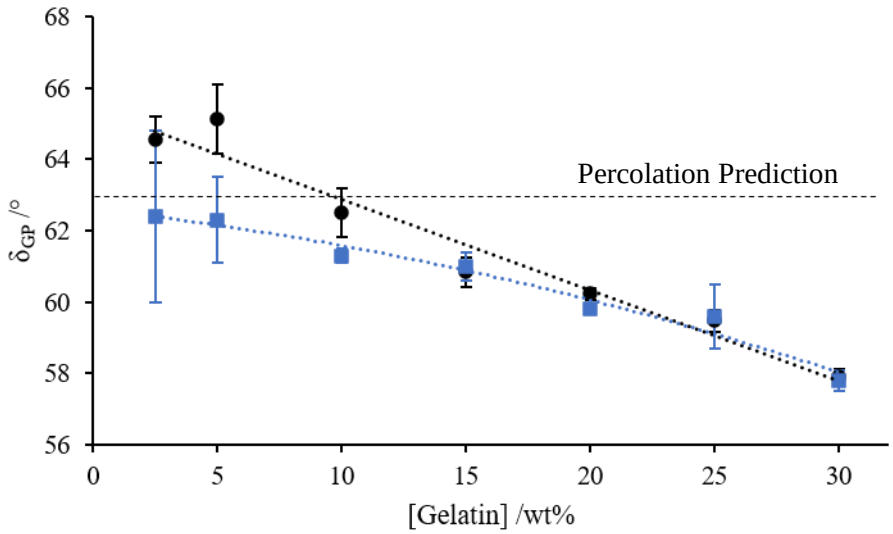

Figure 3-11 *The application of the ERIC procedure to the raw data from the present study (black circles). Once corrected, the data approaches the Percolation Prediction phase angle of 63° (blue squares).*

The percolation prediction illustrated on the figure highlights the limiting value of the gelatin based on a stress relaxation exponent ($\alpha = {}^{\delta}/_{90}$). The theoretical predictions of 3D lattice percolating systems is $\alpha = 0.7$ (52,260,261). Therefore, a maximum phase angle of 63° is approached as gelatin concentration is decreased. As the concentration of the gelatin samples tends to zero, the prediction of a stress relaxation exponent value of 0.7 can be expected as there is a lack of interaction and cross linking necessary within the gel to reach the GP (52). Numerous studies have been conducted on alternative biopolymer systems which support the theoretical percolation predictions (262–265).

3.6 Conclusions

The development of the Enhanced Rheometer Inertial Correction (ERIC) procedure and subsequent application to gelatin gelation is discussed in this chapter. The conclusions of the studies are as follows:

1. Development of an Enhanced Rheometer Inertial Correction (ERIC) procedure. By exploiting the frequency-independent GP, it was possible to develop the ERIC procedure for acquisition of valid GP data at previously inaccessible frequencies when using a CMT rheometer, where previously the inertial artefacts present dominated the measurement. The development of an ERIC GUI has made the procedure accessible to the experimentalist for post-data acquisition correction.
2. Effect of increasing frequency intervals on gelatin gelation. The ERIC procedure reported in this chapter shows that data acquired using a CMT rheometer, at previously inaccessible frequencies, can be corrected post-data acquisition, to obtain data in agreement with SMT rheometers. The data can be corrected to give greater accuracy and precision for the GPs recorded by determining the true inertia constant using a MATLAB code. Typically, the apparent inertia constant reported by the instrument was correct by values of the order of 0.1 μNms^2. A modification of this proportion is larger than the precision offered by the instrument as determined by carrying out repeat calibrations of the rheometer. The inaccuracy in the apparent inertia constants as calibrated appear to be instrument specific. Application of the ERIC procedure may explain apparent discrepancies between identical gelling systems measured on different CMT rheometers. By exploiting the frequency

independent GP of the data, the true inertia constant could be determined, providing validation to the data with increased accuracy and precision of the corrected GP recorded. By accessing previously inaccessible frequencies, the ERIC procedure allows experiments to be conducted at either (i) higher frequency decades, lending it to rapidly gelling systems with $t_{gel} < 100s$ and/or (ii) lower concentration systems.

3. Concentration dependence of gelatin gelation. A previously undocumented concentration dependence was identified for gelatin. Over a range of $2.5\ wt\% \leq c \leq 30\ wt\%$, a limiting phase angle value of 63° at low gelatin concentrations was observed, corresponding to a stress relaxation exponent value of $\alpha = 0.7$. Discrete data points extracted from published literature supported the evidence of a concentration dependence for the gelation of gelatin when plotted alongside the data obtained in the present study.

Chapter 4 Detection of exhaust particulate induced clotting anomalies in fibrin gels

4.1 Introduction

The effect of air pollution on human health has been widely studied (168,175,191,224,227,246). The potential for soot particulates to translocate across the alveolar-capillary membrane within the lungs to the blood stream may result in blood clotting anomalies. The fibrin network that forms the scaffolding within a whole blood clot can be studied using the component proteins, fibrinogen and thrombin. Rheological techniques can be employed to assess the sol-gel transition in fibrin gels to determine whether particulate matter (PM) causes anomalous clotting characteristics to the clot structure.

Weak gelling systems, such a fibrin gels, are susceptible to inertial effects with the raw phase angle indicating the level to which inertial artefacts pollute the data. The instrument manufacturer (TA Instruments) state a limiting raw phase angle of 150° (9) for the AR-G2 CMT rheometer used, beyond which the data may not be valid. The raw phase angles reported by CMT rheometers in this chapter exceed the manufacturers limit ($\delta_{raw} > 175°$), necessitating the use of the ERIC procedure (detailed in Chapter 3) to correct for the discrepancies in the reported GP data between CMT and SMT rheometers.

The studies presented herein were conducted to assess the potential pernicious effects of soot PM on clotting and the microstructure of the resulting fibrin network. The rheological GP data obtained using CMT and SMT rheometers was further assessed by images obtained using Scanning Electron Microscopy (SEM) and Laser Scanning Confocal Microscopy (LSCM) for a range of fibrinogen and thrombin concentrations prior to the addition of the PM.

4.2 Literature Review

The polymerisation of fibrinogen by thrombin to fibrin forms the microstructural scaffold of a blood clot (128). In healthy individuals, fibrinogen is found at a concentration between 2 mg ml^{-1} and 5 mg ml^{-1} (110–112) and as such, is the third most common protein found in human plasma (110). Inflammation and injury can elevate the fibrinogen levels up to 7 mg ml^{-1} (112). The polymerisation of fibrinogen

by thrombin occurs upon initiation of the coagulation cascade and results in the formation of an insoluble fibrin network which allows haemostasis to be maintained (100). Both the *intrinsic* and *extrinsic* coagulation pathway result in thrombin activation and subsequent polymerisation of the fibrinogen monomers to a cross-linked fibrin network (121).

The formation of a fibrin network, along with platelet aggregation, can result in either haemostasis (a healthy result) or pathological vascular occlusion (128). Clots that are formed at higher thrombin concentrations are more structurally stable but are less susceptible to fibrinolysis resulting in possible occlusion of the blood vessels (121). Abnormal clots can result in vascular diseases such as DVT, VTE, PE, stroke and myocardial infarction (54,128,134). Cardiovascular disease is one of the leading causes of death across the world with approximately 30% of deaths being reported in relation to cardiovascular episodes (266,267). Between 2007 and 2017, total deaths from cardiovascular disease increased globally by 21.1% (268).

Whilst nanoparticles have been employed in the treatment of blood disorders and disease (249,250,255,256), a wealth of research has indicated that diesel PM of a similar size, produced due to incomplete combustion, increase the likelihood of adverse effects on blood coagulation (161,168,192,201,224,230,235,236,269). The effects of particulates on coagulation has previously been monitored using techniques involving measurement of a clotting time, microscopy and platelet function tests (161,168,224,234). However, each technique has shortcomings (Section 2.3.4).

The use of rheometric techniques for the detection of anomalous blood coagulation due to the presence of exhaust PM may provide robust quantitative data and provide additional insight into this important phenomenon. Rheometric techniques are advantageous as it is possible to obtain many data points for low viscosity samples over a large range of frequencies. The technique of oscillatory rheology has previously been applied to clotting (270–273) with multi-frequency SAOS procedures later being employed to indicate the frequency-independent GP of gelling materials (59,69). Studies by Curtis et al. (59) and Badiei et al. (69) validated the use of controlled stress parallel superposition (CSPS) on fibrin gels (and later blood) by comparison to SAOS procedures. It was not viable to apply CSPS to the studies presented herein as the microstructural modifications caused by an imposed unidirectional shear had potential

to conceal any deviation observed in the clot microstructure as a result the presence of PM. Therefore, it was necessary to conduct experiments using a standard SAOS GP procedure to determine the effects of soot under quiescent conditions.

4.3 Materials

Human fibrinogen and alpha thrombin were purchased from Enzyme Research UK. Tris-buffered saline 10x solution (TBS) was purchased from Sigma Aldrich UK. Alexa-488 labelled fluorescent fibrinogen was purchased from Thermo Fisher UK.

4.3.1 Thrombin preparation

Human alpha thrombin was purchased in aliquots of 1000 NIH units from Enzyme Research UK. In order to obtain the desired activity of 500 NIH ml^{-1}, 2 ml of deionised water was added into the vacuum sealed container using a syringe. Once all the deionised water was added, the container was gently swirled to encourage the powdered thrombin to dissolve. After all the solids had dissolved, the thrombin was aliquoted into 10 µL volumes for use in experiments. The aliquots were stored in a freezer (at -80 °C) until required for testing.

When required, an aliquot was removed from the -80 °C freezer, thawed at room temperature and placed on ice. A volume of 990 µl of freshly prepared 10 x diluted TBS was added to an Eppendorf tube which was also placed on ice. Once the TBS was appropriately chilled, 10 µl of thrombin was added and the container gently inverted to ensure the solution was completely combined. As a precaution, the prepared thrombin was stored on ice for the duration of the experiments and discarded after four hours (274) to ensure the level of thrombin activity remained consistent throughout all experiments.

4.3.2 Fibrinogen preparation

Human fibrinogen (Enzyme Research UK) was required for the preparation of fibrin-thrombin gels. Fresh 10x TBS was diluted in deionised water prior to the solubilization of the fibrinogen to make a 1x TBS solution. A tube containing the required volume of 1x TBS (as stated by Enzyme Research UK) was heated in a 37°C water bath for approximately 20 minutes prior to addition to the vacuum sealed fibrinogen container. The full volume of warm 1x TBS was inserted into the container holding the fibrinogen using a syringe to pierce through the rubber seal. Once the full volume of 1x TBS was transferred, the glass container was very gently and carefully

swirled to combine the components and sealed with Parafilm. It was then replaced into the 37°C water bath and was gently swirled at 15-minute intervals until the solution became transparent, colourless and homogenous (after approximately 5 ½ hours). At this point, the container was removed from the water bath and the prepared fibrinogen aliquoted into 0.9 ml volumes before being placed into a -80 °C freezer until required for testing.

Prior to preparation of the fibrin-thrombin gels, the necessary number of aliquots were removed from the -80 °C freezer and allowed to thaw to ambient temperature. Once thawed, the required volume of fibrinogen was added to the sample ready for testing. It was not necessary to store the fibrinogen on ice between each experiment. Any remaining defrosted sample was discarded after four hours if not required.

4.3.3 Fluorescent Fibrinogen Preparation

In order to image the microstructure of the fibrin-thrombin network across various LSCM studies, it was necessary to prepare Alexa-488 labelled fibrinogen. Alexa-488 has a maximum absorption wavelength of 495 nm and a maximum emission wavelength of 519 nm (167). The fluorescent fibrinogen contains approximately 15 dye molecules attached to each fibrinogen molecule (275). A 5 mg aliquot of protein was purchased from Thermo Fisher UK. To reconstitute, 3.33 ml 0.1 M sodium bicarbonate (pH 8.3) (275) was added to the bottle of solids and gently swirled to combine. The bottle was wrapped in foil to prevent bleaching of the fluorophore and kept at ambient temperature. At 15-minute intervals, the sample was visually assessed and swirled until complete solubilization had occurred. After approximately two hours, the fluorescent fibrinogen was pipetted into 200 µl aliquots and placed in the -80 °C freezer until required for testing.

Prior to preparation of LSCM slides, the fluorescent fibrinogen was removed from the freezer and immediately wrapped in foil to prevent bleaching of the fluorophores before thawing to ambient temperature.

4.3.4 Soot Samples

A soot solution sample, Soot G[1x], was provided by Dr. E Durand of Cardiff University. A nebuliser was used to capture soot particles produced using a graphite generator in ultrapure water (276). The Soot G[1x] sample was a transparent solution with no visible aggregation of the soot particles present. The geometric mean diameter

of the particles in the gaseous phase was estimated[4] to be 33.0 ± 1.65 nm, with the concentration of the Soot G[1x] solution being 5.60 $x10^9$ particles ml^{-1}. The solution was prepared in ultrapure water. The zeta potential of the particles in solution was also measured[4] to be in the range of -20 mV to 0 mV, suggesting the solutions are unstable suspensions that are prone to aggregation. Further characterisation of the soot solutions can be found in Appendix B.

The Soot G[1x] solution was further concentrated to allow for an increase in the number of particles present in each clot sample without increasing the dilution of the coagulation proteins. These solutions, Soot G[2x] and Soot G[10x], respectively, were produced at Swansea University (as described in Section 4.4.1). The concentration of Soot G[2x] was estimated to be 1.12 $x10^{10}$ particles ml^{-1} and that of Soot G[10x] was estimated as 5.60 $x10^{10}$ particles ml^{-1}.

4.4 Methods

4.4.1 Concentration of the stock soot solution

Once collected from Cardiff University, a proportion of the stock 'Soot G[1x]' solution was concentrated in order to assess the effect of an increased number of particles without increased dilution of the coagulation proteins in both the fibrin gel and blood samples. This was achieved using a Schlenk Line (Figure 4-1) which disturbed the surface of the solution with a jet of N_2, thus increasing the rate of evaporation. A volume of the ultra-pure water dispersant was evaporated, leaving the increased number of particles suspended in the desired volume of solution. A Schlenk Line was used to ensure the pressure of the N_2 blown onto the surface was not so great as to blow the solution out of the sample tube.

[4] By Dr E Durand

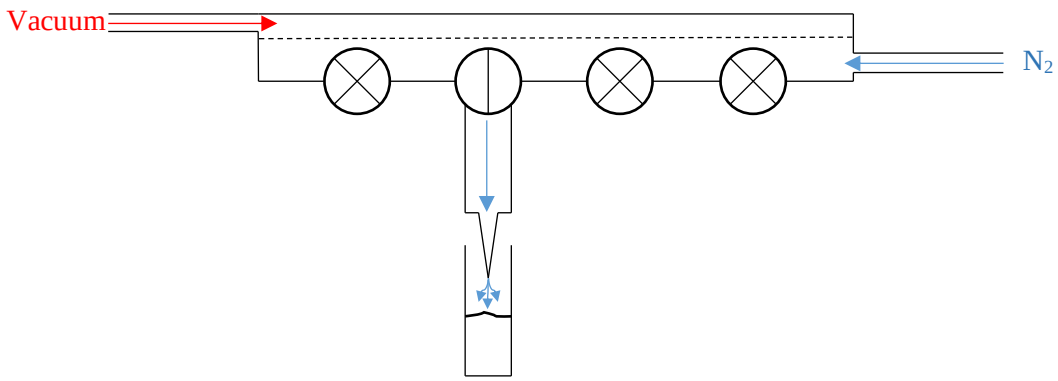

Figure 4-1 *A typical Schlenk Line setup for concentration of soot solution samples. N_2 was used to disturb the surface of the sample, causing evaporation of the dispersant.*

To double the concentration of particles ml^{-1} to give Sample G[2x], 2 ml of stock soot solution was prepared by pipetting it into a glass sample tube. A 1 ml 'blank' control was also prepared in an identical tube as a reference point for the required evaporation. The starting point of the 2 ml solution was indicated by marking the bottom of the meniscus, and by careful comparison with the sealed 'blank' sample, the bottom of the 1 ml meniscus was also marked as a guideline for the completion of the evaporation.

The height of the source of the N_2 from the surface of the soot solution was carefully monitored to ensure that the process was efficient. The sample was left for approximately 90 minutes before the meniscus was level with the 1 ml 'blank' sample, suggesting that half of the solvent had been evaporated. There was no visible change in the solution. It was estimated that the concentration of particles in the solution had been increased from 5.6×10^9 particles ml^{-1} in the stock solution to approximately 1.12×10^{10} particles ml^{-1} in the new 2x concentrated solution.

The stock solution was further concentrated to give Sample G[10x] which contained 10x particles ml^{-1}. The above process was repeated with a starting volume of 10 ml of stock soot solution which was reduced to 1 ml after eight hours. The resulting concentration of soot was estimated to be approximately 5.6×10^{10} particles ml^{-1}.

All samples were stored in glass sample tubes, sealed with a stopper and as an added precaution, Parafilm was used to prevent any further, unwanted, evaporation.

4.4.2 Rheological studies

A 1% TBS-Tween (TBS-T) solution was prepared by combining 0.5 g of Tween-20 surfactant with 49.5 g of 1x TBS. The Tween-20 solution is light sensitive. Therefore, the solution was stored in a foil wrapped glass bottle in the 4 °C refrigerator to prevent degradation.

A strict procedure was followed in order to prepare and load the fibrin-thrombin gel samples onto the rheometer efficiently so as not to compromise the measurement of the gel time parameter. For all experiments, the delay time, t_d, from the addition of thrombin to the sample, thus initiating coagulation, to commencement of the experiment was recorded as < 65 ± 5.0 s.

Firstly, TBS-T was added to a 7 ml bijou tube before a further volume of 1x TBS was added. The two were gently mixed before the required volume of fibrinogen was added. Again, the solution was gently mixed to ensure that the fibrinogen was dispersed within the 1x TBS/TBS-T solution. For all fibrin gel samples, the desired concentration of $CaCl_2$ was 0.005 M, with the required volume being added and combined with the fibrinogen and TBS/TBS-T. It was necessary to include $CaCl_2$ as Ca^{2+} increases the rate and extent of lateral aggregation between fibrinogen fibres (128) and for the initial platelet plug formation in whole blood clots (277). Finally, immediately prior to testing, the necessary volume of thrombin was added before being gently mixed and loaded onto the rheometer.

The samples for the CMT rheological studies were quickly prepared and loaded onto the temperature-controlled Peltier plate system. To perfectly fill the 400 µm shearing gap at 20 °C, the volume of sample required was 124 µl. The 60 mm Al parallel plate upper geometry was manually lowered to the sample to encourage it to 'jump' to the plate due to attractive forces between the sample and the geometry, reducing the risk of bubbles within the sample. Once contact was made between the sample and the geometry, the plate was lowered to the geometry gap to ensure an even load across the geometry set up. A small volume of low viscosity silicon oil (9.8 mPa.s, Brookfield) was placed around the free surface (the circumference of the geometry) to prevent evaporation during testing and the TRIOS procedure was commenced.

All CMT experiments were conducted using an AR-G2 rheometer (TA Instruments) which was set to run a standard GP procedure with a constant temperature of 20 °C

across a frequency decade of 0.4 – 4 Hz. The procedure began with a 10 s preshear at a rate of 100 s^{-1}. The torque input was 4.24 μN.m and each test ran for 1200 s in order to obtain sufficient data both pre- and post-GP. The frequency range selected allowed for an increase number of data points to be collected prior to the GP. To correct for inertial artefacts discussed in Chapter 3, all CMT data was analysed post-acquisition using the ERIC procedure.

4.4.2.1 AR-G2 CMT Thrombin Concentration Study

In order to determine the effect of thrombin concentration on clot structure, a series of gels were prepared with $0.04\ NIH\ ml^{-1} \leq [Th] \leq 0.16\ NIH\ ml^{-1}$ whilst the fibrinogen concentration remained constant at 12 mg ml^{-1}. An AR-G2 rheometer (TA Instruments) was employed with an extended 'test time' of 3600 s to allow for the gel formed to mature, even at the low thrombin concentrations.

4.4.2.2 AR-G2 CMT Fibrinogen Concentration Study

To investigate the effect of fibrinogen concentration on gelation, fibrin gels were prepared over a range of fibrinogen concentrations in the range $4\ mg\ ml^{-1} \leq [Fib] \leq 12\ mg\ ml^{-1}$, with a thrombin concentration of 0.08 NIH ml^{-1}. Samples were prepared both with and without Tween-20, which reduces surface tension artefacts, to assess the effect of the addition of surfactant on the mature microstructure of the fibrin gel formed.

4.4.2.3 ARES-G2 SMT Fibrinogen Concentration Study

An ARES-G2 (TA Instruments) rheometer was used to evaluate the effect of fibrinogen concentration on clotting parameters of fibrin gels without the presence of instrument inertial artefacts. Fibrinogen concentrations of 8 mg ml^{-1}, 10 mg ml^{-1} and 12 mg ml^{-1} were analysed in conjunction with a fixed thrombin concentration of 0.05 NIH ml^{-1}.

The temperature throughout the experiment remained constant at 24 °C. Samples were prepared using the procedure outlined in Section 4.4.2, prior to loading directly onto the temperature-controlled Peltier Plate. The 50mm titanium parallel plate geometry was set to a shearing gap of 400 μm. Exactly 0.785 ml of each sample was rapidly loaded onto the rheometer prior to a small amount of low viscosity silicon oil being placed around the free surface of the geometry once the shearing gap was reached to prevent evaporation of sample material during testing.

Each sample was pre-sheared for 10 s at a shear rate of 100 s^{-1} prior to commencement of the multi frequency time sweep. A maximum strain of 20% was applied to the sample with a corresponding maximum torque of 2.0 μN.m. Four frequencies (3.2 Hz, 1.6 Hz, 0.8 Hz and 0.4 Hz) were employed to determine the frequency independent GP. The third harmonic of the torque waveform was monitored to ensure the linearity of the data. It was not necessary to use the ERIC correction procedure on data acquired using an SMT rheometer as there is no influence from instrument inertia.

4.4.2.4 AR-G2 CMT Soot Concentration Study

Fixed fibrinogen and thrombin concentrations, of 6 mg ml^{-1} and 0.08 NIH ml^{-1} respectively, were selected based upon the data obtained in previous studies to give valid data with an acceptable experimental t_{gel} in order to reduce sample mutation. 'Soot G' solution of varying volumes was included in the preparation of the fibrin-thrombin gels to determine whether there were any clotting anomalies in the data reported compared to fibrin-thrombin gels without the inclusion of soot. The preparation and testing methods outlined in Section 4.4.2 were used. The required volume of soot was added to the reagents prior to the addition of the proteins. In line with literature, the desired volume of the soot sample was sonicated for 15 minutes at room temperature to reduce the aggregation of the particles present (168). The sonicated sample was then combined with 10x TBS to form a 1x TBS soot solution (TBS-S). Prepared soot samples were used immediately.

Initially, the concentration of stock G[1x] solution was tested between 0% and 5% inclusion. Increased volumes of the Soot G[1x] were combined into the fibrin gels, with the TBS balance being altered appropriately to maintain the correct reagent concentrations. Each result obtained was analysed using the ERIC procedure.

As outlined in Section 4.4.2, it was possible to increase the concentration of the soot solution to G[2x] and G[10x]. Volumes of the higher concentration soot solutions were added into the gels to give a 1% overall inclusion at fibrinogen and thrombin concentrations of 6 mg ml^{-1} and 0.08 NIH ml^{-1} respectively.

4.4.3 LSCM Studies Sample Preparation

LSCM studies were carried out to provide supporting image data for the microstructure of the mature F-T gels over the range of fibrinogen, thrombin and soot concentrations. The gels were prepared using 1.5% fluorescent fibrinogen (1.5 mg ml^{-}

[1] stock solution (275), produced as detailed by the manufacturer) labelled with Alexa-488 fluorophore to allow images to be obtained using a Zeiss LSM 710 confocal microscope.

Glass slides were assembled prior to the preparation of the gels to ensure rapid preparation of each sample. Two layers of double-sided tape were used to create a void between the glass slide and the coverslip (278), as shown in Figure 4-2. The edge of the coverslip was firmly pressed onto the tape to prevent any sample evaporation whilst the sample was gelling and being imaged. Care was taken to avoid debris and dust on the area enclosed by the coverslip, along with the coverslip itself, to ensure that good quality images were obtained using the confocal microscope. Gel samples were prepared individually with only a small total volume of sample required as approximately 80µl of solution filled the void in the slide. The samples were left to gel for 40x t_{gel} (75) to produce sufficiently mature gels so that the microstructure could be analysed.

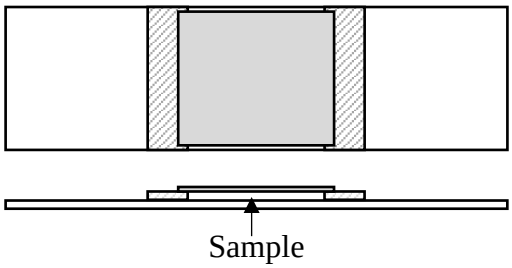

Figure 4-2 *Schematic diagram of an assembled LSCM slide. The hatched area shows the position of the tape used to create the void. Approximately 80 µl of the sample to be imaged was pipetted into the void (grey).*

A Zeiss LSM 710 confocal microscope was used to obtain image data using Zen Black Software. A 40x oil immersion objective was used to capture images of the mature gel network of all the prepared gel samples. A small amount of oil (Zeiss, Immersol 518 F) was placed onto the objective before loading the sample slide. Images were obtained 20 µm from the cover slip (279,280). For each sample, an image was captured of the network before a 4.2x zoom was applied to take a more detailed image of the gel microstructure. Three sites on each slide were imaged to ensure that the images captured were representative of the whole gel network. A 3D z-stack was also captured for each sample to give an understanding of the 3D structure of the gel network. A total of 44 slices were imaged to give a 49.97 x 49.97 x 25.60 µm network

structure. The initial image was captured 20 µm from the coverslip to avoid fibrinogen adsorbed onto the glass surface (280) with a further 25.60 µm being imaged beyond it.

All fibrin gel slides were immediately disposed of using the appropriate waste removal routes after imaging.

4.4.3.1 Thrombin concentration study

To study the effects of thrombin on the fibrin gel microstructure, gel samples were prepared to image using the sample procedure as outlined in Section 4.4.2.1. Samples were prepared at 12 mg ml^{-1} (fixed) fibrinogen concentration with thrombin concentrations of 0.02 NIH ml^{-1}, 0.04 NIH ml^{-1}, 0.08 NIH ml^{-1}, 0.16 NIH ml^{-1} and 0.32 NIH ml^{-1}. The thrombin concentration range was expanded from that of the rheological study (Section 4.4.2.1) as only the mature gel microstructure was of importance for the LSCM studies. Samples were once again prepared with both the inclusion and exclusion of Tween-20 to further determine the potential effect on the mature gel microstructure. For each thrombin concentration, sample slides were prepared in triplicate with three images taken at different locations on the slide to ensure that the acquired images were representative of the global network structure.

4.4.3.2 Fibrinogen concentration study

Gels were prepared, as with the rheological study in Section 4.4.2.2, both including and excluding Tween-20 surfactant, to allow for observations on the potential effect of fibrinogen concentration on the microstructure of the mature gel. In the case of no addition of Tween-20 (TBS-T), 1x TBS was used to complete the volume. The components of the gels were added as discussed in Section 4.4.2. Once the thrombin was added, the sample was immediately pipetted into the void between the glass slide and the cover slip. Care was taken to avoid sample spilling onto the coverslip outside of the desired area. After approx. 30 mins, a layer of clear varnish was painted around the edges of the coverslip to completely enclose the sample in the void. This prevented sampled evaporation throughout the gel network formation and contamination of the microscope objective during imaging.

The fibrin gel samples were left to gel for >40x t_{gel} determined from the rheological experiments to ensure the microstructure had reached maturity across the sample (75). A tent of foil was placed over the samples to prevent the fluorophores bleaching in the

light. The samples were transported to the confocal microscope in darkness to continue to prevent bleaching of the fluorescent fibrinogen. Images were obtained in a darkened room to ensure the best quality images were captured. Triplicate slides of each sample were prepared to ensure reproducibility.

4.4.3.3 Soot concentration study

The final LSCM study conducted involved the inclusion of soot solutions into the fibrin gels. G[1x], G[2x], G[10x] were used in the preparation of gel samples and imaged using the procedures described in Sections 4.4.2 and 4.4.2.4. As with the rheological study, the soot solutions were sonicated for 15 minutes prior to the addition of 10x TBS to form a 1x TBS-S solution. The sample preparation was repeated in triplicate. Fixed concentrations of fibrinogen and thrombin of 6 mg ml^{-1} and 0.08 NIH ml^{-1} respectively with 1% soot inclusion were used throughout the study.

4.4.4 Scanning Electron Microscopy Studies Sample Preparation

SEM images were obtained using a Hitachi S4800 Scanning Electron Microscope. The images were used to further analyse the effect of the fibrinogen concentration, thrombin concentration and soot inclusion on the mature clot microstructure. Whilst SEM images do not require the addition of fluorescently labelled fibrinogen, the preparation procedure is invasive, therefore care must be taken to avoid disrupting the mature clot microstructure.

4.4.4.1 Fibrin gel clot preparation (for Scanning Electron Microscopy)

A total of 200 µl of fibrin gel sample was prepared for each clot over a range of fibrinogen, thrombin and soot concentrations. As with fibrin gel samples prepared for LSCM analysis, gels were allowed to gel for 40x t_{gel}.

Initially, fibrin gels were prepared at set concentrations of 10 mg ml^{-1} fibrinogen and 0.08 NIH ml^{-1} thrombin, both with and without the addition of Tween-20, to visually assess the effect of the addition of the surfactant on the mature microstructure of the gel network. Gels were prepared using an identical procedure (outlined in Section 4.4.2) with one including 0.1% Tween-20 and the other containing no Tween-20.

The thrombin concentration SEM study involved all gel samples being prepared with fibrinogen concentrations of 6 mg ml^{-1} and 10 mg ml^{-1}, whilst the extremes of the thrombin concentration range were added to give concentrations of 0.02 NIH ml^{-1} and

0.32 NIH ml^{-1} respectively. Samples were prepared in line with the method discussed for the rheological study presented in Section 4.4.2.1.

In a third SEM study, to analyse the effect of fibrinogen concentration on the network formed in the gel, fibrinogen concentration was varied over the range $4\ mg\ ml^{-1} \leq [Fib] \leq 12\ mg\ ml^{-1}$ with a constant thrombin concentration of 0.08 NIH ml^{-1}. Each concentration sample contained 0.1% Tween-20. Preparation was consistent with the gels prepared for the rheological study reported in Section 4.4.2.2.

The final study conducted using the SEM aimed to image the fibrin networks with the inclusion of the 'Soot G' solutions. All fibrin-thrombin gel samples for the final SEM study, involving soot concentrations of 1% of the total volume of G[1x], G[2x] and G[10x], were prepared using a fibrinogen concentration of 6 mg ml^{-1} and a thrombin concentration of 0.08 NIH ml^{-1}. Prior to the addition of the soot to the fibrin gels, each soot sample was sonicated for 15 minutes to prevent the aggregation of the soot particles present (168). A 1x TBS-S solution was formed by diluting the 10x TBS solution with the sonicated soot solution. As with all SEM sample preparation, an identical procedure was employed to that used in the rheological studies (Section 4.4.2.4).

4.4.4.2 Washing and dehydration of clot samples

4.4.4.2.1 Preparation of cacodylate buffer

A total volume of 1000 ml of 0.05 M cacodylate buffer was prepared using sodium cacodylate trihydrate ($C_2H_6AsNaO_2.3H_2O$) dissolved deionised water. The buffer solution was then refrigerated at 4 °C until required for SEM sample preparation.

4.4.4.2.2 Preparation of glutaraldehyde solution

An integral part of the SEM sample preparation requires washing the samples in glutaraldehyde to fix the gel networks that had formed, preventing any further development or decay of the gel structure. The glutaraldehyde solution was prepared by diluting 25 % glutaraldehyde solution (Sigma Aldrich UK) to 2 % using the prepared cacodylate buffer (Section 4.4.4.2.1).

4.4.4.3 Preparation of the fibrin clots

Once the fibrin-thrombin clots had reached maturity, each sample was washed using 0.05 M sodium cacodylate buffer to remove excess salt (281). The cacodylate buffer

was removed and replaced at 10-minute intervals with care taken to avoid contamination between samples. The process was repeated three times before the cacodylate buffer was removed and replaced with 2 % glutaraldehyde solution. The samples were left in the 2 % glutaraldehyde solution overnight (approximately 16 hours) in a fume hood to prevent any further gelation in the clots.

After the samples had been fixed in glutaraldehyde overnight, the clots were washed with graduated concentrations of ethanol between 30% to 100%. The final stages of preparation involved transitioning from 100% ethanol to hexamethyldisilazane (HDMS) using a 50:50 ethanol and HDMS mixture. After washing with the combined ethanol and HDMS, pure HDMS was used to rinse the clots three before the remaining HDMS left to evaporate in a fume hood overnight to dry the clot samples fully.

The dry samples were mounted onto stubs suitable for the SEM assembly using carbon tape. The samples were individually removed from the wells and gently pressed onto the tape to minimise damage to the clot structure (Figure 4-3). The fibrin-thrombin clots were easily adhered to the tape.

Figure 4-3 *An example fibrin gel clot mounted onto carbon tape. The sample in this image was not yet sputter coated with a 15nm gold-palladium layer.*

Once all the samples were mounted, the surface of the samples was sputter coated with a 15 nm layer of gold-palladium, using a Polaron Instruments Inc. E5100 at 2.2 kV and 20 mA for 90 s, to improve the quality of the images obtained using the SEM (Figure 4-4). The sputter coated fibrin-thrombin gel samples were stored and imaged as soon as possible.

Figure 4-4 *The final SEM samples after sputter coating with a 15 nm layer of gold-palladium. Examples of both* ***(a)*** *blood clots and* ***(b)*** *fibrin gel clots can be seen.*

4.5 Results and Discussion

4.5.1 Analysis of the addition of Tween-20 to fibrin gels

The effect of the inclusion of Tween-20 on the gel microstructure was analysed, both rheometrically and using imaging techniques, prior to the commencement of the main fibrin gel studies. For low viscosity weak gelling systems, surface tension artefacts can appear as a G' plateau in oscillatory measurements (31), resulting in an anomalous GP being reported since $tan\delta = {G''}/{G'}$. To avoid poor quality data, the surface tension of the sample was reduced by inclusion of a surfactant, Tween-20.

The addition of 0.1 % Tween-20 to the fibrin gels had a substantial impact on the quality of the rheological gel point data. The addition of the surfactant reduces the surface tension within the system which allows for a more defined GP to be recorded. Without the addition of 0.1 % Tween-20 to the gel, it was not possible to obtain a defined GP (Figure 4-5a). The frequency pairs do not intersect to give a definite GP as the material transitioned from viscoelastic liquid to viscoelastic solid. Initially, the four frequencies order as a viscoelastic solid. This was the case for multiple experiments over a range of thrombin ($0.05\ NIH\ ml^{-1} \leq [thrombin] \leq 0.1\ NIH\ ml^{-1}$) and fibrinogen ($4\ mg\ ml^{-1} \leq [fibrinogen] \leq 12\ mg\ ml^{-1}$) concentrations. However, when Tween-20 was incorporated into the gel, the GPs reported were not only more defined but also had a suitable experimental t_{gel}, as seen in Figure 4-5b. The inclusion of Tween-20 can shorten the apparent t_{gel} as the surfactant reduces the possibility of an artificial G' plateau as a result of dominant

surface tension effects, allowing $tan\delta$ and the corresponding t_{gel} to be accurately determined at the GP.

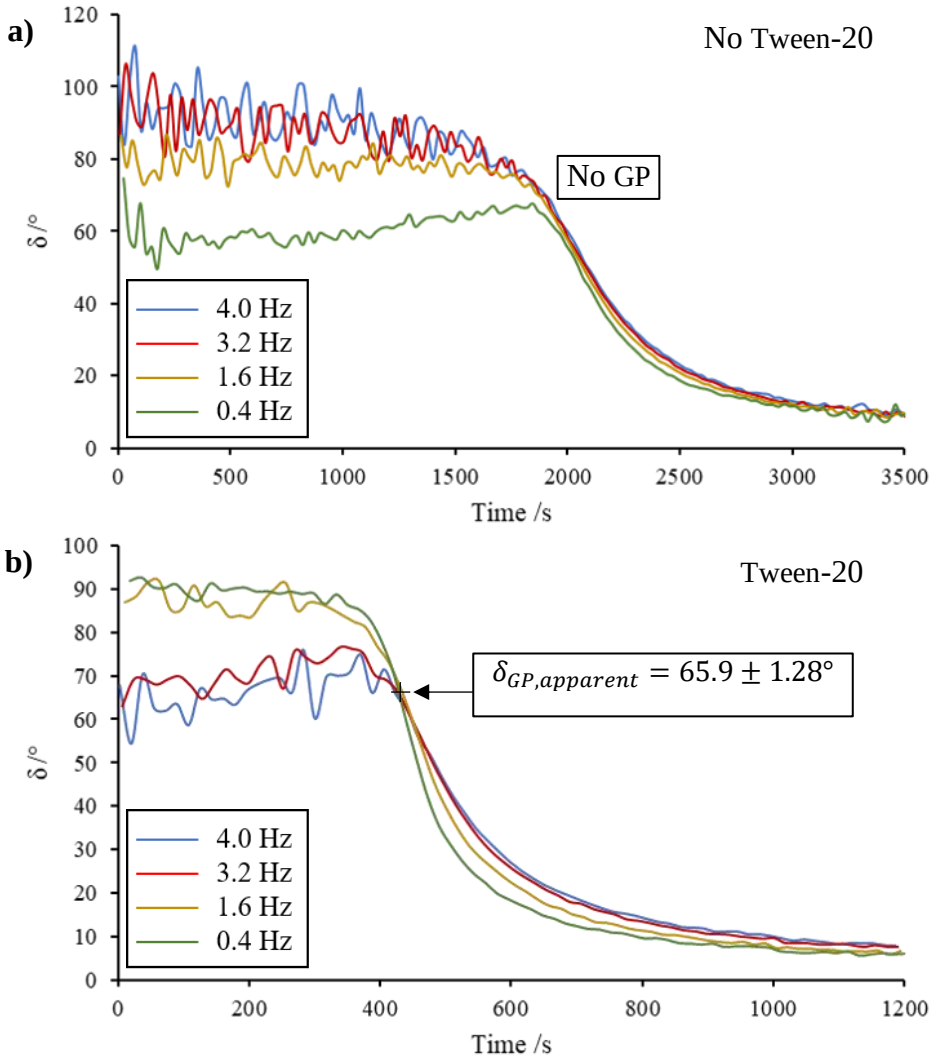

Figure 4-5 *Example fibrin-thrombin GP profiles with a fibrinogen concentration of 10 mg ml^{-1} and a thrombin concentration of 0.08NIH ml^{-1} for* ***a)*** *without addition of Tween-20 and* ***b)*** *with the inclusion of 0.1% Tween-20.*

Whilst GPs were not reported for every experiment, even with the inclusion of Tween-20, due to the weak structural nature of the fibrin gels, it was possible to obtain valid data over a range of thrombin and fibrinogen concentrations. As the concentration of both thrombin and fibrinogen increased, the reported GP became easier to obtain and better defined.

To further understand the effect of the addition of Tween-20 to fibrin-gels, images were captured using LSCM and SEM to assess the mature gel microstructure. The LSCM images show that the addition of Tween-20 has a negligible impact on the mature network. For samples with no addition of Tween-20 (Figure 4-6a) and gels including Tween-20 (Figure 4-6b) no variance in the microstructure was visually observed. The same can be said for the SEM images captured of fibrin gels without the inclusion of Tween-20 (Figure 4-6c) and with the inclusion of Tween-20 (Figure 4-6d). The images obtained using LSCM are more reliable than those of SEM as the clot network remains in its native, hydrated state.

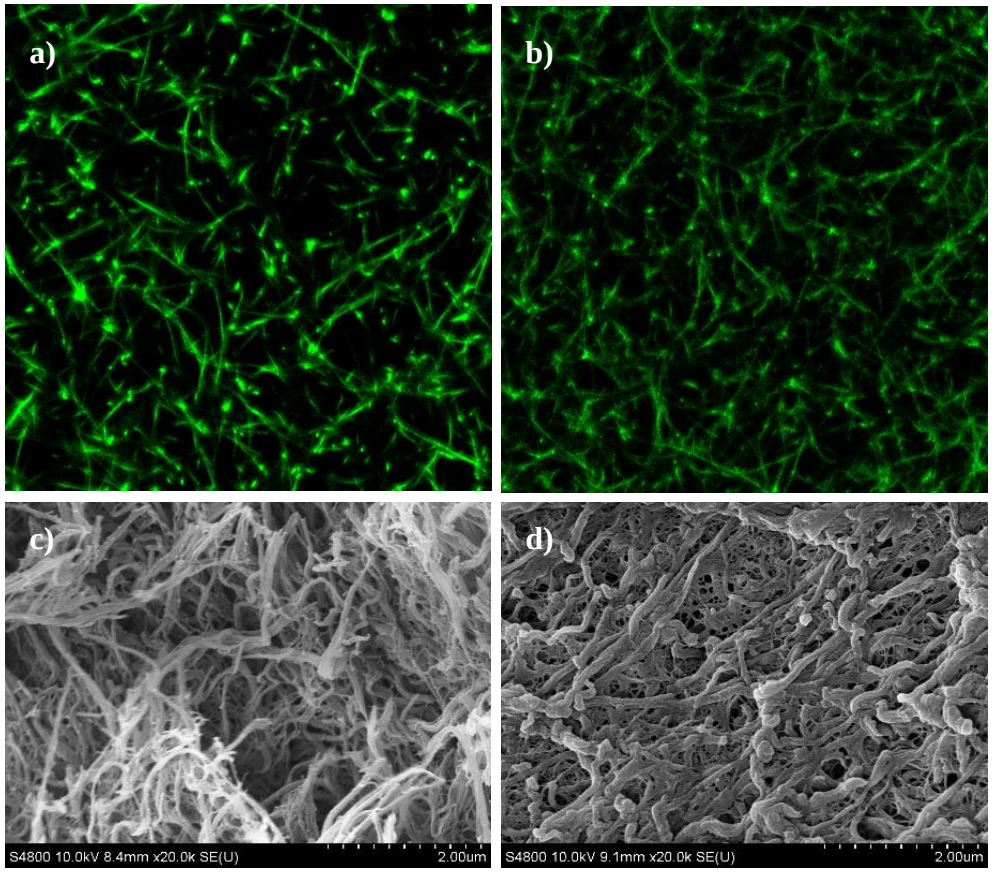

Figure 4-6 *Images captured using LSCM and SEM were used to analyse the effect of the inclusion of Tween-20 on the microstructure of the fibrin gels. Images* ***a)*** *and* ***c)*** *show the microstructure of the mature fibrin gel without the inclusion of Tween-20 (using LSCM and SEM techniques respectively). Images* ***b)*** *and* ***d)*** *show the microstructure of a fibrin gel* ***with*** *the inclusion of 0.1% Tween-20 (using LSCM and SEM techniques respectively).*

The inclusion of Tween-20 surfactant into fibrin gels aids the reduction of surface tension effects by ensuring that there are minimal deviation and migration in the contact line of the sample (31). By lowering the surface tension, the surface tension torque is reduced, ensuring that the reported torque does not detrimentally impact the

data obtained, even in low viscosity weak gelling systems (31). With a reduction in surface tension achieved by the inclusion of Tween-20 into the fibrin gels, the rheological data obtained is greatly improved with minimal effects on the mature gel microstructure. As a result, all further rheological studies were conducted with the inclusion of Tween-20 to ensure valid GP data was accessible.

4.5.2 Thrombin Concentration Study

A thrombin concentration study was conducted using an AR-G2 rheometer to determine the ideal thrombin concentration to employ in future studies as well as assess the microstructure of the gel networks formed. The fibrinogen concentration remained constant throughout the study at 12 mg ml^{-1}, with the inclusion of Tween-20 in the gel sample.

As stated in Section 4.4.2.1, rheological data was obtained over a thrombin range of $0.04\ NIH\ ml^{-1} \leq [Th] \leq 0.16\ NIH\ ml^{-1}$. An example GP for the highest (0.16 NIH ml^{-1}) and lowest (0.04 NIH ml^{-1}) thrombin concentrations studied can be seen in Figure 4-7. Both GP show signs of inertial artefacts as the initial phase angles reported were > 90°, necessitating the application of ERIC post-data acquisition.

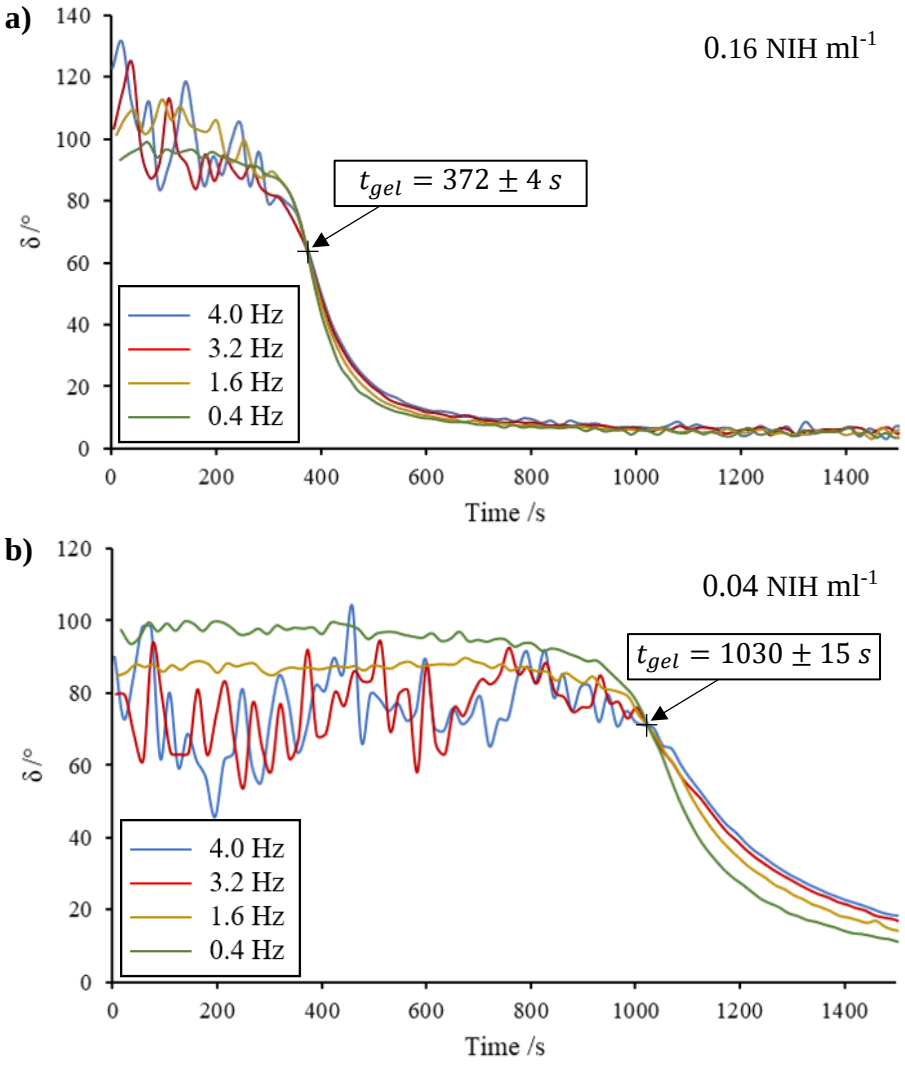

Figure 4-7 *Example GP profiles to illustrate the effect of thrombin concentration on the gel time, t_{gel}, reported. A thrombin concentration of 0.16 NIH ml-1 is shown in* ***a)*** *with a reported t_{gel} of 372 ± 4 s, whereas in* ***b)*** *the thrombin concentration was considerably lower at 0.04 NIH ml^{-1}, resulting in a t_{gel} of 1030 ± 15 s. The fibrinogen concentration for both experiments was 12 mg ml^{-1}with a frequency decade of 0.4-4 Hz.*

As the thrombin concentration present in the fibrin gel increases, the t_{gel} decreases significantly due to faster formation of the fibrin network. The pre- and post-ERIC data obtained throughout the study show strong agreement (Figure 4-8). It was not possible to obtain rheological data at a thrombin concentration higher than 0.16 NIH ml^{-1}, such as 0.32 NIH ml^{-1}, due to the speed at which the gel network forms. The rate of gelation was too fast for valid rheometric data to be obtained pre-GP, with large N_{mu} being recorded. At thrombin concentrations of less than 0.04 NIH ml^{-1} valid GP data could not be obtained due to resolution issues. The GP measurement in fibrin gels

and blood pushes the rheometer's capabilities due to the very weak incipient gel microstructure.

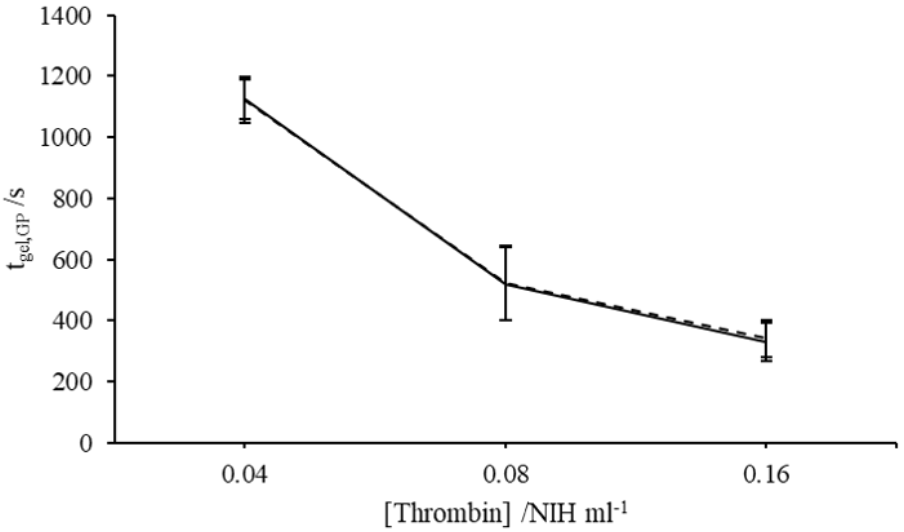

Figure 4-8 *Rheological t_{gel} data obtained for the fibrin gels thrombin concentration study. The fibrinogen concentration of all gels remained constant at 12 mg ml^{-1} whilst the thrombin concentration was varied between 0.04 mg ml^{-1} ≤ [Th] ≤ 0.16 NIH ml^{-1}. The uncorrected pre-ERIC data is shown by the solid line, whereas the dashed line represents the data post ERIC correction.*

As the thrombin concentration was increased, the phase angles reported slightly decreased (Figure 4-9). The decreased phase angles reported lead to higher d_f values (Figure 4-10). The gel networks associated with the d_f values reported at the highest thrombin concentrations of 0.16 NIH ml^{-1} suggests a more dense microstructure, whilst the decreased d_f values reported for the lowest concentration of 0.04 NIH ml^{-1} imply a more open microstructure (128,282,283).

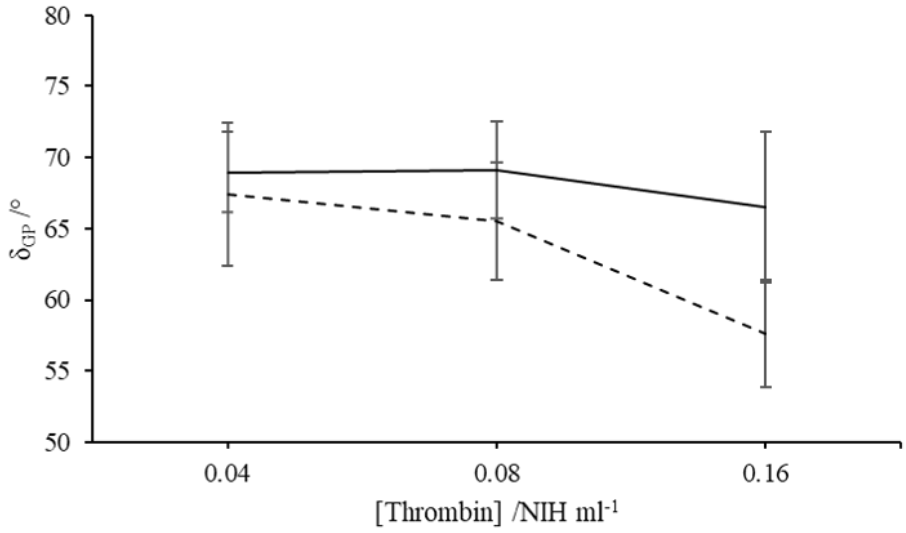

Figure 4-9 *The rheological data obtained for δ_{GP} over a range of thrombin concentrations. The solid line represents the uncorrected δ_{GP} data obtained with the dashed line showing the data post-ERIC correction. The fibrinogen concentration remained constant at 12 mg ml^{-1} throughout the study.*

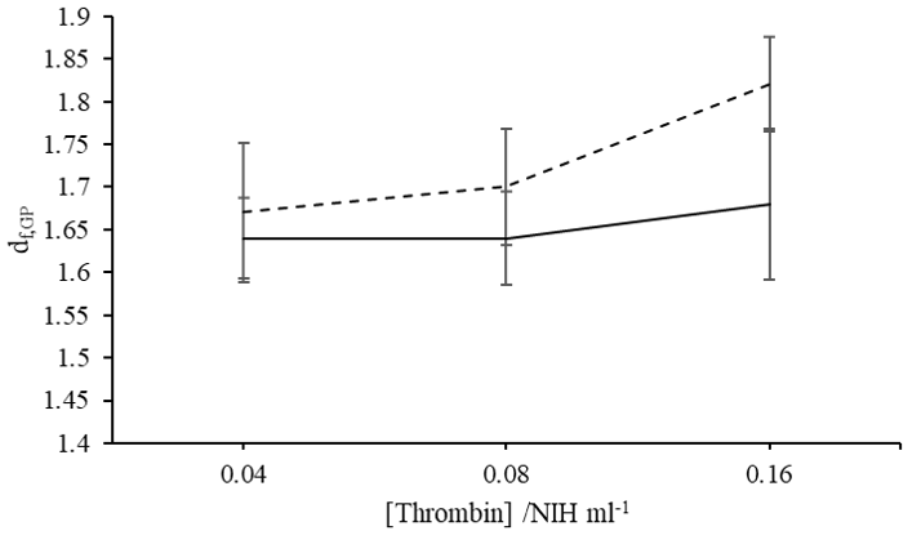

Figure 4-10 *The d_f reported at the GP for each of the thrombin concentrations studied, with a constant fibrinogen concentration of 12 mg ml^{-1}. The uncorrected data is represented by the solid line with the ERIC corrected data shown by the dashed line.*

No statistically significant deviation in the uncorrected d_f values was reported for limiting thrombin concentrations of 0.04 NIH ml^{-1} and 0.16 NIH ml^{-1} when using a T-Test ($p = 0.4206$). However, the post-ERIC data shows a statistically significant increase ($p = 0.0081$) in the corrected d_f values reported between the highest and lowest thrombin concentrations.

Bateman et al. (279) noted an increase in d_f reported with increased thrombin concentrations between 0.01 NIH ml^{-1} and 0.1 NIH ml^{-1}. As the thrombin concentration within the fibrin gel samples increased, the value of d_f increased rapidly to a plateau at 0.1 NH ml^{-1}, suggesting that the clot structure stabilised at the highest thrombin concentration tested in the study (279). The values reported by Bateman et al. for 0.1 NIH ml^{-1} are in agreement with the data obtained at a similar thrombin concentration of 0.08 NIH ml^{-1} in the present study, with d_f recorded as approximately 1.6 to 1.7. On the other hand, Takahashi et al. (280) observed a decrease in the d_f values with increased thrombin concentration reported using dynamic light scattering and LSCM at thrombin concentrations of 0.00125 NIH ml^{-1} and 0.02 NIH ml^{-1}. The reported d_f values of 1.46 ± 0.01 at a thrombin concentration of 0.02 NIH ml^{-1} and 1.54 ± 0.02 at 0.00125 NIH ml^{-1} are substantially lower than the values reported in the present work. The discrepancy in the discussed studies could be as a result of the use of human clotting factor samples (Bateman et al. and the studies presented in this thesis) in comparison with bovine factors (Takahasi et al.).

Further LSCM and SEM studies were conducted to gather images of the mature gel microstructures, as described in Section 4.4.3 and Section 4.4.4, respectively. Comparing the rheological and imaging data indicates agreement between the rheologically reported d_f values and the network structure observed. As expected from the rheologically determined d_f values, the SEM images (Figure 4-11) show a more closely packed structure for the higher thrombin concentration though the fibres present are thinner. Studies by Wolberg (111), Weisel (126) and Bateman (279) observe higher thrombin concentrations resulting in thinner fibres that are closely packed together using SEM and LSCM techniques respectively. Similar fibre thickness was observed at several magnifications across each of thrombin concentrations with fixed fibrinogen concentrations of 6 mg ml^{-1}.

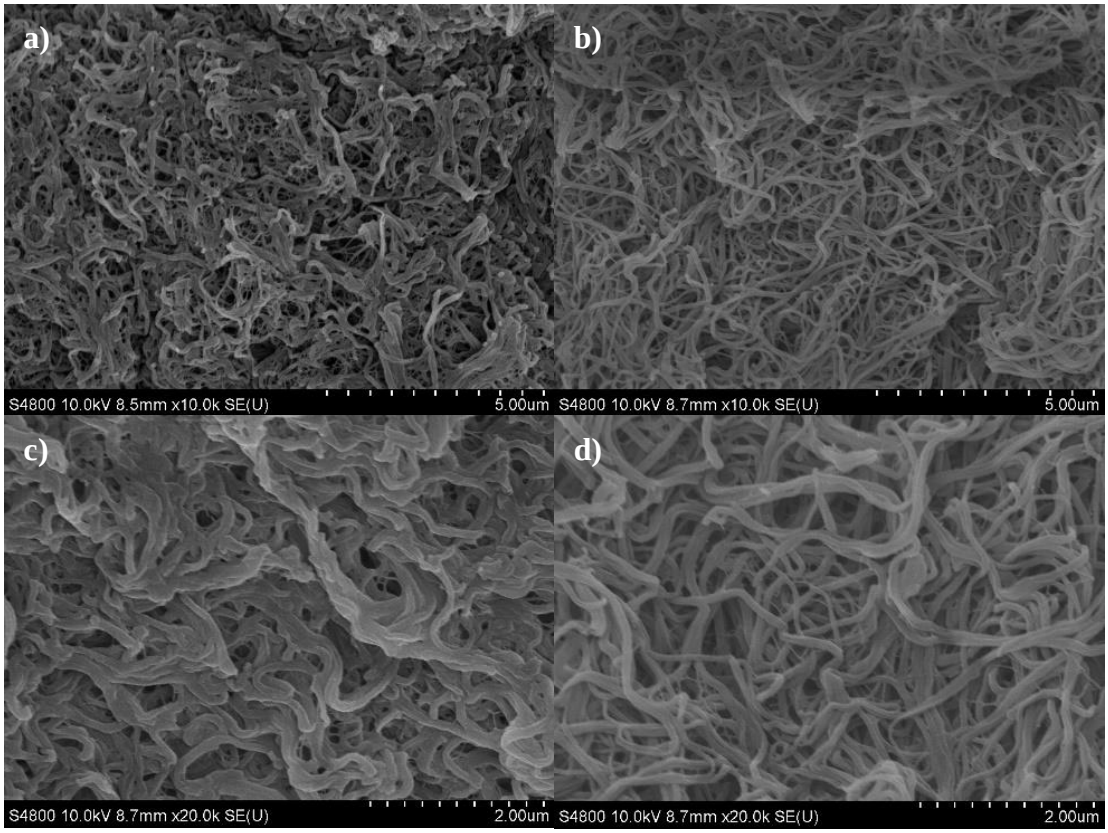

Figure 4-11 *SEM images captured of fibrin gels with a fibrinogen concentration of 6 mg ml^{-1}. The thrombin concentration in* ***a)*** *and* ***c)*** *is 0.02 NIH ml^{-1}, whereas in* ***b)*** *and* ***d)*** *the thrombin concentration is much higher at 0.32 NIH ml^{-1}. The magnification was increased from x10.0k in* ***a)*** *and* ***b)*** *to x20.0k in* ***c)*** *and* ***d)*** *to illustrate the effect of thrombin concentration on the mature microstructure. At the higher thrombin concentration in* ***b)*** *and* ***d)****, the fibres appear to be thinner and less ordered compared to the lower thrombin concentration observed in* ***a)*** *and* ***c)****.The scale bars represent 5μm for x10.0k magnification and 2 μm at x20.0k magnification.*

The images obtained using LSCM are also in agreement with the rheological data suggesting an increased d_f value as the thrombin concentration increases. As seen in Figure 4-12, as the thrombin concentration increases from **a)** 0.02 NIH ml^{-1}, **b)** 0.08 NIH ml^{-1} to **c)** 0.32 NIH ml^{-1}, the quantity of the fluorescent fibres present increases.

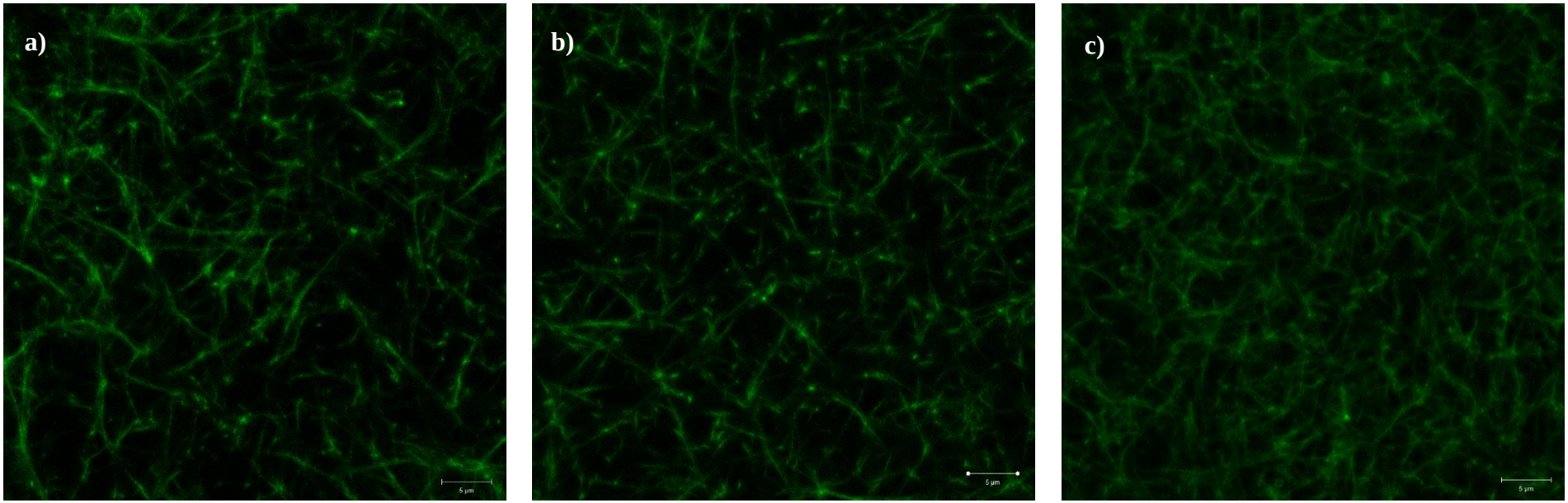

Figure 4-12 *LSCM images gathered for gels with a fibrinogen concentration of 6 mg ml^{-1} and thrombin concentration of a) 0.02 NIH ml^{-1}, b) 0.08 NIH ml^{-1} and c) 0.32 NIH ml^{-1}. Gel samples included 1.5% Alexa-488 fluorescent fibrinogen and 1% Tween-20. The scale bar on each image represents 5 μm.*

As a result of the thrombin concentration study, further studies were conducted with a fixed thrombin concentration of 0.08 NIH ml^{-1} to ensure that the gel time was sufficiently long to allow valid GP data to be obtained within a reasonable experimental time frame.

4.5.3 Fibrinogen Concentration Studies

4.5.3.1 AR-G2 Combined Motor Transducer Rheometer Study

In order to ascertain the necessary fibrinogen concentration for future studies, both GP and image data were obtained over a fibrinogen range of $4\ mg\ ml^{-1} \leq [Fib] \leq 12\ mg\ ml^{-1}$ at a constant thrombin concentration of 0.08 NIH ml^{-1}. The procedures used to prepare and test the fibrin gel samples are detailed in Sections 4.4.2.2. The raw TRIOS GP data files for each experiment were processed using GP Analysis Software[3]. The ERIC procedure (detailed in Chapter 3) was used for post-acquisition correction of inertial artefacts present within the raw data.

Examples of the uncorrected GP data for each of the fibrinogen concentrations can be seen in Figure 4-13. The discrete frequency sweep used frequencies of 0.4 Hz, 1.6 Hz, 3.2 Hz and 4.0 Hz. Due to the weak gel nature of the incipient fibrin gels, there is a lot of noise in the pre-GP data which is shown by the erratic behaviour of the higher frequencies, especially at lower fibrinogen concentrations. Inertial artefacts are clearly present as initial phase angles are in excess of 90°.

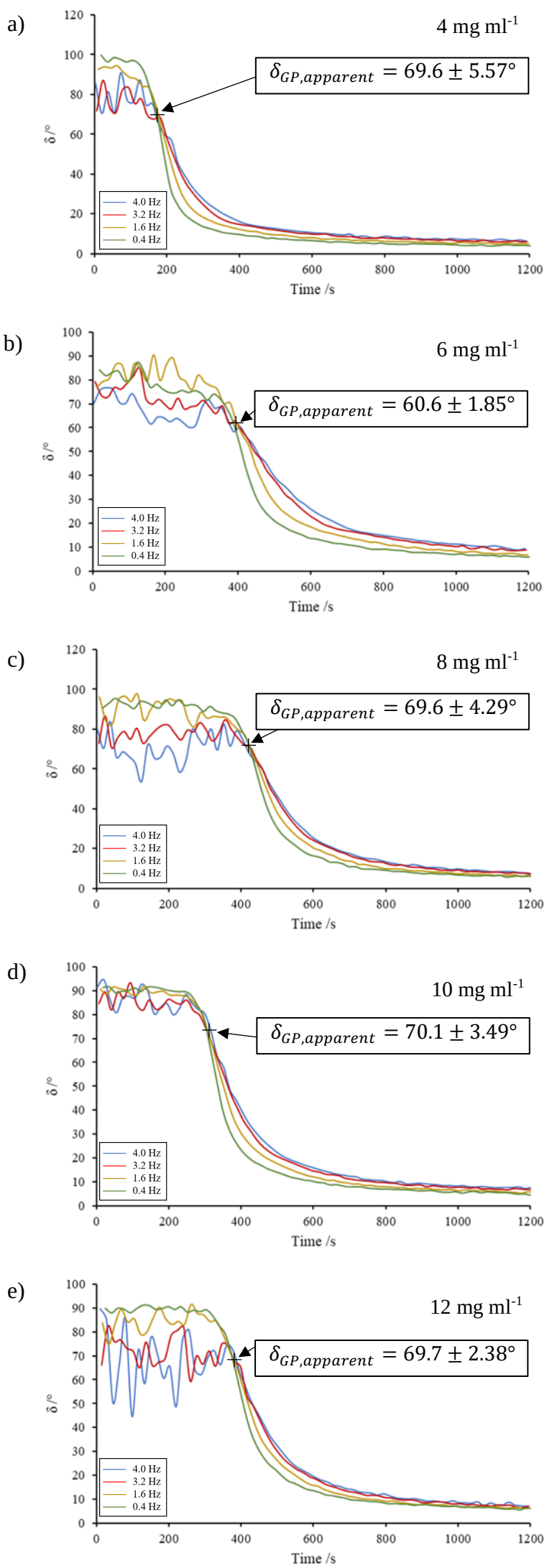

Figure 4-13 *Example GP data for each of the fibrinogen concentrations studied. The thrombin concentration remained unchanged at 0.08 NIH throughout the study. The fibrinogen concentrations shown are a) 4 mg ml^{-1}, b) 6 mg ml^{-1}, c) 8 mg ml^{-1}, d) 10 mg ml^{-1}, e) 12 mg ml^{-1}.*

From the data obtained through the rheological study, it is clear that the t_{gel} of the fibrin gels is closely related to the concentration of the fibrinogen in the sample as seen in Figure 4-14. As the concentration of the fibrinogen present in the gel increases, the t_{gel} increases, suggesting that a diffusion limitation rather than a reaction limitation dominates the kinetics of the gelation process, as previously explored for gelling systems (284). The dependence of t_{gel} on concentration is counterintuitive yet consistent with the relatively constant d_f values observed (within experiment error) over the concentration range.

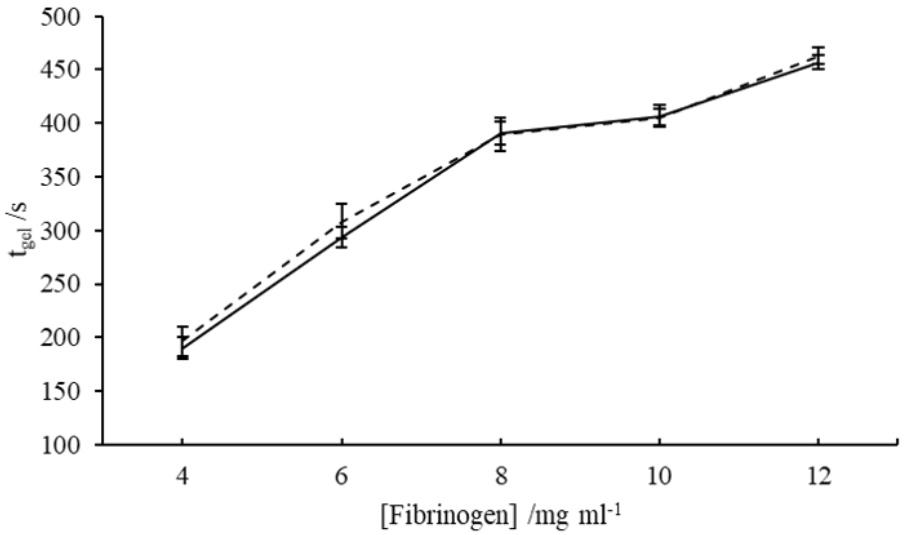

Figure 4-14 *Uncorrected t_{gel} data obtained (solid line) for fibrin thrombin gels over a range of fibrinogen concentrations, $4\ mg\ ml^{-1} \leq [Fibrinogen] \leq 12\ mg\ ml^{-1}$. The data was corrected (dashed line) using the ERIC procedure described in Chapter 3. The thrombin concentration remained constant at 0.08 NIH ml^{-1}.*

As discussed in Chapter 3, the ERIC procedure can be employed to correct the data for instrument inertial artefacts, even at raw phase angles higher than the limit stated by the manufacturer of 150° (9). The raw phase angle at the GP over the frequency range all exceed the manufacturers limit and were found to be $\delta_{raw} > 175°$. As noted in Chapter 3, Figure 3-8, at very high raw phase angles, it is challenging for the ERIC procedure to correct the acquired CMT data back within the SMT range. However, the ERIC corrected data shows strong agreement with the uncorrected t_{gel} data.

Data for the fractal dimension of the fibrin gel at the gel point was calculated using the Muthukumar relationship (152) between phase angle and fractal dimension.

$$\alpha = \frac{d(d+2-2d_f)}{2(d+2-d_f)} \qquad \text{Equation 4.1}$$

Where d_f refers to the fractal dimension, d the space dimension and α, the stress relaxation exponent, $\alpha = \frac{\delta}{90}$ (where δ is the phase angle at the GP). Equation 4.1 can be simplified by selecting $d = 3$ (152) to give

$$d_f = \frac{10\alpha - 15}{2\alpha - 6} \qquad \text{Equation 4.2}$$

The d_f values reported appear to show that the fractal dimension is independent of the fibrinogen concentration in the incipient gel system (Figure 4-15). The application of the ERIC procedure to the data presented little deviation between the raw data reported (solid line) and the data corrected using the ERIC procedure (dashed line). The validity of the data was examined using both analysis of the third harmonic ratio (to assess linearity of the measurement) for each experiment and calculation of the mutation number, N_{mu}.

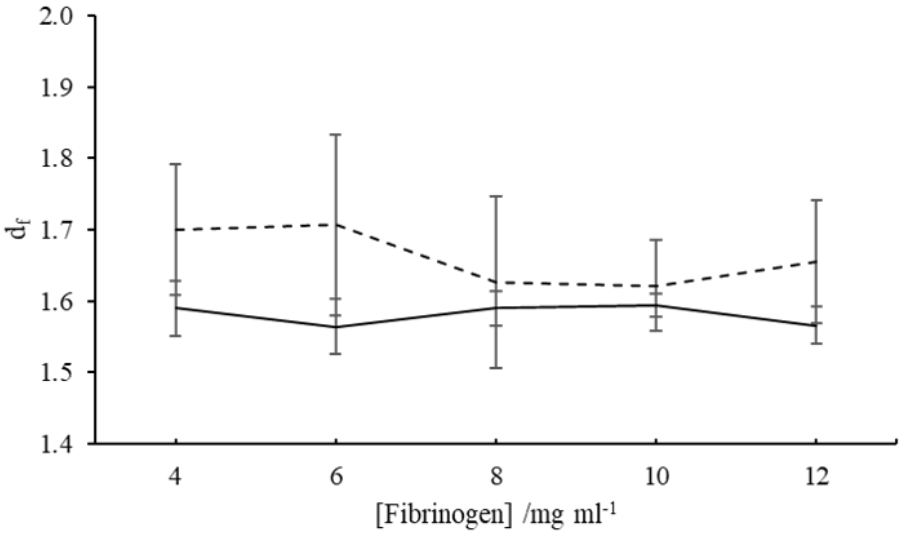

Figure 4-15 *The calculated d_f values for each fibrinogen concentration in the range $4\ mg\ ml^{-1} \leq [Fibrinogen] \leq 12\ mg\ ml^{-1}$, with a fixed thrombin concentration of 0.08 NIH ml-1. The pre-ERIC uncorrected data is shown by the solid line and the post-ERIC corrected data is shown by the dashed line.*

At the GP, there appears to be no relationship between the concentration of fibrinogen present and the fractal dimension recorded. It is possible that this is a result of an excess of fibrinogen present that has not formed part of the branched network in the time, t_{gel}.

In order to further assess the effects of fibrinogen concentration on the gel microstructure, confocal microscopy images were obtained of the mature gels over the fibrinogen range of $4\,mg\,ml^{-1} \leq [Fib] \leq 12\,mg\,ml^{-1}$ with a fixed thrombin concentration of 0.08 NIH ml^{-1}. Gels were prepared in an identical manner to those of the rheological study with the addition of 1.5% Alexa-488 labelled fluorescent fibrinogen (Section 4.4.3.2). All samples for rheological analysis were prepared with Tween-20 in order to obtain a defined GP, whereas LSCM samples were prepared both with and without the surfactant to further assess the potential of its inclusion to affect the network microstructure. Representative images captured for each of the samples can be seen in Figure 4-16.

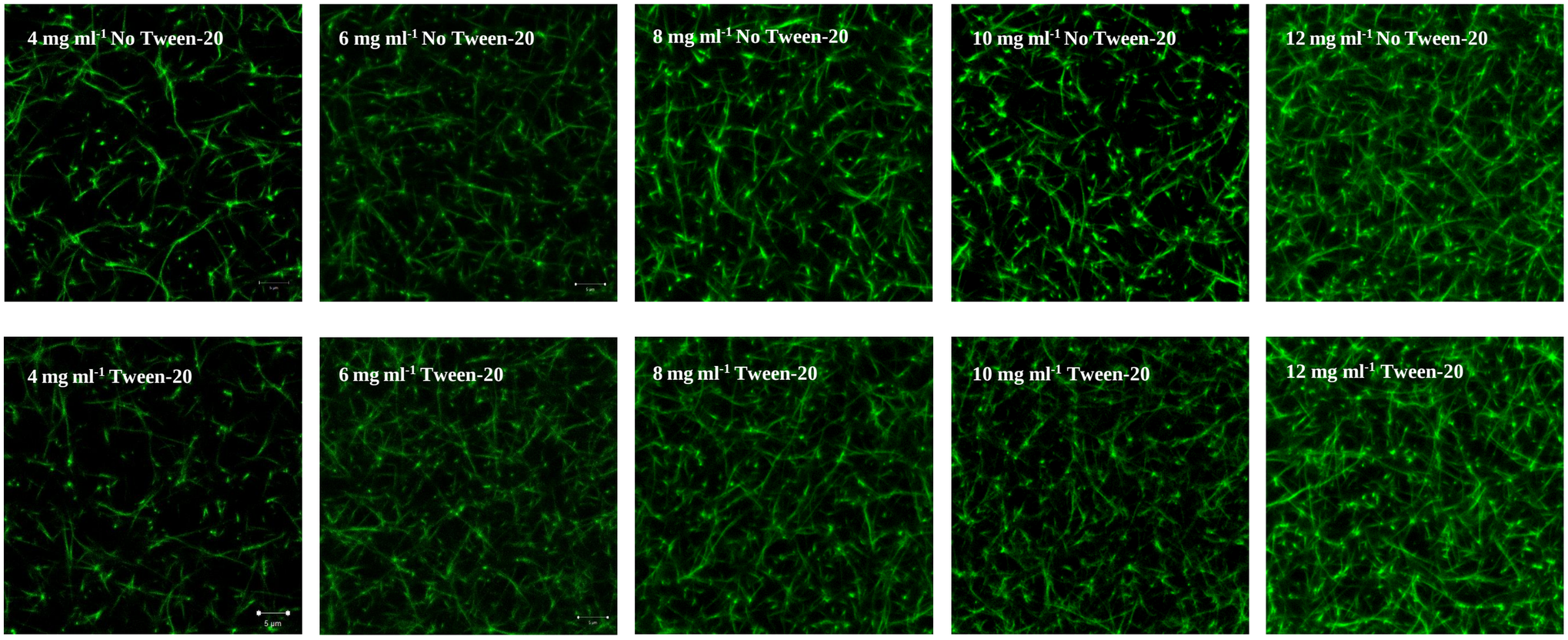

Figure 4-16 *Images captured using LSCM over a range of fibrinogen concentrations with the inclusion of 1.5% Alexa-488 labelled fluorescent fibrinogen. Samples are shown with and without the addition of Tween-20 surfactant, at a fixed thrombin concentration of 0.08 NIH ml^{-1}.*

For the mature gels observed using LSCM (shown in Figure 4-16), it is clear that as the fibrinogen concentration increases, the density of the network microstructure also increases, despite the same behaviour not being observed rheologically in the incipient gels. Clots observed using LSCM are in their native hydrated state. The network formed at a low fibrinogen concentration of 4 mg ml^{-1} appears much more 'open' than the microstructure formed at the other end of the concentration range assessed at 12 mg ml^{-1}. The uncorrected d_f values (obtained from rheology) for 4 mg ml^{-1} and 12 mg ml^{-1} fibrinogen concentration show no statistical significance ($p = 0.5206$) at 1.59 ± 0.034 and 1.57 ± 0.026 respectively. Previous studies have been conducted to analyse the effect of thrombin concentration on the incipient and mature gel structures (75,279,280). By comparison, the fibrinogen concentration study produced far more subtle variance of the mature gel network that those observed in thrombin studies. There is no visual variance in the network structures reported for each concentration regardless of the inclusion of Tween-20 into the gel. The data further supports conclusion that the inclusion of Tween-20 into the gel does not influence the mature microstructure of the network formed.

The SEM images captured of the mature gels over the same concentration range ($4\ mg\ ml^{-1} \leq [Fib] \leq 12\ mg\ ml^{-1}$) with a fixed thrombin concentration of 0.08 NIH ml^{-1} show little deviation in the density of the network formed (Figure 4-17). Whilst a variation in thrombin concentration has previously been shown to have a considerable effect the width of the fibres, this is not apparent for a range of fibrinogen concentrations. This is consistent with the t_{gel} reported for the concentration range, with higher fibrinogen concentrations gelling slower than low fibrinogen concentrations. For example, 12 mg ml^{-1} fibrinogen concentration reported a t_{gel} of 457 ± 6.4 s, whereas at the lowest fibrinogen concentration of 4 mg ml^{-1}, the t_{gel} was considerably faster at 190.2 ± 10.2 s (all samples were prepared with 0.08 NIH ml^{-1} thrombin).

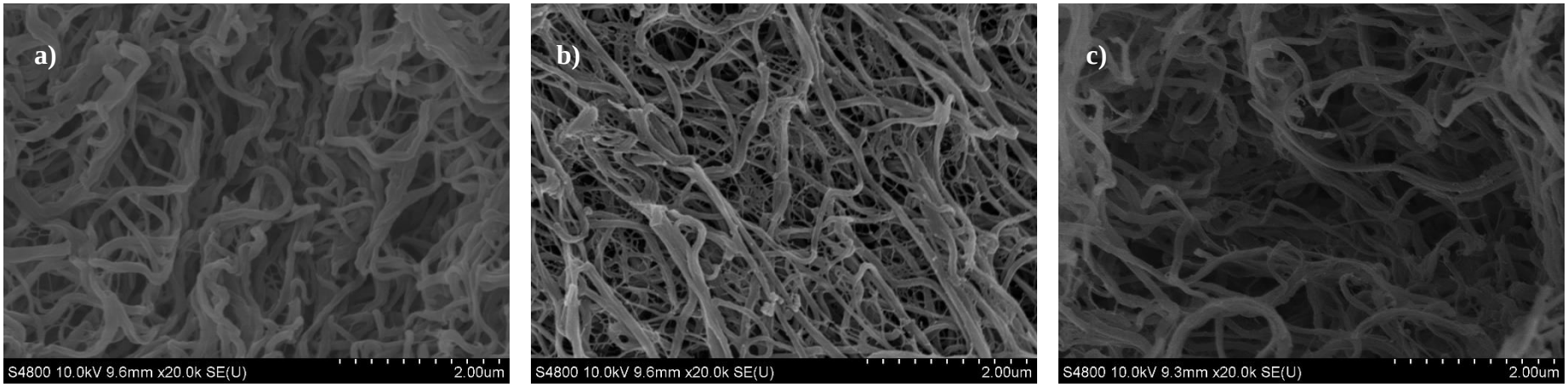

Figure 4-17 *SEM images obtained for fibrin gels prepared with fibrinogen concentrations of* ***a)*** *4 mg ml^{-1},* ***b)*** *8 mg ml^{-1} and* ***c)*** *12 mg ml^{-1}. All samples contain 1% Tween-20 and a thrombin concentration of 0.08 NIH ml^{-1}.*

As previously shown in Figure 4-14, the t_{gel} appears to be fibrinogen concentration dependent. However, the deviation in the t_{gel} over the concentration range is significantly lower than that of the t_{gel} reported for the thrombin concentration range. Using SEM to view the clots formed, it appears that the fibres formed across the fibrinogen range are thicker than those formed at high thrombin concentrations with little deviation in the structure of the clot over the fibrinogen concentration range which is consistent with the rheologically determined d_f values.

The effect of fibrinogen concentration on the mature gel microstructure is much less drastic that that of the thrombin concentration. As seen in Figure 2-4, Weisel showed that at low thrombin concentrations (A), the fibres that form the mature clot network are thicker with few branch points, whereas at higher thrombin concentrations (B) there are many branch points between thinner fibres (126). This does not appear to be the case for the varying fibrinogen concentration as shown in Figure 4-17.

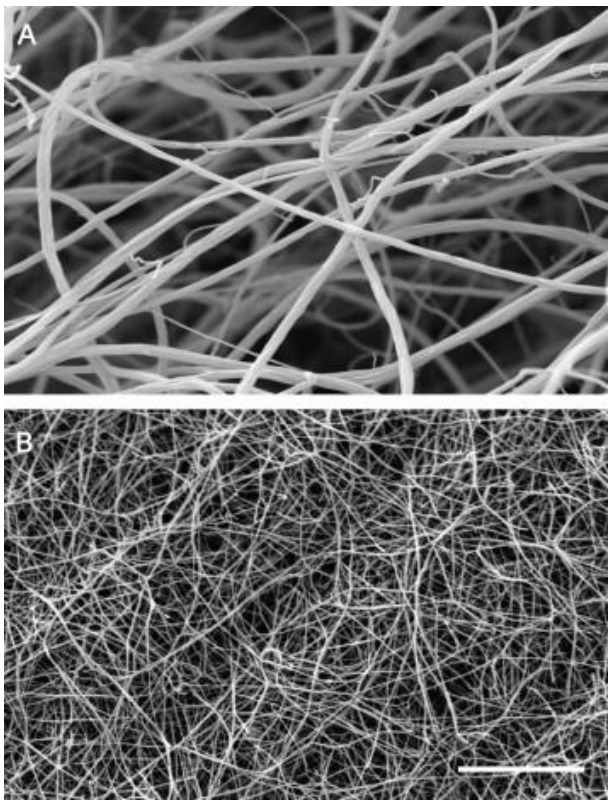

Figure 2-4 *SEM images obtain of fibrin clots from recalcified plasma at a) a low thrombin concentration and b) a high concentration. The scale bar shows 5μm. Reprinted from J. W. Weisel, "The mechanical properties of fibrin for basic scientists and clinicians,"* Biophys. Chem.*, vol. 112, no. 2-3 SPEC. ISS., pp. 267–276, 2004. © 2004 with permission from Elsevier Ltd.*

Based on the results obtained in the fibrinogen and thrombin CMT rheometer studies, a fibrinogen concentration of 6 mg ml^{-1} and thrombin concentration of 0.08 NIH ml^{-1} was selected for analysis of the inclusion of soot. The fibrinogen concentration in plasma of healthy patients can range between $2\ mg\ ml^{-1} \leq [fibrinogen] \leq 5\ mg\ ml^{-1}$ (110–112), with pathological conditions such as inflammation increasing the concentration up to 7 mg ml^{-1} (112). Therefore, the chosen concentration of 6 mg ml^{-1} is within a physiologically pertinent range.

4.5.3.2 ARES-G2 Separate Motor Transducer Rheometer Study

Discrepancies between the CMT data reported above and published data by Sabra et al. (144) on the effect of fibrinogen concentration on the GP required further investigation using a strain controlled (SMT) rheometer, as outlined in Section 4.4.2.3.

The application of ERIC to the CMT data obtained over a range of fibrinogen concentrations at a thrombin concentration fixed at 0.08 NIH ml^{-1} implies that any potential influences from instrument inertia have been corrected. Therefore, a direct comparison can be drawn between the corrected CMT data and data ascertained using an SMT rheometer. Since SMT rheometers do not suffer from instrument inertial artefacts, the GP data reported can be assumed to be more accurate. Figure 4-18 shows the reported t_{gel} obtained using a CMT rheometer in the present study and SMT data reported by Sabra et al., over the fibrinogen range $4\ mg\ ml^{-1} \leq [Fib] \leq 12\ mg\ ml^{-1}$. Whilst both datasets show an apparent increase in the t_{gel} as the fibrinogen concentration increases, the data presented by Sabra et al. for 8 mg ml^{-1} and 12 mg ml^{-1} are significantly higher than those reported using a CMT rheometer in the present work. This could be as a result of variation in thrombin activity between the two studies, despite the minor discrepancy in the thrombin concentrations used.

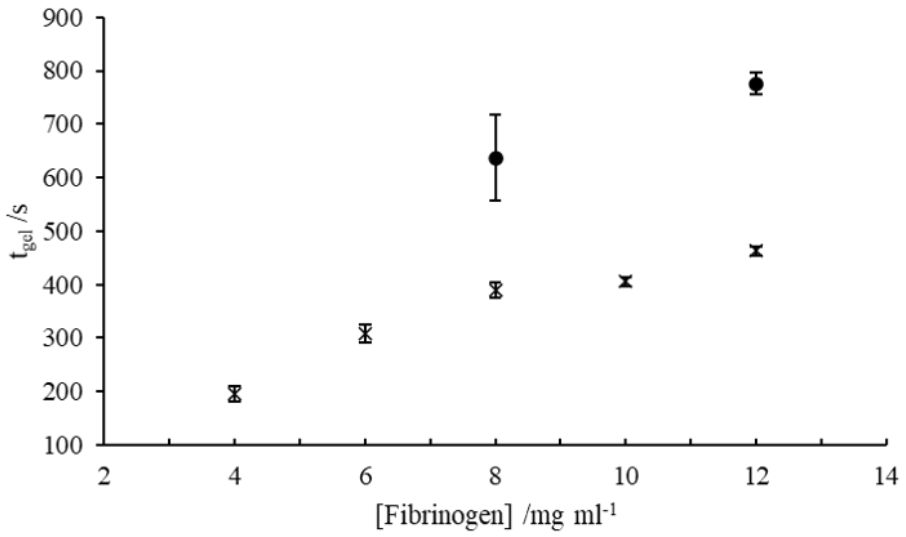

Figure 4-18 *The reported t_{gel} as a function of fibrinogen concentration. The ERIC corrected CMT data from the present study is shown (×) alongside data reported by Sabra et al. (●). The thrombin concentration of the respective studies was 0.08 NIH ml^{-1} for the present work and 0.05 NIH ml^{-1} for the study conducted by Sabra et al.*

The reported d_f at the GP for CMT (present study) and SMT (Sabra et al.) rheometers can be seen in Figure 4-19. By comparing the ERIC corrected CMT data obtained in the present work with SMT data obtained by Sabra et al, it is possible to see a discrepancy between the values reported at high fibrinogen concentrations. Whilst some agreement is shown between the 8 mg ml^{-1} fibrinogen d_f values reported for each of the studies, at 12 mg ml^{-1} the values do not conform. The data collected using a CMT rheometer shows no significant difference, whilst the two concentration values obtained by Sabra et al. suggest a potential increase in d_f as fibrinogen concentration increases.

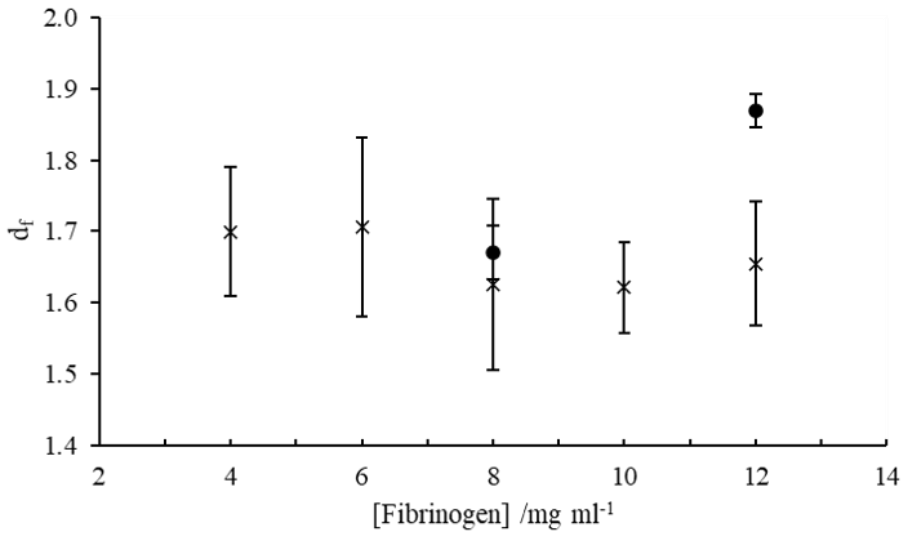

Figure 4-19 *Fractal dimension data reported over a range of fibrinogen concentrations by a CMT rheometer after the application of the ERIC procedure (×) and by Sabra et al. using an SMT rheometer (●). The thrombin concentrations for the reported data are 0.08 NIH ml^{-1} in the current work and 0.05 NIH ml^{-1} for the study conducted by Sabra et al.*

The paper by Sabra et al. reports no assessment of linearity, mutation artefacts or sample inertia. The GPs appear to be visually assessed, with no suggestion that the third harmonic was monitored throughout sample testing. On the contrary, the waveforms reported in the present study were monitored to ensure they remained sinusoidal for the duration of the experiment. An example of the input and response waveform observed throughout the present study can be seen in Figure 4-20. Whilst noise is seen in the output stress waveform because of the weak gel structure, the shape is characteristically sinusoidal suggesting that the system is linear.

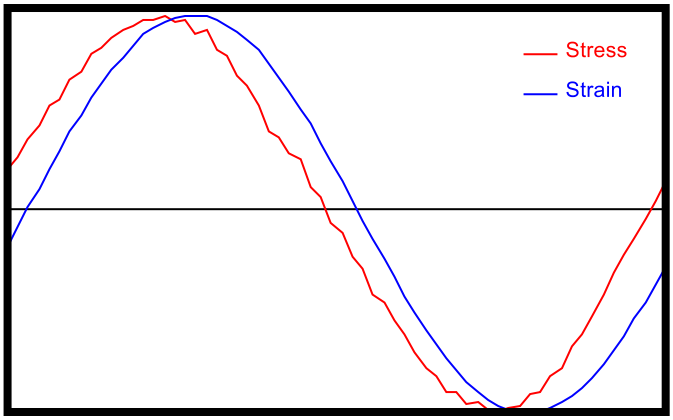

Figure 4-20 *An example of the input and response waveforms observed during the SMT fibrin gels study. Both waveforms display sinusoidal behaviour, indicating that the linearity of the test is not compromised.*

The data presented by Sabra et al. reports that as the fibrinogen concentration increases at a fixed thrombin concentration, the d_f values recorded also increase. The study also suggests that as the fibrinogen concentration increases, the t_{gel} is prolonged, contrary to the effect observed when thrombin concentration is increased. The conclusion drawn from the study by Sabra et al is that the manipulation of fibrinogen and thrombin concentrations used in the formation of fibrin networks can be detected by the reported t_{gel} and d_f at the GP.

In an attempt to verify the results of Sabra et al., a similar study was conducted as part of the present work using an ARES-G2 SMT rheometer. In the 12 months prior to the study, the ARES-G2 rheometer used had undergone transducer, normal force, torque and motor calibration with ± 5% agreement with the standards outlined by the instrument manufacturer, TA Instruments. The procedure used throughout the SMT study in the present work was formatted based on the published method of Sabra et al. (144). Without the inclusion of Tween-20 to the fibrin gel sample, it was not possible to obtain a GP as the resulting data reported only a viscoelastic solid response. The addition of Tween-20 reduced the surface tension of the sample during testing making it possible to determine the frequency independent GP.

In line with the results published by Sabra et al. (144), the t_{gel} reported for fibrin gels prepared with 0.05 NIH ml^{-1} thrombin concentration over a range of fibrinogen concentrations of $8\ mg\ ml^{-1} \leq [Fibrinogen] \leq 12\ mg\ ml^{-1}$, show agreement that as the fibrinogen concentration increases, the reported t_{gel} increases (Figure 4-21). It is only possible to directly compare the data reported at 8 mg ml^{-1} and 12 mg ml^{-1} as no further fibrinogen concentrations were studied by Sabra et al (144). At these two

fibrinogen concentrations, the standard deviations calculated by Sabra et al. appear to be large compared to the t_{gel} obtained in the present study. The quality of the GPs reported in the published work could be questioned as the roots are not well defined and they appear to be visually assessed. There is also evidence of sample inertia in the work by Sabra et al. as the initial phase angles reported are $\delta > 90°$.

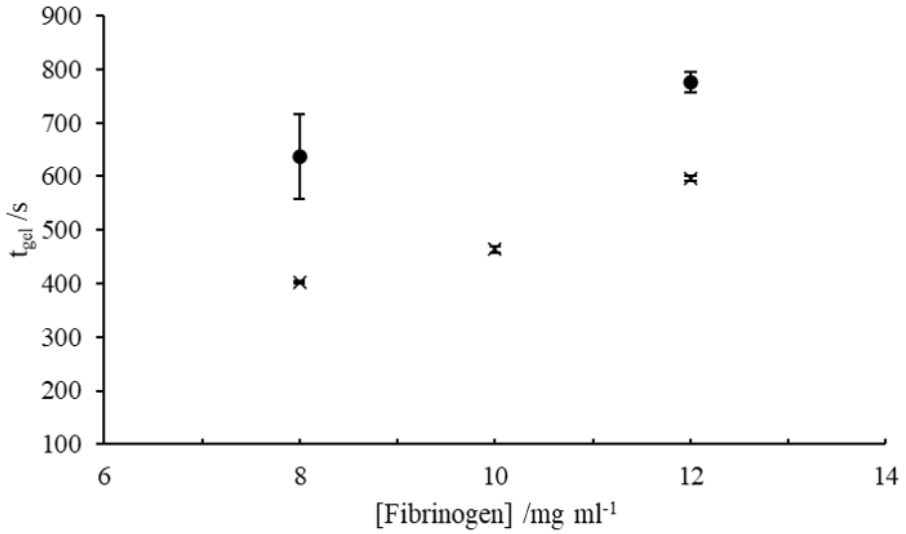

Figure 4-21 *SMT data showing the effect on t_{gel} as fibrinogen concentration was increased from $8\ mg\ ml^{-1} \leq [Fibrinogen] \leq 12\ mg\ ml^{-1}$. The data reported in the present work (×) and that published by Sabra et al. (●) remained at a fixed thrombin concentration of 0.05 NIH ml^{-1}.*

The d_f data reported at the GP by Sabra et al. can be directly compared to the SMT d_f data acquired at the GP in the present study (Figure 4-22). Whilst the data obtained for 8 mg ml^{-1} fibrinogen concentration shows strong agreement between both studies, there is a large discrepancy between the data reported for each of the studies at 12 mg ml^{-1}. Without the presence of a third data point, it is not possible to draw a clear conclusion as to the effect of fibrinogen concentration on the d_f values reported by Sabra et al. (144). However, in the present study, results were produced in triplicate over three concentrations which show a clear correlation between all data points reported and displaying a moderate decrease in d_f as fibrinogen concentration increased. The increase in d_f reported by Sabra et al. (144) could be an indication of strain stiffening with an increase in the reported G'. It is unclear whether the linearity of the experiments conducted by Sabra et al. was considered as it is not described adequately within the publication.

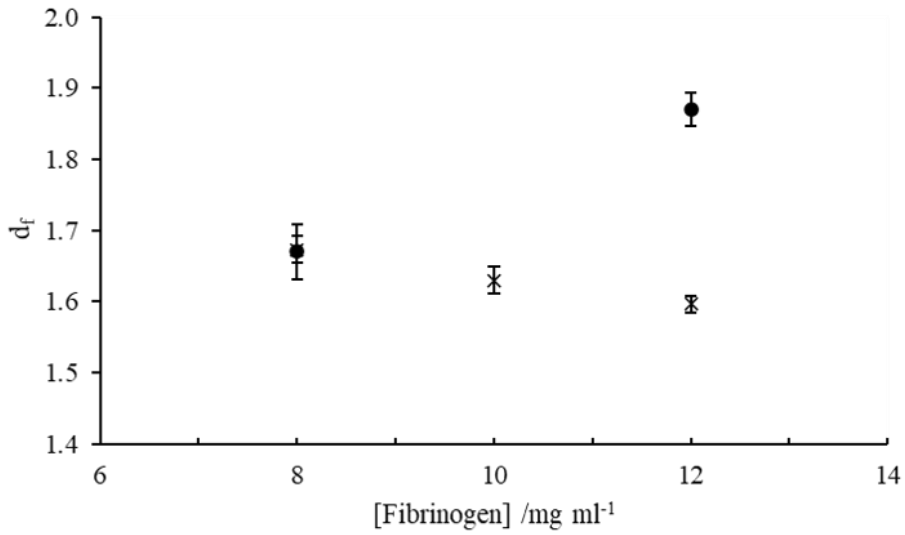

Figure 4-22 *The reported d_f values over a range of fibrinogen concentrations using SMT rheometers. The thrombin concentration in both the present study (×) and data reported by Sabra et al. (●) remained constant at 0.05 NIH ml^{-1}.*

Data was obtained using CMT and SMT rheometers in the present study at a fixed thrombin concentrations of 0.08 NIH ml^{-1} and 0.05 NIH ml^{-1}, respectively, over a range of fibrinogen concentrations $4\ mg\ ml^{-1} \leq [Fibrinogen] \leq 12\ mg\ ml^{-1}$. As seen in Figure 4-23, after the application of the ERIC procedure, the CMT data shows agreement with the SMT data that as the fibrinogen concentration increases, the t_{gel} also increases. This is in agreement with the work conducted by Sabra et al. (144).

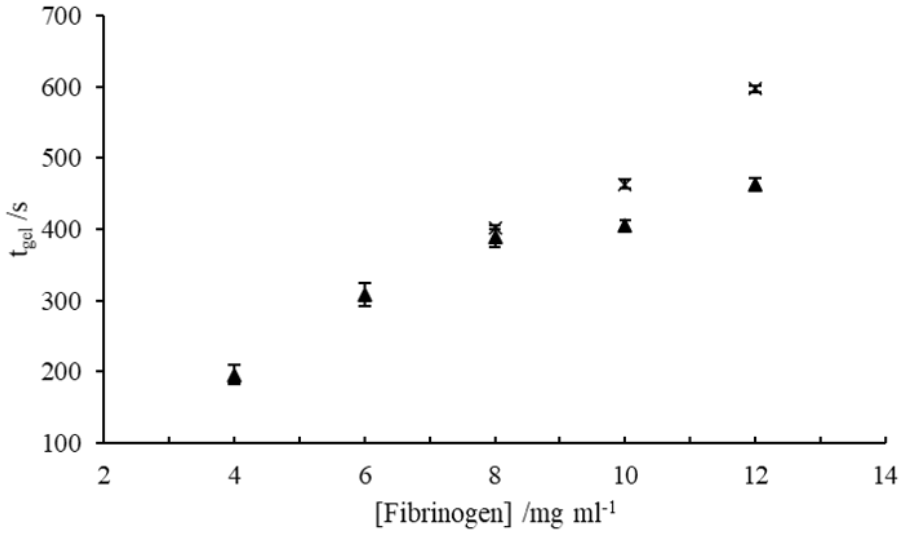

Figure 4-23 *Effect of fibrinogen concentration on t_{gel} for studies conducted using CMT and SMT rheometers. The CMT data (▲) obtained at thrombin concentration of 0.08 NIH ml^{-1} and the SMT data (×) reported for thrombin concentration of 0.05 NIH ml^{-1}, were conducted as part of the present work.*

A comparison can be drawn between the d_f data obtained using the ARES-G2 strain-controlled rheometer and the AR-G2 stress-controlled rheometer after the application of the ERIC procedure. The results obtained for d_f using both CMT and SMT rheometers in the present work can be seen in Figure 4-24. Both the ERIC corrected CMT and SMT data shows strong agreement at higher fibrinogen concentrations, with the thrombin concentrations remaining constant at 0.08 NIH ml^{-1} and 0.05 NIH ml^{-1}, respectively. The data acquired using a strain-controlled rheometer can be considered more accurate due to the absence of instrument inertia.

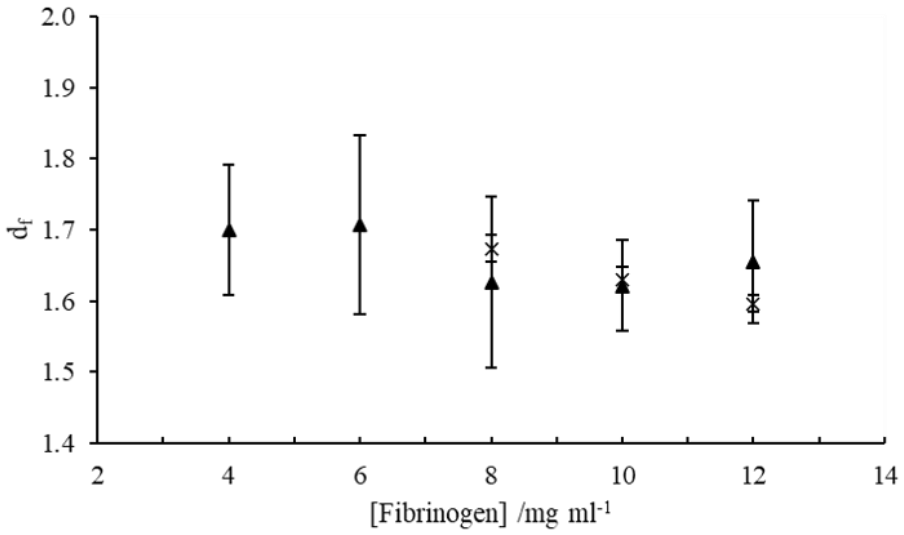

Figure 4-24 *The reported d_f values obtained using a CMT and SMT rheometer over a range of fibrinogen concentrations between $4\ mg\ ml^{-1} \leq [Fibrinogen] \leq 12\ mg\ ml^{-1}$.. In the present work, the CMT data (▲) was obtained at a fixed thrombin concentration of 0.08 NIH ml^{-1}, whilst the SMT data (×) was obtained at 0.05 NIH ml^{-1}.*

To further understand the effect of fibrinogen and thrombin concentration on the microstructure of the incipient gel network, the d_f values obtained in the present SMT study are presented as a function of fibrinogen to thrombin ratio (F/T) in Figure 4-25. As F/T increases, the d_f values reported in the present SMT study decrease. This appears to be due to the drastic effect that thrombin concentration has on the microstructure of the gel network formed in comparison to the effect of fibrinogen concentration (75,144).

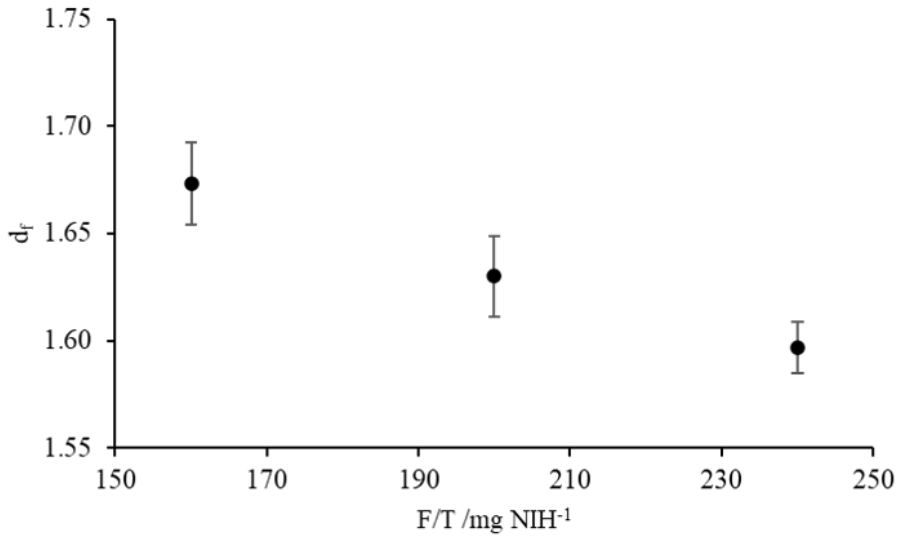

Figure 4-25 *The effect of fibrinogen to thrombin ratio (F/T) is seen in the d_f values reported for the present SMT rheometer study.*

4.5.4 Soot Concentration Study

4.5.4.1 G[1x] Concentration Study

As discussed in Section 4.4.2.4, initial soot experiments were conducted using a CMT rheometer by increasing the volume of sample G[1x] included in the fibrin-thrombin gels to increase the number of particles present. The concentration of Soot G[1x] was estimated to be 5.6 x10^9 particles ml^{-1}. A volume of $0\% \leq G[1x] \leq 5\%$ of the total volume was included in the fibrin gel samples prepared. The number of particles present in the gels over this range was between 2.80 x10^9 particles ml^{-1} at 0.5% G[1x] and 2.8 x10^{10} particles ml^{-1} at 5% G[1x] inclusion. The dilution of the gel reagents was not influenced during the process as the TBS balance was altered to accommodate the soot solutions. As the G[1x] soot inclusion increased, it became more challenging to obtain GP data, resulting in an increased number of experiments required to achieve the desired number of repeats. The fibrinogen and thrombin concentrations remained constant throughout the study at 6 mg ml^{-1} and 0.08 NIH ml^{-1} respectively.

The δ_{GP} reported for each of the soot G[1x] concentrations within the fibrin-thrombin gels do not appear to show a dependence on the number of particles present (Figure 4-26). The uncorrected data shown in Figure 4-26a) indicates no statistical significance between the TBS control samples (0% inclusion) and the highest inclusion of the G[1x] at 5% inclusion ($p = 0.8296$). The TBS control sample reported a mean phase angle at the GP of 69.4 ± 4.2° whereas the 5% soot inclusion

samples reported at phase angle of 69.0 ± 4.9°. The ERIC corrected data, reported in Figure 4-26b), shows a slight increase in δ_{GP} as a function of concentration. However, there is no statistical significance between the highest and lowest reported δ_{GP} values although there is a large reduction in the p-value ($p > 0.228$).

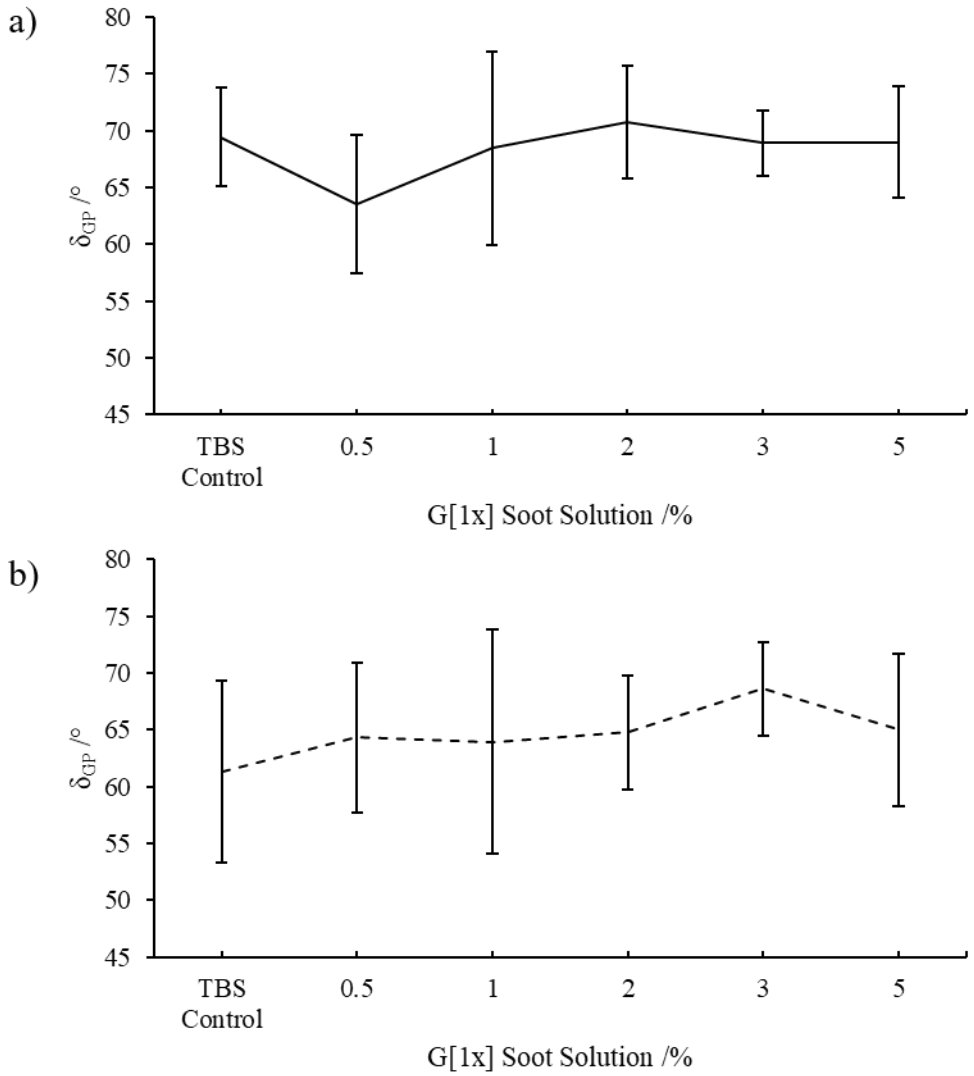

Figure 4-26 *The effect of increased soot particle concentration on δ_{GP}. Shown in a) is the uncorrected δ_{GP} data and b) the data ERIC corrected data. The fibrinogen and thrombin concentrations remained constant throughout the study 6 mg ml^{-1} and 0.08 NIH ml^{-1}, respectively.*

The corresponding d_f values calculated for each soot G[1x] inclusion (0% to 5%) further suggest a lack of soot concentration dependence shown by the δ_{GP} data (Figure 4-27). The uncorrected data in Figure 4-27a) shows a slight decrease in the reported d_f values for gels prepared with increasing inclusions of soot G[1x]. No statistical significance is reported for ($0.2528 \leq p \leq 0.8630$) between the uncorrected soot inclusion data sets (0.5% to 5%) and the TBS control samples (0%). The data reported

in Figure 4-27b) represents the ERIC corrected d_f data for increasing G[1x] inclusions. Once again, there appears to be no significant variation in the corrected d_f values, with $p > 0.2339$ for all samples across the range of 0.5% to 5% Soot G[1x] inclusion in comparison with the TBS control samples.

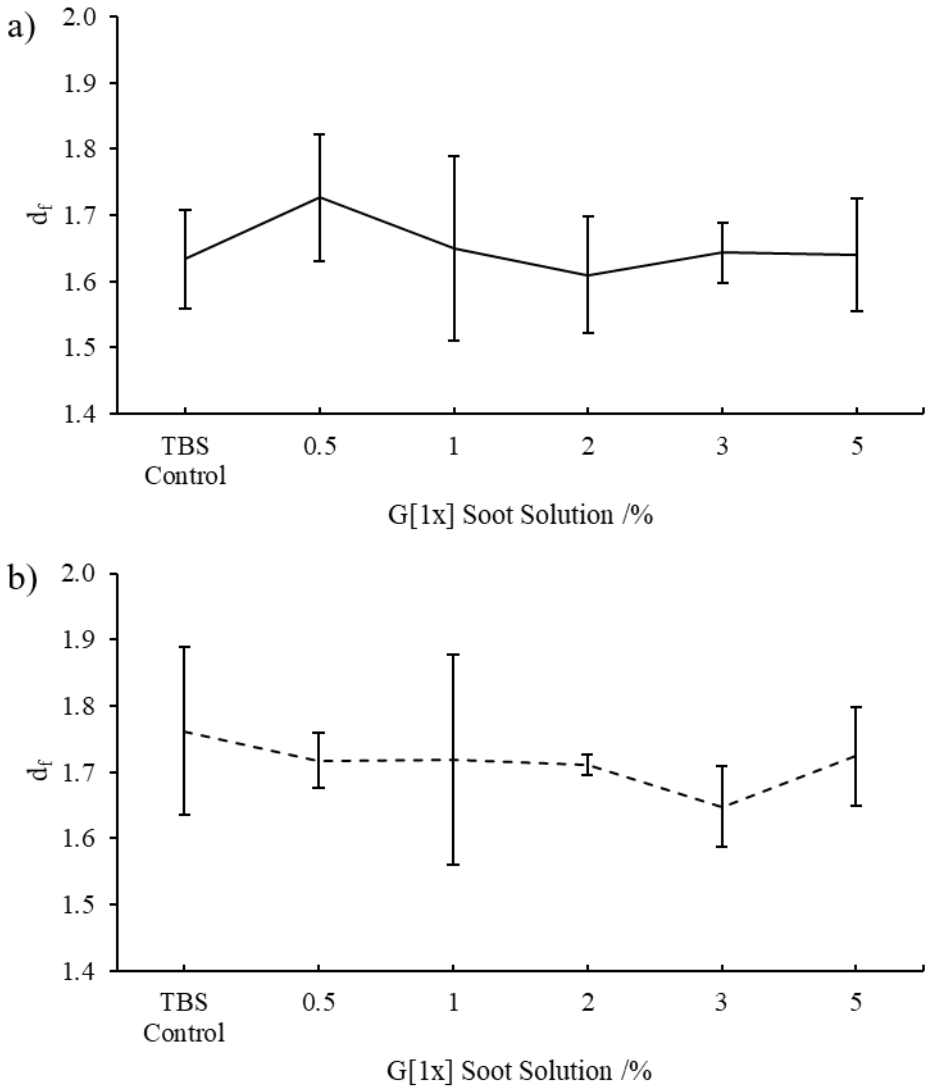

Figure 4-27 *The d_f data obtained over a range of soot particle concentrations between 0.5 % and 5% inclusion alongside a TBS control. The pre-ERIC data is shown in a), whilst the post-ERIC application data is Represented in b). The fibrinogen and thrombin concentrations remained constant at 6 mg ml^{-1} and 0.08 NIH ml^{-1}, respectively.*

The t_{gel} reported over the soot inclusion range once again showed little deviation as the volume of Soot G[1x] solution increased (Figure 4-28). Neither the uncorrected or ERIC corrected data shows clear dependence on concentration with $0.235 \leq p \leq 0.975$ reported between the control sample (0%) and the samples with a soot inclusion (0.5% to 5%). The mean t_{gel} reported for the control sample was 345.7 ± 58.4 s,

resulting in an acceptable N_{mu} value of 0.097 (Table 4-1). Despite the shortest t_{gel} of 294.7 ± 9.7 s reported for 1% soot G[1x] inclusion, the N_{mu} calculation still satisfies $N_{mu} < 0.15$ (259) with a value of 0.135.

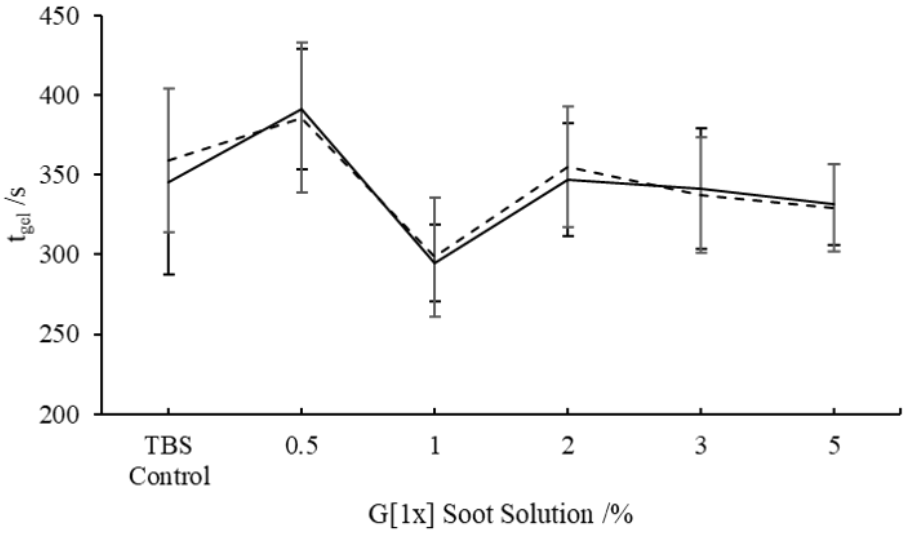

Figure 4-28 *The t_{gel} data for the inclusion of 0.5-5% volume Soot G[1x] solution study for fibrin gels with fibrinogen and thrombin concentrations of 6 mg ml^{-1} and 0.08 NIH ml^{-1}, respectively.. There appears to be no conclusive effect on the t_{gel} with increasing soot concentration for either the pre- (solid line) or the post-ERIC (dashed line) data.*

Table 4-1 *presents the gel time data (mean ± standard deviation) over a range of low soot concentrations.*

		Pre-ERIC	
		t_{gel} /s	**N_{mu}**
Soot G[1x] inclusion	**0%**	345.7 ± 58.4	0.097
	0.5%	391.7 ± 38.0	0.141
	1%	294.7 ± 24.0	0.135
	2%	347.0 ± 35.5	0.118
	3%	341.7 ± 38.0	0.129
	5%	331.5± 25.0	0.138

The ERIC corrected t_{gel} data shows similar behaviour to the uncorrected data with only minor alterations for each soot G[1x] concentration. Again, no statistical significance between the control samples and the soot samples was determined using t-tests with $0.148 \leq p \leq 0.905$ for the post-ERIC data over 0% to 5% soot G[1x]

inclusion. The deviation between repeated GP experiments is represented by the standard deviation error bars on Figure 4-26, which are similar for both the corrected and uncorrected data.

Volumes of low concentration Soot G[1x] appear to have little impact on the GP reported over a range of 0% to 5% soot inclusion. Based on the results obtained through the inclusion of increasing volumes of Soot G[1x], highly concentrated soot solutions were prepared (as discussed in Section 4.4.1) in order to study the effects on fibrin gel clotting. Soot G[2x] and G[10x]) were concentrated to give particle concentrations of 1.12 $x10^{10}$ and 5.6 $x10^{10}$ particles ml^{-1} respectively. The further study was carried out to assess whether higher numbers of particles had an increased effect on the GP of the fibrin gels without compromising the quality of the GP.

4.5.4.2 Highly Concentrated Soot Study

The final study conducted as part of the research to determine the effect of the inclusion of soot on fibrin gel clots involved the use of highly concentrated soot solutions. Using the procedure in Section 4.4.1, the soot G[1x] sample was concentrated to give G[2x] and G[10x] samples that were then added to the F-T gels to analyse the effects on the gel microstructure. The concentrations of the new, more concentrated G[2x] and G[10x] samples were estimated to be 1.12 $x10^{10}$ and 5.60 $x10^{10}$ particles ml^{-1} respectively. A rheological study was conducted using a CMT rheometer and the procedure outlined in Section 4.4.2.4 before supporting LSCM and SEM images were obtained as detailed in Section 4.4.3.3 and Section 4.4.4.3. The fibrinogen and thrombin concentrations remained constant at 6 mg ml^{-1} and 0.08 NIH ml^{-1} respectively, with 1% soot inclusion (of the total sample volume) being added to the gel.

The d_f data for the fibrin gels with the inclusion of 1% of the total volume of concentrated soot solutions can be seen in Figure 4-29. There does not appear to be a convincing overall effect on the reported d_f values as the soot concentration is increased. There is a significant decrease in the uncorrected d_f values calculated for the G[2x] and G[10x] as 1.57 ± 0.09 ($p = 0.011$) and 1.58 ± 0.11 ($p = 0.033$) respectively compared to the reported d_f value for the TBS control sample of 1.67 ± 0.06. Once corrected using the ERIC procedure, no statistical significance is reported

with T-Tests determining that data corrected for all soot solutions have $p \geq 0.069$ compared to the control samples.

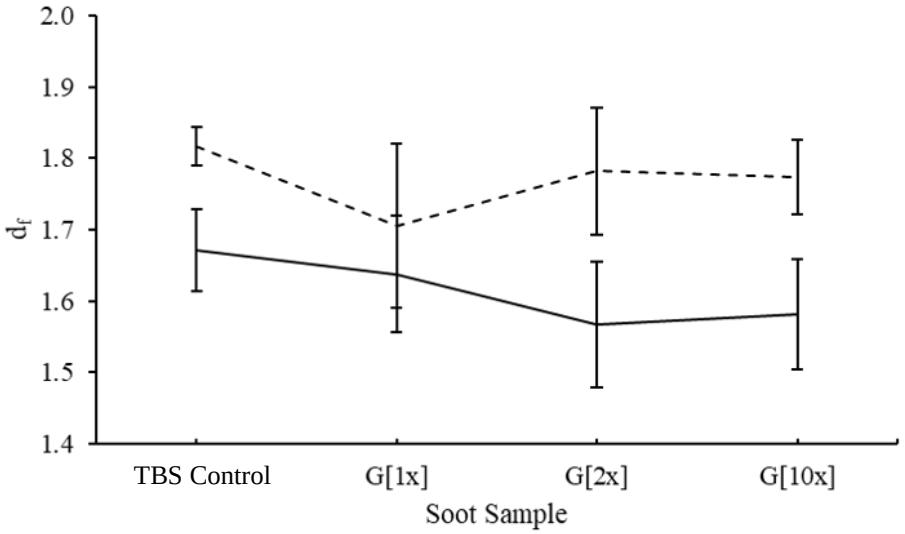

Figure 4-29 *The corresponding d_f values reported at the GP for each soot concentration. Pre-ERIC data is shown with a solid line and post-ERIC data is shown by a dashed line. A TBS control set was included for comparison of data obtained with the inclusion of soot solutions G[1x], G[2x] and G[10x].*

For samples containing G[1x], no statistical significance was reported between the uncorrected and ERIC corrected d_f data ($p = 0.388$). However, for the TBS control and higher soot concentration samples, the ERIC corrected data is significantly different to that of the uncorrected d_f data with T-Test returning all values of $p \leq 0.003$ between the two datasets, thus demonstrating that the ERIC correction procedure is crucial in performing GP analysis in weak gelling systems.

Dixon's Outlier Q-Tests (285) were employed to identify the presence any outliers in the rheological dataset. Using a confidence interval of 90% with a total of five runs for each soot concentration, any values returned as Q > 0.642 using Eq. 4.3 were classed as an outlier (286). It was only acceptable to reject one outlier per dataset (286). An example calculation is shown in Eq 4.4 for the lowest value of d_f using sample G[1x] pre-ERIC. The calculated 0.143 << 0.642, meaning the result is not an outlier for the d_f dataset.

$$Q = \left|\frac{gap}{range}\right| \qquad \text{Eq 4.3}$$

$$Q = \left|\frac{(1.57 - 1.53)}{(1.81 - 1.53)}\right| = 0.143 \qquad \text{Eq 4.4}$$

Two outliers were found and discarded across the data. For the data discarded, experiments were replicated, with further Q-Tests completed to ensure that the new dataset was valid.

Figure 4-30 shows that the inclusion of any soot concentration results in a decrease in the t_{gel} at the GP compared to the TBS control samples. Using a T-test to analyse the connotations of the reported t_{gel}, there is a significant difference reported between the uncorrected t_{gel} control sample data and data for each of the gels with the inclusion of concentrated soot solutions, with $p \leq 0.032$. The ERIC corrected control sample reported a t_{gel} of 375.0 ± 18.0 s whereas all gels with the addition of the soot solutions reported t_{gel} of 312.6 ± 26.7 s to 317.0 ± 35.3 s. The corrected data also shows statistical significance as all calculated p values for the samples with the inclusion of soot solutions were $p \leq 0.021$ compared to the TBS control samples.

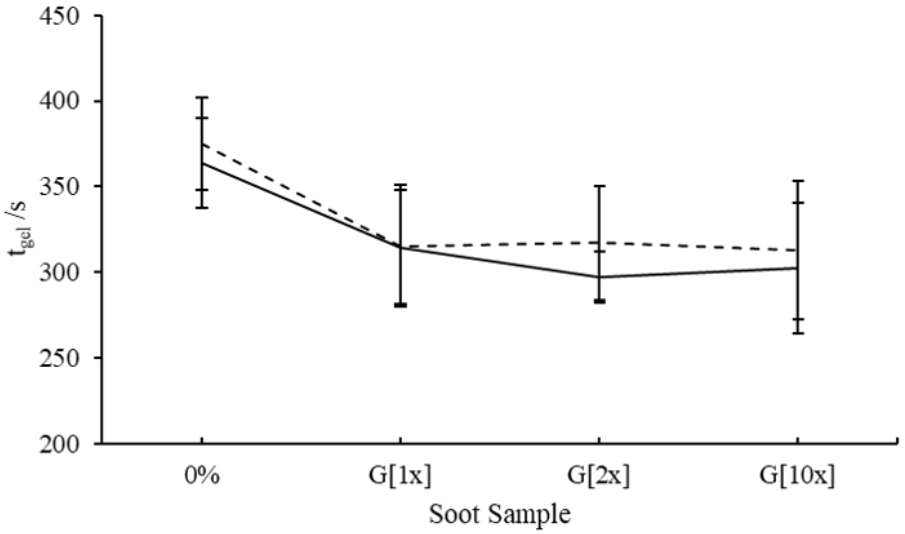

Figure 4-30 *The t_{gel} recorded for each of the soot solutions, G[1x], G[2x] and G[10x]. By comparison with the TBS control samples (0%), the inclusion of soot decreases the gel time of the fibrin thrombin gels. Both the uncorrected (solid line) and ERIC corrected (dashed line) show agreement.*

It is possible for carbon based particles to have an effect on the activity of the thrombin present due to protein surface interactions (253). The inclusion of the soot solution in the gel samples could increase the coagulability of the clot, thus reducing the clotting time observed.

Whilst statistical significance was identified for high soot concentrations in comparison with the TBS control sample in terms of t_{gel} data, it is less clear for the reported δ_{GP} data. As the soot concentration increases, there appears to be a slight increase in the uncorrected δ_{GP} reported Figure 4-31. The uncorrected δ_{GP} data (solid line) shows a significant increase for the concentrated soot solutions, G[2x] and G[10x] compared to the control sample, where $p = 0.009$ and $p = 0.026$ respectively. No significance was reported between the uncorrected δ_{GP} saline control sample and soot solution G[1x] (stock solution) where $p = 0.569$. Once the ERIC procedure was applied to the δ_{GP} data (dashed line), no significance between the soot solutions and the control samples as $p \geq 0.069$ was calculated for all concentrations.

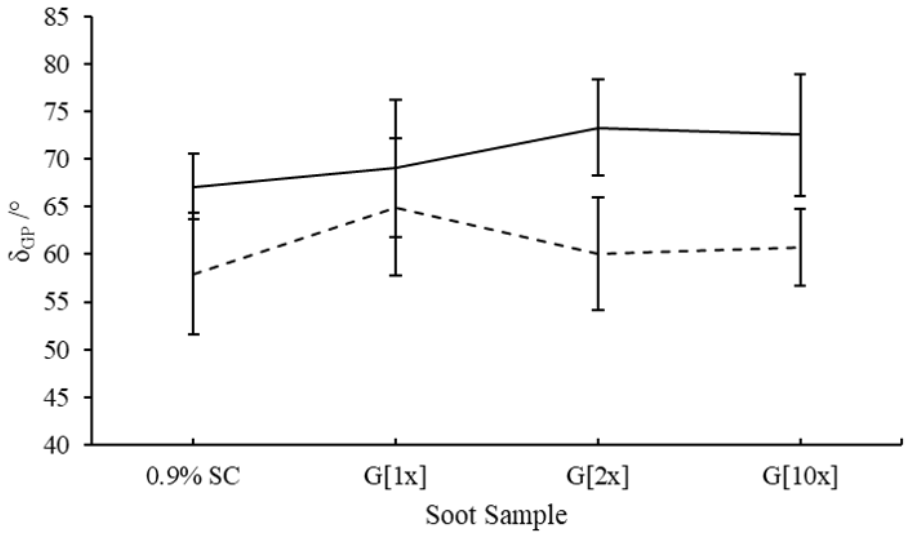

Figure 4-31 *The reported δ_{GP} for the soot solutions G[1x], G[2x] and G[10x] alongside a TBS control. The uncorrected data is shown by the solid line and the ERIC corrected data represented by the dashed line.*

Comparison between the uncorrected and ERIC corrected δ_{GP} data shows there is a significant decrease in all cases except G[1x] after the application of the correction procedure. For the higher soot concentrations of G[2x] and G[10x], the p values were determined to be $p = 0.0029$ and $p = 0.0012$ respectively between the uncorrected and ERIC corrected δ_{GP} data. The phase angles in these cases were reduced from 73.3 ± 5.05 ° to 60.1 ± 6.73 ° for the G[2x] data and 72.5 ± 6.36 ° to 60.7 ± 6.73 ° for the G[10x] data GP once the ERIC correction was applied suggesting the correction has a significant effect on the GP reported.

To visually assess the mature microstructure of the fibrin gels, LSCM images were obtained for 1% inclusion of each of the soot concentration solutions (Figure 4-32). The gels were prepared as discussed in Section 4.4.3.3.

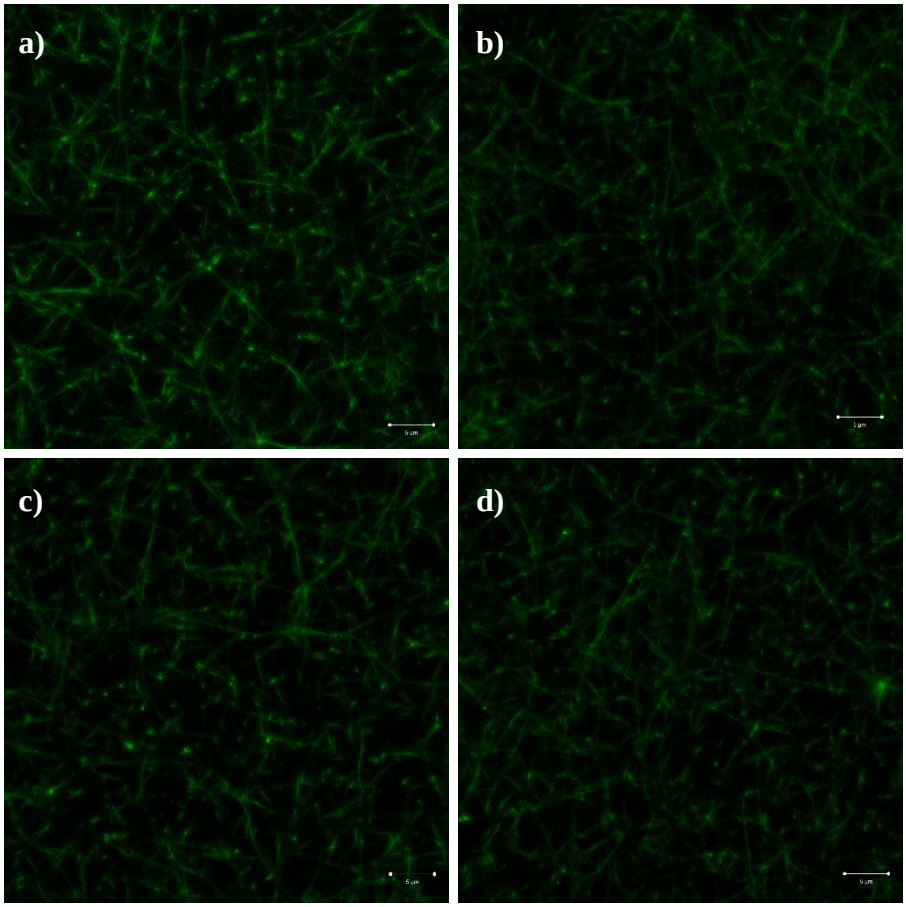

Figure 4-32 *LSCM images obtained for each of the soot solutions (G[1x], G[2x] and G[10x]) alongside a TBS control sample. The fibrinogen concentration of all samples was 6 mg ml^{-1} and a thrombin concentration of 0.08 NIH ml^{-1}. The images show* ***a)*** *TBS control,* ***b)*** *1% Soot G[1x] inclusion,* ***c)*** *1% Soot G[2x] inclusion and* ***d)*** *1% Soot G[10x] inclusion. The scale bar shows 5 μm.*

The LSCM data appears to agree with the rheological data with very little variation in the mature microstructure observed as the number of soot particles increased. Compared with the TBS control sample in (Figure 4-32a), the gels with the inclusion of soot solutions show similar fibre distribution (Figure 4-32b to Figure 4-32d). Due to the requirement of a fluorescent label to examine the fibres present in the microstructure, it was not possible to directly observe the soot particles present as they were unlabelled and did not fluoresce. In order to assess the soot particles within the gel network, SEM images were gathered of identically prepared mature clot structures with the inclusion of 1% soot concentration samples.

It was possible to observe the soot particles (circled in red) within the mature gel network (Figure 4-33). The soot particles appear to be randomly distributed throughout the mature gel and even at high soot concentrations, they are sparsely dispersed throughout the fibrin gel network.

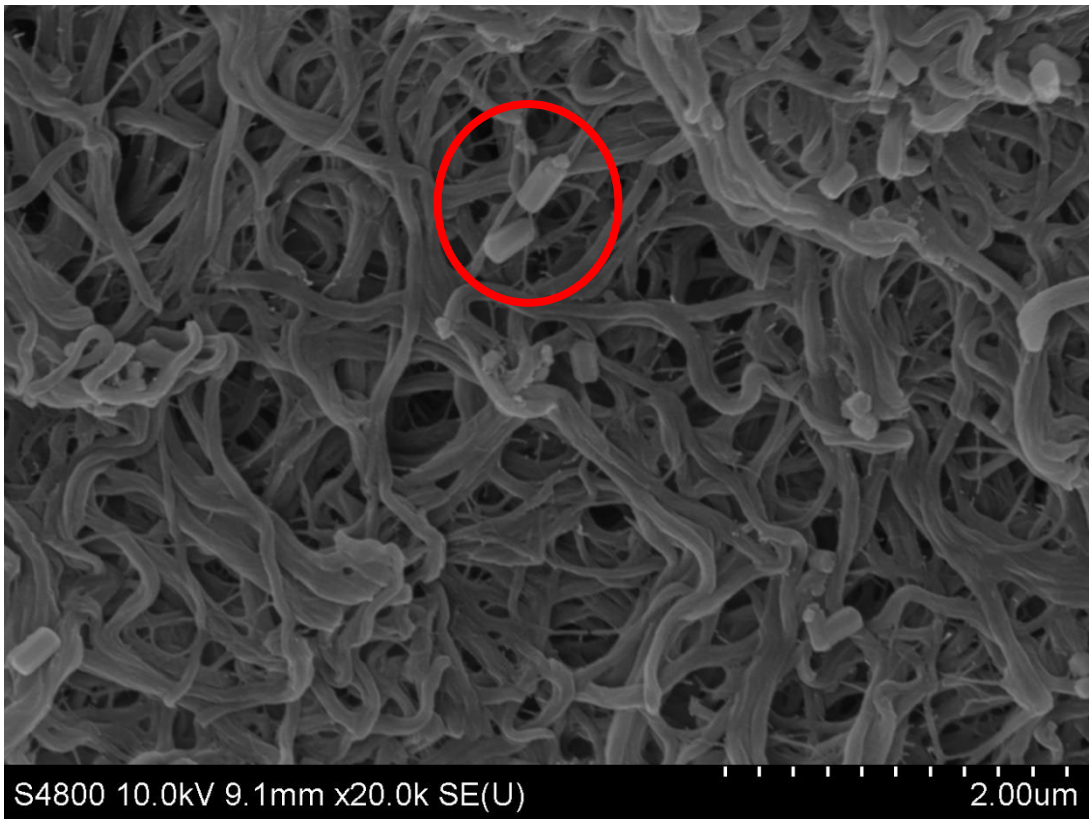

Figure 4-33 *SEM image of a mature fibrin gel with the inclusion of 1% G[10x] soot solution. The presence of soot particles can be seen in the image with an example circled in red. The fibrin gel had a fibrinogen concentration of 6 mg ml^{-1} and thrombin concentration of 0.08 NIH ml^{-1}.*

SEM images were obtained for all soot solutions, as well as a TBS control sample. The 1% inclusion of each soot solution into the fibrin gels can be seen in Figure 4-34. Fibrin gels were prepared with a fibrinogen concentration of 6 mg ml^{-1} and thrombin concentration of 0.08 NIH ml^{-1}. The SEM images can be used to view the structure of the network as well as the arrangement of individual fibres. It appears that the addition of the soot solutions to the fibrin causes little deviation fibre network compared to the saline control network, which shows some agreement with the d_f reported for the incipient gel at the GP. It is possible to see that as the soot solution included becomes more concentrated, there are a larger number of visible soot particles present within the fibrin gel sample.

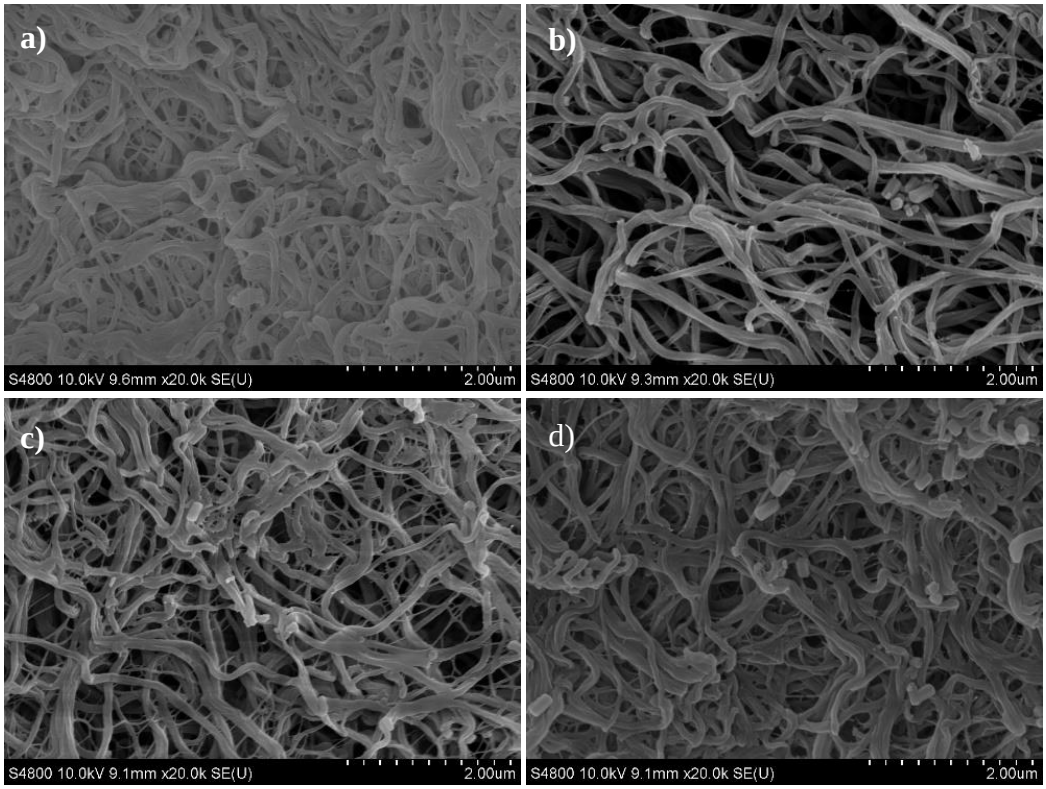

Figure 4-34 *SEM images gathered for each of the soot concentrations* ***a)*** *TBS control,* ***b)*** *1% inclusion G[1x] solution,* ***c)*** *1% inclusion G[2x] solution,* ***d)*** *1% inclusion G[10x] solution. The fibrinogen concentration for all gels was 6 mg ml^{-1}, with a thrombin concentration of 0.08 NIH ml^{-1}.*

Combining the data obtained for both low and high soot solution concentration studies gives an overview of the effect of soot PM on fibrin gel formation as the number of particles increases. The data shown in Figure 4-35 represents a) the δ_{GP} data and b) the d_f data reported as the number of particles included in the sample was increased across the soot solution range. The uncorrected phase angles appear to suggest a slight decrease initially, followed by an increase in δ_{GP} as the particle concentration increases with a corresponding increase, then decrease in the d_f values reported. However, once the ERIC procedure is applied, the d_f values indicate a slight increase from 3.4 x10^9 particles ml^{-1}, commensurate with literature for alternative pathologies (148,149).

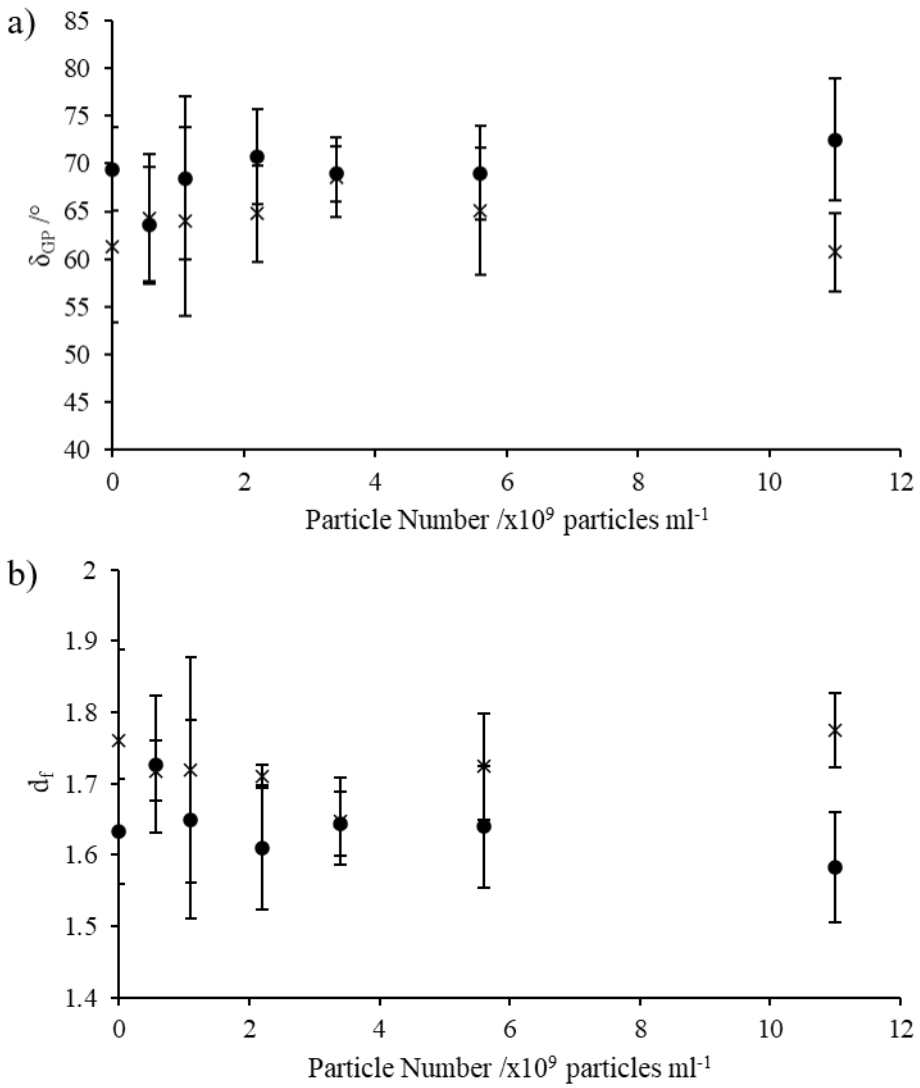

Figure 4-35 *Reported GP data for the combined low and high soot concentration inclusions into fibrin gels. The data for* ***a)*** *the* δ_{GP} *as a function of particle number and* ***b)*** *the corresponding* d_f *values are presented.*

As seen in Figure 4-36, as the number of particles present in the gel samples increased, it appears that the t_{gel} decreases, with an anomalous data point at 1.1 x10^9 particles ml^{-1}. Assuming a confidence interval of 10%, both the pre- and post-ERIC data show a significant decrease in the t_{gel} across the number of particles included between 5.6 x10^8 particles ml^{-1} to 1.1 x10^{10} particles ml^{-1} ($p = 0.0183$ and $p = 0.0571$ for pre- and post-ERIC analysis, respectively). This decrease in clot time has also been observed in patient suffering from vascular illness such as ischaemic stroke (148) and could act as a potential biomarker.

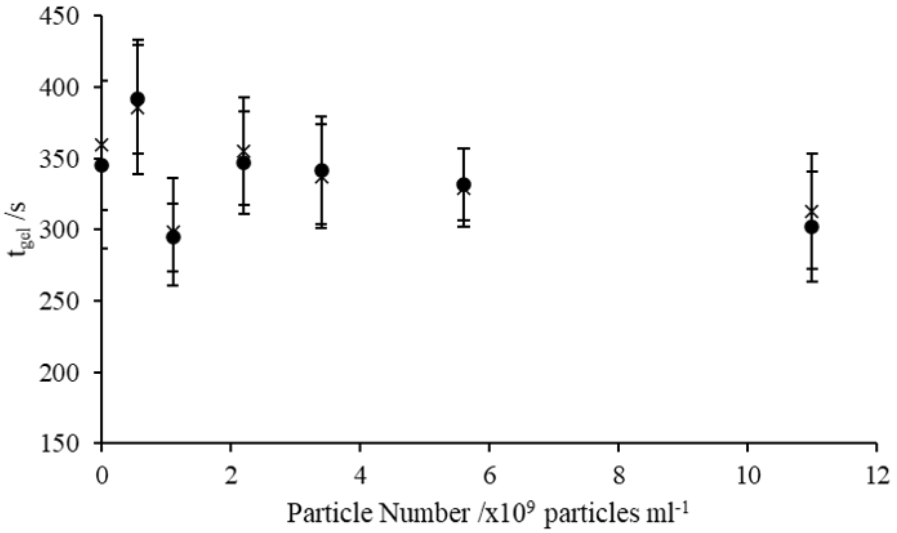

Figure 4-36 *The resultant t_{gel} as particle number inclusion within the fibrin gel sample was increased. The uncorrected data is represented by closed circles (●) and the ERIC corrected data is shown by crosses (×).*

The inclusion of concentrated soot solutions appears to have little effect on the rheological data reported at the GP. The d_f and phase angle data reported does not show a convincing association with the increased presence of soot particles. There appears to be a dependence on the gel time reported as the soot concentration increased, in agreement with the previous studies, The LSCM and SEM images captured of the fibrin gels over the soot concentration range appear to support the notion that the inclusion of soot particles does not have a steric effect on the fibrin gel network formation, at least at the number concentration studied herein.

4.6 Conclusions

Several studies concerning fibrin-thrombin gels and the effect of soot particulates on the resulting network architecture were detailed in this chapter. The conclusions are given as follows:

1. Effect of the addition of surfactant (Tween-20) on the microstructure of the fibrin gels. The quality of the GP data was found to be greatly improved upon inclusion of Tween-20. The addition of the surfactant into the fibrin gels reduces the impact of surface tension on the torque produced, allowing valid rheological measurements to be obtained, even in a low viscosity weak gelling system (31). Supporting image analysis appears to show that the addition of Tween-20 has little effect on the microstructure of the mature fibrin gel. All subsequent studies were conducted in the presence of Tween-20 to reduce the influence of surface tension artefacts.
2. Effect of thrombin concentration on gel architecture. A strong association between thrombin concentration and t_{gel} was observed, with high thrombin concentration gels undergoing gelation much faster than low thrombin concentration samples. A small dependency was observed between the d_f and thrombin concentration which was enhanced by the use of the ERIC procedure. Images obtained using LSCM and SEM techniques showed an increase in the density of fibres present in clots as the thrombin concentration increased. It was not possible to obtain valid rheological data outside of the experimental range due to the rapid network formation at high thrombin concentrations and low thrombin concentrations forming weak gels that were beyond the rheometer's capabilities. From the data obtained, the thrombin concentration for studies concerning soot inclusion was determined to be 0.08 NIH ml^{-1}, within the physiologically relevant range (287).
3. Effect of fibrinogen concentration on fibrin gel formation. The increase in t_{gel} as the concentration of fibrinogen present in the fibrin gels increases appears to suggest that the kinetics of the gelation process are dominated by a possible diffusion limitation rather than expected reaction limitation. The d_f data obtained at the GP shows little deviation across the fibrinogen range employed. The rheological and image data acquired over the fibrinogen concentration CMT study resulted in the use of 6 mg ml^{-1} for further CMT studies. At this

concentration, it was possible to obtain valid GP data within a physiologically accurate range.

4. Effect of low concentrations of soot particulates on fibrin gels. Low concentrations of soot solutions appeared to have little effect on the GPs reported for fibrin gels with fibrinogen concentration of 6 mg ml^{-1} and thrombin concentration of 0.08 NIH ml^{-1}. Inclusions of Soot G[1x] over a range of 0.5% to 5% show little evidence of deviation in the incipient gel rheological data or the mature gel microstructure, imaged using LSCM and SEM. The Soot G[1x] solution was concentrated to produce two- and ten-times concentrated solutions (Soot G[2x] and Soot G[10x], respectively).
5. Effect of highly concentrated soot particulates on fibrin gels. The final study conducted to assess the potential adverse effects caused by the inclusion of soot in fibrin gel clots was performed using concentrated soot solutions Soot G[2x] and Soot G[10x]. Little deviation was observed in the reported δ_{GP} and d_f with the inclusion of increasing soot concentrations, which was supported by the images of the mature gel structures captured using LSCM and SEM. The t_{gel} was decreased with the inclusion of soot, perhaps as an altered activation pathway of the thrombin present in the fibrin gels.

The inclusion of soot into fibrin gels does not appear to have a steric effect, with the effect on GP parameters and the mature microstructure formed being inconclusive. However, it was possible that the soot particulates could have a biochemical effect on the incipient blood clot formed due to the presence of platelets and the resulting clot microstructure. This is the focus of Chapter 5.

Chapter 5 Detection of exhaust particulate induced clotting anomalies in whole blood

5.1 Introduction

Understanding the health implications associated with inhalation of particulate matter is of upmost importance as it has been suggested that the coagulability of the blood is affected by the presence of such particulates, thus enhancing the risk of cardio-pulmonary disease. Fine particulate matter has been shown to penetrate deep into the lung where it can translocate across the gas-blood barrier into the blood stream. The translocation of particles has conventionally been thought to trigger an inflammatory response, initiate an oxidative stress mechanism, or cause increased plasma viscosity due to increased coagulation proteins present in the blood (181,226). Rheological techniques can be employed to assess the impact of particulates on the incipient gel network.

The soot particles introduced to the whole blood clots in the present study are estimated to be of a similar size to the fibrinogen monomers that form the structural scaffold of the clot. In Chapter 4, analysis of fibrin gel clots found no evidence that a steric effect was apparent in the clots formed with the inclusion of soot particles. Therefore, a study of whole blood clots with the inclusion of particulate matter was conducted to ascertain whether the presence of blood cells and platelets resulted in a biochemical response that leads to potentially dangerous alterations to the incipient clot.

The research contained within the following chapter was conducted in order to further understand the potential soot particulate induced blood clotting anomalies using rheological techniques. Previously published human and animal studies into the effects of exhaust PM on blood clot formation have suggested that platelet activation may be responsible for the increased coagulability of blood after exposure to soot particles (236,239). A rheological approach was applied in the present study of whole blood samples, with a 5% haemodilution to assess whether the presence of RBCs and platelets resulted in a biochemical effect that lead to anomalous clot formation.

The stock Soot G solution was obtained from Cardiff University, with the higher concentration soot solutions being prepared at Swansea University as discussed in Section 4.4.1. Whole blood samples were obtained from 20 eligible volunteers for

rheological assessment of clotting characteristics with the inclusion of 5% 'Soot G' solutions alongside a TBS control. Supporting SEM clot samples were prepared in an identical manner to aid the assessment of the effects of the soot particles on the clot microstructure. All rheological data was obtained using an AR-G2 CMT rheometer.

5.2 Literature Review

Until recently, the study of blood using rheological techniques was focussed on the diagnosis and monitoring of infection and disease (288) using TEG, free oscillation rheometry and oscillatory shear (74,142,153,157). However, more recent studies have developed sophisticated techniques that allow for the analysis of blood clotting anomalies such as VTE by using a novel biomarker of clot microstructure (54,74,147,289,290).

The flow of blood has been comprehensively studied (291–294). Blood flow occurs in a shear rate range of 10^0 to 10^3 s^{-1} (1) but can be disrupted by large proteins and erythrocytes (295). The flow conditions at the blood vessel wall are responsible for the speed at which the necessary factors are distributed to the injury site during blood coagulation (296). The clot sustains more permanent deformation due to blood flow if it displays a large viscous component, whereas clots with a greater elastic element return to their initial conformation if the stress is relieved (130). Barnes speculated that the permanently altered shape of some blood clots with large viscous components resulted in the thrombus being pressed against the blood vessel wall, becoming less obstructive (1).

The environment surrounding clot formation can impact on the rheological properties observed for different types of venous clot (297). The viscoelastic and mechanical properties of a mature blood clot can be used to determine the strength of the clot structure under flow conditions and the likelihood of the clot rupturing (158). This can be achieved by applying a stress and measuring the resulting strain before calculating the elastic modulus of the fibrin polymer network (126). Strong blood clots are responsible for a blockage within the blood vessel that can cause thrombosis or ischemia (298). The complex modulus observed can give an indication as to the possibility of clot rupture, resulting in an embolism (158).

Previous studies have exposed limitations in the rheometric techniques used. For example, FTMS can be used in GP identification for transient systems. Since FTMS

is based on the Boltzmann Superposition Principle, the stresses are additive meaning that the linear viscoelastic limit can be exceeded and the microstructure of the weak gelling system compromised (18).

Sensitive SAOS GP experiments can be employed to extract valuable data regarding the formation of the fibrin network within a blood clot, from viscoelastic liquid to viscoelastic solid. SAOS can be used to investigate the viscoelastic behaviour of the gelling material within the linear region without compromising the microstructure of the sample being tested (299). The frequency independent GP offers data relating to the incipient gel network which is established during coagulation, as well as the clotting time (153). The GP typically occurs quite rapidly in the polymerisation process when between 15-20 % of the fibrinogen within the sample has been incorporated into the gel structure (128,163). Once the GP has occurred, the stiffness of the clot network increases (300) as the fibrin polymers formed post-GP are integrated into the microstructure of the existing gel network (120).

A 'healthy index' was established by Evans et al (74) for characterisation of the incipient blood using rheological techniques to analyse the fractal dimension of the whole blood clot. For healthy individuals, the 'healthy' d_f value was determined to be 1.74 ± 0.07 (74). Pathologies can cause abnormality in the development of the microstructure of the whole blood clot which act as a biomarker for diagnosis and monitoring of disease. Studies conducted on patients suffering from prothrombotic disease have shown an increase in the d_f values reported in comparison to the 'healthy index' (148,149).

Research into the effects of air pollution on health have been conducted in both animal and human cohorts. A large-scale human study conducted by Baccarelli et al. concluded that proximity to major roads resulted in an approximately linear increase in the risk of thrombotic tendencies such as DVT (246). Whilst some studies have suggested elevated fibrinogen levels as a response to the presence of soot particles (173,174), others have concluded that the initiation of abnormal clots may be as a result of platelet dependent haemostasis (168,231,235–237).

It is possible for PM to enter the body through the airways and penetrate deep into the lungs (178,184). Smaller particles, with a diameter of < 2.5 μm can reach the alveoli and translocate across the gas-blood barrier into the blood stream

(179,184,185,191,199,201). Literature has shown that both long- and short-term exposure to PM increases the risk of death due to cardiovascular disease (176,185) because of increased blood coagulability as a result of inflammation of the lungs (176,216).

Platelet activation has been discussed as a possible mechanism for increased risk of thromboembolic disease. The interaction between a stimulus, such as fibrinogen and thrombin, and the surface of platelets initiate platelet activation (301). Platelets are responsible for binding to the damaged blood vessel and forming a thrombi to promote haemostasis, with activated platelets resulting in potential thrombus formation leading to thromboembolic disease (302). Initially, studies were carried out in hamsters with Nemmar et al. concluding that the thrombotic events experienced after exposure to PM was consistent with the kinetics of platelet activation (168). A further study by Lucking et al. applied similar theories to determine that the inhalation of PM was responsible for an increased risk of thrombus development in humans as a result of platelet activation (239).

5.3 Whole Blood Study Materials and Methods

5.3.1 Ethical Approval

Ethical approval (2019-002) was obtained from the College of Engineering Research Ethics Committee to cover the project entitled 'The detection of particulate matter induced blood clotting anomalies using rheometric techniques'. The Ethical Approval application can be seen in Appendix C.

The study was conducted using blood samples from healthy blood donors. Prior to the collection of blood samples, the aims of the project were explained, along with the Eligibility Guidelines for participation in the study. The risks of a blood draw were outlined by the phlebotomist prior to consent being given. Each patient was required to check their own eligibility for the study and give informed consent to participate in the rheological and SEM studies. A copy of the consent form signed by both the participant and the researcher was held within a locked cabinet with the Patient Room for the duration of the study. A further copy was given to the patient for their records.

Patient information was immediately anonymised with results being stored on a password protected computer. Personal patient information was only contained on the

consent form and each volunteer was immediately given a unique numerical code that was used for further records.

5.3.2 Materials

5.3.2.1 Blood

Blood was obtained from healthy volunteers by a trained phlebotomist in the Patient Room adjoining the Rheology Laboratory in the Centre for Nanohealth at Swansea University. The blood sample was drawn from the volunteer's median cubital vein using a 21-gauge butterfly needle (Greiner Bio-One GmbH, Austria) into two Vacuette® containers (Greiner Bio-One GmbH, Austria). The tube containing the initial 3 ml of blood was immediately discarded as increased levels of TF are present in the initial draw due to the insertion of the needle. A further 3 ml was drawn from each patient into an additive-free Vacuette® container (Greiner Bio-One GmbH, Austria). Blood samples were utilised immediately, with the appropriate volume of additive free blood being removed from the tube for testing. The majority of blood samples were required for rheological testing with only a few samples needed to prepare SEM samples of the blood clots. Any blood sample remaining after preparation was disposed of immediately using appropriate waste disposal procedures. No blood samples were stored at any point throughout the studies.

5.3.2.2 Soot Solutions

As discussed in Section 4.4.1, Soot G[1x] was further concentrated to give solutions with two and ten times the original concentration of soot particles, Soot G[2x] and Soot G[10x] respectively. Soot samples G[1x], G[2x] and G[10x] were prepared identically to the fibrin gels study, prior to the addition to blood. A small volume of required soot solution was sonicated for 15 minutes at ambient temperature to reduce aggregation of the particles. Immediately prior to the addition of the soot solution to the whole blood sample, a volume of 10x TBS was combined with the sonicated soot solution to achieve a 1x TBS-S solution compatible with the whole blood. Prepared soot samples were used without delay. Any waste containing soot solutions was disposed of using the appropriate disposal procedures.

5.3.3 Methods

5.3.3.1 Rheometry

Rheological studies were conducted using an AR-G2 CMT rheometer (TA Instruments) using TRIOS software. A standard inertia correction (SIC) procedure was carried out before each experiment as described in Section 3.4.2.1. A standard SAOS GP procedure was employed with a parallel plate geometry. It was preferable to select a parallel plate geometry over a cone and plate due to cellular matter present within the whole blood samples (69).

Blood samples were prepared with the inclusion of a range of soot particle concentrations. The soot solutions were prepared as described in Section 5.3.2.2 above. By using a range of concentrated soot samples, it was possible to assess the effect of soot on the blood clots formed without altering the blood dilution. The study was conducted using additive free whole blood to allow for the inclusion of soot solutions without exceeding the dilution threshold of 20% observed by Lawrence et al. At 20% haemodilution, a significant decrease in the reported d_f values was detected (143), therefore a dilution of 5% was employed within the present study to ensure the clot characteristics observed were not compromised by sample preparation.

The volume of soot solution required was prepared in advance of the blood draw to allow for a quick preparation and loading of the blood-soot sample onto the rheometer. Each sample was sonicated for 15 minutes before 10x TBS was combined with the soot solution to for the required volume of 1x TBS-S. To obtain an accurate t_{gel}, the required volume of whole blood was immediately added to the soot solutions before being gently combined and loaded onto the rheometer. The delay time for all experiments was recorded as < 65 ± 5 s from blood draw to commencement of the TRIOS procedure.

A volume of 122 µl of the combined blood-soot was loaded onto the rheometer Peltier plate, set to 37 °C, before the upper 60 mm aluminium parallel plate geometry was manually lowered to within a few microns of the blood-soot sample, in line with the fibrin gels procedure used. Manually performing this procedure enabled the blood sample to 'jump' to the plate therefore reducing the risk of bubbles being trapped in the sample between the plates. Once contact had been made between the sample and the upper geometry, the gap was set to 380 µm using the TRIOS software command.

The temperature of the experiments was maintained at 37°C throughout loading and testing.

An initial pre-shear was conducted for 10 s at 100 s^{-1} shear rate to prevent settling of the blood cells present before a standard SAOS GP procedure commenced. A torque of 6.0 μN.m was applied to the sample over four discrete frequencies of 2.1 Hz, 1.7 Hz, 0.9 Hz and 0.4 Hz. The third harmonic and stress/strain waveforms were monitored throughout testing to ensure the experiment was conducted under linear conditions. Each experiment ran for a duration of 1500 s to ensure sufficient data was obtained both pre- and post-GP.

Blood samples were disposed of immediately after testing using the appropriate disposal systems. The clot formed during testing was cleared from the Peltier plate. The rheometer components that were in contact with the blood were cleaned using a soap and water solution and rinsed with water prior to having 70% ethanol applied to sanitise the surfaces.

5.3.3.2 SEM Sample Preparation

SEM Samples were prepared to visually analyse the mature clot microstructure formed with the inclusion of increasing concentrations of soot particles. Whole blood from three healthy donors was combined with soot to give a 5% Soot G solution inclusion over a range of sample concentrations (G[1x], G[2x] and G[10x], along with a saline control). A volume of 200 μl of the blood-soot was immediately pipetted into a 12-well plate where the clot was left to gel to a mature clot. Clots were left for 40 x t_{gel} determined in the rheological study (approximately 3.5 hours) to ensure the gel network had reached maturity (75). The clots were further treated with glutaraldehyde, ethanol and HDMS in an identical manner to the fibrin-thrombin gel clots as outlined in Section 4.4.4 prior to imaging. The dried clots were mounted onto carbon tape on SEM compatible stubs before each sample was sputter coated with a 15 nm layer of gold-palladium to enhance the conductivity of the sample and therefore the quality of the images obtained.

Images were captured using a Hitachi S4800 Scanning Electron Microscope. The magnification was increased over each sample to give an idea of the overall network structure as well as the local microstructure. All blood clot samples were imaged immediately after sputter coating as storage was not possible due to Human Tissue Act

restrictions. The entirety of the samples was disposed of immediately following imaging through the appropriate waste disposal methods.

5.4 Results and Discussion

5.4.1 Rheometry

Blood-soot experiments were conducted as outlined in Section 5.3.3.1 using an AR-G2 CMT rheometer (TA Instruments). The data acquired was assessed using the GP Analysis Software[3] to determine the uncorrected GP before application of the ERIC correction procedure (Chapter 3). The linearity of the experiments was monitored throughout testing through analysis of the reported waveforms and the third harmonic.

An example uncorrected GP for each of the soot solutions can be seen in Figure 5-1.

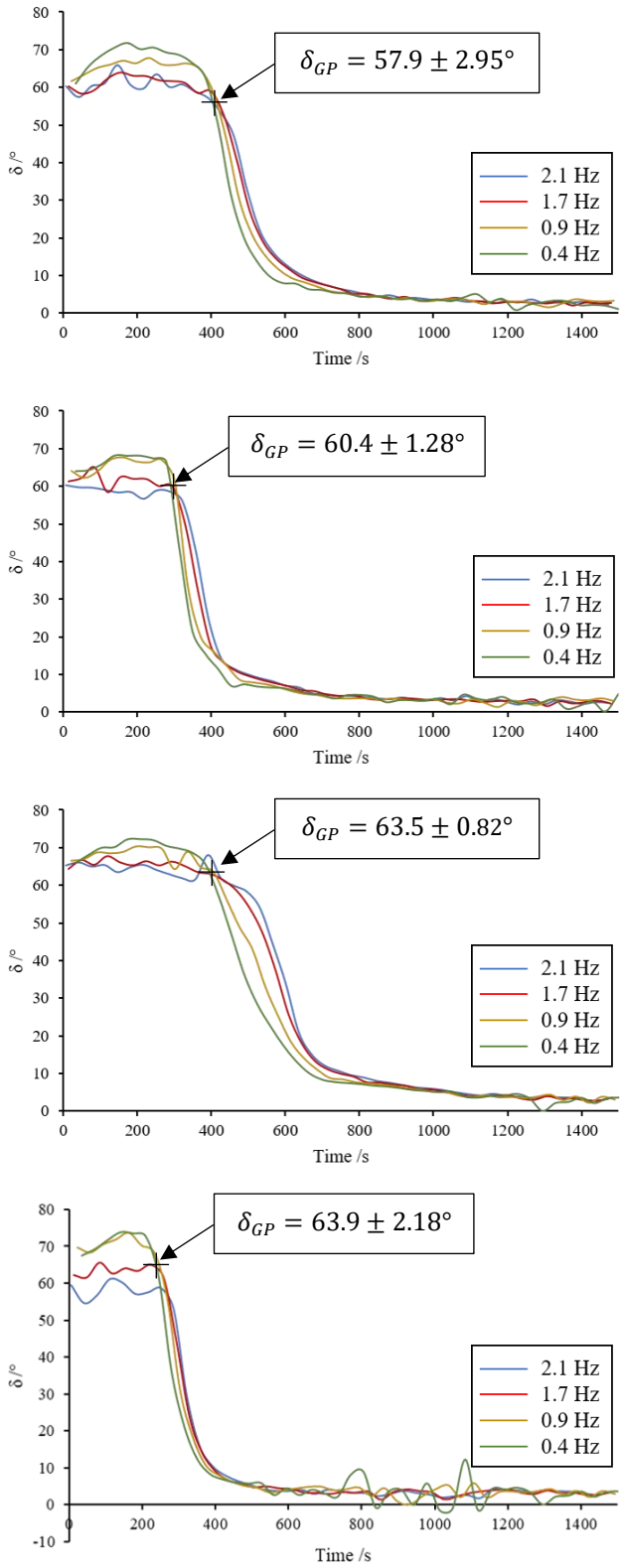

Figure 5-1 *Uncorrected GP for individual experiments at each soot concentration in whole blood. The reported phase angle at the GP for a) a TBS control experiment, b) 5% dilution with G[1x], c) 5% dilution with G[2x] and d) 5% dilution G[10x].*

The frequencies employed to ascertain the frequency independent GP were 2.1 Hz, 1.7 Hz, 0.9 Hz and 0.4 Hz, shown by the blue, red, yellow and green curves. With the inclusion of an increased number of soot particles, the total number of individual experiments required to produce valid quintuplicate data for each concentration increased. Repeating the experiments five-fold ensured that the results obtained were reproducible given the biological nature of the whole blood samples.

As the number of soot particles included within the blood clot increases, it became increasingly challenging to obtain valid GP data. The deviation between the pairs of roots became more spread out as the soot sample concentration increased, implying the reported GP data became less accurate. The increased deviation in the roots necessitated the use of the ERIC procedure to determine the corrected GP for the whole blood clots with the inclusion of soot PM.

In order to establish understanding of the characteristics of the whole blood clot, parameters ascertained at the GP were analysed. The phase angle at the GP, δ_{GP}, was monitored as the soot concentration included within the whole blood samples was increased from a TBS control to 5% Soot G[10x] solution. As the number of soot particles included in the samples was increased, the uncorrected δ_{GP} shows an increase in phase angle at the GP (Figure 5-2).

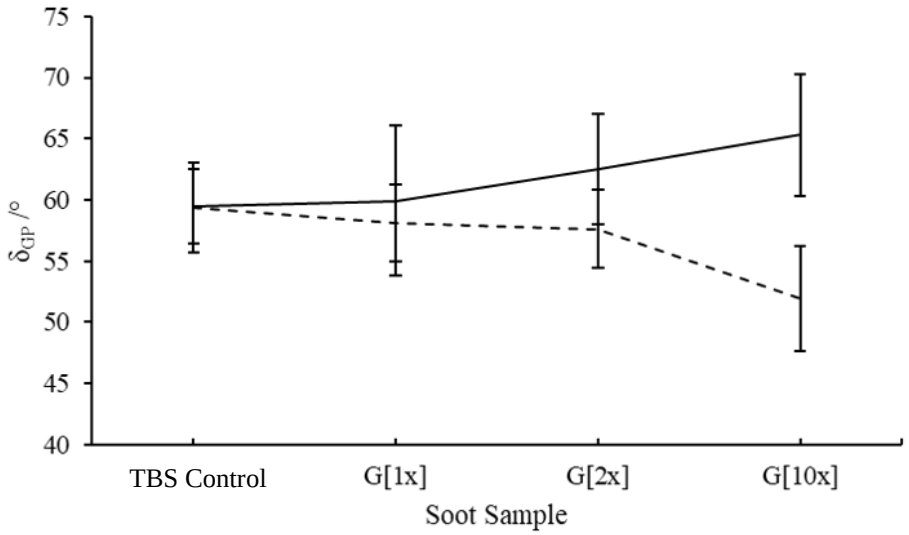

Figure 5-2 *The effect of soot particulate matter at a range of concentrations in whole blood on the phase angle at the GP. The pre-ERIC (solid line) and post-ERIC (dashed line) are shown.*

There is statistical significance reported (assuming a 10% confidence interval) for the uncorrected δ_{GP} with t-Tests reporting $p > 0.05692$ for all soot solutions in

comparison with the TBS control samples. After the application of ERIC, the corrected data appears to suggest a decrease in the δ_{GP} with increasing soot concentration. Whilst the data for Soot G[1x] and Soot G[2x] do not show a significant decrease in comparison to the saline control data, with the inclusion of Soot G[10x] a significantly lower δ_{GP} was confirmed using a t-Test ($p = 0.00243$). For Soot G[10x] samples there is a statistically significant correction in the data once the ERIC procedure is applied to the uncorrected data ($p = 0.00058$). A decrease in δ_{GP}, as seen in the ERIC corrected data, suggests that the clot formed is denser which is consistent with the potential occlusions within blood vessels observed in patients suffering from cardiopulmonary diseases.

Using Muthukumar's relationship (Equation 2.2), it is possible to determine the d_f value from the δ_{GP} for each of the soot concentrations. Without the ERIC correction, the conclusion for the uncorrected data shown in Figure 5-3 (solid line) would have been that as the soot concentration within the clot increased, the reported d_f values at the GP decreased from 1.79 ± 0.05 for the TBS control sample to 1.70 ± 0.08 for the highest soot concentration of 5% Soot G[10x].

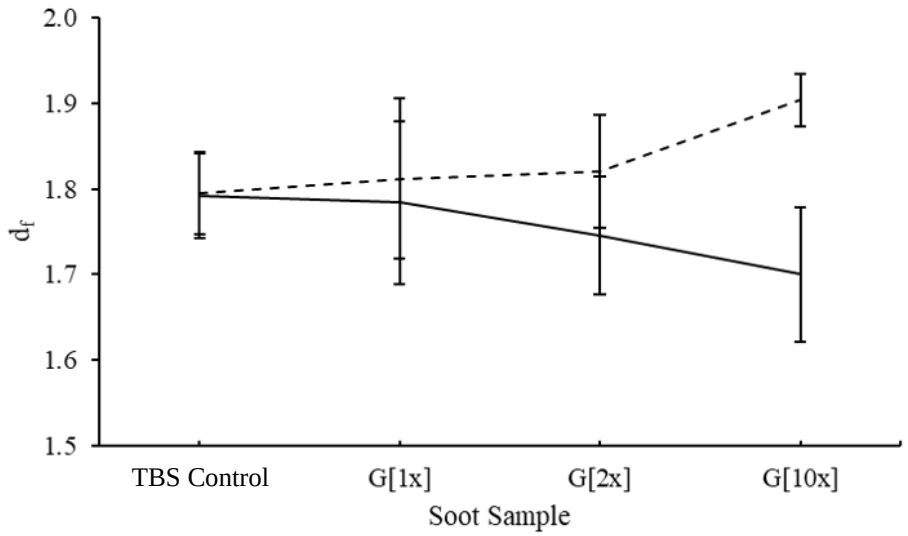

Figure 5-3 *The effect of soot particulate matter in whole blood on the reported fractal dimension, d_f. The pre-ERIC (solid line) and post-ERIC (dashed line) are shown.*

However, the δ_{raw} at the GP were reported to be $\delta_{raw} > 173.1°$ for all blood samples, suggesting a large inertial influence on the data obtained. As the δ_{raw} exceeds the limiting δ_{raw} stated by the instrument manufacturer to be 150° (9), it was necessary

to apply the ERIC procedure to the data. An example of an ERIC corrected GP with 5% inclusion of Soot G[10x] can be seen in Figure 5-4.

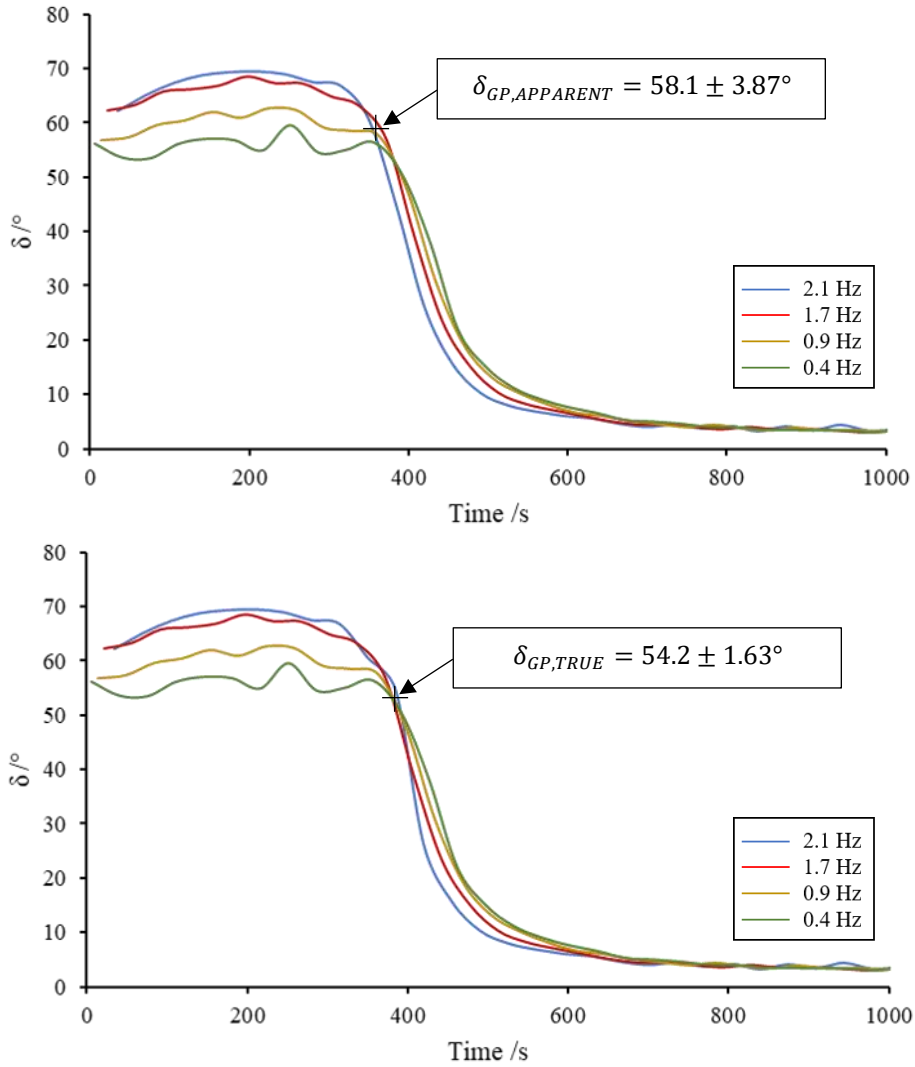

Figure 5-4 *Examples of a) an uncorrected blood GP and b) an ERIC corrected blood GP. The blood sample was prepared with the inclusion of 5% G[10x] soot solution.*

Applying the ERIC procedure to the data obtained using an AR-G2 CMT rheometer shows an increase in the corrected d_f values as the soot concentration included in the clot samples increases (Figure 5-3, dashed line). The G[10x] corrected d_f data was determined to be 1.90 ± 0.03 which is a statistically significant increase compared to the TBS control ($p = 0.00272$) and is significantly increased compared to the uncorrected G[10x] data reported as 1.70 ± 0.08 ($p = 0.00066$). The TBS control samples both record similar values to the 'healthy index' stated as 1.74 ± 0.07 (5), with increased deviation from this healthy value as the soot inclusion increases. The increase in d_f suggested by the ERIC corrected data corresponds to a denser

microstructure and stronger clot which has previously been reported in literature for the analysis of pathologies such as ischemic strokes (148), coronary artery disease (149) and lung cancer (290).

The clotting time, t_{gel}, of the whole blood samples was reported at the GP for each clot. The mean t_{gel} for each soot sample concentration are plotted in Figure 5-5.

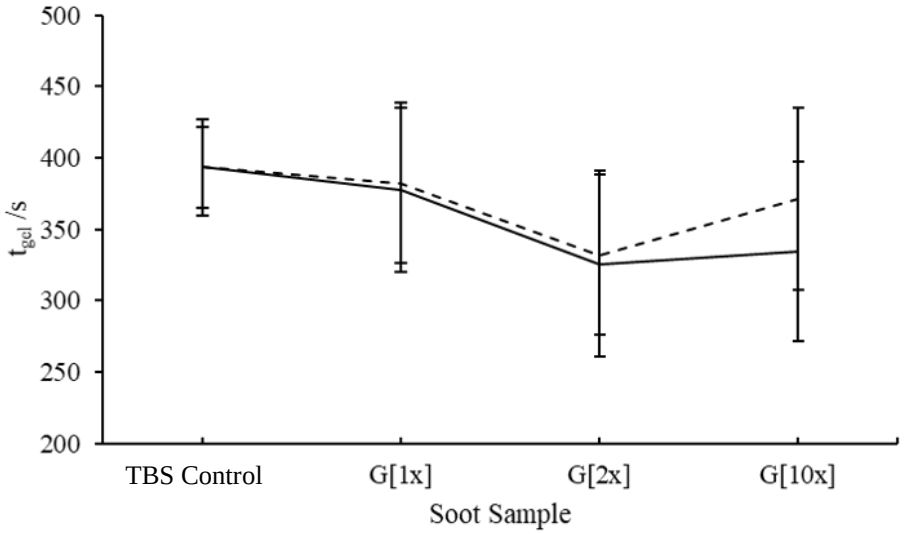

Figure 5-5 *The t_{gel} reported over a range of soot concentrations as a 5% dilution of whole blood. The pre-ERIC (solid line) and post-ERIC (dashed line) are shown.*

The inclusion of the soot particles does not appear to have a substantial impact on the reported t_{gel} at any soot particle concentration. Initially, the uncorrected data and the ERIC corrected data show correlation such that the TBS control sample is corrected from 393 ± 21 s to 393 ± 20 s after the application of the ERIC procedure. However, the reported t_{gel} values for the corrected and uncorrected data at G[10x] show the same deviation. It appears that the ERIC correction procedure has more of an influence on the reported t_{gel} at G[10x] compared to the uncorrected data, possibly due to the decrease in definition of the raw GP data recorded as the inclusion of soot particles increased. Despite the difference in the uncorrected and ERIC corrected t_{gel} values at G[10x], the correction was not statistically significant as $p = 0.3856$. With the inclusion of 5% G[10x] soot solution, the t_{gel} was corrected from 334 ± 21 s to 371 ± 42 s after ERIC correction. There is a slight decrease in the uncorrected and ERIC corrected t_{gel} data, with statistical significance reported in the p values reported

(assuming a 10% confidence interval) when comparing each soot solution with the TBS control ($p < 0.0600$) for both datasets using t-Tests.

Whilst time-only techniques such as prothrombin time give an indication of the clotting characteristics, it is necessary to employ alternative rheologically reported indicators alongside the t_{gel} of the sample in order to ascertain understanding of the effect of pathologies on the clot microstructure. Previous studies have hypothesised the use of t_{gel} as a biomarker for clotting characteristics (54,290). However, the data presented in the current study suggests that it is not possible to solely rely on the t_{gel} of the whole blood clot with the inclusion of soot to determine whether there is an increased likelihood of thrombotic tendencies. This is supported by the study conducted by Lawrence et al. which showed that t_{gel} cannot be used as an independent biomarker as there was no significant difference reported between a healthy cohort and those suffering from VTE (54).

The increase in clot density suggested by the corrected d_f appears to be as a result of platelet activation in the whole blood sample due to the inclusion of soot particles. The platelets in the whole blood sample stimulate the generation of thrombin, with the thrombin present acting as a powerful agonist in platelet activation (303). The platelet activation and aggregation in humans is as a result of coagulation factors (232). The fibrin network formed from polymerisation of fibrinogen monomers creates the structure of a blood clot and is responsible for the stability of the initial platelet plug. It has been suggested that platelets respond to the presence of PM (168,239) which results in a disrupted process for the generation of thrombin. The modified timing of the thrombin burst through the coagulation cascade results in an alternative microstructure of the clot formed. As thrombin is also responsible for the formation of the fibrin network, it is plausible that the fibrin promotes the procoagulant activity of the activated platelets (303). The enhanced disruption caused by an increase in soot PM appears to lead to a denser clot that could trigger thromboembolic events.

5.4.2 SEM Study

Whereas it was possible to employ LSCM techniques for image analysis of fibrin gels, whole blood clots could only be assessed using SEM imaging due to the presence of blood cells and platelets. To support the data obtained in the rheological blood study, SEM images were captured to visually assess the effects of soot particles in whole

blood clots. Clot samples were produced in triplicate for numerous donors with the images presented herein being from a single healthy donor for each of the figures to give a representative image of the clots observed. Due to the delicate and fragile nature of the blood clots once washed and dehydrated, it was more challenging to mount the mature clots onto the carbon tape than the equivalent fibrin gel clots. An example blood clot prior to sputter coating can be seen in Figure 5-6.

Figure 5-6 *A prepared blood clot for SEM imaging prior to sputter coating. The clots were mounted to the SEM stubs using carbon tape once the washing and drying process was completed. The blood clots were left to develop for 40x* t_{gel} *to ensure the mature microstructure was observed once dehydrated and sputter coated.*

Despite multiple attempts, it was not possible to obtain high-magnification images of the soot within whole blood clots as a result of the sample 'charging'. This resulted in blurred, low-quality images. Therefore, it was not feasible to observe the soot particles within the blood clots as a significantly high magnification could not be reached.

Representative images of the whole blood clots appear to show a progressive increase in fibre density as the soot concentration increases, as seen in Figure 5-7. Image a) was obtained as a TBS control sample, with b)-d) containing 5% G[1x], G[2x] and G[10x], respectively.

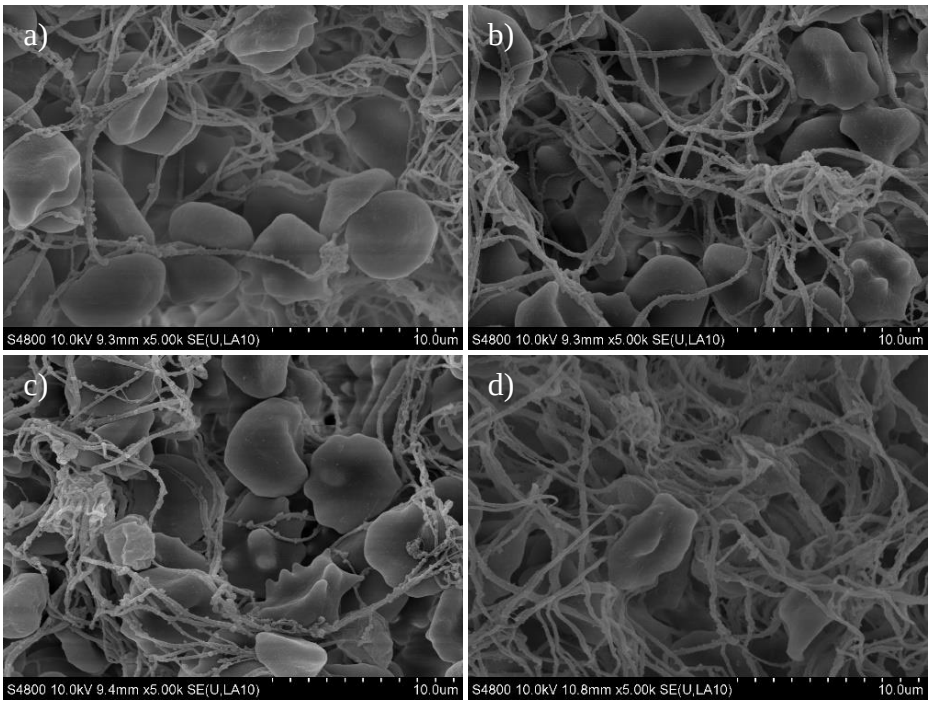

Figure 5-7 *SEM images of whole blood clots with 10% inclusion of a) TBS control, b) Soot G[1x] c) Soot G[2x] and d) Soot G[10x]. The whole blood clot sample was obtained from one patient, with each of the clots prepared from the same blood draw.*

The increase in fibre density with the increase in the number of soot particles is consistent with the ERIC corrected d_f values. At the highest soot concentration, G[10x], d_f was reported by ERIC to be 1.90 ± 0.03 which is considerably higher than the TBS control ERIC deterined d_f value of 1.79 ± 0.05. The d_f reported for blood clots with the inclusion of G[10x] is substantially higher than the 'healthy index' reported by Evans et al of 1.74 ± 0.07 (5), whereas the TBS control d_f is much closer to the 'healthy' value. This increase in fibre density and the rheologically obtained d_f has been observed in previous studies where d_f has been investigated for use as a biomarker for cardiopulmonary disease (148,149,290).

A selection of the RBCs in the samples presented in Figure 5-7 show some signs of distortion. Some genetic and pathological conditions can affect the shape of the RBCs (304), causing them to exhibit 'spiky' cell surface behaviour (305,306). The eligible volunteers assembled as part of the present study were considered healthy individuals, therefore, it is likely that the increased number of 'spiky' RBCs is as a result of increased soot particles in the higher soot concentration samples rather than genetic conditions. Pajnič et al. observed NP agglomeration between RBCs dosed with carbon

black and echinocytes were observed using SEM in samples of washed erythrocytes with the addition of ZnO nanomaterial (248), resulting in similar modifications to the cell membrane as seen in Figure 5-7 b)-d).

It is also possible for this phenomenon to be observed as a result of the SEM clot sample preparation conditions such as extracellular ionic strength and pH (307). Each SEM sample was prepared simultaneously in an identical manner, using the procedure discussed in Section 4.4.4. It is possible that the solutions used to fix and dehydrate the samples have distorted the cell membranes. However, only a small sample of the RBCs present within the saline control sample display 'spiky' characteristics with an increased number present in the clot including 5% G[10x], as observed across all blood SEM samples.

5.5 Conclusions

The results of work presented in this chapter appear to support previously published conclusions, drawn from both animal and human studies, that PM can behave as a powerful agonist in the progression of the clotting cascade. The size of the particles that can translocate across the gas-blood barrier are similar to those of the monomers that form the fibrin microstructure within the whole blood clot, causing potential disruption to the formation of the clot. The sensitive haemorheological techniques provide a platform for analysis of the formation of the structural fibrin network in the early stages of clot development. This proves advantageous compared to previous, simpler techniques that rely solely on a single parameter such as clotting time to behave as a biomarker. The concluding remarks from this chapter are summarised as follows:

1. Evaluation of PM induced blood clotting abnormalities using rheometric techniques. The present study appears to suggest that at high soot concentrations, abnormalities in clotting characteristics are detected using rheological techniques. Whilst the t_{gel} does not appear to behave as an independent biomarker, the d_f reported at the ERIC corrected GP for each of the soot concentrations appears to indicate an increase in the density of the clots formed as the soot concentration increases. The increase in clot density could elevate the risk of thromboembolic disease, such as MI, DVT and PE. The increase in microstructure density suggested by the rheological data is

supported by the SEM images obtained of the whole blood clots with the inclusion of soot solutions. The fibrin network appears to increase in density as the soot concentration increases, with an increased presence of ‘spiky’ red blood cells.

2. The biochemical effect of PM on blood coagulation. Whole blood appears to show a biochemical effect that is not observed in fibrin gels. It is likely that platelet activation is responsible for the clotting anomalies observed with the inclusion of high concentrations of soot particles in whole blood clots, which it is not possible to observe in fibrin gel clots formed of the component clotting factors, fibrinogen and thrombin. The interruption to the clotting cascade caused by the presence of soot PM within the whole blood sample results in abnormal thrombin generation which ultimately has adverse effects on the microstructure of the incipient clot. The increased density of the clot after exposure to highly concentrated soot solutions could cause potential exacerbation of thrombotic disease.

Chapter 6 Conclusions and Recommendations

The research presented in this thesis shows that rheometric techniques can be employed to detect blood clotting anomalies induced due to the inclusion of soot particulates. A biochemical effect is observed in whole blood samples that was not detected in fibrin gels, suggesting that high concentrations of soot particulates could cause platelet activation that is responsible for the clotting anomalies observed in whole blood.

Development of the Enhanced Rheometer Inertia Correction (ERIC) procedure allows the experimentalist to obtain valid GP data using a CMT rheometer at previously inaccessible frequencies. The application of the ERIC procedure post-data acquisition to CMT GPs results in agreement with GP data obtained using an SMT rheometer. The inaccurate inertia constant, I_c, reported by the instrument appears to be instrument specific and is routinely corrected by the ERIC procedure in the order of 0.1 μNms^2, which is larger than the precision reported by the instrument during repeat calibrations. Modifications to I_c reported by the rheometer through a SIC procedure were corrected using a MATLAB code to determine the true inertia constant, I_t. Exploitation of the frequency independent GP combined with I_t, made it possible to obtain valid data with enhanced accuracy and precision of the GP determined after the application of the ERIC procedure.

For weak gelling systems, the $\delta_{raw} < 150°$ limit outlined by the manufacturers for the AR series CMT rheometers used in this thesis has routinely been exceeded, indicating that inertial artefacts are dominant within the system and data may not be valid (9). Application of the ERIC procedure now allows the experimentalist to obtain valid GP data at either higher frequency decades (for rapidly gelling systems with $t_{gel} < 100s$) or lower concentration systems.

As a result, a previously undocumented concentration dependence was established over a range of gelatin concentrations between $2.5\ wt\% \leq c \leq 30\ wt\%$. The ERIC procedure was applied to the GP data obtained and agreement was shown between the corrected CMT data and GP data ascertained using an SMT rheometer. At low gelatin concentrations, a limiting phase angle of 63° was observed, which is in agreement with a stress relaxation exponent of $\alpha = 0.7$, comparable with theoretical predictions for

percolating systems. Previous studies validated the suggestion of a concentration dependence for the gelation of gelatin (7,77).

For low viscosity fibrin gels, with low fibrinogen and thrombin concentration as studied in this thesis, it was necessary to include Tween-20 surfactant into the GP in order to obtain valid GP data by reducing the surface tension of the sample. The inclusion of Tween-20 greatly improved the quality of the rheological GP data obtained without compromising the microstructure of the gel formed. As a result of the inclusion of Tween-20 into the fibrin gels, it was possible to determine the effect of thrombin and fibrinogen concentration on the incipient gel, as well as analyse any modifications to the gel formation due to the inclusion of soot particulates.

From the studies conducted, it became clear that thrombin concentration had a more dramatic effect on the gel formed than fibrinogen concentration. Thrombin concentration has a strong association with the t_{gel}, with high thrombin concentrations gelling much more rapidly and forming a denser clot than lower concentrations. A slight increase in t_{gel} was observed as fibrinogen concentration increased, suggesting a possible diffusion limitation rather than reaction limitation to describe the kinetics of the gelation process. Application of ERIC to fibrin gels allowed for direct comparison with SMT data previously reported (144). In order to assess the effects of the inclusion of soot particulates into fibrin gels, fixed fibrinogen and thrombin concentrations were employed of 6 mg ml^{-1} and 0.08 NIH ml^{-1} respectively.

Initially, low concentrations of soot particulates (<5% Soot G[1x]) were included within the fibrin gels with the resulting GP data returning inconclusive. As a result, the Soot G[1x] solution was further concentrated to give a two- and ten-times concentration (Soot G[2x] and Soot G[10x], respectively) to increase the number of particles present within the fibrin gel without increasing the dilution. The application of the ERIC procedure to the fibrin gels with the inclusion of soot particulates allowed for any modifications to the GP data reported to be because of the presence of PM and not due to inertial artefacts. The reported δ_{GP} and d_f at high soot concentrations showed little deviation as the number of particles increased. However, the t_{gel} decreased as the soot concentration within the fibrin gel increased suggesting a possible altered activation pathway of thrombin present in the gel samples. There is no

suggestion of a steric effect with the inclusion of soot particulates into fibrin gels as much of the data obtained was inconclusive.

Finally, the soot particulates were included within additive-free whole blood samples. Whole blood samples were drawn from healthy volunteers by a trained phlebotomist. As with the fibrin gels, the application of ERIC to blood GP data obtained allowed for any potential adverse alterations to the coagulation characteristics to be analysed without inertial artefacts dominating the data.

Using rheometric techniques, it was possible to demonstrate potentially harmful alterations to clotting responses in whole blood samples due to the presence of soot particulate matter. As the concentration of soot particulates increased in the clot samples, the resulting GP data appears to suggest that both the microstructure and the clotting time is affected. The t_{gel} parameter does not appear to behave as an independent biomarker for modified clotting response. However, the ERIC corrected GP d_f data appears to suggest an increase in the clot density as the soot concentration within the clot increases. Elevated d_f values have been associated with increased risk of thromboembolic disease, such as MI, DVT and PE. The presence of soot PM within the whole blood clot could cause a disturbance in the clotting cascade, resulting in abnormal thrombin generation and potentially adverse effects on the clotting characteristics of the sample.

6.1 Recommendation for future work

In order to gain a clearer understanding of the effects of fibrinogen concentration on the GP, further rheometric studies are required using both CMT and SMT rheometers. From the CMT data, it is clear that there is little deviation in d_f values reported at the GP, yet the SMT data appears to show an increase in d_f as fibrinogen concentration increases. The size of the standard deviations reported at each fibrinogen concentration for the CMT rheometer is much greater than those reported by the SMT data. As a result, a further SMT study with a wider range of fibrinogen and thrombin concentrations would give a clearer conclusion on the effects of fibrinogen and thrombin concentration on the incipient clot microstructure. Furthermore, employing an SMT rheometer to study the effects of soot particles on fibrin clot formation should be considered as the instrument appears to allow more accurate GP data to be obtained.

The research within this study was conducted using a model soot solution produced by Cardiff University using a generator to simulate the resultant soot particulate matter from incomplete combustion. Employing well characterised nanoparticles, such as carbon black, alongside the unique soot solutions would give a greater understanding of the potential adverse effects of particulate matter on blood clotting. Furthermore, clotting anomalies have been observed in humans and animals using alternative techniques, so it would be advantageous to apply rheometric techniques to samples of soot produced by combustion engines to ascertain sensitive information on the potential pernicious effects caused by the presence of particulate matter in whole blood.

Due to time constraints, it was not possible to undertake a whole blood study over a broader range of soot concentrations. From the data obtained, it is clear that there is a critical soot concentration at which anomalous clotting responses are observed using rheological techniques with the precise concentration yet to be determined. This could be rectified by carrying out experiments at soot concentrations between G[2x] and G[10x] to determine at which point there is a critical effect on the clotting.

Further analysis of platelet activation throughout the clotting process would allow for a better understanding of the kinetics of the coagulation cascade. This could be achieved by running a study using a platelet analyser alongside the rheological study. It was not possible to achieve this during the given timeframe due to equipment training requirements and the increased number of donors required to complete a further study.

7. Appendices

A. Published work

1. Hudson RE, Holder AJ, Hawkins KM, Williams PR, Curtis DJ. An enhanced rheometer inertia correction procedure (ERIC) for the study of gelling systems using combined motor-transducer rheometers. Phys Fluids. 2017;29(12).

PHYSICS OF FLUIDS 29, 121602 (2017)

An enhanced rheometer inertia correction procedure (*ERIC*) for the study of gelling systems using combined motor-transducer rheometers

R. E. Hudson,[1,2] A. J. Holder,[1] K. M. Hawkins,[3] P. R. Williams,[1] and D. J. Curtis[1,a)]
[1]*Complex Fluids Research Group, College of Engineering, Swansea University, Swansea, United Kingdom*
[2]*College of Science, Swansea University, Swansea, United Kingdom*
[3]*Medical School, Swansea University, Swansea, United Kingdom*

(Received 28 June 2017; accepted 23 August 2017; published online 18 September 2017)

The rheological characterisation of viscoelastic materials undergoing a sol-gel transition at the Gel Point (GP) has important applications in a wide range of industrial, biological, and clinical environments and can provide information regarding both kinetic and microstructural aspects of gelation. The most rigorous basis for identifying the GP involves exploiting the frequency dependence of the real and imaginary parts of the complex shear modulus of the critical gel (the system at the GP) measured under small amplitude oscillatory shear conditions. This approach to GP identification requires that rheological data be obtained over a range of oscillatory shear frequencies. Such measurements are limited by sample mutation considerations (at low frequencies) and, when experiments are conducted using combined motor-transducer (CMT) rheometers, by instrument inertia considerations (at high frequencies). Together, sample mutation and inertia induced artefacts can lead to significant errors in the determination of the GP. Overcoming such artefacts is important, however, as the extension of the range of frequencies available to the experimentalist promises both more accurate GP determination and the ability to study rapidly gelling samples. Herein, we exploit the frequency independent viscoelastic properties of the critical gel to develop and evaluate an enhanced rheometer inertia correction procedure. The procedure allows acquisition of valid GP data at previously inaccessible frequencies (using CMT rheometers) and is applied in a study of the concentration dependence of bovine gelatin gelation GP parameters. A previously unreported concentration dependence of the stress relaxation exponent (α) for critical gelatin gels has been identified, which approaches a limiting value ($\alpha = 0.7$) at low gelatin concentrations, this being in agreement with previous studies and theoretical predictions for percolating systems at the GP. [http://dx.doi.org/10.1063/1.4993308]

I. INTRODUCTION

Inertial effects can dominate rheological measurements performed by combined motor-transducer (CMT) rheometers (also known as controlled stress rheometers) on low viscosity systems or samples with weak gel network structures (Krieger, 1990), such effects being most severe at high frequencies (Klemuk and Titze, 2009; Krieger, 1990; Läuger and Stettin, 2016; and Walters, 1975). The design of CMT rheometers requires the torque developed by the instrument to both deform the sample under investigation and accelerate the moving components of the rheometer. Standard practice requires that the instrument is calibrated without the sample present in order to determine the inertial characteristics of the rheometer-geometry assembly and to allow subsequent correction of the raw data. Separate motor-transducer (SMT) rheometers (also known as controlled strain) are not susceptible to instrument inertia artefacts since the torque sensing element remains static during data acquisition (Franck, 2003).

An inertia correction is routinely applied to raw storage modulus data (G'_{raw}) by the software controlling CMT rheometers such that

$$G' = G'_{raw} - I_c\omega^2 k_g, \tag{1}$$

where G' denotes the apparent storage modulus of the material, I_c denotes a calibrated inertia constant, ω denotes the angular frequency, and k_g denotes a geometry factor (Franck, 2005). However, the inertia constant can only be determined to finite precision and there will always be some uncertainty regarding the accuracy of G' extracted from the raw waveforms where the magnitude of the term $I_c\omega^2 k_g$ may represent a dominant part of G'_{raw} (Ewoldt *et al.*, 2015). Further, a momentum balance can be used to show that the inertial term has no imaginary component (Klemuk and Titze, 2009), and hence the loss modulus, G'', is unaffected by the presence of instrument inertia (Franck, 2005). The raw phase angle, δ_{raw}, measured by the instrument is often used as a measure of the extent to which the inertial artefacts pollute the raw data. Instrument manufacturers recommend caution where δ_{raw} exceeds a stated value that is dependent on the rheometer model, e.g., the TA Instruments

a)Author to whom correspondence should be addressed: d.j.curtis@swansea.ac.uk

AR-2000ex model has a limiting raw phase angle of 150° (TA Instruments, 2016).

Motivated by a significant discrepancy between gel point (GP) data obtained using CMT and SMT rheometers ($\delta_{GP} = 72.8° \pm 6.9°$ and $62.7° \pm 1.0°$, respectively, for low concentration gelatin samples, see Sec. IV), we exploit the characteristic rheological behaviour of the critical gel (i.e., frequency independent phase angle, δ) (Chambon and Winter, 1987) to develop an Enhanced Rheometer Inertia Correction (ERIC) procedure. The ERIC procedure can be used to correct GP data in the post-acquisition phase. In the present work, the ERIC procedure was used in a study of the concentration dependence of the stress relaxation properties of bovine gelatin at the GP.

Characterisation of the sol-gel transition, which occurs at the GP of a material undergoing gelation, can provide information concerning the evolving microstructural properties of the material under investigation (Curtis *et al.*, 2011 and Lawrence *et al.*, 2015). At the GP the storage and loss moduli scale as identical power laws in frequency ($G' \sim G'' \sim \omega^{\alpha}$) (Chambon *et al.*, 1986) with the parameter α ($0 < \alpha < 1$), termed the stress relaxation exponent, which is sensitive to the microstructure of the sample spanning incipient gel network that forms at the GP. The measurement of α is often challenging and is limited by sample mutation (Mours and Winter, 1994) and, as demonstrated in the present work, instrument inertia artefacts (when using CMT rheometers). Examples of the utility of GP data are widespread in terms of physical and chemical gels (Djabourov *et al.*, 1988a; Hawkins *et al.*, 2008; Hsu and Jamieson, 1993; Djabourov *et al.*, 1988b; and Michon *et al.*, 1993). Recently, GP characterisation of coagulating blood has been shown to provide a novel biomarker for healthy coagulation (Evans *et al.*, 2010) and a predictor of clot microstructure (Curtis *et al.*, 2013).

Gelatin is a common biopolymer derived from the hydrolysis of collagen. Whilst at temperatures above the maximum gelation temperature (~33.6 °C) (Tosh and Marangoni, 2004), gelatin displays near Newtonian rheological properties, upon cooling, a thermoreversible gelation process occurs to form a physically crosslinked biopolymer network (Boedtker and Doty, 1954; Tosh and Marangoni, 2004; and Wolf and Keller, 1996). The thermoreversible nature of gelatin gelation makes the system an ideal test material for studies involving the validation of novel rheometric approaches (Curtis *et al.*, 2015a; Curtis *et al.*, 2015b; and Hawkins *et al.*, 2008).

II. MATERIALS AND METHODS

A. Gelatin preparation

Appropriate quantities of gelatin powder (Fisher G/0150/53) and type I deionised water were combined and shaken vigorously for 5 min before being placed in a 60 °C water bath for 45 min to ensure complete dissolution. The solutions were agitated for 1 min every 10 min and retained at 60 °C for no longer than 45 min to prevent degradation. Aliquots of each concentration (2.5 wt. % $\leq c \leq$ 30 wt. %) of gelatin were stored in a refrigerator (4 °C) and melted at 60 °C for 45 min prior to being loaded to the rheometer.

B. Rheometry

1. CMT rheometers

Rheological measurements were conducted using a 60 mm acrylic plate geometry fitted to a TA Instruments AR-2000ex rheometer or a 60 mm aluminium plate geometry fitted to a TA Instruments AR-G2 rheometer; both systems used Peltier plate temperature control. Gelatin samples were loaded onto the rheometer at 34 °C before the upper geometry was lowered into place and the test commenced at which point the temperature was quenched to the test temperature. To satisfy the gap loading condition (Schrag, 1977), which ensures that the velocity gradient across the geometry gap is uniform thus confirming negligible sample inertia effects, a shearing gap of 150 μm was used. Inertia correction studies were completed using 2.5 wt. % gelatin. A sequence of gel point experiments was performed with each experiment covering a decade of frequency, the highest frequency being systematically increased from 1 Hz to 12 Hz (with the corresponding lowest frequencies being 0.1 Hz–1.2 Hz, respectively). All tests were performed at 19 °C such that gelation occurred over approximately 900 s to minimise sample mutation effects at the GP (Mours and Winter, 1994). The mutation number is calculated for the lowest frequency using $N_{mu} = \frac{\Delta t}{G'} \frac{dG'}{dt}$ (Mours and Winter, 1994), where Δt denotes the data point acquisition time. Under the conditions presented above, a typical mutation number would be 0.062.

Concentration dependence of gelatin gelation was studied using the AR-2000ex rheometer fitted with a 60 mm acrylic plate geometry. A frequency range of 0.3–3.0 Hz was used for all experiments. Since the gel time of gelatin is strongly dependent on both concentration and gelation temperature, it was infeasible to maintain a constant temperature for this set of experiments. Hence, the temperature was varied from 19 °C (for 2.5 wt. % Gelatin) to 32.5 °C (for 30 wt. % Gelatin). No temperature dependence of the stress relaxation characteristics of the gels was observed in preliminary tests, in agreement with the literature data (Hawkins *et al.*, 2008). Sample mutation was assessed and data omitted where the mutation number was found to exceed 0.15 (Mours and Winter, 1994). Furthermore, for all experiments linear viscoelastic measurements were confirmed by ensuring that the magnitude of the third harmonic of the displacement signal remained insignificant at the gel point (Hawkins *et al.*, 2010). A thin layer of low viscosity silicone oil (9.8 mPas, Brookfield) was applied to the free surface of the sample to prevent evaporation during the experiment.

2. SMT rheometer

A TA Instruments ARES-G2 rheometer fitted with a 40 mm parallel plate geometry (and Peltier plate temperature control accessory) was loaded with an appropriate volume of 2.5 wt. % gelatin. During loading, the Peltier plate temperature was set to 30 °C. As for the CMT rheometer studies, a gap of 150 μm was employed to ensure the gap loading assumption was valid. A pre-shear of 100 s^{-1} for 10 s was applied to ensure symmetrical loading before multiple consecutive frequency sweeps were performed (0.9–3.5 Hz) at 20 °C. The transient nature of the gelation process requires that the strain amplitude

decreases throughout the experiment to (i) achieve a resolvable torque signal at all stages of gelation and (ii) maintain linear viscoelastic measurements. Hence, the strain amplitude was decreased by 25% (from an initial value of 100%) where the torque exceeded 3 μNm, harmonic analysis of the signals at the GP revealed no higher harmonic contribution to the stress waveform confirming linear conditions (Hawkins *et al.*, 2010).

C. Enhanced rheometer inertia correction (ERIC)

Following Eq. (1), the value of G' reported by the instrument is dependent on the both the true value of the storage modulus, G'_t, and the calibrated inertia constant, I_c. The value of the latter is routinely determined during preparation of the instrument but the finite precision and accuracy of this calibration can cause the true inertia constant, which characterises the instrument-geometry assembly (I_t), to differ from the calibrated Inertia Constant (I_c) by a small deviation of ΔI. Hence it can be written from Eq. (1) that

$$G'_t(\omega) = G'(\omega) + (I_t - I_c)\,\omega^2 k_g = G'(\omega) + \Delta I \omega^2 k_g. \quad (2)$$

A MATLAB routine was used to incrementally change the value of ΔI in Eq. (2) whilst monitoring the standard deviation of the roots of the gel point data (Evans *et al.*, 2010). A root can be defined as the time and phase angle of the intersection between each pair of frequencies [see Fig. 1(a)] with the deviation in the positions of the roots providing a measure of the accuracy of the GP data. The procedure was coded as a MATLAB (The MathWorks, Inc., 2016a). GUI (ERIC) and is freely available from the corresponding author. Briefly, the procedure involved fitting a 5 parameter logistic equation to the $\delta(t)$ data for each frequency and determining the location of the intersection between each pair of fitted curves (i.e., each root), the apparent GP was then defined at the mean phase angle and mean time of all roots. The standard deviation (with respect to time) of the roots was taken as a measure of the accuracy of the GP. The procedure was repeated for $-0.2\ \mu\text{Nms} \le \Delta I \le 0.2\ \mu\text{Nms}$ with the true GP being identified where varying ΔI caused a minimum in the standard deviation of the GP roots.

The ω^2 dependence of the inertia correction [Eq. (2)] prevents the ERIC procedure from generating an erroneous pseudo-GP if the material does not display this phenomenon. This can be demonstrated by assuming hypothetical (and valid) non-GP data in which G' and G'' display separate power law dependencies on angular frequency such that

$$G' = k_1\omega^{\alpha}, \quad G'' = k_2\omega^{\beta}, \quad (\alpha \neq \beta).$$

From Eq. (2) a corrected value of G' would be expressed as

$$G'_c = k_1\omega^{\alpha} + \Delta I \cdot K_g \cdot \omega^2.$$

A pseudo-GP would require frequency independent $\tan\delta$, i.e.,

$$\frac{G''(\omega)}{G'_c(\omega)} = \frac{k_2\omega^{\beta}}{k_1\omega^{\alpha} + \Delta I \cdot k_g \cdot \omega^2} = c,$$

where "c" is a constant. Rearranging for $\Delta I \cdot k_g$ gives

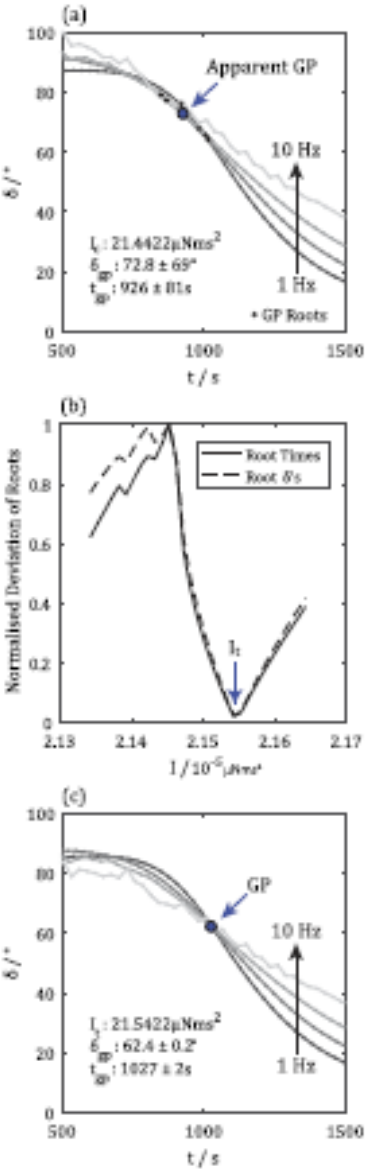

FIG. 1. (a) An apparent gel point (1.0–10 Hz) before correction showing the large deviation in the "roots" position and resultant difficulty in defining the GP as a consequence of inertia induced artefacts (*lines refer to data recorded at different frequencies*); (b) optimisation data for determination of I_t; and (c) a corrected gel point with converged roots.

$$\Delta I \cdot k_g = \frac{k_2}{c}\omega^{(\beta-2)} + k_1\omega^{(\alpha-2)},$$

and since ΔI and k_g are, by definition, independent of frequency, pseudo-GP data can only exist where $\alpha = \beta = 2$ or $k_1 = k_2 = 0$, neither of which are viable GP conditions [since at a GP $0 < (\alpha = \beta) < 1$, and both G' and G'' must be non-zero], hence the ERIC procedure cannot generate a GP if one does not exist.

III. RESULTS AND DISCUSSION

Figure 1(a) shows typical uncorrected GP data (acquired over a frequency range of 1.0 Hz–10 Hz) as reported by the instrument with an apparent GP at 72.8° ± 6.9°. This value is

significantly above the value of 62.7° ± 1.0° obtained using an SMT rheometer (ARES-G2 in the present study) and displays a high degree of uncertainty reflective of the large deviation of the positions of the GP roots. The deviation in the root positions (±6.9°) should alert the experimentalist to inadequacies in the GP acquisition procedure, which may be caused by several experimental issues, for example; sample mutation (Hawkins *et al.*, 2010 and Mours and Winter, 1994); sample inertia (Schrag, 1977); evaporation of the sample (Hellström *et al.*, 2015); under/over/asymmetric loading (Ewoldt *et al.*, 2015) or instrument inertia. In the present study, the effect of inaccurate instrument inertia calibration has been isolated by careful experimental design and data verification (see Sec. II). The corrected instrument inertia constant (I_i) was determined using ERIC; Fig. 1(b) shows the deviation in the root positions for a range of I_i with the "optimum" value being determined as 21.5422 μNm^2 (this representing a 0.46% change from the calibrated value). Figure 1(c) shows the "corrected" GP data (after application of the ERIC routine) with an apparent GP at 62.4° ± 0.2° in excellent agreement with the SMT rheometer results.

Figure 2 shows both uncorrected (circles) and corrected (squares) GP data for gelatin acquired over increasing frequency intervals (with the minimum frequency being a decade lower than the maximum frequency reported on the abscissa). It can clearly be seen that increasing the frequency window over which the data are acquired drives the uncorrected data to higher values of the δ at the GP with increasing deviation in the root positions (leading to less precise GP determination). However, appropriate correction of the data (using ERIC) allows both accurate and precise GP determination over the entire range of frequency windows studied herein. The result has important applications in the analysis of rapidly evolving strain sensitive gelling systems for which the use of techniques such as Fourier transform mechanical spectroscopy has been shown to be inappropriate (Hawkins *et al.*, 2008).

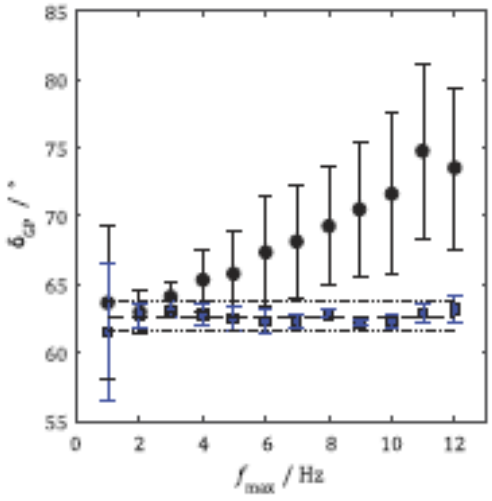

FIG. 2. Phase angle of the raw GP data (circles) collected over a range of frequencies, along with the corrected GPs for the same data sets (squares). The corrected data are shown to be back within the acceptable limit for the concentration of gelatin. In order to reflect the uncertainties associated with the measurements, error bars reflect the larger of either (i) the standard deviation between repeats or (ii) the deviation of the root positions.

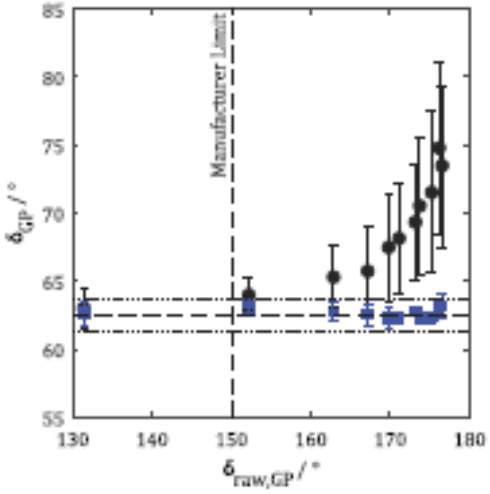

FIG. 3. Apparent (black circles) and corrected (blue squares) GP data as a function of δ_{raw} at the apparent GP (highest frequency). Horizontal lines show the SMT rheometer mean (dashed) and standard deviation (dotted). The vertical line shows the manufacturer's stated limiting δ_{raw} (TA Instruments, 2016). In order to reflect the uncertainties associated with the measurements, error bars reflect the larger of either (i) the standard deviation between repeats or (ii) the deviation of the root positions.

It should be noted that the dramatic improvement in both the precision and accuracy of the GP data has been achieved by an average 0.46% change in the calibrated inertia constant, whilst repeated calibration of the instrument inertia was found to generate a 0.15% deviation in this value. Hence, some systematic error in the calibrated inertia constant appears to exist for the AR-2000ex used in the present study, which limits the validity of data where the raw phase angle is in excess of 150° (see Fig. 3), thus preventing comparison of rheometric data obtained using other rheometers. This is in agreement with the manufacturer's stated limitation of the AR-2000ex instrument (TA Instruments, 2016).

To test the hypothesis that the ERIC procedure could be applied to correct this systematic error, thus allowing valid data to be acquired at high raw phase angles, two TA Instruments AR-G2 rheometers were used to determine the apparent GP using a frequency range of 1–10 Hz, both rheometers had undergone manufacturer servicing and calibration within a period of 12 months prior to the present study. Using standard instrument inertia calibrations, a significant difference between the data obtained using the two instruments was apparent (AR-G2 I: 61.5° ± 2.0°/AR-G2 II: 69.0° ± 4.4°-see Fig. 4). The ERIC procedure was then performed on all data obtained using these two instruments, and a Student t-test ($n = 8$) was used to compare the distribution of δ_{GP} obtained using standard inertia calibration (SIC) procedures and ERIC. No significant difference was observed between the distributions of δ_{GP} using SIC and ERIC for AR-G2 I ($p = 0.39$) indicating that the standard procedure was sufficiently accurate for this rheometer. However, for AR-G2 II, a significant difference ($p = 0.003$) was found between the distributions indicating that the accuracy of the SIC protocols appears to be instrument-specific. Following the application of the ERIC procedures, no significant difference was observed between the data acquired using the two AR-G2 instruments ($p = 0.16$).

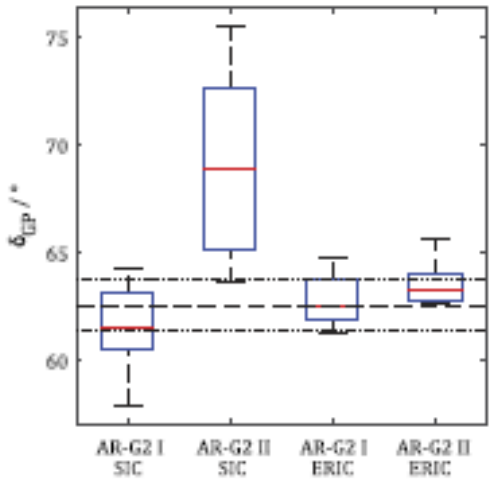

FIG. 4. Comparison of gel point results from two AR-G2 rheometers using standard inertia calibration (SIC) and ERIC. A significant difference between the rheometers is apparent using the SIC ($p = 0.0004$), whilst no significant difference is apparent after the application of the ERIC routine ($p = 0.16$). Horizontal lines show the mean and standard deviation of data acquired using the SMT rheometer.

In the present study, the concentration dependence of gelatin gelation has been studied (see Fig. 5) using a CMT rheometer with data processing using both the SIC and ERIC procedures, the use of ERIC allowing the concentration range to be extended as low as 2.5 wt. %. Figure 5(a) shows the data obtained in the present study (and corrected using the SIC procedure) with the literature data from both Hawkins *et al.* (2008) and Curtis *et al.* (2015a; 2015b). Both studies show excellent agreement with the present data despite the fact that the studies have been using differing techniques. In the latter study, Curtis *et al.* used an SMT rheometer to study gelatin at 30 wt. % using multi-frequency rheometric techniques that allowed data to be accessed up to 10 Hz. Good agreement between the present data and the data of Curtis *et al.* should be expected given the high concentration of gelatin. This causes the torque generated by the (significantly more viscous) material to dominate the measurement thus reducing the raw phase angle (in the present CMT data) to within acceptable limits. Hawkins *et al.* employed Fourier Transform Mechanical Spectroscopy (FTMS) (implemented using a CMT rheometer) to obtain data. Their data agree with that presented herein at low concentrations and is likely to suffer from the same instrument inertia artefacts as described above, leading to the aforementioned discrepancy between data obtained using SMT and CMT rheometers.

Post-acquisition application of the ERIC procedure has allowed the data presented in Fig. 5(a) to be corrected to account for the inaccuracy in the inertia constant [as shown in Fig. 5(b)]. Agreement between the SMT and CMT rheometers is then recovered (CMT: 63.1° ± 0.6°/SMT: 62.7° ± 1.0°) confirming the validity of the ERIC procedure. Further, the corrected data appear to show that a maximum phase of angle of 63° is approached as gelatin concentration is decreased. This limiting value corresponds to a limiting stress relaxation exponent ($\alpha = \delta/90$) commensurate with theoretical predictions for percolating systems ($\alpha = 0.7$) (Adam *et al.*, 1981; Martin *et al.*, 1988; and de Gennes, 1979) and experimental observations of other biopolymer systems (Audebrand *et al.*, 2003; Axelos and Kolb, 1990; Werner *et al.*, 2006; and Yu *et al.*, 1997).

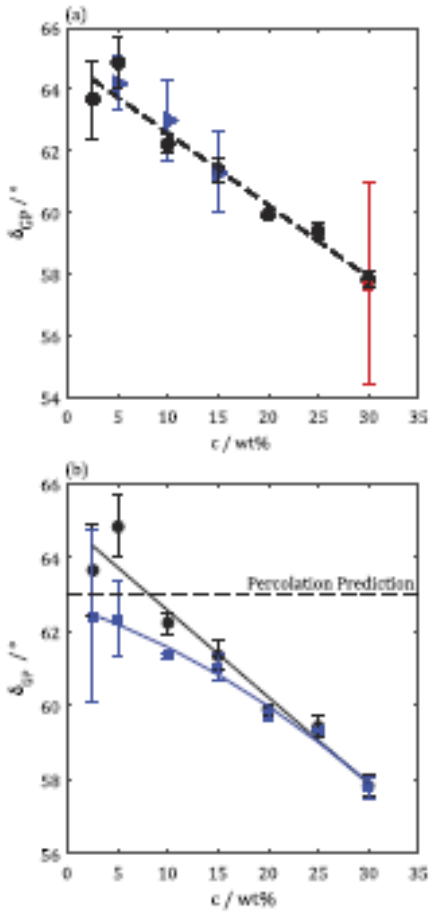

FIG. 5. Concentration dependence of δ_{GP}. (a) shows data from the present study (0.3–3 Hz, black circles) using standard instrument correction procedures, Hawkins *et al.* (0.2–3.2 Hz, SAOS and Fourier Transform Mechanical Spectroscopy, blue triangles) (Hawkins *et al.*, 2008) and Curtis *et al.* (0.1–10 Hz, Optimal Fourier Rheometry and Fourier transform mechanical spectroscopy, red squares) (Curtis *et al.*, 2015a; 2015b). Excellent agreement between these CMT rheometer based studies is observed, but a clear discrepancy is also evident at 2.5 wt. % with data obtained using a SMT rheometer (62.7° ± 1.0°), herein. (b) shows the effect of applying the ERIC procedure to data from the present study (standard inertia correction—black circles, ERIC—blue squares) along with the percolation theory prediction of the value of δ_{GP}.

IV. CONCLUSIONS

The ERIC inertia correction procedure reported herein offers the experimentalist enhanced precision and accuracy of GP measurements and has facilitated the acquisition of valid GP data at previously inaccessible frequencies (where instrument inertia effects dominate the measurement). The typical modification to the inertia constant (of the order 0.1 μNms^2) is larger than the precision of the inertia constant as determined through repeated calibrations. This suggests that there may be an underlying inaccuracy associated with this form of instrument calibration procedure and that application of the

ERIC procedure may provide a basis for identifying discrepancies between results obtained on different CMT instruments. A previously unreported concentration dependence of the stress relaxation exponent for critical gelation gels has been reported with a limiting value δ_{GP} of 63° (corresponding to $\alpha = 0.7$) being identified at low gelatin concentrations.

ACKNOWLEDGMENTS

This work was supported by the National Research Network (NRN) Wales and EPSRC Grant Nos. EP/K03099X/1 and EP/L024799/1.

Adam, M., Delsanti, M., Durand, D., Hild, G., and Munch, J. P., "Mechanical properties near gelation threshold, comparison with classical and 3d percolation theories," Pure Appl. Chem. **53**(8), 1489–1494 (1981).

Audebrand, M., Garnier, C., Kolb, M., and Axelos, M. A. V., "Gelation of pectin-alginate mixture: Ultrastructure and rheological properties," in *3rd International Symposium on Food Rheology and Structure* (ETH Zurich, 2003), pp. 517–518.

Axelos, M. A. and Kolb, M., "Crosslinked biopolymers: Experimental evidence for scalar percolation theory," Phys. Rev. Lett. **64**(12), 1457–1460 (1990).

Boedtker, H. and Doty, P., "A study of gelatin molecules, aggregates, and gels," J. Phys. Chem. **58**, 968–983 (1954).

Chambon, F., Petrovic, Z. S., Macknight, W. J., and Winter, H. H., "Rheology of model polyurethanes at the gel point," Macromolecules **19**(8), 2146–2149 (1986).

Chambon, F. and Winter, H. H., "Linear viscoelasticity at the gel point of a crosslinking PDMS with imbalanced stoichiometry," J. Rheol. **31**(8), 683–697 (1987).

Curtis, D. J., Brown, M. R., Hawkins, K., Evans, P. A., Lawrence, M. J., Rees, P., and Williams, P. R., "Rheometrical and molecular dynamics simulation studies of incipient clot formation in fibrin-thrombin gels: An activation limited aggregation approach," J. Non-Newtonian Fluid Mech. **166**(16), 932–938 (2011).

Curtis, D. J., Williams, P. R., Badiei, N., Campbell, A. I., Hawkins, K., Evans, P. A., and Brown, M. R., "A study of microstructural templating in fibrin–thrombin gel networks by spectral and viscoelastic analysis," Soft Matter **9**(19), 4883 (2013).

Curtis, D. J., Badiei, N., Holder, A., Claypole, J., Deganello, D., Brown, M. R., Lawrence, M. J., Evans, P. A., Williams, P. R., and Hawkins, K., "Assessment of the stress relaxation characteristics of critical gels formed under unidirectional shear flow by controlled stress parallel superposition rheometry," J. Non-Newtonian Fluid Mech. **222**, 227–233 (2015a).

Curtis, D. J., Holder, A., Badiei, N., Claypole, J., Walters, M., Thomas, B., Barrow, M., Deganello, D., Brown, M. R., Williams, P. R., and Hawkins, K., "Validation of optimal Fourier rheometry for rapidly gelling materials and its application in the study of collagen gelation," J. Non-Newtonian Fluid Mech. **222**, 253–259 (2015b).

de Gennes, P.-G., *Scaling Concepts in Polymer Physics* (Cornell University Press, 1979).

Djabourov, M., Leblond, J., and Papon, P., "Gelation of aqueous gelatin solutions. I. Structural investigation," J. Phys. **49**, 319–332 (1988a).

Djabourov, M., Leblond, J., and Papon, P., "Gelation of aqueous gelatin solutions. II. Rheology of the sol-gel transition, " J. Phys. **49**(2), 333–343 (1988b).

Evans, P. A., Lawrence, M., Morris, R. H. K., Thirumalai, N., Munro, R., Wakeman, L., Beddel, A., Williams, P. R., Barrow, M., Curtis, D., Brown, M. R., and Hawkins, K., "Fractal analysis of viscoelastic data with automated gel point location and its potential application in the investigation of therapeutically modified blood coagulation," Rheol. Acta **49**(9), 901–908 (2010).

Ewoldt, R. H., Johnston, M. T., and Caretta, L. M., "Experimental challenges of shear rheology: How to avoid bad data," in *Complex Fluids in Biological Systems*, edited by S. E. Spagnolie (Springer, New York, 2015), pp. 207–241.

Franck, A., "Measuring structure of low viscosity fluids in oscillation using rheometers with and without a separate torque transducer, "Annu. Trans. - Nord. Rheol. Soc. **11**, 95–100 (2003).

Franck, A., *Instrument Inertia Correction During Dynamic Mechanical Testing* (TA Instruments, 2005).

Hawkins, K., Lawrence, M., Williams, P. R., and Williams, R. L., "A study of gelatin gelation by Fourier transform mechanical spectroscopy," J. Non-Newtonian Fluid Mech. **148**(1), 127–133 (2008).

Hawkins, K., Evans, P. A., Lawrence, M., Curtis, D., Davies, M., and Williams, P. R., "The development of rheometry for strain-sensitive gelling systems and its application in a study of fibrin–thrombin gel formation," Rheol. Acta **49**, 891–900 (2010).

Hellström, L. H. O., Samaha, M. A., Wang, K. M., Smits, A. J., and Hultmark, M., "Errors in parallel-plate and cone-plate rheometer measurements due to sample underfill," Meas. Sci. Technol. **26**(1), 015301 (2015).

Hsu, S. and Jamieson, A. M., "Viscoelastic behaviour at the thermal sol-gel transition of gelatin," Polymer **34**(12), 2602–2608 (1993).

Klemuk, S. A. and Titze, I. R., "Determining motor inertia of a stress-controlled rheometer," J. Rheol. **53**(4), 765 (2009).

Krieger, I. M., "Bingham award lecture—1989: The role of instrument inertia in controlled-stress rheometers," J. Rheol. **34**(4), 471–483 (1990).

Läuger, J. and Stettin, H., "Effects of instrument and fluid inertia in oscillatory shear in rotational rheometers," J. Rheol. **60**(3), 393–406 (2016).

Lawrence, M. J., Sabra, A., Mills, G., Pillai, S. G., Abdullah, W., Hawkins, K., Morris, R. H. K., Davidson, S. J., D'Silva, L. A., Curtis, D. J., Brown, M. R., Weisel, J. W., Williams, P. R., and Evans, P. A., "A new biomarker quantifies differences in clot microstructure in patients with venous thromboembolism," Br. J. Haematol. **168**(4), 571–575 (2015).

Martin, J. E., Adolf, D., and Wilcoxon, J. P., "Viscoelasticity of near-critical gels," Phys. Rev. Lett. **61**(22), 2620–2623 (1988).

Michon, C., Cuvelier, G., and Launay, B., "Concentration dependence of the critical viscoelastic properties of gelatin at the gel point," Rheol. Acta **32**(1), 94–103 (1993).

Mours, M. and Winter, H. H., "Time-resolved rheometry," Rheol. Acta **33**(5), 385–397 (1994).

Schrag, J. L., "Deviation of velocity gradient profiles from the 'gap loading' and 'surface loading' limits in dynamic simple shear experiments," Trans. Soc. Rheol. **21**(3), 399–413 (1977).

TA Instruments, *Rheology Theory and Applications* (TA Instruments, 2016).

Tosh, S. M. and Marangoni, A. G., "Determination of the maximum gelation temperature in gelatin gels," Appl. Phys. Lett. **84**, 4242 (2004).

The MathWorks, Inc., MATLAB, The MathWorks, Inc., Natick, Massachusetts, 2016.

Walters, K., *Rheometry*, 1st ed. (Springer, USA, 1975).

Werner, B., Bu, H., Kjøniksen, A., and Arne, S., "Characterization of gelation of aqueous pectin via the Ugi multicomponent condensation reaction," Polym. Bull. **589**, 579–589 (2006).

Wolf, F. A. and Keller, R. C. A., "Characterization of helical structures in gelatin networks and model polypeptides by circular dichroism," in *Gels* (Steinkopff, Darmstadt, 1996), pp. 9–14.

Yu, J. M., Blacher, S., Brouers, F., L'Homme, G., and Jérôme, R., "Triblock copolymer based thermoreversible gels. 4. Effect of the midblock and characterization of the sol–gel transition," Macromolecules **30**(16), 4619–4625 (1997).

Authorship Statement

Declaration:

The following people and institutions contributed to the publication of the work undertaken as part of this thesis:

Candidate	Rebecca E. Hudson College of Engineering/College of Science, Swansea University
Author 1	Rebecca E. Hudson College of Engineering/College of Science, Swansea University
Author 2	Alexander J. Holder College of Engineering, Swansea University
Author 3	Karl M. Hawkins Medical School, Swansea University
Author 4	P. Rhodri Williams College of Engineering, Swansea University
Author 5	Daniel J. Curtis College of Engineering, Swansea University

Paper 1: An enhanced rheometer inertia correction procedure (ERIC) for the study of gelling systems using combined motor transducer rheometers.

Located in Chapter 3.

Candidate contributed to experimental work, data analysis and writing the paper. Estimate of contribution: 60 %

Author 1 (the Candidate) contributed to experimental work, data analysis and writing the paper. Estimate of contribution: 60 %

Author 2 contributed experimental work and writing the paper. Estimate of contribution: 10 %

Author 3 contributed to writing the paper. Estimate of contribution: 5 %

Author 4 contributed to writing the paper. Estimate of contribution: 5 %

Author 5 contributed data analysis, development of the corresponding ERIC GUI and writing of the paper. Estimate of contribution: 20 %

We the undersigned agree with the above stated ‘proportion of work undertaken’ for each of the above published peer-reviewed manuscripts contributing to this thesis:

Candidate

Author 1

Author 2

Author 3

Author 4

Author 5

B. Soot solution characterisation

Soot Characterisation Study

Soot G[1x] was produced at Cardiff University using a graphite generator (276). The particles present in the soot solution were estimated[4] to have geometric mean diameter of 33 ± 1.65 nm in the gas phase (276).

A previous study by Anderlohr and Schaber showed that transfer of flame-synthesized aerosols of silica nanoparticles between phases was possible with negligible influence on the particles size distribution (308). Initially, particle size was measured as an aerosol using a scanning mobility particle sizer before dynamic light scattering was employed to measure the size of the same particles in the liquid phase. Finally, a liquid nanoparticle sizer determined the diameter of the particles within droplets in a re-atomised aerosol. The size of the particles measured in aerosol prior to and post-suspension in liquid showed strong agreement with geometric mean diameters of approx. 60 nm compared to the diameter for the same particles in liquid suspension being determined to be in the range of 160-180 nm (308). The study concluded that the discrepancies in the reported particles diameter in the gas and liquid phase was as a result of the techniques used, rather than aggregation of particles in a liquid suspension (308).

To gain understanding of the particles in the Soot G[1x] solution, a Malvern Zetasizer Nano-ZS was used to analyse the hydrodynamic diameter and zeta potential (ZP). The hydrodynamic diameter is a measure of not only the core particle size, but also any surface structure (309). The particles were suspended in ultra-pure water. Disposable folded capillary cells were used to obtain data on both the particle size and the zeta potential (ZP). Data was obtained to assess the effect of i) time, ii) salinity and iii) the addition of Tween-20 surfactant on size and ZP of the particles in the solution.

To evaluate the size and ZP of the particles suspended in the stock solution, the refractive index (RI) of the solution and the type of carbon particles present were used to create standard operating procedures (SOP). The respective SOP were used for each experiment (size and ZP). The RI of the dispersant, water, was set as 1.330 with a viscosity of 0.8872 cP at 25 °C (310). The viscosity of the dispersant was assumed to be the viscosity of the sample. For the particle material, carbon, the RI was set as 2.420 with an absorption of 0.900 (310). During the evaluation of the effect of salinity on the

particles, along with the effect of Tween-20, the RI of the dispersant was input as 1.335 due to the addition of TBS to the soot solution (310). All TBS and Tween-20 study samples were sonicated for 15 minutes prior the addition of the required volume of TBS and testing (168).

From each sample, data was obtained for the size and the ZP. A Z-Average from a total of 10 runs were completed for each size experiment, whilst average ZP data was obtained using a maximum of 100 runs with no delay between the measurements. The first measurement of each run was discarded as the instrument temperature stabilised, with guidance being taken on the quality of later runs from the software. Any data that was deemed below quality by the software was removed from analysis. The predominant issue raised by the instrument software was a high polydispersity index (PDI) for individual runs. The PDI gives dimensionless analysis of the broadness of the size distribution determined from the cumulant analysis (309). If the PDI coefficient data was > 0.07 and therefore not agreeable with a monodispersed sample, as outlined in ISO 22412:2017 (311), it was discarded.

Prior to loading the sample into the cell, the cell was wet using deionised (DI) water to prevent bubbles being trapped in the sample. Any excess DI water was shaken out of the cell. Samples were loaded into the folded capillary cells using a syringe. Initially, the cell was held upside down as the sample was loaded until it reached the 'U', at which point, the cell was righted, and the rest of the sample injected to ensure that no bubbles were caused in the cell. Stoppers were inserted into the cell to prevent sample evaporation during testing.

The cell containing the sample was loaded into the Zetasizer and the required SOP was run to obtain the data. Size data and ZP data were collected in consecutive experiments before a new sample was loaded.

Time study

Throughout the time study conducted over 15 days, fresh samples were prepared each day with one being sonicated for 15 minutes (168) and another being the Soot G[1x] solution without any ultrasonication. This was done to assess whether the sonication of the sample affected the particle size by breaking up any potential aggregation of the particles in the stock solution over time. 1 ml of sample was prepared each time with the sonicated sample being sonicated immediately prior to testing.

The data in Figure 7-1a shows the mean hydrodynamic diameter of the particles in stock soot (G[1x]) solution over a study period of 15 days, beginning with the day of manufacture of the solution, day zero. There are large fluctuations in the size recorded on consecutive days due to the fractal shape of the particles dispersed within the solution. The fractal nature of the particles resulted in the diameter reported to be overestimated. Even at the extremes from the initial values recorded for the sonicated and unsonicated data, there is no statistical significance as $p >> 0.05$. There effect of time of particles size appears to be inconclusive, with no clear suggestion of particle agglomeration. A large proportion of the data sits within the range of 400-600 nm, significantly increased from the 33 nm mobility diameter measured for particles in the gas phase[4], possibly as a result of the low iconic concentration of the solvent. A low iconic concentrations, the thickness of the electric double layer is increased which reduces the diffusion speed, resulting in an overestimated hydrodynamic diameter (312). Three days after manufacture, the ZP of the sample appears to become more steady, perhaps as a result of particle stabilisation (Figure 7-1b).

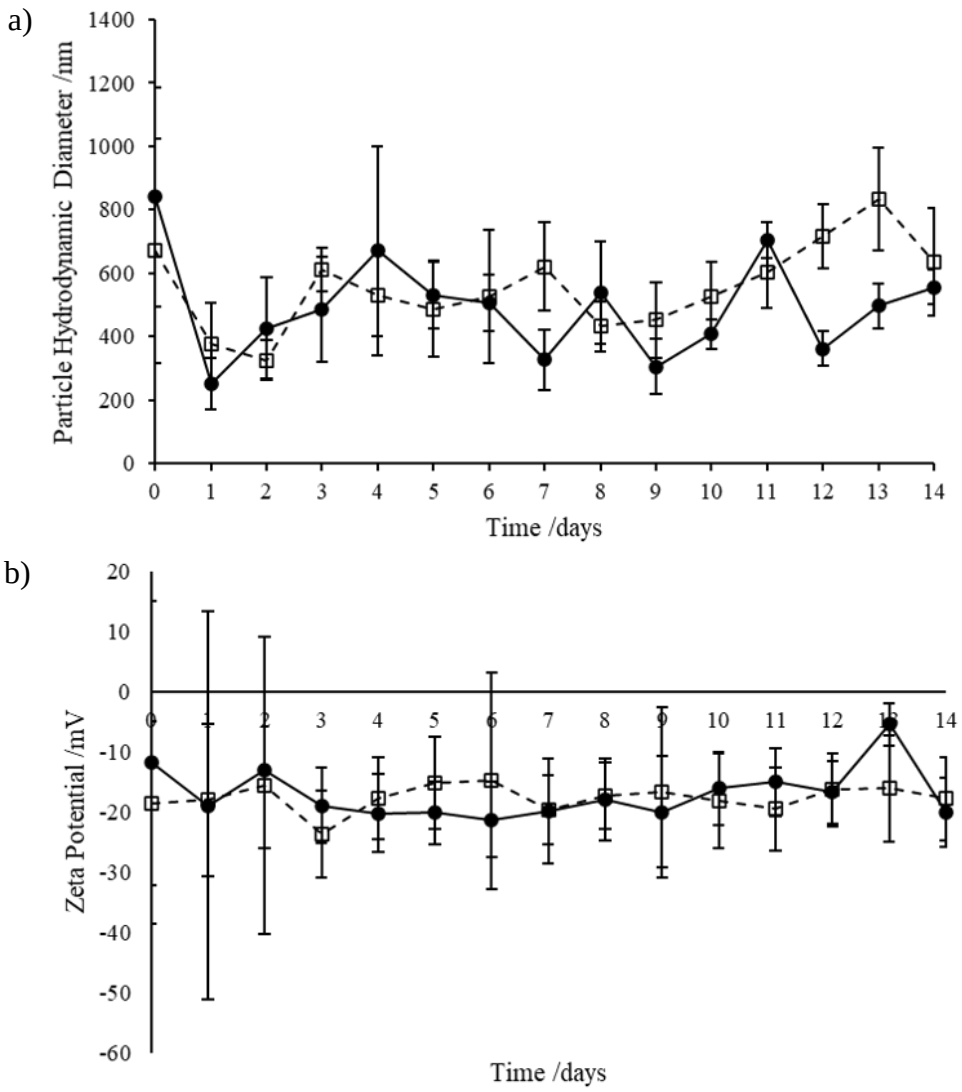

Figure 7-1 *Data reported using a Malvern Zetasizer Nano-ZS to assess a) the hydrodynamic diameter of the particles suspended in Soot G[1x] solution and b) the corresponding zeta potential of the solutions. The data was obtained over a period of two weeks, beginning on the day of manufacture. Solution were measured without sonication prior to measurement (open squares, dashed line) and after 15 minutes of sonication (closed circles, solid line) at room temperature.*

Solutions can be considered unstable when the ZP reported is in the range $-30\ mV \leq ZP \leq 30\ mV$ (313). As Figure 7-1b shows, the ZP data obtained over the time study all lie within the stated range, suggesting that the solution is unstable and could be subject to particle aggregation. There were no visible signs of aggregation or sedimentation over the course of the study involving only G[1x]. The erratic hydrodynamic diameters recorded support the lack of evidence of particle aggregation. However, as a precaution in studies of clots containing soot particulates, all soot solutions were sonicated for 15 minutes prior to addition to ensure that aggregation of particles was at a minimum.

Salinity study

As the core study involved the inclusion of the soot solutions into fibrin gels and whole blood clots, it was imperative to assess the effect of salinity on the samples. Required volumes of 10x TBS were added to the stock solution to analyse the effect of the increased salinity over particle hydrodynamic diameter and ZP. For the salinity of the soot solutions to be compatible with fibrin-thrombin gels and blood, the 10x TBS needed diluting to 1x TBS using the stock soot solution. As a result, the upper limit of TBS added was to dilute to 1x TBS (100%) and the lower limit was set as no TBS in the stock soot solution (0%). Several samples were prepared in between these limits at 20% intervals. Previous work has shown that ZP can be significantly reduced in high salt concentrations (313) as the pH of the solution is altered. Whilst the concentrations of TBS could not be worked with in later studies, it was possible to establish the increase in pH as the saline content increased (Figure 7-2).

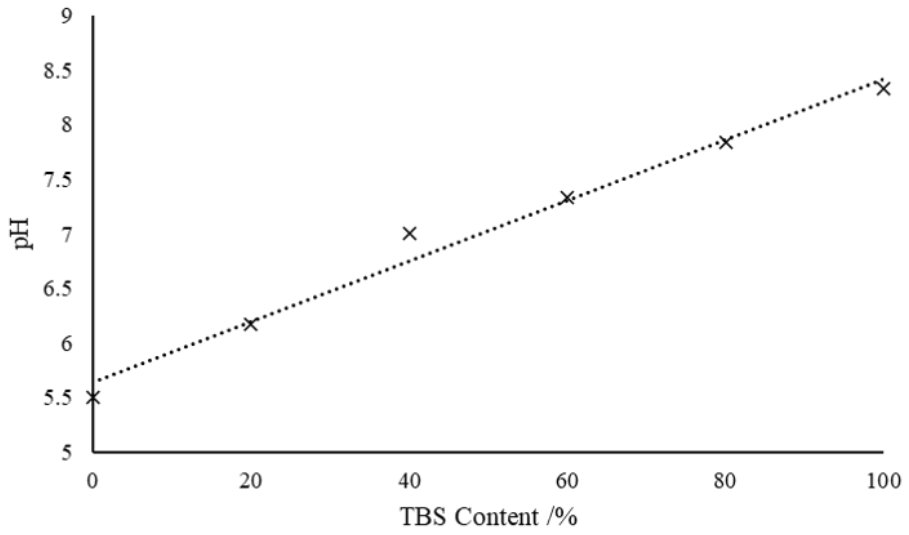

Figure 7-2 *The effect of increasing TBS concentration on pH of Soot G[1x] solutions.*

With the increased salinity, the pH of the solution increased over a range from pH5 at 0% TBS up to pH8 at 100% TBS. The results on the effect of pH on particle size appears to be inconclusive (Figure 7-3) with little deviation in the reported hydrodynamic diameters as the concentration of TBS approached the desired concentration. All samples were sonicated prior to assessment using the Zetasizer and therefore the fluctuations in the size could be as a result of the fractal nature of the soot particles present in the solutions.

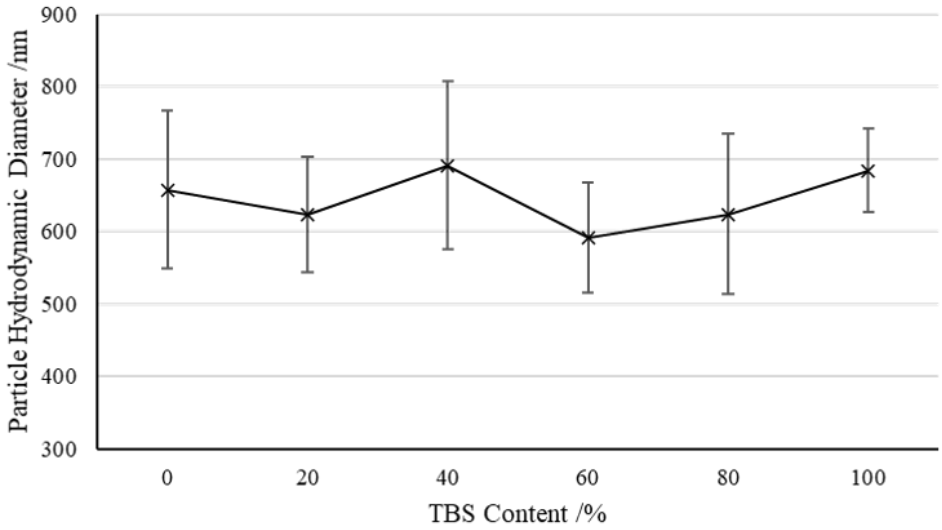

Figure 7-3 *Reported hydrodynamic diameters over a range of TBS concentrations. 100% TBS refers to the physiologically relevant TBS concentration required for compatibility with biopolymer experiments (1x TBS).*

The ZP of the soot solutions over the saline concentration range tested appears to fluctuate with an overall decrease in ZP as the TBS within the sample increased, up to the physiologically relevant 1x TBS (100%) sample (Figure 7-4). The reduction in ZP as the salinity increased suggests that the solutions became less stable and more likely to aggregate as the amount of TBS within the sample increased.

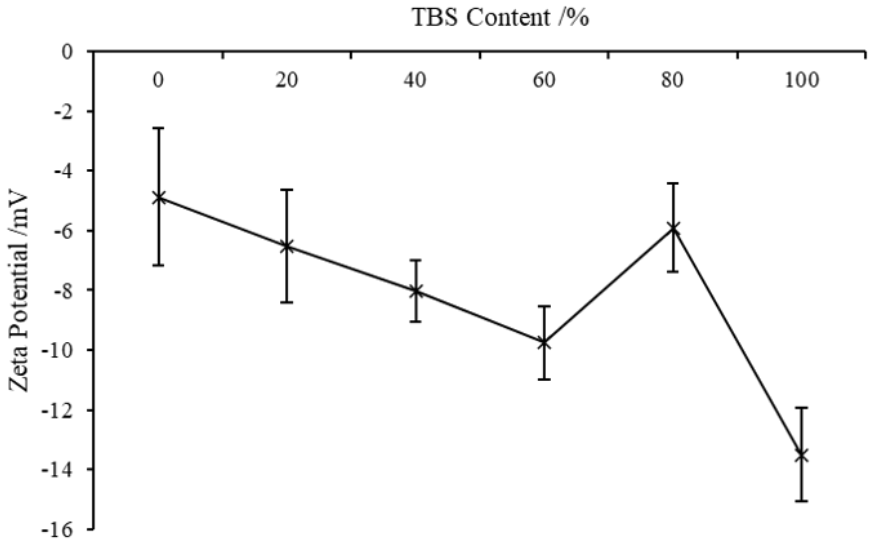

Figure 7-4 *Zeta potential reported for increasing TBS additions to Soot G[1x] solution.*

Alongside the Zetasizer data, the samples were visibly inspected and approximately one hour after testing, a film appeared to coat the sample tube containing 1x TBS (100% TBS content). An example of this can be seen in Figure 7-5 where a sample

from each saline concentration was lined up, with the only visible observation being a colour change from a colourless solution to very faint pink film on the tube (circled). Rheological experiments require a duration of approximately 25 minutes to obtain the desired measurements, and during that time frame, there were no visible alterations observed in the soot solution. However, the final study conducted using the Zetasizer to acquire size and ZP data involved the addition of Tween-20 surfactant to improve the quality of the rheologically reported GP data.

Figure 7-5 *Image of samples one hour after Zetasizer analysis. The TBS concentration within the sample increased (as illustrated by the arrow). At 1xTBS required for biological samples (100% TBS in the present study), there appeared to be a faint pink film present on the walls of the sample tube (circled). All other samples remained colourless.*

Tween-20 study

The inclusion of Tween-20 into the fibrin gel samples is necessary for rheological measurements in order to obtain valid GP data. The addition of Tween-20 surfactant to the soot solutions was conducted under 1x TBS saline conditions. Tween-20 was incorporated to have a 1 % concentration so as to be consistent with rheological data collection. Three separate soot samples with the inclusion of were prepared and tested with the data being shown in Figure 7-6.

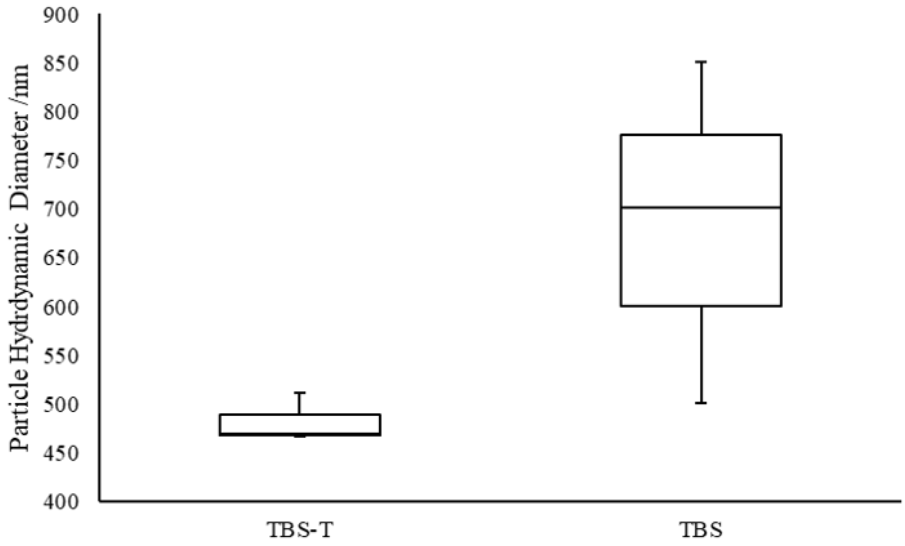

Figure 7-6 *Effect of the inclusion of Tween-20 into the soot solution on particle size compared with only TBS. Both samples were prepared with 1x TBS concentration.*

With the inclusion of Tween-20 into the Soot G[1x] solution, the size reported is significantly reduced in comparison to the samples containing only 1x TBS ($p = 0.0213$). The size reported for each run are lower than of those reported in the saline and time studies with the TBS-T particle sizes being in a much smaller range of 468 nm to 511 nm compared to the TBS size range of 500 nm to 851nm. The range of the data is dramatically reduced with the inclusion of Tween-20.

The ZP data collected for the samples with the addition of Tween-20 show a significant decrease in the ZP reported compared to the TBS only samples ($p = 0.0188$). For the 1x TBS only samples, there is a large range of ZP reported between -17.19 mV and -7.97 mV, whereas the TBS-T results reported a greatly reduced range of -4.64 mV to -6.43 mV.

Neither the numerical data nor the visual assessment of the samples suggests aggregation of the particles in the solution. There were no visible signs of aggregation and sedimentation documented in the TBS-T samples and after one hour. Despite the 1x TBS concentration present, the samples still appeared to be colourless with no film on the sample tubes. After 12 weeks, the solution containing 1x TBS with Tween-20 remained colourless with no signs of aggregation, yet the sample with 1x TBS only had fully coated the sample tube with film as seen in Figure 7-7.

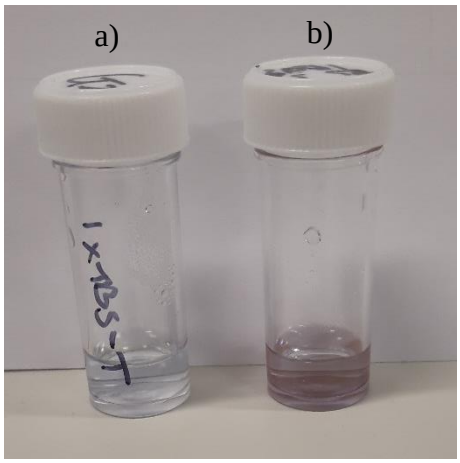

Figure 7-7 *Samples containing a) TBS and Tween-20 and b) only TBS, 12 weeks after Zetasizer analysis. It appears that the presence of Tween-20 prevents the aggregation of particles into a red film seen in b).*

As discussed in Section 4.4.1, the Soot G[1x] solution obtained from Cardiff University was further concentrated at Swansea University to give two- and ten-times particle concentration (Soot G[2x] and Soot G[10x] solutions respectively). It was not possible to obtain DLS data for the latter two samples as the volume of concentrated solution produced was no sufficient.

SEM samples were prepared to image the individual soot particles within the solutions. Unfortunately, it was not possible to obtain images of the soot particles for each of the solutions due to sample charging. However, it was possible to view the soot particles within the fibrin clots, as indicated in Figure 4-33.

The size of the reported particles using SEM is in agreement with the diameter measured in the gas phase suggested by Cardiff University for the particles suspended in Soot G[1x] solution. As a result, it is possible to be confident in the suggested size of the particles during manufacturing, despite the transfer of particles between phases. Therefore, the particles suspended in the soot solutions included into fibrin gels and whole blood clots within this thesis can be assumed to be of a similar size to the fibrinogen monomers.

C. Ethical Approval Application

Ethical approval was granted by Swansea University College of Engineering Research Ethics Committee for the project entitled 'Detection of exhaust particulate induced blood clotting anomalies using rheometric techniques'. The application was approved on 5th February 2019 (2019-002). A copy of the application approved by the committee is appended below.

APPLICATION FOR ETHICAL COMMITTEE APPROVAL OF A RESEARCH PROJECT

In accordance with A-STEM and College of Engineering Safety Policy, all research undertaken by staff or students linked with A-STEM or in the College of Engineering more widely must be approved by the College of Engineering Research Ethics Committee.

RESEARCH MAY ONLY COMMENCE ONCE ETHICAL APPROVAL HAS BEEN OBTAINED

The researcher(s) should complete the form in consultation with the project supervisor. After completing and signing the form students should ask their supervisor to sign it. The form should be submitted electronically to Coe-researchethics@swansea.ac.uk.

Applicants will be informed of the Committee's decision via email to the project leader/supervisor.

1. TITLE OF PROJECT

Detection of Exhaust Particulate Induced Blood Clotting Anomalies using Rheometric Techniques

2. DATE OF PROJECT COMMENCEMENT AND PROPOSED DURATION OF THE STUDY

Sept 2016 - Sept 2020

3. NAMES AND STATUS OF THE RESEARCH TEAM

Miss. Rebecca Hudson (PGR Student)
Dr D Curtis (Primary Supervisor)
Prof. P.R. Williams (Secondary Supervisor)
Dr. K. Hawkins (CoM)
Miss. Bethan Morgan (PGR Student, CoM) – Trained Phlebotomist.

4. RATIONALE AND REFERENCES

With reference to appropriate sources of information (using the Harvard system), describe in no more than 200 words the background to the proposed project.

The potential health damaging consequences of inhaling particulate material, such as that found in certain engine exhausts, is an area of significant scientific, commercial and societal interest. Several studies have mooted that the inhalation of sufficiently small diameter particles (<< 10 micron) may result in increased cardiovascular and cardiopulmonary mortalities due to changes in blood coagulability. The inhalation of diesel exhaust particles at concentrations found within urban environments is known to impair endogenous fibrinolysis and the regulation of vascular tone - two important complementary factors in the human circulation system. This suggests a potential mechanism by which air pollution may enhance or exacerbate atherothrombosis and acute myocardial infarction but no definitive data is available.

Research at Swansea has resulted in a new haemorheometric test for abnormal blood clot formation which, for the first time, detects pernicious abnormalities in clot properties at the earliest stage of their formation. This test detects anomalies in the assembly of the fibrin network - the clot's principal microstructural component. The current project explores the potential of this technique to monitor clot abnormalities caused by the presence of particulate matter. ***Part of the work will involve studying samples of whole human blood, systematically dosed, ex vivo, with a range of particulate materials from engine exhaust systems.***

5. OBJECTIVES

State the objectives of the project, i.e. one or more precise statements of what the project is designed to achieve.

The clot's fibrin network is formed from the polymerisation of fibrinogen molecules *whose size is similar to that of the inhaled particulate mass*. Thus this test has the potential to respond with particular sensitivity to the presence of any thrombogenic entities at this length scale. It is proposed to exploit the sensitivity of this test by

- Establishing whether the presence of particulates from engine exhausts does, in fact, lead to pernicious alterations in blood clot properties;
- Ascertaining at what concentrations such effects may arise.
- Ascertaining the most significant factors in terms of clot modification (particle size, shape and concentration)

6.1 STUDY DESIGN

Outline the chosen study design (e.g., cross-sectional, longitudinal, intervention, RCT, questionnaire etc)

Only part of the project involves the use of human blood samples. No clinical trial is being undertaken and we will only explore the effect of different concentrations/morphologies of particles on the clot microstructure. No personal data will be recorded.

6.2. STUDY DESIGN

- state the number and characteristics of study participants
- state the inclusion criteria for participants
- state the exclusion criteria for participants and identify any requirements for health screening
- state whether the study will involve vulnerable populations (i.e. young, elderly, clinical etc.)
- state the requirements/commitments expected of the participants (e.g. time, exertion level etc)

It is anticipated that around 60 blood samples (9 ml) will be required. Before participating in the study volunteers will be asked to confirm that they:

- are not, or do not think they are, infected with Hepatitis B or Hepatitis C.
- are not, or do not think they are, infected with HIV (the AIDS virus).
- have not, or have not had, a sexual partner who is infected with hepatitis or HIV.
- are not unwell at the moment.
- are not anaemic or receiving treatment for anaemia or iron deficiency.
- are not pregnant.
- have not donated >100 ml of blood, including to the National Blood Service, in the last four weeks.
- have not donated any volume of blood within the last week.
- do not have any long-term health conditions/concerns.
- have a BMI > 18.5

No vulnerable populations will be involved in the study. These criteria being necessary to (i) prevent unwell volunteers providing samples (ii) provide additional protection to experimentalists from blood bourne viruses and (iii) avoid spurious results as a consequence of known/unknown interactions of drugs with the coagulation system. Participants will be required to attend the Biorheology lab for approximately 10 mins whilst a trained phlebotomist takes the blood sample. No follow up will be required and there will be no ongoing commitments. The tests being performed are not recognized diagnostic procedures and have not undergone clinical trials; hence, the significance of incidental findings is unknown. For this reason, the results of the test will not be shared with the donor under any circumstances. Samples will be anonymized from the outset

6.3. PARTICIPANT RECRUITMENT

How and where will participants be recruited?

Participants will be recruited from the general university population of staff and PGR students. We will not approach undergraduate students.

6.4 DATA COLLECTION METHODS

- describe all of the data collection/experimental procedures to be undertaken
- state any dietary supplementation that will be given to participants and provide full details in Section 6.5
- state the inclusion of participant information and consent forms (in appendices)
- refer to the use of the ACA/ACSM health screening questionnaire where appropriate (usually for high intensity/maximal effort exercise. Note that the ACSM have updated their guidelines in a consensus statement dated 2015. Any questions regarding this please contact the chair of the committee.)

Experimentation will be limited to (i) rheological analysis of the clotting characteristics of the blood sample (using an AR-G2, AR-2000ex ir ARES-G2 rheometer) in the presence of varying concentrations of particulate material and (ii) SEM imaging of clot microstructure. A Participant Information Sheet and Consent Form are appended.

Samples will not be stored and will be disposed of through the clinical waste disposal routes at CNH. An SOP for the sampling and testing procedures is appended.

All paper records will be stored in a locked filing cabinet in the patient room (Room B10) adjacent to the rheology laboratory. All data will be anonymised and stored on a password protected computer running the rheometer (in the CNH rheology laboratory). Where data analysis requires that data be used on laptop computers these will be password protected and anonymised data will be stored in encrypted folders. Where necessary, anonymised data may be published in appropriate journals.

6.5 DATA ANALYSIS TECHNIQUES

- describe the techniques that will be used to analyse the data

Standard statistical techniques including regression, ANOVA / ANCOVA and t-tests as appropriate. SEM imaging may be subject to fractal analysis.

6.6. STORAGE AND DISPOSAL OF DATA AND SAMPLES

describe the procedures to be undertaken for the storage and disposal of data and samples
- identify the people who will have the responsibility for the storage and disposal of data and samples
- identify the people who will have access to the data and samples
- state the period for which the data will be retained on study completion (normally 5 years, or end of award)

Samples will not be stored and will be disposed of through the clinical waste disposal routes at CNH as detailed in the SOP. All data will be anonymized from the outset but (anonymised) data may be shared within the research team or used in publications.

6.7 HOW DO YOU PROPOSE TO ENSURE PARTICIPANT CONFIDENTIALITY AND ANONYMITY?

No personal data will be associated with the samples which will be referred to by number in all electronic and written records. Personal information will only appear on the Consent Form.

7. LOCATION OF THE PREMISES WHERE THE RESEARCH WILL BE CONDUCTED.

- list the location(s) where the data collection and analysis will be carried out
- identify the person who will be present to supervise the research at that location
- If a first aider is relevant, please specify the first aider

Phlebotomy will be carried out in the patient room (Rm 10), adjacent to the rheology laboratory (Rm 11), in the Centre for NanoHealth. Rheological testing and preparation of SEM samples will be undertaken in the Rheology Laboratory (Rm11). Used samples will be immediately disposed of using the appropriate waste disposal methods (see attached SOP). Local (CNH) first aiders will be informed that the phlebotomy activity is taking place

8. POTENTIAL PARTICIPANT RISKS AND DISCOMFORTS

- identify any potential physical risk or discomfort that participants might experience as a result of participation in the study.
- identify any potential psychological risk or discomfort that participants might experience as a result of participation in the study.
- Identify the referral process/care pathway if any untoward events occur

The risks involved in drawing blood from a vein may include, but are not limited to, momentary discomfort at the site of the blood draw, possible bruising, redness, and swelling around the site, bleeding at the site, feeling of lightheadedness when the blood is drawn, and rarely, infection at the site of the blood draw and nerve damage.

Most of the above require no action. In the event of lightheadedness, the participant would be asked to remain on the phlebotomy chair until the lightheadedness has passed. A first aider would be called in the event of a participant fainting.

9.1. HOW WILL INFORMED CONSENT BE SOUGHT?

Will any organisations be used to access the sample population?
Will parental/coach/teacher consent be required? If so, please specify which and how this will be obtained and recorded?

The motivation and methodology will be explained to participants who will be provided with an information sheet. Participants will be asked to sign a consent form before blood is collected.

9.2 INFORMATION SHEETS AND CONSENT/ASSENT FORMS

- Have you included a participant information sheet for the participants of the study? **YES**
- Have you included a parental/guardian information sheet for the parents/guardians of the study? **NA**
- Have you included a participant consent (or assent) form for the participants in the study? **YES**
- Have you included a parental/guardian consent form for the participants of the study? **NA**

10. IF YOUR PROPSED RESEARCH IS WITH VULNERABLE POPULATIONS (E.G., CHILDREN, PEOPLE WITH A DISABILITY), HAS AN UP-TO-DATE DISCLOSURE AND BARRING SERVICE (DBS) CHECK (PREVIOUSLY CRB) IF UK, OR EQUIVALENT NON-UK, CLEARANCE BEEN REQUESTED AND/OR OBTAINED FOR ALL RESEARCHERS? EVIDENCE OF THIS WILL BE REQUIRED.

NA

11. STUDENT DECLARATION

Please read the following declarations carefully and provide details below of any ways in which your project deviates from these. Having done this, each student listed in section 2 is required to sign where indicated.

- ☐ ***I have ensured that there will be no active deception of participants.***
- ☐ ***I have ensured that no data will be personally identifiable.***
- ☐ ***I have ensured that no participant should suffer any undue physical or psychological discomfort (unless specified and justified in methodology).***
- ☐ ***I certify that there will be no administration of potentially harmful drugs, medicines or foodstuffs.***
- ☐ ***I will obtain written permission from an appropriate authority before recruiting members of any outside institution as participants.***
- ☐ ***I certify that the participants will not experience any potentially unpleasant stimulation or deprivation.***
- ☐ ***I certify that any ethical considerations raised by this proposal have been discussed in detail with my supervisor.***
- ☐ ***I certify that the above statements are true with the following exception(s):***

Student/Researcher signature: (include a signature for each student in research team)

[redacted]

Rebecca Hudson
Date: 29th January 2019

[redacted]

Bethan Morgan
Date: 29/01/19

12. SUPERVISOR'S APPROVAL

Supervisor's signature:

[redacted]

Dan Curtis
Date: 29th January 2019

Participant Information Sheet

Research Centre: Centre for NanoHealth
Research Group: Complex Fluids Research Group
Participant identification number:

Name of researcher: Rebecca Hudson; Dr Dan Curtis (PI); Prof Rhodri Williams
Contact details for research team: [redacted]

Version 1.1-P2
Date 3.12.18

What are my rights as a participant?
Donation of blood for research is voluntary and you should not be placed under any pressure to donate. You do not have to agree to give a blood sample nor explain if you choose not to, refusal will have no effect on your employment or on your status or marks if a student. You are free to withdraw at any time, if you wish to do so please contact the research team.

What will participation involve?
Participation will involve the collection of blood by a trained phlebotomist in the patient room adjoining the rheology lab at Swansea University on one or more occasions. The sample(s) will be processed and tested immediately. The volume of blood collected will vary on each occasion, but will never exceed the maximum 50 ml. Each participant will not donate blood on more than one occasion per two weeks.

What will my sample be used for?
Participant blood samples will be used in order to study the process of blood clotting in the presence of soot particles. This will involve an investigation of the mechanical properties of human blood during the processes of clot formation and breakdown by the *in-vitro* addition of different therapies. Samples will be anonymised immediately and the techniques being employed are not recognized clinical tests, hence data concerning your blood samples will not be shared with you. Anonymised data may be published in appropriate journals.

What are the risks?
The risks involved in drawing blood from a vein may include, but are not limited to, momentary discomfort at the site of the blood draw, possible bruising, redness, and swelling around the site, bleeding at the site, feeling of lightheadedness when the blood is drawn, and rarely, infection at the site of the blood draw and nerve damage.

How will the risks be managed?
In order to protect participants and researchers we ask that the attached eligibility guidelines are followed. If you think that you may not be eligible for participation, please inform the researcher collecting your sample. It is recognised that some of the conditions may be sensitive, and you will not be asked to give any details.

In order to reduce the risk to participants only the most straight forward blood collections are performed. The researcher collecting blood may assess you for venipuncture and decide not to undertake the draw, this is nothing to worry about. Ease of blood collection can be influenced by many on the day factors including hydration state and recent meals, and there is no need to be concerned if this happens.

How will my information be handled?

Data GDPR and Confidentiality

Your data will be processed in accordance with the General Data Protection Regulation 2016 (GDPR). All information collected about you will be kept strictly confidential. Your data will only be viewed by the researcher/research team.

All electronic data will be stored on a password-protected computer file on the PC operating the rheometer in the rheology laboratory (Room B11, Centre for NanoHealth, ILS2 Building). All paper records will be stored in a locked filing cabinet in the patient room (Room B10) adjacent to the rheology laboratory.

Please note that the data we will collect for our study will be made anonymous immediately, thus it will not be possible to identify and remove your data at a later date. Therefore, if you decide to have your data withdrawn, please let us know before you leave the phlebotomy room.

Data Protection Privacy Notice

The data controller for this project will be Swansea University. The University Data Protection Officer provides oversight of university activities involving the processing of personal data, and can be contacted at the Vice Chancellors Office: dataprotection@swansea.ac.uk.

Your personal data will be processed for the purposes outlined in this information sheet.

Standard ethical procedures will involve you providing your consent to participate in this study by completing the consent form that has been provided to you. However, the legal basis on which this task is being performed is public interest, approved by the departmental Research Ethics Committee.

If you are concerned about how your personal data is being processed, please contact Swansea University's Data Protection Officer dataprotection@swansea.ac.uk.

Details of your individual rights are available on the ICO website at: https://ico.org.uk/for-organisations/data-protection-reform/overview-of-the-gdpr/individuals-rights/

Will my sample(s) be used by other people?
Samples will not be used by other people.

Who can I contact for further information?
If you have any further questions or queries, you wish to withdraw from the study, or would like information about the results of the research please feel free to contact Rebecca Hudson [redacted] or Dr Dan Curtis [redacted].

What if I have concerns about this research?
If you are worried about this research, or if you are concerned about how it is being conducted, you can contact the research misconduct team at Swansea University by emailing: researchmisconduct@swansea.ac.uk.

Eligibility Guidelines

For reasons of safety we request that you do not donate to this study if you:

- know you are, or think you might be, infected with Hepatitis B or Hepatitis C.
- know you are, or think you might be, infected with HIV (the AIDS virus).
- have, or have had, a sexual partner who is infected with hepatitis or HIV.
- are unwell at the moment.
- are anaemic or receiving treatment for anaemia or iron deficiency.
- are, or may be, pregnant.
- have donated >100 ml of blood, including to the National Blood Service, in the last four weeks.
- have donated any volume of blood within the last week.
- have any long-term health conditions/concerns.
- Have a BMI > 18.5

We additionally request that you do not participate if you have taken any of the following in the last 24 hours:

- Anti-coagulants (heparin, warfarin etc.)
- Coagulants (vitamin K, antihaemophillic factor, desmopressin etc.)
- The Combined Oral Contraceptive Pill
- NSAIDs (ibuprofen etc.)
- SSRIs (fluoxetine, paroxetine, sertraline etc.)
- Clot Busting Drugs (alteplase, streptokinase etc.)
- Excessive Alcohol
- Recreational Drugs

Consent for Blood Sample Collection

Thank you for reading the information about our research. If you would like to take part, please read and sign this form.

Research Centre: Centre for NanoHealth, Swansea University
Research Group: Complex Fluids Research Group
Participant identification number:
Name of researcher: Rebecca Hudson
Contact details for research team: [redacted]

	Please initial boxes
1. I have read the attached information sheet on this project, Version 1.1-P2. dated 3.12.18 and have been given a copy to keep. I have been able to ask questions about the project and I understand why the research is being done and any risks involved.	☐
2. I agree to give a sample of blood for research in this project. I understand how the sample will be collected, that giving a sample for this research is voluntary and that I am free to withdraw my approval for use of the sample at any time ***prior to leaving the phlebotomy room*** without giving a reason and without my legal rights being affected.	☐
3. I understand that I will not benefit financially if this research leads to the development of a new treatment or medical test.	☐
4. I know how to contact the research team if I need to, and how to get information about the results of the research.	☐
5. I understand that data regarding the sample I provide may be used in reports and academic publications in an anonymous fashion	☐

..... Date .....
Signature

.....
Name of participant (BLOCK CAPITALS)

..... Date .....
Signature

.....
Name of researcher (BLOCK CAPITALS)

Thank you for agreeing to participate in this research project!

Rheology of Blood Coagulation Protocol

- Calibrate instrument according to the manual

- Blood will be collected (by a qualified phlebotomist) from the median cubital vein using a 21-gauge butterfly line (Greiner Bio-One, Item No.: 450085). The first 3 ml of blood will be discarded using an additive-free Vaccutte® tube (Greiner Bio-One, Item No.: 454241). Further samples will be collected using appropriate vacutainers (containing anti-coagulants). The phlebotomy will be carried out at the Centre for NanoHealth Patient Room (Rm 10). Some samples will be centrifuged to obtain plasma.

- To investigate the effect of particulates on the clot rheological characteristics the blood will be dosed *in vitro* to with particulates (in solution) supplied by collaborators at Cardiff University.

- Approximately 1ml of sample (containing blood and particulates) will be loaded onto the lower plate of a rheometer situated in Rm 11 of the Centre for NanoHealth. The experiment will be initiated using the rheometer software. All files will be stored on the rheometers Desktop computers and the filenames will contain the code linking the sample to the participant.

- All experiments using whole blood will be carried out immediately after testing.

- Where necessary, preparation of samples for SEM imaging (a process which takes 4 days to complete) will be initiated immediately following the blood sample being obtained; the clot will be imaged immediately upon completion of this process. Hence no blood will be stored as part of this project.

- All waste will be disposed of according to the correct procedure below.

Rheology Laboratory Waste Disposal Procedures

Yellow sharps box: All sharps, scalpels and semi sharps (i.e. items that could pierce a bag, e.g. pipette tips)
Red lid bin: Anatomical waste e.g. blood, tissue. Separate bins for human and animal waste.
Purple lid bin: Cytotoxic waste
Yellow bags: Biologically contaminated materials that are not disposed of through other routes.
Red bags: Chemically contaminated materials that are not disposed of through other routes.
Non-hazardous waste should go into the normal bins (black bags) as long as it hasn't been contaminated with anything (cardboard boxes from deliveries etc.).

D. Nomenclature

Symbol	Definition	Unit
α	Stress relaxation exponent	-
A	Area	m^2
β	Angle of displacement	°
c	Concentration	wt%
d_f	Fractal Dimension	-
δ	Phase angle	°
δ_{GP}	Phase angle at the GP	°
δ_{raw}	Raw phase angle	°
d	Shearing gap	µm
d_e	Embedding Space	-
f	Frequency	Hz
F	Force	N
G	Elastic modulus	Pa
G'	Storage Modulus	Pa
G'_{raw}	Calibrated storage modulus	Pa
G'_C	Corrected storage modulus	Pa
G''	Loss Modulus	Pa
G^*	Complex Modulus	Pa
$G(t)$	Relaxation Modulus	Pa
γ	Shear strain	-
$\dot{\gamma}$	Shear strain rate	s^{-1}
γ_0	Strain amplitude	-
h	Height	m
I_c	Calibrated inertia constant	µN m s^2
I_t	True inertia constant	µN m s^2
k_g	Geometry factor	-
k_σ	Conversion factor	-
M	Torque	N m
M_m	Material torque	N m
M_i	Instrument torque	N m

μ	Viscosity	Pa s
N_{mu}	Mutation Number	-
p_c	Percolation threshold	-
p_s	Sticking probability	-
r	Radius	m
σ	Shear Stress	Pa
σ_0	Stress amplitude	Pa
σ_E	Elastic stress	Pa
σ_V	Viscous stress	Pa
σ_T	Total stress	Pa
S	Gel strength	Pa $s^{1/2}$
θ	Angular displacement	rad
t	Time	s
t_c	Critical time	s
t_d	Delay time	s
t_{gel}	Gel time	s
$tan\delta$	Loss tangent	°
τ	Relaxation time	s
τ_r	Retardation time	s
τ_s	Stress tensor	Pa
v	Velocity	m s^{-1}
ω	Angular frequency	rad s^{-1}
x	Displacement	m

References

1. Barnes HA. A Handbook of Elementary Rheology. 1st ed. The University of Wales Institute of Non-Newtonian Fluid Mechanics; 2000.

2. Barnes HA, Hutton J. ., Walters K. An Introduction to Rheology. Vol. 3. 1989. 1–199 p.

3. Walters K. History of Rheology. In: Rheology. 2004. p. 1–19.

4. Tanner RI, Walters K. Rheology : an historical perspective. Elsevier; 1998. 255 p.

5. Evans PA, Hawkins K, Morris RHK, Thirumalai N, Munro R, Wakeman L, et al. Gel point and fractal microstructure of incipient blood clots are significant new markers of hemostasis for healthy and anticoagulated blood. Blood. 2010;116(17):3341–6.

6. Michon C, Cuvelier G, Launay B. Concentration dependence of the critical viscoelastic properties of gelatin at the gel point. Rheol Acta. 1993 Jan;32(1):94–103.

7. Hawkins K, Lawrence M, Williams PR, Williams RL. A study of gelatin gelation by Fourier transform mechanical spectroscopy. JNNFM. 2008;148(1):127–33.

8. Malvern Instruments. A Basic Introduction to Rheology Shear Flow. 2016;

9. TA Instruments. Rheology Theory and Applications. 2016.

10. Rukke E-O, Pedersen AL, Schüller RB. Rheological characteristics of commercial tomato concentrate and corresponding ketchup. Annu Trans Nord Rheol Soc. 2016;24.

11. Bodnár T, Sequeira A, Prosi M. On the shear-thinning and viscoelastic effects of blood flow under various flow rates. Appl Math Comput. 2011;217(11):5055–67.

12. Crawford NC, Popp LB, Johns KE, Caire LM, Peterson BN, Liberatore MW. Shear thickening of corn starch suspensions: Does concentration matter? J Colloid Interface Sci. 2013;396:83–9.

13. Slatter P. The rheological characterisation of sludges. Water Sci Technol. 1997;36(11):9–18.

14. Whorlow RW. Rheological techniques. 2nd Edition. Chicester: E. Horwood; 1992. 447 p.

15. Chhabra RP, Richardson JF. Non-Newtonian Flow and Applied Rheology. Second Edi. Elsevier, editor. 2008. 518 p.

16. TA Instruments. ARES-G2 Rheometer. 2018.

17. Hyun K, Wilhelm M, Klein CO, Soo Cho K, Nam JG, Ahn KH, et al. A Review of Nonlinear Oscillatory Shear Tests: Analysis and Application of Large Amplitude Oscillatory Shear (LAOS). Prog Polym Sci. 2011;36(12):1697–753.

18. Hawkins K, Evans PA, Lawrence M, Curtis D, Davies M, Williams PR, et al. The development of rheometry for strain-sensitive gelling systems and its application in a study of fibrin–thrombin gel formation. Rheol Acta. 2010;49:891–900.

19. Wilhelm M, Reinheimer P, Ortseifer M, Neidhofer T, Spiess HW. The crossover between linear and non-linear mechanical behaviour in polymer solutions as detected by Fourier-transform rheology. Rheol Acta. 2000;39(3):241–6.

20. Tschoegl NW. The Phenomenological Theory of Linear Viscoelastic Behavior: An Introduction. 1989.

21. Ferry JD. Viscoelastic properties of polymers. Wiley; 1980. 641 p.

22. Mewis J, Wagner NJ. Colloidal suspension rheology. Cambridge University Press; 2012. 393 p.

23. Instruments TA. Rheology : An Introduction. 2018.

24. Klemuk SA, Titze IR. Determining Motor Inertia of a Stress-Controlled Rheometer. J Rheol (N Y N Y). 2009;53(4):765.

25. Krieger IM. Bingham Award Lecture—1989: The role of instrument inertia in controlled-stress rheometers. J Rheol (N Y N Y). 1990 May;34(4):471–83.

26. Läuger J, Stettin H. Effects of instrument and fluid inertia in oscillatory shear

in rotational rheometers. J Rheol (N Y N Y). 2016;60(3):393–406.

27. Walters K. Rheometry. 1st ed. Springer US; 1975. 278 p.

28. Mours M, Winter HH. Time-resolved rheometry. Rheol Acta. 1994;33(5):385–97.

29. Winter HH, Mours M. Rheology of Polymers Near Liquid-Solid Transitions. In: Neutron Spin Echo Spectroscopy Viscoelasticity Rheology. 1997. p. 165–234.

30. Franck AP. Importance of inertia correction for controlled stress rheometers. Theor Appl Rheol. 1992 Jan 1;982–4.

31. Ewoldt RH, Johnston MT, Caretta LM. Experimental challenges of shear rheology: how to avoid bad data. In: S.E. Spagnolie, editor. Complex Fluids in Biological Systems. New York: Springer; 2015. p. 207–41.

32. Franck A. Instrument Inertia Correction during Dynamic Mechanical Testing. 2005.

33. Deshpande A. Techniques in oscillatory shear rheology. 2018.

34. Moreno R. Rheology. In: Buschow K, editor. Encyclopedia of Materials: Science and Technology. 2nd Edition. Elsevier; 2001. p. 8192–6.

35. Murata H. Polymerization: Rheology - Theory and Application to Biomaterials. In: Polymerization. 2012. p. 403–25.

36. Winter HH, Chambon F. Analysis of Linear Viscoelasticity of a Crosslinking Polymer at the Gel Point. J Rheol (N Y N Y). 1986;30(2):367–82.

37. Chambon F, Petrovic ZS, Macknight WJ, Winter HH. Rheology of Model Polyurethanes at the Gel Point. Macromolecules. 1986;19(8):2146–9.

38. Tassieri M, Laurati M, Curtis DJ, Auhl DW, Coppola S, Scalfati A, et al. i-Rheo: Measuring the materials' linear viscoelastic properties "in a step"! J Rheol (N Y N Y). 2016;60(4):649–60.

39. TA Instruments. TA Instruments Rheometers.

40. TA Instruments. TA Instruments Rheometer Manual AR2000. :13–6.

41. TA Instruments. TA Instruments Rheometers AR2000. :1–11.

42. Costello B. The AR-G2 Magnetic Bearing Rheometer. 2005;1–6.

43. Franck A. Measuring structure of low viscosity fluids in oscillation using rheometers with and without a separate torque transducer. Annu Trans Nord Rheol Soc. 2003;11:95–100.

44. TA Instruments. AR 2000 Rheometer. Vol. 49, Rheoemetric Series Operators Manual. 2007.

45. Schrag JL. Deviation of Velocity Gradient Profiles from the "Gap Loading" and "Surface Loading" Limits in Dynamic Simple Shear Experiments. Trans Soc Rheol. 1977 Sep;21(3):399–413.

46. Giles D, Macosko C. Shear rheometry. TA Instruments. 2010;

47. Djabourov M, Leblond J, Papon P. Gelation of aqueous gelatin solutions. I. Structural investigation. J Phys. 1988;49:319–32.

48. Djabourov M, Leblond J, Papon P. Gelation of aqueous gelatin solutions. II. Rheology of the sol-gel transition. J Phys. 1988;49(2):333–43.

49. Hawkins K, Lawrence M, Williams P, Williams R. A study of gelatin gelation by Fourier transform mechanical spectroscopy. J Non-Newtonian Fluid Mech. 2008;148:127–33.

50. Hsu S, Jamieson AM. Viscoelastic behaviour at the thermal sol-gel transition of gelatin. Polymer (Guildf). 1993 Jan;34(12):2602–8.

51. Vilgis TA, Winter HH. Mechanical selfsimilarity of polymers during chemical gelation. Colloid Polym Sci. 1988;266(6):494–500.

52. Martin JE, Adolf D, Wilcoxon JP. Viscoelasticity of Near-Critical Gels. Phys Rev Lett. 1988;61(22):2620–3.

53. Curtis DJ, Brown MR, Hawkins K, Evans PA, Lawrence MJ, Rees P, et al. Rheometrical and molecular dynamics simulation studies of incipient clot formation in fibrin-thrombin gels: An activation limited aggregation approach. J Nonnewton Fluid Mech. 2011;166(16):932–8.

54. Lawrence MJ, Sabra A, Mills G, Pillai SG, Abdullah W, Hawkins K, et al. A

new biomarker quantifies differences in clot microstructure in patients with venous thromboembolism. Br J Haematol. 2015 Feb;168(4):571–5.

55. Flory PJ. Molecular Size Distribution in Three Dimensional Polymers. I. Gelation. J Am Chem Soc. 1941;63(11):3083–90.

56. Winter HH. Can the Gel Point of a Cross-linking Polymer Be Detected by the G'-G" Crossover? Vol. 27, Polymer Engineering and Science. 1987. p. 1698–702.

57. Winter HH. Gel Point. Encycl Polym Sci Technol. 2016;1–15.

58. Winter HH, Morganelli P, Chambon F. Stoichiometry effects on rheology of model polyurethanes at the gel point. Macromolecules. 1988;21(2):532–5.

59. Curtis DJ, Badiei N, Holder A, Claypole J, Deganello D, Brown MR, et al. Assessment of the stress relaxation characteristics of critical gels formed under unidirectional shear flow by controlled stress parallel superposition rheometry. J Nonnewton Fluid Mech. 2015;222:227–33.

60. Chambon F, Winter HH. Linear Viscoelasticity at the Gel Point of a Crosslinking PDMS with Imbalanced Stoichiometry. J Rheol (N Y N Y). 1987 Nov 24;31(8):683–97.

61. Stockmayer WH. Theory of Molecular Size Distribution and Gel Formation in Branched Polymers II. General Cross Linking. J Chem Phys. 1944 Apr 22;12(4):125–31.

62. Stauffer D. Scaling Theory of Percolation Clusters. Phys Rep. 1979;54(1):1–74.

63. Stauffer D, Aharony A. Introduction to Percolation Therory. 2nd ed. Vol. 2. London: Taylor & Francis Ltd; 1994. 25 p.

64. Christensen K. Percolation theory. 2002.

65. Witten TA, Sander LM. Diffusion-Limited Aggregation, a Kinetic Critical Phenomenon. Phys Rev Lett. 1981;47(19):1400–3.

66. Lin MY, Lindsay HM, Weitz DA, Ball RC, Klein R, Meakin P. Universal reaction-limited colloid aggregation. Phys Rev A. 1990;41(4):2005–20.

67. Kolb M, Botet R, Jullien R. Scaling of Kinetically Growing Clusters. Phys Rev Lett. 1983;51(13):1123–6.

68. Schaefer DW, Martin JE, Wiltzius P, Cannell DS. Fractal geometry of colloidal aggregates. Phys Rev Lett. 1984;52(26):2371–4.

69. Badiei N, Sowedan AM, Curtis DJ, Brown MR, Lawrence MJ, Campbell AI, et al. Effects of unidirectional flow shear stresses on the formation, fractal microstructure and rigidity of incipient whole blood clots and fibrin gels. Clin Hemorheol Microcirc. 2015;60(4):451–64.

70. Sandroff CJ, Weitz D., Lin M. Colloidal aggregation revisited: New insights based on fractal structure amd surface-enhanced Raman scattering. Surf Sci. 1985;158(147):147–64.

71. Asnaghi D, Carpineti M, Giglio M, Sozzi M. Coagulation kinetics and aggregate morphology in the intermediate regimes between diffusion-limited and reaction-limited cluster aggregation. Phys Rev A. 1992;45(2):1018–23.

72. Meakin P, Family F. Structure and dynamics of reaction-limited aggregation. Phys Rev A. 1987;36(11):5498–501.

73. Ball RC, Weitz DA, Witten TA, Leyvraz F. Universal kinetics in reaction-limited aggregation. Phys Rev Lett. 1987;58(3):274–7.

74. Evans PA, Hawkins K, Morris RHK, Thirumalai N, Munro R, Wakeman L, et al. Gel point and fractal microstructure of incipient blood clots are significant new markers of hemostasis for healthy and anticoagulated blood. Blood. 2010 Oct 28;116(17):3341–6.

75. Curtis DJ, Williams PR, Badiei N, Campbell AI, Hawkins K, Evans PA, et al. A study of microstructural templating in fibrin–thrombin gel networks by spectral and viscoelastic analysis. Soft Matter. 2013;9(19):4883.

76. Holly EE, Venkataraman SK, Chambon F, Henning Winter H. Fourier transform mechanical spectroscopy of viscoelastic materials with transient structure. Vol. 27, Journal of Non-Newtonian Fluid Mechanics. 1988. p. 17–26.

77. Curtis DJ, Holder A, Badiei N, Claypole J, Walters M, Thomas B, et al. Validation of Optimal Fourier Rheometry for rapidly gelling materials and its

application in the study of collagen gelation. JNNFM. 2015;222:253–9.

78. Winter HH, Morganelli P, Chambon F. Stoichiometry effects on rheology of model polyurethanes at the gel point. Macromolecules. 1988 Mar;21(2):532–5.

79. Nijenhuis K te. Gelatin. In: Thermoreversible Networks. 1997. p. 160–93.

80. Gallegos C, Franco JM. Rheology of food, cosmetics and pharmaceuticals. Curr Opin Colloid Interface Sci. 1999 Aug 1;4(4):288–93.

81. Digenis GA, Gold TB, Shah VP. Cross-Linking of Gelatin Capsules and Its Relevance to Their in Vitro-in Vivo Performance. J Pharm Sci. 1994 Jul 1;83(7):915–21.

82. Normand V, Ravey JC. Dynamic study of gelatin gels by creep measurements. Rheol Acta. 1997;36(6):610–7.

83. Wolf FA, Keller RCA. Characterization of helical structures in gelatin networks and model polypeptides by circular dichroism. In: Gels. Darmstadt: Steinkopff; 1996. p. 9–14.

84. Tosh SM, Marangoni AG. Determination of the maximum gelation temperature in gelatin gels. Cit Appl Phys Lett. 2004;84(4242).

85. Boedtker H, Doty P. a Study of Gelatin Molecules, Aggregates and Gels. Gelatin Mol Aggregates Gel. 1954;58:968–83.

86. Ptaszek P, Basu S. Chapter 15 – Rheological Properties of Gelatin and Advances in Measurement. In: Advances in Food Rheology and its Applications. 2017. p. 377–404.

87. Jones GMJ. Rheological Properties of Gelatin, Carrageenan and Locust Bean Gun Mixtures. 2004.

88. Djabourov M, Lechaire JP, Gaill F. Structure and rheology of gelatin and collagen gels. Biorheology. 30(3–4):191–205.

89. Pang Z, Deeth H, Sopade P, Sharma R, Bansal N. Rheology, texture and microstructure of gelatin gels with and without milk proteins. Food Hydrocoll. 2014;35:484–93.

90. Osorio FA, Bilbao E, Bustos R, Alvarez F. Effects of concentration, bloom

degree, and pH on gelatin melting and gelling temperatures using small amplitude oscillatory rheology. Int J Food Prop. 2007;10(4):841–51.

91. Curtis DJ, Badiei N, Holder A, Claypole J, Deganello D, Brown MR, et al. Assessment of the stress relaxation characteristics of critical gels formed under unidirectional shear flow by controlled stress parallel superposition rheometry. J Nonnewton Fluid Mech. 2014;222:227–33.

92. Quemada D. Blood Rheology and its Implications in the Flow of Blood. In: Arteries and Arterial Blood Flow. Springer, Vienna; 1983. p. 1–118.

93. Nader E, Skinner S, Romana M, Fort R, Lemonne N, Guillot N, et al. Blood Rheology: Key Parameters, Impact on Blood Flow, Role in Sickle Cell Disease and Effects of Exercise. Front Physiol. 2019;10(October):1–14.

94. Stuart J, Kenny MW. Blood rheology. J Clin Pathol. 1980;33:417–29.

95. Nash GB. Blood rheology and ischaemia. Eye. 1991;5(2):151–8.

96. Li X, Peng Z, Lei H, Dao M, Karniadakis GE. Probing red blood cell mechanics, rheology and dynamics with a two-component multi-scale model. Philos Trans R Soc A Math Phys Eng Sci. 2014;372(2021).

97. Cokelet GR. The Rheology of Human Blood. 1963.

98. Morris CL, Smith CM, Blackshear PL. A new method for measuring the yield stress in thin layers of sedimenting blood. Biophys J. 1987;52(2):229–40.

99. Mehri R, Mavriplis C, Fenech M. Red blood cell aggregates and their effect on non-Newtonian blood viscosity at low hematocrit in a two-fluid low shear rate microfluidic system. PLoS One. 2018;13(7).

100. Austin SK. Haemostasis. Med (United Kingdom). 2017;45(4):204–8.

101. Dahlbäck B. Blood coagulation. Lancet. 2000;335:1627–32.

102. Smith SA, Travers RJ, Morrissey JH. Initiation of clotting cascade. Crit Rev Biochem Mol Biol. 2016;50(4):326–36.

103. Weisel JW, Litvinov RI. Fibrin Formation, Structure and Properties. Subcell Biochem. 2017;82:405–56.

104. Palta S, Saroa R, Palta A. Overview of the coagulation system. Indian J Anaesth. 2014;58(5):515–23.

105. Chaudhry R, Babiker HM. Physiology, Coagulation Pathways. StatPearls. 2018.

106. Mackman N. The role of tissue factor and factor VIIa in hemostasis. Anesth Analg. 2009;108(5):1447–52.

107. Triplett DA. Coagulation and bleeding disorders: Review and update. Clin Chem. 2000;46(8):1260–9.

108. Nemerson Y. Tissue Factor and Hemostasis. J Am Soc Hematol. 1988;71(1):1181–95.

109. Pieters M, Wolberg AS. Fibrinogen and fibrin: An illustrated review. Res Pract Thromb Haemost. 2019;(January):1–12.

110. Hudson NE. Biophysical Mechanisms Mediating Fibrin Fiber Lysis. Biomed Res Int. 2017;2017.

111. Wolberg AS. Thrombin generation and fibrin clot structure. Blood Rev. 2007;21(3):131–42.

112. Kattula S, JR B, Wolberg AS. Fibrinogen and fibrin in hemostasis and thrombosis. Arterioscler Thromb Vasc Biol. 2017;37(3):e13–21.

113. Weisel JW, Phillips GN, Cohen C. A model from electron microscopy for the molecular structure of fibrinogen and fibrin. Nature. 1981;289(5795):263–7.

114. Blombäck B. Fibrinogen and fibrin - Proteins with complex roles in hemostasis and thrombosis. Thromb Res. 1996;83(1):1–75.

115. Göbel K, Eichler S, Wiendl H, Chavakis T, Kleinschnitz C, Meuth SG. The coagulation factors fibrinogen, thrombin, and factor XII in inflammatory disorders-a systematic review. Front Immunol. 2018;9(JUL).

116. Howie PW. Blood clotting and fibrinolysis in pregnancy. Postgrad Med J. 1979;55:362–6.

117. Choi JW, Pai SH. Tissue plasminogen activator levels change with plasma fibrinogen concentrations during pregnancy. Ann Hematol. 2002;81(11):611–

5.

118. Hayakawa M. Dynamics of fibrinogen in acute phases of trauma. J Intensive Care. 2017;5(1):4–9.

119. Inaba K, Karamanos E, Lustenberger T, Schöchl H, Shulman I, Nelson J, et al. Impact of fibrinogen levels on outcomes after acute injury in patients requiring a massive transfusion. J Am Coll Surg. 2013;216(2):290–7.

120. Blombäck B, Bark N. Fibrinopeptides and fibrin gel structure. Biophys Chem. 2004;112:147–51.

121. Chapin JC, Hajjar KA. Fibrinolysis and the control of blood coagulation. Blood Rev. 2015;29(1):17–24.

122. Lorand L, Mann KG. Introduction: Blood Coagulation. Methods Enzymol. 1993;222(1980).

123. Johari V, Loke C. Brief Overview of the Coagulation Cascade. Disease-a-Month. 2012;58(8):421–3.

124. Ferry JD, Morrison PR. Preparation and Properties of Serum and Plasma Proteins . VIII . The Conversion of Human Fibrinogen to Fibrin under Various Conditions. J Am Chem Soc. 1947;69(2):388–400.

125. Jobling L, Eyre L. Haemostasis, blood platelets and coagulation. Anaesth Intensive Care Med. 2013;14(2):51–3.

126. Weisel JW. The mechanical properties of fibrin for basic scientists and clinicians. Biophys Chem. 2004;112(2-3 SPEC. ISS.):267–76.

127. Undas A. Prothrombotic Fibrin Clot Phenotype in Patients with Deep Vein Thrombosis and Pulmonary Embolism: A New Risk Factor for Recurrence. Biomed Res Int. 2017;2017.

128. Weisel JW, Litvinov RI. Mechanisms of fibrin polymerization and clinical implications. Blood. 2013;121(10):1712–9.

129. Rijken DC, Uitte De Willige S. Inhibition of Fibrinolysis by Coagulation Factor XIII. Biomed Res Int. 2017;2017:6.

130. Weisel JW. Structure of fibrin: Impact on clot stability. J Thromb Haemost.

2007;5(SUPPL. 1):116–24.

131. Aoki N. Fibrinolysis: Its initiation and regulation. J Protein Chem. 1986;5(4):269–77.

132. Angelini P, Leachman R. Streptokinase thrombolysis in acute myocardial infarction: A turning point. Texas Hear Inst J. 1983;10(4):387–95.

133. Ernst E. Plasma fibrinogen — an independent cardiovascular risk factor. J Intern Med. 1990;227(6):365–72.

134. Næss IA, Christiansen SC, Romundstad P, Cannegieter SC, Rosendaal FR, Hammerstrøm J. Incidence and mortality of venous thrombosis: A population-based study. J Thromb Haemost. 2007;5(4):692–9.

135. Rosendaal FR. Causes of venous thrombosis. Thromb J. 2016;14(Suppl 1).

136. Litvinov RI, Weisel JW. What Is the Biological and Clinical Relevance of Fibrin? Semin Thromb Hemost. 2016;42(4):333–43.

137. Neeves KB, Illing DAR, Diamond SL. Thrombin flux and wall shear rate regulate fibrin fiber deposition state during polymerization under flow. Biophys J. 2010;98(7):1344–52.

138. Stone J, Hangge P, Albadawi H, Wallace A, Shamoun F, Knuttien MG, et al. Deep vein thrombosis: Pathogenesis, diagnosis, and medical management. Cardiovasc Diagn Ther. 2017;7(Suppl 3):S276–84.

139. Ariëns RAS. Novel mechanisms that regulate clot structure/function. Thromb Res. 2016;141:S25–7.

140. Campbell RA, Machlus KR, Wolberg AS. Smoking Out the Cause of Thrombosis. Ateriosclerosis, Thromb Vasc Biol. 2010;30(1):7–8.

141. Ariëns RAS. Denser matters. Blood. 2009;114(19):3978–9.

142. Evans PA, Hawkins K, Lawrence M, Barrow MS, Williams PR, Williams RL. Studies of whole blood coagulation by oscillatory shear, thromboelastography and free oscillation rheometry. Clin Hemorheol Microcirc. 2008;38(4):267–77.

143. Lawrence MJ, Kumar S, Hawkins K, Boden S, Rutt H, Mills G, et al. A new structural biomarker that quantifies and predicts changes in clot strength and

quality in a model of progressive haemodilution. Thromb Res. 2014;134(2):488–94.

144. Sabra A, Lawrence MJ, Curtis D, Hawkins K, Williams PR, Evans PA. In vitro clot model to evaluate fibrin-thrombin effects on fractal dimension of incipient blood clot. Clin Hemorheol Microcirc. 2019;1–7.

145. Evans PA, Hawkins K, Williams PR, Williams RL. Rheometrical detection of incipient blood clot formation by Fourier transform mechanical spectroscopy. J Nonnewton Fluid Mech. 2008 Jan;148(1–3):122–6.

146. Evans PA, Lawrence M, Morris RHK, Thirumalai N, Munro R, Wakeman L, et al. Fractal analysis of viscoelastic data with automated gel point location and its potential application in the investigation of therapeutically modified blood coagulation. Rheol Acta. 2010 Sep 25;49(9):901–8.

147. Lawrence M, Sabra A, Mills G, Pillai S, Abdullah W, Hawkins K, et al. A new biomarker quantifies differences in clot microstructure in patients with venous thromboembolism. Br J Haematol. 2015;168(4):571–5.

148. Stanford SN, Sabra A, D'Silva L, Lawrence M, Morris RHK, Storton S, et al. The changes in clot microstructure in patients with ischaemic stroke and the effects of therapeutic intervention: A prospective observational study. BMC Neurol. 2015;15(1):1–8.

149. Sabra A, Lawrence MJ, Aubrey R, Obaid D, Chase A, Smith D, et al. Characterisation of clot microstructure properties in stable coronary artery disease. Open Hear. 2017;4(2):562.

150. Lawrence MJ, Sabra A, Thomas P, Obaid DR, D'Silva LA, Morris RHK, et al. Fractal dimension: A novel clot microstructure biomarker use in ST elevation myocardial infarction patients. Atherosclerosis. 2015;240(2):402–7.

151. Losa GA, Merlini D, Nonnenmacher TF, Weibel ER. Fractals in biology and medicine. Vol III. Birkhäuser Verlag; 2002.

152. Muthukumar M. Screening Effect on Viscoelasticity near the Gel Point. Macromolecules. 1989;22:4656–8.

153. Evans PA, Hawkins K, Williams PR. Rheometry for Blood Coagulation

Studies. Rheol Rev. 2006;1:255–91.

154. Thakur M, Ahmed AB. A review of thromboelastography. Int J Perioper Ultrasound Appl Technol. 2012;1(1):25–9.

155. Mallett S V., Cox DJ a. Thrombelastography. Br J Anaesth. 1992;69(3):307–13.

156. da Luz LT, Nascimento B, Rizoli S. Thrombelastography (TEG): practical considerations on its clinical use in trauma resuscitation. Scand J Trauma Resusc Emerg Med. 2013;21(29):533–40.

157. McCrath DJ, Cerboni E, Frumento RJ, Hirsh AL, Bennett-Guerrero E. Thromboelastography maximum amplitude predicts postoperative thrombotic complications including myocardial infarction. Anesth Analg. 2005;100(6):1576–83.

158. Soleimani S, Pennati G, Dubini G. A Study on Ratio of Loss to Storage Modulus for the Blood Clot. Int J Eng. 2014;27(8):1167–72.

159. Poller L. Prothrombin Time. In: Laboratory Techniques in Thrombosis. Springer Dordrecht; 1999. p. 45–61.

160. Yang R, L M. Prothrombin Time. In: StatPearls. StatPearls Publishing; 2013. p. 799–803.

161. Baccarelli A, Zanobetti A, Martinelli I, Grillo P, Hou L, Giacomini S, et al. Effects of exposure to air pollution on blood coagulation. J Thromb Haemost. 2007;5(2):252–60.

162. Gersh KC, Chandrasekaran N, Weisel JW. Fibrin network structure and clot mechanical properties are altered by incorporation of erythrocytes. Thromb Haemost. 2009;102(6):1169–75.

163. Chernysh IN, Weisel JW. Dynamic imaging of fibrin network formation correlated with other measures of polymerization. Blood. 2008;111(10):4854–61.

164. Claxton NS, Fellers TJ, Davidson MW. Laser Scanning Confocal Microscopy. 2006.

165. Collet JP, Lesty C, Montalescot G, Weisel JW. Dynamic changes of fibrin architecture during fibrin formation and intrinsic fibrinolysis of fibrin-rich clots. J Biol Chem. 2003;278(24):21331–5.

166. Paddock SW. Principles and practices of laser scanning confocal microscopy. Appl Biochem Biotechnol - Part B Mol Biotechnol. 2000;16(2):127–49.

167. Müller M. Introduction to Confocal Fluorescence Microscopy. 2nd ed. Bellingham: SPIE Press; 2006. 120 p.

168. Nemmar A, Hoet PHM, Dinsdale D, Vermylen J, Hoylaerts MF, Nemery B. Diesel exhaust particles in lung acutely enhance experimental peripheral thrombosis. Circulation. 2003;107(8):1202–8.

169. Kundu SK, Heilmann EJ, Sio R, Garcia C, Davidson RM, Ostgaard RA. Description of an in vitro platelet function analyzer - PFA-100®. Semin Thromb Hemost. 1995 Mar 9;21(SUPPL. 2):106–12.

170. Franchini M. The platelet-function analyzer (PFA-100®) for evaluating primary hemostasis. Hematology. 2005;10(3):177–81.

171. Rumley A, Poorhang E. Standard Operating Procedure for Determination of Clottable (Clauss) Fibrinogen. 2005.

172. Clauss A. Gerinnungsphysiologische Schnellmethode zur Bestimmung des Fibrinogens. Acta Haematol. 1957;17(4):237–46.

173. Bind M-A, Baccarelli A, Zanobetti A, Tarantini L, Suh H, Vokonas P, et al. Air pollution and markers of coagulation, inflammation and endothelial function: Associations and epigene-environment interactions in an elderly cohort. Epidemiology. 2012;23(2):332–40.

174. Zeka A, Sullivan JR, Vokonas PS, Sparrow D, Schwartz J. Inflammatory markers and particulate air pollution: Characterizing the pathway to disease. Int J Epidemiol. 2006;35(5):1347–54.

175. Bonzini M, Tripodi A, Artoni A, Tarantini L, Marinelli B, Bertazzi PA, et al. Effects of inhalable particulate matter on blood coagulation. J Thromb Haemost. 2010;8(4):662–8.

176. Pope III CA, Dockery DW. Health effects of fine particulate air pollution: Lines that connect. J Air Waste Manag Assoc. 2006;56(6):709–42.

177. Reijnders L. Human health hazards of persistent inorganic and carbon nanoparticles. J Mater Sci. 2012;47(13):5061–73.

178. Mills NL, Amin N, Robinson SD, Anand A, Davies J, Patel D, et al. Do inhaled carbon nanoparticles translocate directly into the circulation in humans? Am J Respir Crit Care Med. 2006;173(4):426–31.

179. Brook RD, Franklin B, Cascio W, Hong Y, Howard G, Lipsett M, et al. Air Pollution and Cardiovascular Disease. Circulation. 2004;109(21):2655–2671.

180. Brook RD, Brook JR, Urch B, Vincent R, Rajagopalan S, Silverman F. Inhalation of fine particulate air pollution and ozone causes acute arterial vasoconstriction in healthy adults. Circulation. 2002;105(13):1534–6.

181. Pekkanen J, Brunner EJ, Anderson HR, Tiittanen P, Atkinson RW. Daily concentrations of air pollution and plasma fibrinogen in London. Occup Environ Med. 2000;57(12):818–22.

182. Mannucci PM. Fine particulate: It matters. J Thromb Haemost. 2010;8(4):659–61.

183. Baccarelli A, Barretta F, Dou C, Zhang X, McCracken JP, Díaz A, et al. Effects of particulate air pollution on blood pressure in a highly exposed population in Beijing, China: A repeated-measure study. Environ Heal A Glob Access Sci Source. 2011;10(1):1–10.

184. Cooper DM, Loxham M. Particulate matter and the airway epithelium: The special case of the underground? Eur Respir Rev. 2019;28(153).

185. Brook RD. Cardiovascular effects of air pollution. Clin Sci. 2008;115(5–6):175–87.

186. Nel A. Air Pollution – Related Illness : Effects of Particles. Science (80-). 2005;308(1):804–6.

187. Dunea D, Iordache S, Pohoata A. Fine particulate matter in Urban environments: A trigger of respiratory symptoms in sensitive children. Int J

Environ Res Public Health. 2016;13(12).

188. Raftis JB, Miller MR. Nanoparticle translocation and multi-organ toxicity: A particularly small problem. Nano Today. 2019;26:8–12.

189. Air Quality Expert Group. Fine Particulate Matter (PM2.5) in the United Kingdom. Vol. 1, Department for Environment, Food and Rural Affairs. 2012.

190. Transport for London. PM2.5 concentrations and exposure in London. Vol. 1, Greater London Authority. 2017.

191. Vermylen J, Nemmar A, Nemery B, Hoylaerts MF. Ambient air pollution and acute myocardial infarction. J Thromb Haemost. 2005;3(9):1955–61.

192. Donaldson K, Tran L, Jimenez LA, Duffin R, Newby DE, Mills N, et al. Combustion-derived nanoparticles: A review of their toxicology following inhalation exposure. Part Fibre Toxicol. 2005;2:1–14.

193. Chernyshev V V., Zakharenko AM, Ugay SM, Hien TT, Hai LH, Olesik SM, et al. Morphological and chemical composition of particulate matter in buses exhaust. Toxicol Reports. 2019;6(October 2018):120–5.

194. Charlson R. The Atmosphere. Int Geophys. 2000;72:132–58.

195. Steiner S, Bisig C, Petri-Fink A, Rothen-Rutishauser B. Diesel exhaust: current knowledge of adverse effects and underlying cellular mechanisms. Arch Toxicol. 2016;90(7):1541–53.

196. Niranjan R, Thakur AK. The toxicological mechanisms of environmental soot (black carbon) and carbon black: Focus on Oxidative stress and inflammatory pathways. Front Immunol. 2017;8(JUN):1–20.

197. Niessner R. The many faces of soot: Characterization of soot nanoparticles produced by engines. Angew Chemie - Int Ed. 2014;53(46):12366–79.

198. Rosen H, Hansen ADA, Dod RL, Novakov T. Soot in urban atmospheres: Determination by an optical absorption technique. Science (80-). 1980;208(4445):741–4.

199. Miller MR, Raftis JB, Langrish JP, McLean SG, Samutrtai P, Connell SP, et al. Inhaled Nanoparticles Accumulate at Sites of Vascular Disease. ACS Nano.

2017;11(5):4542–52.

200. Ebelt ST, Petkau AJ, Vedal S, Fisher T V., Brauer M. Exposure of chronic obstructive pulmonary disease patients to particulate matter: Relationships between personal and ambient air concentrations. J Air Waste Manag Assoc. 2000;50(7):1081–94.

201. Nemmar A, Inuwa IM. Diesel exhaust particles in blood trigger systemic and pulmonary morphological alterations. Toxicol Lett. 2008;176(1):20–30.

202. Nemmar A, Hoet PHM, Vanquickenborne B, Dinsdale D, Thomeer M, Hoylaerts MF, et al. Passage of inhaled particles into the blood circulation in humans. Circulation. 2002;105(4):411–4.

203. Nemmar A, Al-Maskari S, Ali BH, Al-Amri IS. Cardiovascular and lung inflammatory effects induced by systemically administered diesel exhaust particles in rats. Am J Physiol - Lung Cell Mol Physiol. 2007;292(3):664–70.

204. Sydbom A, Blomberg A, Parnia S, Stenfors N, Sandström T, Dahlén S-E. Health effects of diesel exhaust emissions. Eur Respir J. 2001;17:733–46.

205. Arnal C, Alzueta MU, Millera A, Bilbao R. Experimental and kinetic study of the interaction of a commercial soot with NO at high temperature. Combust Sci Technol. 2012;184(7–8):1191–206.

206. Marsh H, Rodríguez-Reinoso F. Production and Reference Material. In: Activated Carbon. Elsevier; 2006. p. 454–508.

207. Zhu J, Lee KO, Yozgatligil A, Choi MY. Effects of engine operating conditions on morphology, microstructure, and fractal geometry of light-duty diesel engine particulates. Proc Combust Inst. 2005;30 II(2):2781–9.

208. Burtscher H. Physical characterization of particulate emissions from diesel engines: A review. J Aerosol Sci. 2005;36(7):896–932.

209. Miller FJ, Gardner DE, Graham JA, Lee RE, Wilson WE, Bachmann JD. Size Considerations for Establishing a Standard for Inhalable Particles. J Air Pollut Control Assoc. 1979;29(6):610–5.

210. Oberdörster G, Sharp Z, Atudorei V, Elder A, Gelein R, Lunts A, et al.

Extrapulmonary translocation of ultrafine carbon particles following whole-body inhalation exposure of rats. J Toxicol Environ Heal - Part A. 2002;65(20):1531–43.

211. Harrison RM, Laxen D, Moorcroft S, Laxen K. Processes affecting concentrations of fine particulate matter (PM2.5) in the UK atmosphere. Atmos Environ. 2012;46:115–24.

212. Chow JC. Measurement methods to determine compliance with ambient air quality standards for suspended particles. J Air Waste Manag Assoc. 1995;45(5):320–82.

213. Environmental Protection Agency. National Ambient Air Quality Standards for Particulate Matter; Proposed Rule. 2006.

214. Peters A, Dockery DW, Muller JE, Mittleman MA. Increased particulate air pollution and the triggering of myocardial infarction. Circulation. 2001;103(23):2810–5.

215. Newby DE, Mannucci PM, Tell GS, Baccarelli AA, Brook RD, Donaldson K, et al. Expert position paper on air pollution and cardiovascular disease. Eur Heart J. 2015;36(2):83–93.

216. Chuang KJ, Chan CC, Su TC, Lee C Te, Tang CS. The effect of urban air pollution on inflammation, oxidative stress, coagulation, and autonomic dysfunction in young adults. Am J Respir Crit Care Med. 2007;176(4):370–6.

217. Vermylen J, Hoylaerts MF. The procoagulant effects of air pollution. J Thromb Haemost. 2007;5(2):250–1.

218. Nakane H. Translocation of particles deposited in the respiratory system: A systematic review and statistical analysis. Environ Health Prev Med. 2012;17(4):263–74.

219. Pope CA, Burnett RT, Thurston GD, Thun MJ, Calle EE, Krewski D, et al. Cardiovascular Mortality and Long-Term Exposure to Particulate Air Pollution: Epidemiological Evidence of General Pathophysiological Pathways of Disease. Circulation. 2004;109(1):71–7.

220. Ward-Caviness CK, Nwanaji-Enwerem JC, Wolf K, Wahl S, Colicino E,

Trevisi L, et al. Long-term exposure to air pollution is associated with biological aging. Oncotarget. 2016;7(46):74510–25.

221. Betteridge DJ. What is oxidative stress? Metabolism. 2000;49(2 SUPPL. 1):3–8.

222. Seaton A, Godden D, MacNee W, Donaldson K. Particulate air pollution and acute health effects. Lancet. 1995;345(8943):176–8.

223. Rückerl R, Ibald-Mulli A, Koenig W, Schneider A, Woelke G, Cyrys J, et al. Air pollution and markers of inflammation and coagulation in patients with coronary heart disease. Am J Respir Crit Care Med. 2006;173(4):432–41.

224. Baccarelli A, Martinelli I, Zanobetti A, Grillo P, Hou LF, Bertazzi PA, et al. Exposure to particulate air pollution and risk of deep vein thrombosis. Arch Intern Med. 2008;168(9):920–7.

225. Lind P, Hedblad B, Stavenow L, Janzon L, Eriksson KF, Lindgärde F. Influence of plasma fibrinogen levels on the incidence of myocardial infarction and death is modified by other inflammation-sensitive proteins a long-term cohort study. Arterioscler Thromb Vasc Biol. 2001;21(3):452–8.

226. Peters A, Döring A, Wichmann HE, Koenig W. Increased plasma viscosity during an air pollution episode: A link to mortality? Lancet. 1997;349(9065):1582–7.

227. Ghio AJ, Kim C, Devlin RB. Concentrated Ambient Air Particles Induce Mild Pulmonary Inflammation in Healthy Human Volunteers. Crit Care Med. 2000;162(3):981–8.

228. Schwartz J. Air pollution and blood markers of cardiovascular risk. Environ Health Perspect. 2001;109(SUPPL. 3):405–9.

229. Su TC, Chan CC, Liau CS, Lin L yu, Kao H li, Chuang KJ. Urban air pollution increases plasma fibrinogen and plasminogen activator inhibitor-1 levels in susceptible patients. Eur J Prev Cardiol. 2006;13(5):849–52.

230. Seaton A, Soutar A, Crawford V, Elton R, McNerlan S, Cherrie J, et al. Particulate air pollution and the blood. Thorax. 1999;54(11):1027–32.

231. Kim H, Oh SJ, Kwak HC, Kim JK, Lim CH, Yang JS, et al. The impact of intratracheally instilled carbon black on the cardiovascular system of rats: Elevation of blood homocysteine and hyperactivity of platelets. J Toxicol Environ Heal - Part A Curr Issues. 2012 Jan 1;75(24):1471–83.

232. Radomski A, Jurasz P, Alonso-Escolano D, Drews M, Morandi M, Malinski T, et al. Nanoparticle-induced platelet aggregation and vascular thrombosis. Br J Pharmacol. 2005;146(6):882–93.

233. Nemmar A, Nemery B, Hoet PHM, Vermylen J, Hoylaerts MF. Pulmonary Inflammation and Thrombogenicity Caused by Diesel Particles in Hamsters: Role of Histamine. Am J Respir Crit Care Med. 2003;168(11):1366–72.

234. Nemmar A, Hoet PHM, Vermylen J, Nemery B, Hoylaerts MF. Pharmacological stabilization of mast cells abrogates late thrombotic events induced by diesel exhaust particles in hamsters. Circulation. 2004;110(12):1670–7.

235. Nemmar A, Hoylaerts MF, Hoet PHM, Nemery B. Possible mechanisms of the cardiovascular effects of inhaled particles: Systemic translocation and prothrombotic effects. Toxicol Lett. 2004;149(1–3):243–53.

236. Nemmar A, Hoylaerts MF, Hoet PHM, Dinsdale D, Smith T, Xu H, et al. Ultrafine particles affect experimental thrombosis in an in vivo hamster model. Am J Respir Crit Care Med. 2002;166(7):998–1004.

237. Nemmar A, Vanbilloen H, Hoylaerts MF, Hoet PHM, Verbruggen A, Nemery B. Passage of Intratracheally Instilled Ultrafine Particles from the Lung into the Systemic Circulation in Hamster. Am J Respir Crit Care Med. 2001;164(9):1665–8.

238. Mills NL, Törnqvist H, Robinson SD, Gonzalez M, Darnley K, MacNee W, et al. Diesel exhaust inhalation causes vascular dysfunction and impaired endogenous fibrinolysis. Circulation. 2005;112(25):3930–6.

239. Lucking AJ, Lundback M, Mills NL, Faratian D, Barath SL, Pourazar J, et al. Diesel exhaust inhalation increases thrombus formation in man. Eur Heart J. 2008;29(24):3043–51.

240. Bové H, Bongaerts E, Slenders E, Bijnens EM, Saenen ND, Gyselaers W, et al. Ambient black carbon particles reach the fetal side of human placenta. Nat Commun. 2019;10(3866):1–7.

241. Kampa M, Castanas E. Human health effects of air pollution. Environ Pollut. 2008;151(2):362–7.

242. Ritz B, Wilhelm M, Hoggatt KJ, Ghosh JKC. Ambient air pollution and preterm birth in the environment and pregnancy outcomes study at the University of California, Los Angeles. Am J Epidemiol. 2007;166(9):1045–52.

243. Pedersen M, Giorgis-Allemand L, Bernard C, Aguilera I, Andersen AMN, Ballester F, et al. Ambient air pollution and low birthweight: A European cohort study (ESCAPE). Lancet Respir Med. 2013 Nov 1;1(9):695–704.

244. Slama R, Morgestern V, Cyrys J, Zutavern A, Herbarth O, Wichmann HE, et al. Traffic-related atmospheric pollutants levels during pregnancy and offspring's term birth weight: A study relying on a land-use regression exposure model. Environ Health Perspect. 2007 Sep;115(9):1283–92.

245. Lamichhane DK, Leem J, Lee J, Kim H. A meta-analysis of exposure to particulate matter and adverse birth outcomes. Environ Health Toxicol. 2015;30(1):1–19.

246. Baccarelli A, Martinelli I, Pegoraro V, Melly S, Grillo P, Zanobetti A, et al. Living Near Major Traffic Roads and the Risk of Deep Vein Thrombosis. Circulation. 2010;119(24):3118–24.

247. Dales RE, Cakmak S, Vidal CB. Air pollution and hospitalization for venous thromboembolic disease in Chile. J Thromb Haemost. 2010;8(4):669–74.

248. Pajnič M, Drašler B, Šuštar V, Krek JL, Štukelj R, Šimundić M, et al. Effect of carbon black nanomaterial on biological membranes revealed by shape of human erythrocytes, platelets and phospholipid vesicles. J Nanobiotechnology. 2015;13(1):1–17.

249. Jeyaraj M, Sathishkumar G, Sivanandhan G, MubarakAli D, Rajesh M, Arun R, et al. Biogenic silver nanoparticles for cancer treatment: An experimental report. Colloids Surfaces B Biointerfaces. 2013;106:86–92.

250. Kumar A, Ma H, Zhang X, Huang K, Jin S, Liu J, et al. Gold nanoparticles functionalized with therapeutic and targeted peptides for cancer treatment. Biomaterials. 2012;33(4):1180–9.

251. Gisbert-Garzarán M, Manzano M, Vallet-Regí M. pH-responsive mesoporous silica and carbon nanoparticles for drug delivery. Bioengineering. 2017;4(1).

252. Buxton DB, Lee SC, Wickline SA, Ferrari M. Recommendations of the National Heart, Lung, and Blood Institute Nanotechnology Working Group. Circulation. 2003;108(22):2737–42.

253. Ilinskaya AN, Dobrovolskaia MA. Nanoparticles and the blood coagulation system. Part II: safety concerns. Nanomedicine. 2014;8(6):969–81.

254. Ilinskaya AN, Dobrovolskaia MA. Nanoparticles and the blood coagulation system. Part I: Benefits of nanotechnology. Vol. 8, Nanomedicine. Future Medicine Ltd.; 2013. p. 773–84.

255. Mohan CC, Chennazhi KP, Menon D. In vitro hemocompatibility and vascular endothelial cell functionality on titania nanostructures under static and dynamic conditions for improved coronary stenting applications. Acta Biomater. 2013;9(12):9568–77.

256. Roy SC, Paulose M, Grimes CA. The effect of TiO2 nanotubes in the enhancement of blood clotting for the control of hemorrhage. Biomaterials. 2007;28(31):4667–72.

257. Hudson RE, Holder AJ, Hawkins KM, Williams PR, Curtis DJ. An enhanced rheometer inertia correction procedure (ERIC) for the study of gelling systems using combined motor-transducer rheometers. Phys Fluids. 2017;29(12).

258. MATLAB 2016a Natick, Massachusetts: The MathWorks Inc.

259. Mours M, Winter HH. Time-resolved rheometry. Rheol Acta. 1994;33(5):385–97.

260. Adam M, Delsanti M, Durand D, Hild G, Munch JP. Mechanical properties near gelation threshold, comparison with classical and 3d percolation theories. Pure Appl Chem. 1981 Jan 1;53(8):1489–94.

261. Gennes P-G de. Scaling concepts in polymer physics. Cornell University Press; 1979. 324 p.

262. Audebrand M, Garnier C, Kolb M, Axelos MA V. Gelation of Pectin-Alginate Mixture˚: Ultrastructure and Rheological Properties. In: 3rd International Symposium on Food Rheology and Structure. 2003. p. 517–8.

263. Axelos MA., Kolb M. Crosslinked Biopolymers: Experimental Evidence for Scalar Percolation Theory. Phys Rev Lett. 1990;64(12):1457–60.

264. Werner B, Bu H, Kjøniksen A, Arne S. Characterization of Gelation of Aqueous Pectin via the Ugi Multicomponent Condensation Reaction. Polym Bull. 2006;589:579–89.

265. Yu JM, Blacher S, Brouers F, Homme GL, Je R. Triblock Copolymer Based Thermoreversible Gels . 4 . Effect of the Midblock and Characterization of the Sol - Gel Transition. Macromolecules. 1997;9297(97):4619–25.

266. Townsend N, Bhatnagar P, Wilkins E, Wickramasinghe K, Rayner M. Cardiovscular Disease Statistics 2015. 2015. 1–75 p.

267. Bhatnagar P, Wickramasinghe K, Williams J, Rayner M, Townsend N. The epidemiology of cardiovascular disease in the UK 2014. Heart. 2015;101(15):1182–9.

268. Roth GA, Abate D, Abate KH, Abay SM, Abbafati C, Abbasi N, et al. Global, regional, and national age-sex-specific mortality for 282 causes of death in 195 countries and territories, 1980–2017: a systematic analysis for the Global Burden of Disease Study 2017. Lancet. 2018;392(10159):1736–88.

269. Pajnič M, Drašler B, Šuštar V, Krek JL, Štukelj R, Šimundić M, et al. Effect of carbon black nanomaterial on biological membranes revealed by shape of human erythrocytes, platelets and phospholipid vesicles. J Nanobiotechnology. 2015;13(1):1–17.

270. Fukada E, Kaibara M. Rheological measurements of fibrin gels during clotting. Thromb Res. 1976;8(SUPPL. 2):49–58.

271. Isogai Y, Iida A, Chikatsu I, Mochizuki K, Abe M. Dynamic viscoelasticity of blood during clotting in health and disease. Biorheology. 1973;10(3):411–24.

272. Roberts WW, Lorand L, Mockros LF. Viscoelastic properties of fibrin clots. Biorheology. 1973;10(1):29–42.

273. Vlastos G, Lerche D, Koch B, Samba O, Pohl M. The effect of parallel combined steady and oscillatory shear flows on blood and polymer solutions. Rheol Acta. 1997;36(2):160–72.

274. Kumar V, Madsen T, Zhu H, Semple E. Stability of human thrombin produced from 11 ml of plasma using the thrombin processing device. J Extra Corpor Technol. 2005;37(4):390–5.

275. Molecular Probes. Fibrinogen Conjugates. 2003;28812(1995):1–2.

276. Durand EF. Towards improved correction methodology for regulatory aircraft engine nvPM measurement. 2019.

277. Mikaelsson ME. The Role of Calcium in Coagulation and Anticoagulation. In: Coagulation and Blood Transfusion. Springer US; 1991. p. 29–37.

278. Hibbs AR. Confocal Microscopy for Biologists. Confocal Microsc Biol. 2004;

279. Bateman RM, Leong H, Podor T, Hodgson KC, Kareco T, Walley KR. The Effect of Thrombin Concentration on Fibrin Clot Structure Imaged by Multiphoton Microscopy and Quantified by Fractal Analysis. Microsc Microanal. 2005;11(S02):1018–9.

280. Takahashi A, Kita R, Shinozaki T, Kubota K, Kaibara M. Real space observation of three-dimensional network structure of hydrated fibrin gel. Colloid Polym Sci. 2003;281(9):832–8.

281. Badiei N, Sowedan AM, Curtis DJ, Brown MR, Lawrence MJ, Campbell AI, et al. Effects of unidirectional flow shear stresses on the formation, fractal microstructure and rigidity of incipient whole blood clots and fibrin gels. Clin Hemorheol Microcirc. 2015;60(4):451–64.

282. Ryan EA, Mockros LF, Weisel JW, Lorand L. Structural Origins of Clot Rheology. Biophys J. 1999;77(5):2813–26.

283. Wufsus AR, Rana K, Brown A, Dorgan JR, Liberatore MW, Neeves KB. Elastic behavior and platelet retraction in low- and high-density fibrin gels. Biophys J.

2015;108(1):173–83.

284. Hagman J, Lorén N, Hermansson AM. Effect of gelatin gelation kinetics on probe diffusion determined by FRAP and rheology. Biomacromolecules. 2010;11(12):3359–66.

285. Dixon WJ. Analysis of Extreme Values. Ann Math Stat. 1950;21(4):488–506.

286. Rorabacher DB. Statistical Treatment for Rejection of Deviant Values: Critical Values of Dixon's "Q" Parameter and Related Subrange Ratios at the 95% Confidence Level. Anal Chem. 1991;63(2):139–46.

287. Ryan EA, Mockros LF, Weisel JW, Lorand L. Structural Origins of Fibrin Clot Rheology. Biophys J. 1999;77(5):2813–26.

288. Lowe GDO. Blood rheology in general medicine and surgery. In: Bailliere's Clinical Haematology. 1987. p. 827–61.

289. Williams PR, Hawkins KM, Wright C, Evans PA, Simpkin H, Barrow MS, et al. Rheometrical and computational studies of blood viscoelasticity during coagulation. Clin Hemorheol Microcirc. 2006;35(1–2):123–7.

290. Davies NA, Harrison NK, Morris RHK, Noble S, Lawrence MJ, D'Silva LA, et al. Fractal Dimension (df) as a new structural biomarker of clot microstructure in different stages of lung cancer. Thromb Haemost. 2015;114(6):1063–80.

291. Kuijper PHM, Gallardo Torres HI, Lammers JWJ, Sixma JJ, Koenderman L, Zwaginga JJ. Platelet and fibrin deposition at the damaged vessel wall: Cooperative substrates for neutrophil adhesion under flow conditions. Blood. 1997;89(1):166–75.

292. Shibeshi SS, Collins WE. The rheology of blood flow in a branced arterial system. Appl Rheol. 2005;15(6):398–405.

293. Wayland H. Rheology and the Microcirculation. Gastroenterology. 1967;52(2):342–55.

294. Lipowsky HH, Kovalcheck S, Zweifach BW. The distribution of blood rheological parameters in the microvasculature of cat mesentery. Circ Res. 1978;43(5):738–49.

295. Lee AJ. The role of rheological and haemostatic factors in hypertension. J Hum Hypertens. 1997;11(12):767–76.

296. Hathcock JJ. Flow effects on coagulation and thrombosis. Arterioscler Thromb Vasc Biol. 2006;26(8):1729–37.

297. Anand M, Rajagopal K, Rajagopal KR. A viscoelastic fluid model for describing the mechanics of a coarse ligated plasma clot. Theor Comput Fluid Dyn. 2006;20(4):239–50.

298. van Kempen THS, Donders WP, van de Vosse FN, Peters GWM. A constitutive model for developing blood clots with various compositions and their nonlinear viscoelastic behavior. Biomech Model Mechanobiol. 2016;15(2):279–91.

299. Sousa PC, Pinho FT, Alves MA, Oliveira MSN. A review of hemorheology: Measuring techniques and recent advances. Korea Aust Rheol J. 2016;28(1):1–22.

300. Janmey PA, Winer JP, Weisel JW. Fibrin gels and their clinical and bioengineering applications. J R Soc Interface. 2009;6(30):1–10.

301. Gorbet MB, Sefton M V. Biomaterial-associated thrombosis: Roles of coagulation factors, complement, platelets and leukocytes. Biomaterials. 2004;25(26):5681–703.

302. Yun SH, Sim EH, Goh RY, Park JI, Han JY. Platelet activation: The mechanisms and potential biomarkers. Biomed Res Int. 2016;2016:10–4.

303. Heemskerk JWM, Bevers EM, Lindhout T. Platelet activation and blood coagulation. Thromb Haemost. 2002;88(2):186–93.

304. Diez-Silva M, Dao M, Han J, Lim C-T, Suresh S. Shape and Biomechanical Characteristics of Human Red Blood Cells in Health and Disease. MRS Bull. 2010;35(5):382–8.

305. Pidiatrie F. Spiky Red Cells. Br Med J. 1970;2(5701):68.

306. Bosman GJCGM. Disturbed red blood cell structure and function: An exploration of the role of red blood cells in neurodegeneration. Front Med. 2018;5(JUL):1–6.

307. Geekiyanage NM, Balanant MA, Sauret E, Saha S, Flower R, Lim CT, et al. A coarse-grained red blood cell membrane model to study stomatocyte-discocyteechinocyte morphologies. PLoS One. 2019;14(4):1–25.

308. Anderlohr C, Schaber K. Direct transfer of gas-borne nanoparticles into liquid suspensions by means of a wet electrostatic precipitator. Aerosol Sci Technol. 2015;49(12):1281–90.

309. Shaw R. Dynamic Light Scattering Training: Achieving reliable nano particle sizing. Malvern. 2014.

310. Malvern Instruments. Sample dispersion and refractive index guide. 2007.

311. Standardization IO of. ISO 22412:2017, Particle size analysis — Dynamic light scattering (DLS). 2017.

312. Malvern Instruments. Dynamic Light Scattering : An Introduction in 30 Minutes. 2014.

313. Malvern Instruments. Zeta Potential: An Introduction in 30 Minutes. Vol. 2. 2014.

314. Curtis DJ, Holder A, Badiei N, Claypole J, Walters M, Thomas B, et al. Validation of Optimal Fourier Rheometry for rapidly gelling materials and its application in the study of collagen gelation. J Nonnewton Fluid Mech. 2015;222:253–9.